5-2017

Jet-hadron correlations relative to the event plane Pb--Pb collisions at the LHC in ALICE

Joel Anthony Mazer
University of Tennessee, Knoxville, jmazer@vols.utk.edu

To the Graduate Council:

I am submitting herewith a dissertation written by Joel Anthony Mazer entitled "Jet-hadron correlations relative to the event plane Pb--Pb collisions at the LHC in ALICE." I have examined the final electronic copy of this dissertation for form and content and recommend that it be accepted in partial fulfillment of the requirements for the degree of Doctor of Philosophy, with a major in Physics.

Christine Nattrass, Major Professor

We have read this dissertation and recommend its acceptance:

Soren Sorensen, Edmund Perfect, Kenneth Read

Accepted for the Council:

Dixie L. Thompson

Vice Provost and Dean of the Graduate School

(Original signatures are on file with official student records.)

Jet-hadron correlations relative to the event plane in Pb–Pb collisions at the LHC in ALICE

A Dissertation Presented for the

Doctor of Philosophy

Degree

The University of Tennessee, Knoxville

Joel Anthony Mazer

May 2017

Acknowledgements

I would first like to express my gratitude to my supervisor, Christine Nattrass, who kept a sense of humor even when I lost mine. Her selfless time and care to offer help, review my work, and answer my endless questions were of most help to me producing this thesis work and building me as a graduate student. She also makes a heck of a mead.

I would like to thank the rest of my doctoral committee: Soren Sorensen, Ken Read and Ed Perfect. Ed for serving as my member from outside of the Physics Department. Soren and his enthusiam, discussions, and hospitality were very appreciated. Ken for his lengthy conversations, error analysis advice, and his ability to bring a unique witt to our group. Irakli, Adam, Charles, and Kyle for useful discussions. To some genuine friends, who had helpful conversations along the way: Adam Holt, Craig, and Brett. And also Chris, for lending an ear, his time, and providing help when he could. I also thank the rest of the RHIP group at both UTK and ORNL.

I am further grateful to the analysis groups of ALICE: PWGJE, EMCal Jet, Jet-hadron correlations, EMCal and Correlations groups. I thank the jetters who came to the meetings and listened to all my analysis updates. To Joern, Oliver, Jana, and Marco, who served as jet conveners and provided helpful discussions and offered insightful suggestions to the analysis. To Alice and Jochen for serving as my ARC. To Rosi, Salvatore, Redmer, and Marta for your aid in coding, framework logistics, GIT commits, and the occassional lego train. To the Yale group for our continued jet-hadron team work. To Megan Connors for insight, discussion and providing me

with my first jet-related code. Which I would transform and build off of into my main AliROOT task. To Terry, for introducing me to the EMCal lab, the "tunnel" and for mentoring with everything EMCal. To Martin, who continued with EMCal support. To David, for Physics and life discussions, ping pong, your skis and boots, mentorship, and a great supervisor while at CERN.

I would lastly like to extend my thanks and appreciation to my family, my grandmother and mother in particular. They both kept on me to stay focused and knew I would never give up. My mom listened to tons of rants and complaints about how much I always had to do. I can never fully thank my girlfriend, JoAnna, who supported me unconditionally during the last 2+ years of the analysis, which were the hardest on many levels. She put up with my crankiness, sleeplessness, tons of complaints, watched me go crazy, and still loved me.

THANK YOU!

Abstract

In relativistic heavy ion collisions at the Large Hadron Collider (LHC), a hot, dense and strongly interacting medium known as the Quark Gluon Plasma (QGP) is produced. Quarks and gluons from incoming nuclei collide to produce partons at high momenta early in the collisions. By fragmenting into collimated sprays of hadrons, these partons form 'jets'. Within the framework of perturbative Quantum Chromodynamics (pQCD), jet production is well understood in pp collisions. We can use jets measured in pp interactions as a baseline reference for comparing to heavy ion collision systems to detect and study jet quenching. The jet quenching mechanism can be studied through the angular correlations of trigger jets with charged hadrons and is examined in transverse momentum bins of the trigger jets, transverse momentum bins of the associated hadrons, and studied as a function of collision centrality. A highly robust and precise background subtraction method is used in this analysis to remove the complex, flow dominated, heavy ion background. The analysis of angular correlations for different orientations of the trigger jet relative to the event plane allows for the study of the path length dependence of medium modifications to jets. The event plane dependence of azimuthal angular correlations of charged hadrons with respect to the axis of an R=0.2 reconstructed 'trigger' full (charged + neutral) jet in Pb–Pb collisions at $\sqrt{s_{NN}} = 2.76$ TeV in ALICE will be discussed. Results will be compared for three angular bins of the trigger jet relative to the event plane in mid-peripheral events. The status of jet yields and widths relative to the event plane will be discussed. There is no significant event plane dependence within the current

uncertainties. Path length dependence of energy loss is seen to be a secondary effect to statistical fluctuations and in-medium energy loss mechanisms.

Table of Contents

List of Tables

List of Figures

Chapter 1

Introduction

This chapter will introduce and summarize the fundamental particles and their interactions within the Standard Model of Physics. It will explain briefly how theory describes this model and the properties of the fundamental particles. After an understanding of the basic properties is given, the evolutionary phases of the universe will be discussed and the early stages will be looked at by discussing the nuclear phase diagram. In high energy heavy-ion collisions a medium of deconfined quarks and gluons can be created allowing us to study the state of nuclear matter which existed slightly after the Big Bang. Ch. 2 will look into experimental signatures of this medium and discuss various probes that can be used experimentally to gain a better understanding of this phase of nuclear matter. In particular, the use of jets as a probe, which form early in a collision from an initial hard scattering will be the center point of this thesis. Jets will be discussed in much more depth in Ch. 3. This thesis will show the measurement of jet-hadron correlations relative to the event plane in order to study the path length dependence of potential interactions with the medium. This will improve our understanding of energy loss. The experimental setup used for this analysis will be overviewed in Ch. 4. The analysis will be introduced in Ch. 5 and the various experimental methods will be will be discussed in Ch. 6. Finally, the results will be shown in Ch. 7 with a conclusion and followed by an outlook in Ch. 8.

1.1 Standard Model

All known matter consists of leptons, quarks, and force mediators. This is represented by the table summarizing all fundamental particles in Fig. 1.1 [2]. There are 12 elementary particles which have a spin $s = 1/2$, called fermions. These 12 fermions each have a corresponding anti-particle. The fermions are arranged by how they interact. A summary of available Standard Model interactions are shown in Fig. 1.2 [3]. These particles do not interact with each other directly, but do so through force carriers for the strong, weak, and electromagnetic interactions. These force carriers include gluons, photons, and the $W^{\pm}$ and Z^0 bosons and are commonly referred to as gauge bosons. In addition there is a newly discovered Higgs boson which has no spin, electric charge, or color charge, and is the quantum excitation of the Higgs field.

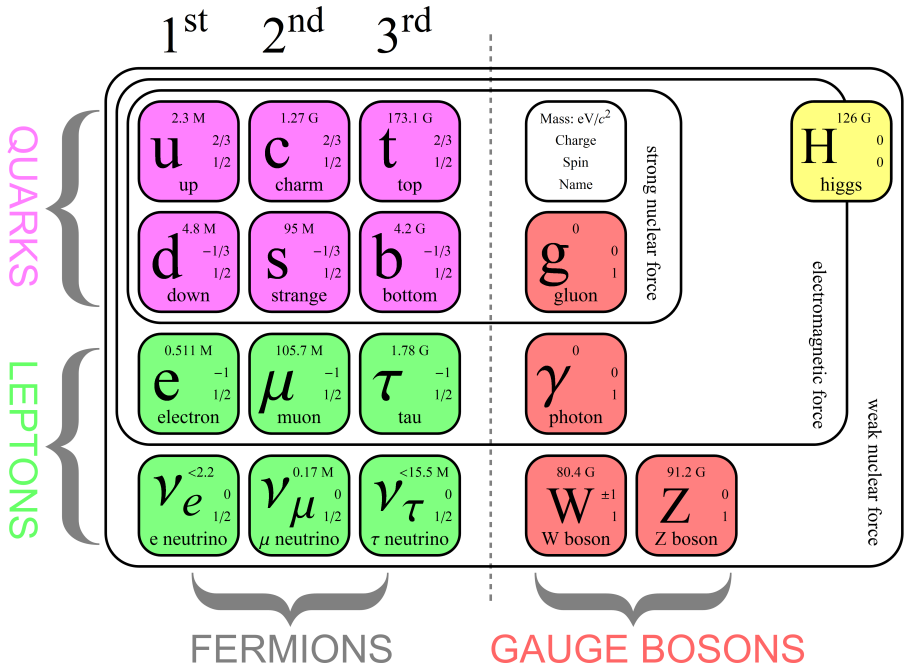

Figure 1.1: Summary of all fundamental particles [2].

The fermions consist of six quarks and six leptons. Pairs of each are grouped by generation (1st, 2nd, or 3rd). The pairs are formed from a classification of similar physical behavior. The members of each generation are arranged such that as the

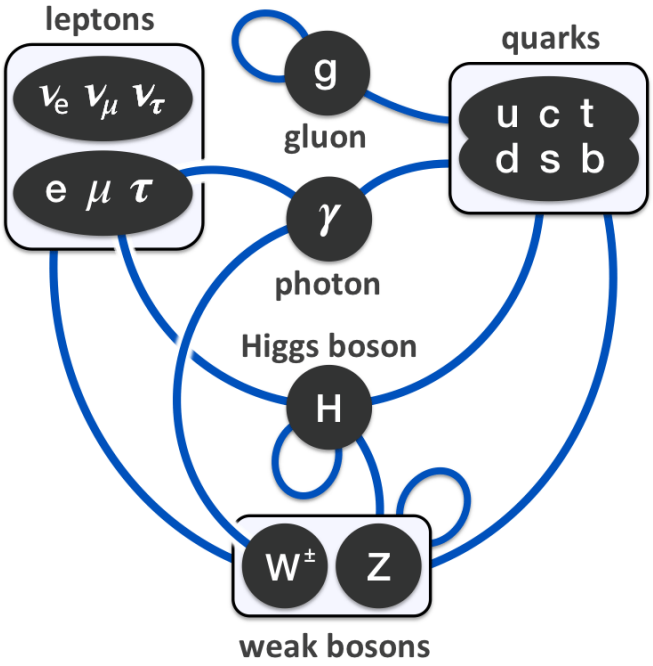

Figure 1.2: The interaction scheme for particles of the Standard Model of Physics [3].

generation increases ($1 \rightarrow 2$, $2 \rightarrow 3$), so to does the instability and mass of the particles, except for the neutrinios. In addition, charged particles belonging to the 1st generation do not decay. It is these particles, the up quark (u), down quark (d), and the electron (e) that make up normal matter. The protons and neutrons, or nucleons, form the nuclei of all atoms and are orbited by electrons. Hardron of made up of two families of subatomic particles: baryons and mesons. Baryons are the bound states of three quarks, while mesons are the bound states of a quark-antiquark pair. Charged particles from the 2nd and 3rd generations are more exotic and die off by decaying with very short lifetimes [4].

The remaining six fermions carry no color charge and consist of the electron, muon, and tau along with their corresponding neutrinos. The electron, muon, and tau each have a charge of -1 and interact via the electromagnetic force, with photons as their force carriers. The three corresponding neutrinos carry no charge, but interact via the weak nuclear force with gauge bosons as their force carriers [4].

The six quarks carry color charge, which allows them to interact via the strong force. The strong force is described by quantum chromodynamics (QCD) which is discussed in Sec. 1.2. Color charges are analogous to the electrical charges of Quantum ElectroDynamics (QED), but differ in that instead of being a scalar quantity, they are a quantum vector of charge [5]. The strong force increases with distance of separation. As this separation increases, the potential energy exceeds the pair-production energy and a quark-antiquark pair can be produced. Due to their production, we are never able to isolate and observe a quark by itself. This property is called confinement [6,7].

1.2 Quantum chromodynamics (QCD)

Quantum ChromoDynamics (QCD) is a non-abelian gauge theory used to describe the strong interaction experienced by quarks and gluons. Properties of QCD include confinement and asymptotic freedom. Asymptotic freedom refers to the effect of the strong force between quarks becoming weaker at smaller distances, allowing them to act like independent particles. A part of QCD theory is the indication for a new phase of nuclear matter existing at very high energy densities. QED and its' extension to the Electroweak Standard Model work very well until we approach the energy scale where the strength of the coupling constant, or strength of the interaction, becomes infinite [8]. All theories which are not asymptotically free suffer from this singuarlity, but QCD can be completely defined with only a few parameters [8]. The coupling constant α_s is shown in Fig. 1.3 [8] as a function of momentum transfer, Q. A comparison is shown between various theories and different sets of experimental data. In QCD, the coupling constant is large at low momentum transfer and decreases logarithmically with Q^2 [8]. This allows for the interaction strength to be computed perturbatively when the coupling is small. A direct consequence of this is the phenomenon of asymptotic freedom.

At low energy, QCD states, "Any strongly interacting system at zero temperature and density must be a color singlet at distance scale larger than Λ_{QCD}" [5].

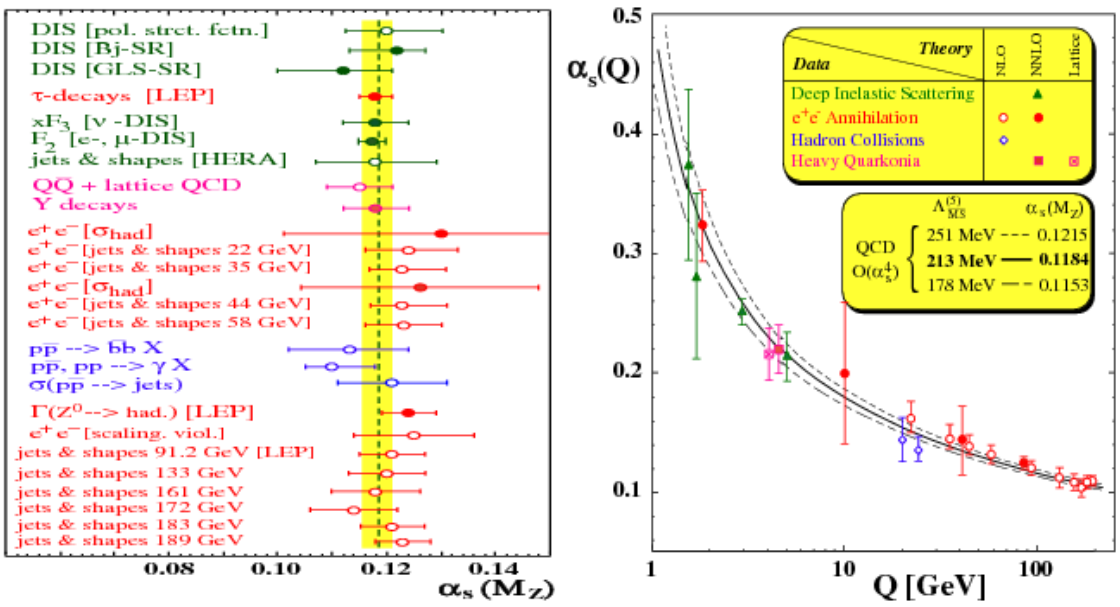

Figure 1.3: Left: Summary of α_s. Right: Running coupling constant (α_s) as a function of momentum transfer Q compared for experimental data of different processes and various theoretical predictions [8].

Consequentially, isolated quarks cannot exist freely in nature. This is another key property of QCD which makes it unique. The confinement of quarks and gluons is purely a theoretical conjecture that is consistent with experiment, but will remain hard to prove within the QCD framework [5]. Due to the effects of confinement and the behaviour of the coupling, the interaction strength grows with the distance between a quark-antiquark pair. Consequently, when bound quarks are separted, analogously to a stretched spring, at some limit it will break into a new spring, and for the quark/antiquark pair, it will become more energetically favorable to create a new quark/antiquark pair from the potential energy of the system. This process is illustrated in Fig. 1.4 [9].

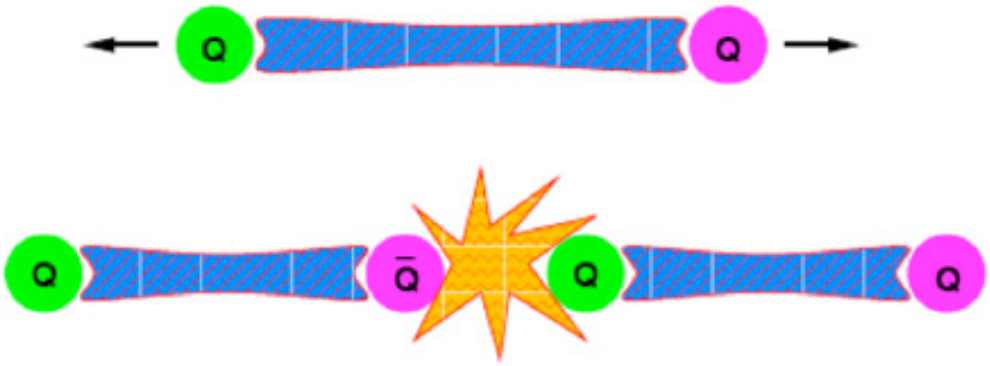

Figure 1.4: Cartoon illustration of color confinement of quarks [9].

1.3 Phases of nuclear matter

Solid nuclear matter at low temperature and pressure consists of protons and neutrons bound inside of nuclei. When nuclear matter is at high temperatures and energy densities, it is a liquid called a Quark Gluon Plasma (QGP) and is characterized by the deconfinement of quarks and gluons. The QGP existed a few millionths of a second after the Big Bang. The evolution of the state of the Universe since the Big Bang is shown in Fig. 1.5 [10]. As the QGP expanded and cooled, hadron formation began. The existence of a QGP can be inferred from lattice gauge simulations of QCD [11]. Lattice gauge simulations predict the phase transition from hadrons to quarks and gluons close to a critical temperature of $T_c \approx 170$ MeV for zero net baryon density [12].

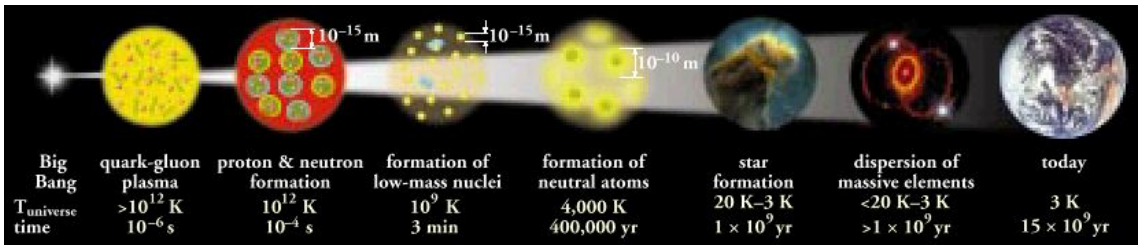

Figure 1.5: Evolution of state of the Universe from the Big Bang to today [10].

The phase diagram of nuclear matter is shown in Fig. 1.6 [13]. The y-axis is temperature T and the x-axis is the baryon chemical potential μ_B. Baryon chemical potential denotes the net baryon number in the system. When the baryon chemical potential is very low, this signifies a balance between the number of baryons and anti-baryons in the system. For low μ_B and at high temperature, we would have a state on this phase diagram comparable to that of the early universe. Normal nuclear matter occurs at low temperatures (near the x-axis) and at a baryon chemical potential close to 1 GeV. As temperatures increase, the system forms a hadron gas. At even higher temperatures, the system undergoes a phase transition to a QGP. At low μ_B and high T, this transition is known to be a crossover transition [14]. At high μ_B and low T the transition is thought to be first order [14]. Therefore at intermediate values, a critical point is predicted to occur. The Large Hadron Collider experiment expects to reach temperatures of 2-4 times that of the critical temperature in the collisions of highly energetic heavy ions [15]. In a high energy Pb-Pb collision, the system would quickly reach a state above the first order transition line, but with a μ_B to the left of the critical point.

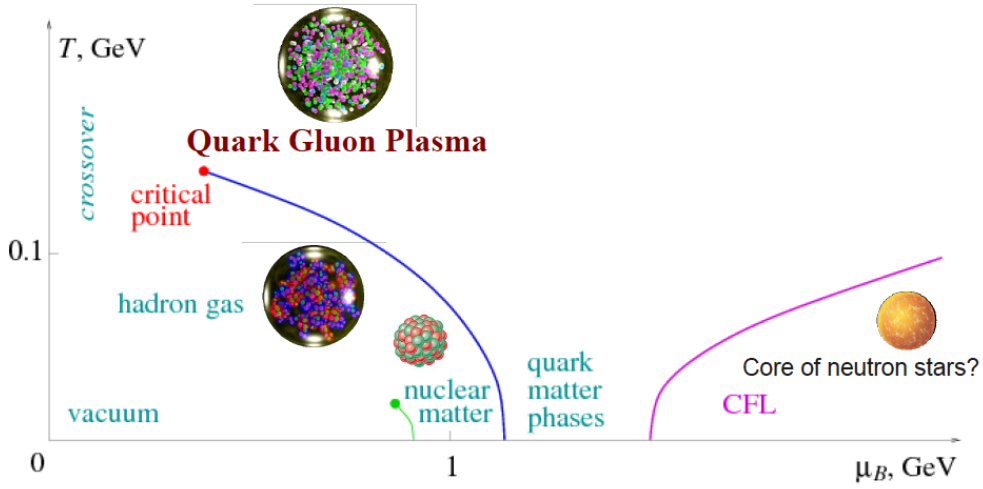

Figure 1.6: Phase diagram of the QGP [13].

1.4 Heavy-ion collisions

Temperature and baryon density are the most common parameters used to represent the phase diagram, shown in Fig. 1.6. The QGP region of this nuclear phase diagram can be accessed either by increasing the baryon density, by compressing the nuclear matter, or by increasing the temperature above the phase transition threshold [16,17]. The first approach can not be acheived in the lab, but by colliding high energy heavy-ions, strongly interacting matter with an energy density required to reach the critical temperature can be achieved. This threshold is on the order of 1 GeV/fm^3 [18,19].

By understanding the evolution of the system in relativistic heavy-ion collisions, experimental observables and probes, discussed in Ch. 2, can be used to prove the existence and properties of the QGP. The time evolution of a high energy heavy-ion collision is shown in Fig. 1.7 [20]. The evolution of the system can be described well by hydrodynamics because the mean free path of the interaction system is small compared to the system size [21]. After the two length contracted discs approach each other and begin to collide, collisions between partons can happen, resulting in heavy quarks or jets. When the nuclei overlap, they can create the mean energy density required to produce a QGP. During this interaction, the nuclei melt, freeing the quarks and gluons. The system then begins propagating particles outward where particle production begins to take over [17]. These new particles along with some of the original particles from the colliding nuclei can interact with the created medium. As the system expands and cools to the critical temperature, a phase transition to a hadronic phase takes place. This new phase is characterized by a changed in the effective degrees of freedom (from partons to hadrons) [21]. The system is still in a local thermal equilibrium at this point allowing inelastic interactions to take place. The system will continue to evolve and eventually reach a chemical freezeout temperature where inelastic collisions will cease [22]. This is characterized by a mixed phase of a hadron gas and a QGP. The medium cools further and reaches a period of thermal freezeout defined by the stoppage of hadronic collisions [22]. It is here that

the kinematic properties of the outgoing hadrons are defined [21]. These hadrons continue moving outward where they are eventually detected individually.

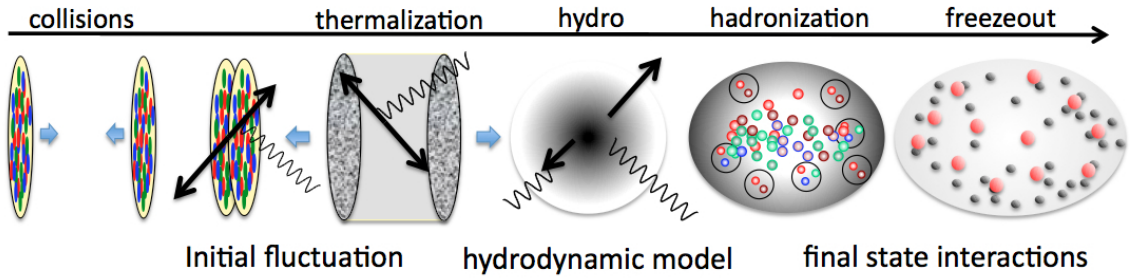

Figure 1.7: The time evolution of a high energy heavy-ion collision [20].

In a reference system such as pp collisions, where no QGP is formed, the partons directly freeze-out into a hadron phase. By comparing the kinematic properties and chemical composition of the produced particles between a A-A collisional system to the baseline system where no QGP is produced, information about the QGP can be explored.

1.5 Summary

This chapter set the groundwork on introducing the fundamental particles and their interactions, QCD, the time evolution of the Universe and relating to the nuclear phase diagram. Chapter 2 will introduce the various experimental techniques used to study the QGP and infer its properties. The primary probe used in this thesis, jets, will be fully introduced in Chapter 3. The goal of this thesis is to use jets as a probe of the QGP by studying the charged particle azimuthal correlations relative to a trigger jet. These correlations will be separated such that the trigger jets will be shown in different relative orientations to the reconstructed event plane. The event plane will be discussed in Sec. 2.2, 2.3, and the calculation of and corrections for its measurement in 6.1. By looking at jet-hadron correlations relative to the event plane,

we can use the variable path length length to explore energy loss mechanisms of the medium.

Chapter 2

Studying the QGP and its signatures

2.1 The beginning

In 1974, T. D. Lee, proposed the idea that quarks and gluons could exist in a state where they could freely flow within a given volume due to the weak attraction at small distances [23, 24]. It was suggested that collisions of heavy nuclei could create this strongly interacting matter at high energy density [23, 25]. This phase of matter was soon named "the Quark Gluon Plasma" [23]. As theories further developed into the 1980's, dedicated programs to study the QGP through heavy-ion collisions began. The first was the Super Proton Synchrotron (SPS) at the European Organisation for Nuclear Research (CERN) [26]. The energy densities required to create the QGP are currently reached in high energy heavy-ion collisions at the Relativistic Heavy Ion Collider (RHIC) located at the Brookhaven National Lab (BNL) and the Large Hadron Collider at CERN. This chapter will introduce some of the properties which are used in defining the process of a heavy-ion collision. In addition, various signatures used in experiment to determine properties of the QGP will be discussed.

2.2 QGP studies

We know from previous studies that the QGP is a hot, dense liquid of quarks and gluons which is nearly opaque to colored probes [27–30]. As the system expands in the presence of a QGP, it cools and eventually becomes so dilute that its constituents hadronize [31]. These hadrons are often classified as "soft" or "hard" [32], where the distinction comes from Q^2, the momentum transferred in a collision. Momentum transverse to the beam pipe, referred to by p_T, is useful in characterizing the physics of high energy collisions. In this work we consider particles with p_T <2 GeV/c soft, with p_T >6 GeV/c hard, and the range 2< p_T <6 to be intermediate. Most hard particles are created by hard parton scattering early in the collision while most soft particles are generally created later when the medium has expanded and cooled [33].

The reaction plane geometry of a noncentral heavy-ion collision with incoming nuclei is shown in Fig. 2.1 [13]. The reaction plane is the plane defined by the beam direction (z-axis) and the impact parameter direction (x-axis) [34]. Many processes depend on the reaction plane and can be understood from analyzing the dynamical properties of the resulting hadrons.

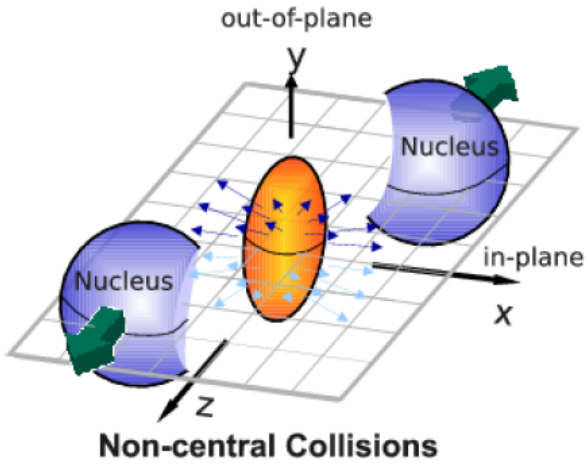

Figure 2.1: Cartoon depiction of the reaction plane geometry of noncentral heavy-ion collisions with incoming nuclei [13].

2.3 Soft Probes

During heavy-ion collisions, thermal QCD matter is produced. It is generally dominated by soft partons in the momentum (temperature) range of 100-300 MeV [35]. Over 99% of particles produced in heavy-ion collisions emerge with a momentum lower than 2 GeV/c [36]. Soft processes can give access to the size, temperature, composition, and dynamics of the QGP [36].

2.3.1 Flow

In a heavy-ion collision, the colliding nuclei are generally not head-on. The overlap of the colliding nuclei is described by centrality, which is expressed as a percentage of the cross section, ranging from 0-100% of all the collisions. The dense overlap region is approximately ellipsoidal [37], as seen in Fig. 2.1 [13]. The overlap causes a pressure gradient with an angular dependence, which is largest in the direction of the reaction plane rather than orthogonal to it [37,38]. This causes more particles to be produced along the direction of the reaction plane [38]. Initial state spatial deformations in the overlap region are converted into an anisotropic momentum distribution in the final state [31,34,39]. This occurs for nondue to the very strong interactions between the quarks and gluons and is an indication that the system is exhibiting collective motion [40]. The resulting asymmetry causes the medium to expand non-uniformily from the existing pressure gradients pushing outwards. This collective expansion of the medium is called flow and is a signal that partons are strongly interacting in the presence of a QGP [31]. For a non-viscous ideal fluid, the Euler relation, given by Eqn. 2.1, says the pressure gradient drives the collective flow [41].

$$\frac{d}{dt}(\varepsilon\vec{v}) = -\nabla P \tag{2.1}$$

The azimuthal anisotropy of the particle yield is the clearest signature of collective flow in heavy-ion collisions [31]. The final state particle yield can be written by a Fourier series, given by Eqn. 2.2 to show the azimuthal dependence [34, 42].

$$E\frac{d^3N}{d^3p} = \frac{1}{2\pi}\frac{d^2N}{p_T dp_T dy}\left(1 + \sum_{n=1}^{\infty} 2v_n \cos[n\left(\phi - \psi_R\right)]\right) \tag{2.2}$$

E is the energy of the particle, p the momentum, p_T the transverse momentum, ϕ the azimuthal angle, ψ_R the reaction plane angle, and y the rapidity [34]. Rapidity, given by Eqn. 2.3 [43],

$$y = \frac{1}{2}\ln\left[\frac{(E + p_z)}{(E - p_z)}\right] = \frac{1}{2}\ln\left[\frac{(E + p_z)^2}{(E^2 - p_z^2)}\right] \tag{2.3}$$

is used to describe the kinematics of a particle relative to the beam axis. It is more useful than a polar angle since particle production is constant with rapidity. The strength of the asymmetry is characterized by the coefficients v_n. The second coefficient, v_2, is called the elliptic flow. Particle production is enhanced in the direction orthogonal to the reaction place. At low energies, this is due to the effect that the spectator parts of the nuclei block the matter in the direction of the reaction plane and squeeze it out in the opposite direction. At higher center of mass energies, these spectator components free the way sufficiently quickly and particle production is enhanced in the reaction plane. This phenomenon is expected in hydrodynamic scenarios in which the larger pressure gradients within the reaction plane drive a stronger expansion. The observed asymmetries are roughly consistent with a qualitative hydrodynamic picture of the collision [42].

Because it agrees with hydrodynamic models [31], the magnitude of flow is a probe of the level of thermalization of the medium and a characteristic of the number of interactions. This has led the community to accept the notion that the strongly coupled QGP flows like the perfect liquid [27] which has a value of shear viscosity to entropy density η/s near a minimum bound of $\frac{1}{4\pi}$ [44], proposed by [45]. The flow of

particles in the QGP is a clear sign that they are behaving in a collective way with nearly no resistance [27, 46].

Elliptic flow scaled by the number of constituent quarks for different hadrons is shown in Fig. 2.2 [47]. It can be seen that scaling the flow parameters by the quark content n_q resolves the baryon-meson separation of final state hadrons [47]. This view is consistent with quark degrees of freedom in the initial flowing matter [37] and can be interpreted as evidence of the collectivity developed at the partonic stage of the evolution of the system in heavy-ion collisions [48]. There have been evidence of deviations from quark scaling measured by PHENIX for noncentral collisions [49].

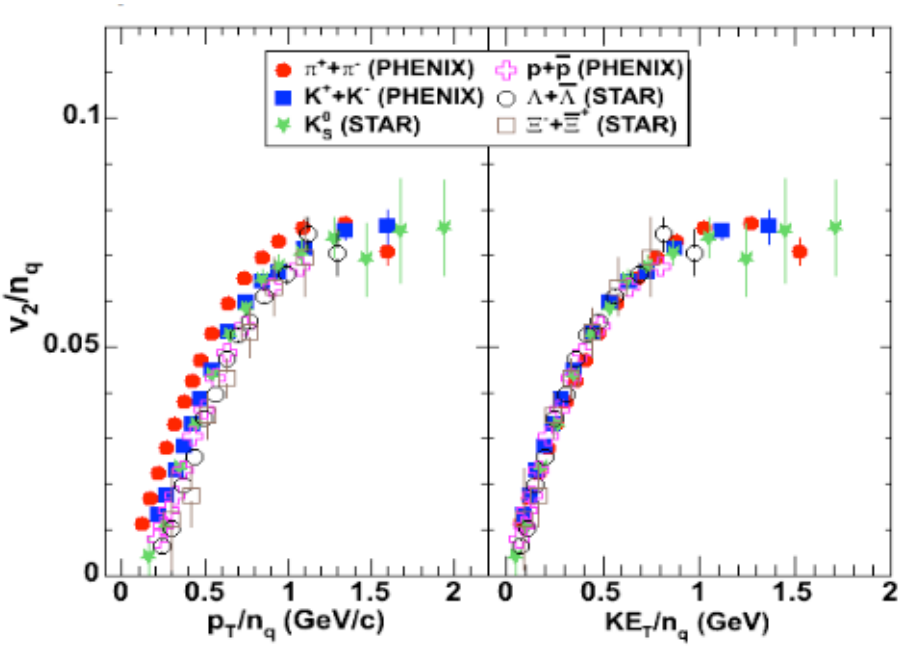

Figure 2.2: Quark scaling of elliptic flow component v_2 for p_T and KE_T [37]. By scaling the flow parameters by the quark content n_q resolves the baryon-meson separation of final state hadrons [47].

2.3.2 Baryon enhancement

Inclusive baryon/meson ratios can be measured to study the particle production in the medium. Baryon/meson ratio measurements in heavy-ion collisions have revealed

a significant enhancement at intermediate p_T compared to pp collisions [50]. This is generally interpreted as evidence that the dominant mechanism of particle production in the thermal medium is not vacuum fragmentation [50].

The p/π ratio for both Pb–Pb collisions at $\sqrt{s_{NN}} = 2.76$ TeV and pp collisions at $\sqrt{s} = 7$ TeV is shown in Fig. 2.3 [51]. The plot shows baryon enhancement for intermediate p_T in Pb–Pb collisions relative to pp collisions. The large ratio at intermediate p_T is evidence for particle formation distinctly different in heavy-ion collisions from the fragmentation process in elementary e^+e^- and pp collisions [52]. Above $p_T = 8$ GeV/c, the baryon/meson ratio in heavy-ion collisions is consistent with the ratio in pp collisions.

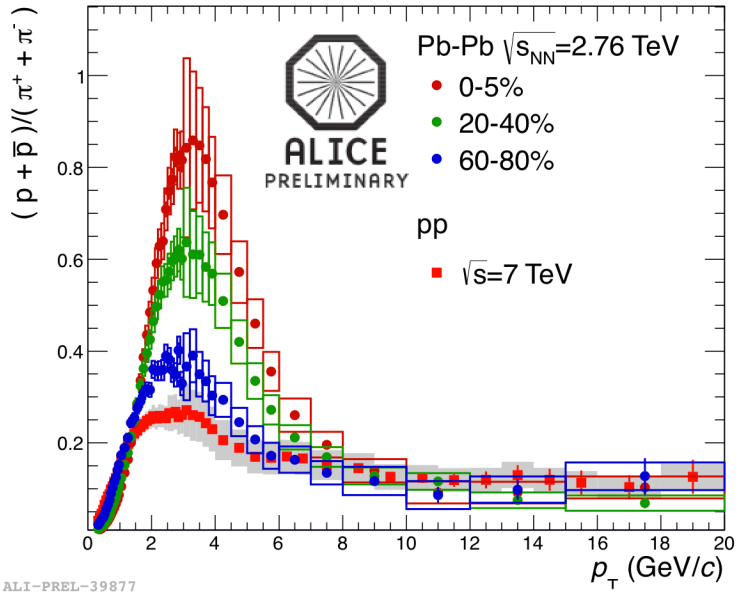

Figure 2.3: Baryon/meson ratio is shown for centralities of 0-5%, 20-40%, and 60-80% in Pb–Pb collisions at $\sqrt{s_{NN}} = 2.76$ TeV. Also shown is the ratio for pp collisions at $\sqrt{s} = 7$ TeV. This shows baryon enhancement of Pb–Pb collisions compared to pp collisions [51].

This baryon enhancement in the intermediate transverse momentum region is generally understood to come from hadronization through recombination of quarks in the medium [50,53]. This is summarized by the cartoon schematic in Fig. 2.4 [54]. The recombination model assumes particle production occurs from quarks which are near

each other in space and relative velocity. In recombination, the hadron momentum is the sum of the momenta of the partons that recombine. We see in Fig. 2.4 that the quark distribution is steeply falling with increasing p_T, which shows that making a 6 GeV/c meson from two 3 GeV/c quarks is more favorable than the fragmentation of a 8 GeV/c parton. For similar reasons, this particle production mechanism is used to also explain the constituent quark scaling.

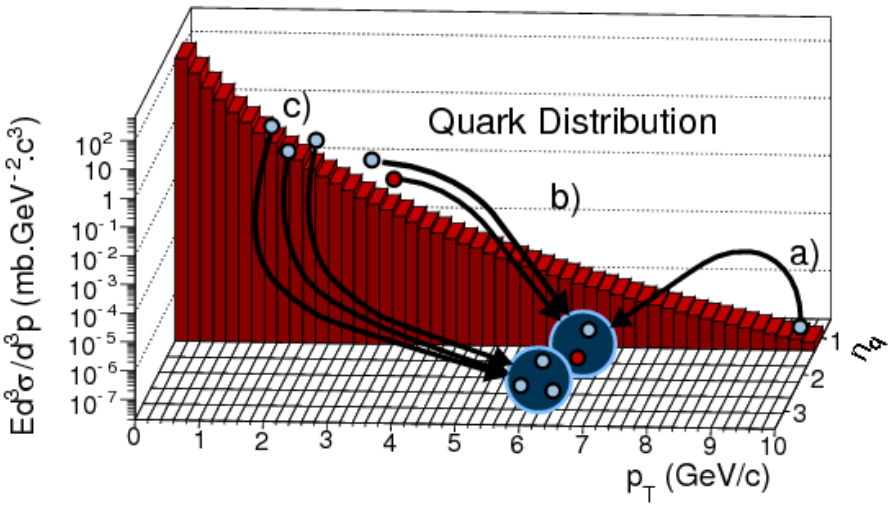

Figure 2.4: Cartoon schematic of recombination and fragmentation to a p_T spectrum of partons [54].

2.3.3 Transverse energy measurement (E_T)

The mean transverse energy (E_T) per unit pseudorapidity $\langle dE_T/d\eta \rangle$ gives a measure of the amount of longitudinal energy of the colliding nuclei which is carried off by particles produced in the transverse direction [55]. E_T can provide information on the energy densities attained and studies of the $\sqrt{s_{NN}}$ and centrality dependence can offer insight into the conditions of the system prior to both thermal and chemical equilibrium [55].

The precision tracking detectors and electromagnetic calorimeters of ALICE allow for the use of multiple methods when measuring E_T. Results are comparable for four different methods of $\langle dE_T/d\eta \rangle$ [55]. The ALICE measurement of $\langle dE_T/d\eta \rangle / (\langle dN_{ch}/d\eta \rangle)$ for Pb–Pb collisions at $\sqrt{s_{NN}} = 2.76$ TeV for 0-5% centrality at midrapidity is compared in Fig. 2.5 to prior measurements made at different $\sqrt{s_{NN}}$. The extrapolation band from Fig. 2.5 underestimates the observed value reported by ALICE. While the measurement was higher than expected at LHC collisional energies, it showed up as an increase in mean energy per particle and not as increased particle production which was seen at lower $\sqrt{s_{NN}}$ energies [55].

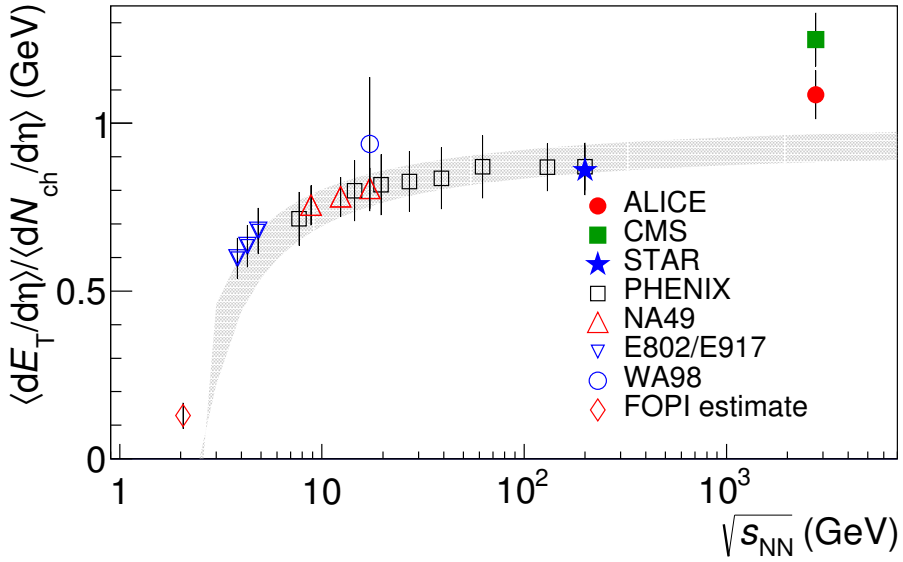

Figure 2.5: The comparison of $\langle dE_T/d\eta \rangle / (\langle dN_{ch}/d\eta \rangle)$ at midrapidity for different $\sqrt{s_{NN}}$. The ALICE and CMS result are from $\sqrt{s_{NN}} = 2.76$ TeV Pb–Pb collisions for 0-5% central events. Also included are the results from central collisions at midrapidity from additional $\sqrt{s_{NN}}$ energies [55]. The band is the fit to lower energies and extrapolated to higher energies with the width representing the uncertainty [55].

From $\langle dE_T/d\eta \rangle$, the volume-averaged energy density ε can be estimated by [56]:

$$\varepsilon = \frac{1}{Ac\tau_0} J \left\langle \frac{dE_T}{d\eta} \right\rangle \tag{2.4}$$

where c is the speed of light, τ_0 is the formation time, A is the effective transverse collisional area, and J is the Jacobian for the transformation between $\langle dE_T/d\eta \rangle$ and $\langle dE_T/dy \rangle$ [55, 56]. Figure 2.6 shows the energy density, reported as $\varepsilon\tau_0$, versus $\langle N_{part} \rangle$ measured by ALICE for Pb–Pb collisions at $\sqrt{s_{NN}}$ = 2.76 TeV. Estimating the formation time as 1 fm/c gives an energy density for the 0-5% most central events of 12.3 ± 1.0 GeV/fm^3, which is over 2x that observed in 0-5% central Au–Au collisions at $\sqrt{s_{NN}}$ = 200 GeV. The energy densities reported for all N_{part} are above the expected threshold of 1.0 GeV/fm^3 to produce the QGP, indicating that a QGP is formed even in peripheral collisions.

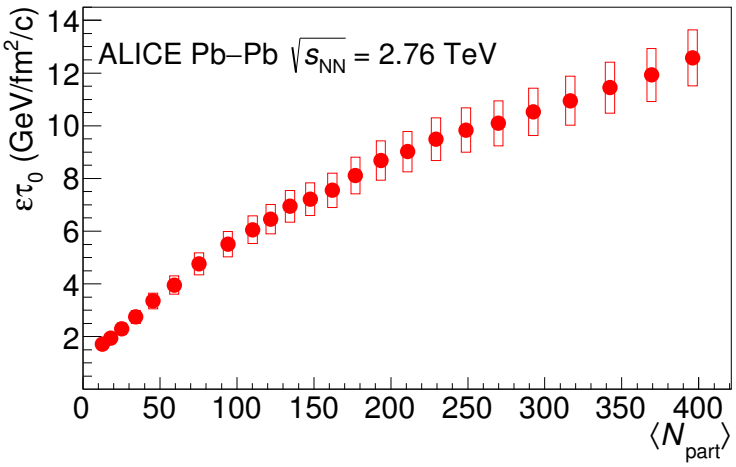

Figure 2.6: The energy density, reported as $\varepsilon\tau_0$, versus $\langle N_{part} \rangle$ measured by ALICE for Pb–Pb collisions at $\sqrt{s_{NN}}$ =2.76 TeV. Estimation was done using Eqn.2.4, R = 7.17 fm, and the measured $\langle dE_T/d\eta \rangle$ [55].

2.3.4 Photons

Direct photons are generally defined as photons not originating from hadronic decays [57]. The most common sources of direct photons in A+A collisions are (1) pQCD direct photons produced from the initial hard scattering, (2) thermal photons radiated by the medium, (3) thermal photons coming from the hadron gas which is formed after hadronization, and (4) photons which get produced in parton-medium interactions

[57]. Photons do not participate via strong interactions and thus provide a probe which exists in the final state and carries information from early in the collision. They aid in the studies of the initial hard scattering processes and the resulting parton distributions.

Direct photons

The production of direct photons in high energy heavy-ion collisions was first measured by the WA98 Collaboration in S+Au (200A GeV) and Pb–Pb (158A GeV) collisions at SPS [58, 59]. PHENIX measured direct photons in pp [60] at $\sqrt{s}$ = 200 GeV which showed that pQCD can describe the direct photon cross section for $1 < p_T < 20$ GeV/c well [57]. The pp result was then compared to Au–Au collisions. This R_{AA} measurement is expected to be close to unity since the direct photons do not lose energy in the medium and have a production yield which is proportional to the initial hard scattering [57]. Figure 2.7 and Fig. 2.8 show the PHENIX direct photon R_{AA} measurement versus p_T for central collisions and as a function of N_{part} for $\sqrt{s_{NN}}$ = 200 GeV [61]. Up to p_T = 20 GeV/c and across all centralities, the R_{AA} is consistent with 1 to within uncertainties. CMS saw similar results in their measurement [62]. This interesting result verified expectations and validated the concept of "N_{coll}-scaling" [63], the number of nucleon-nucleon collisions equivalent to a single A+A collision.

Thermal photons

Much of the low p_T spectrum of direct photons was thought to have come from hadronic sources due to thermal radiation of the QGP being low at SPS energies [58]. At RHIC and LHC energies, direct photons with p_T of 1-3 GeV/c are considered thermal photons and most come from emissions by the medium [64]. Analogously to Black Body Radiation, when these thermal photons are emitted by the medium, they serve as a thermometer of the medium [65]. By taking the slope of the p_T spectra

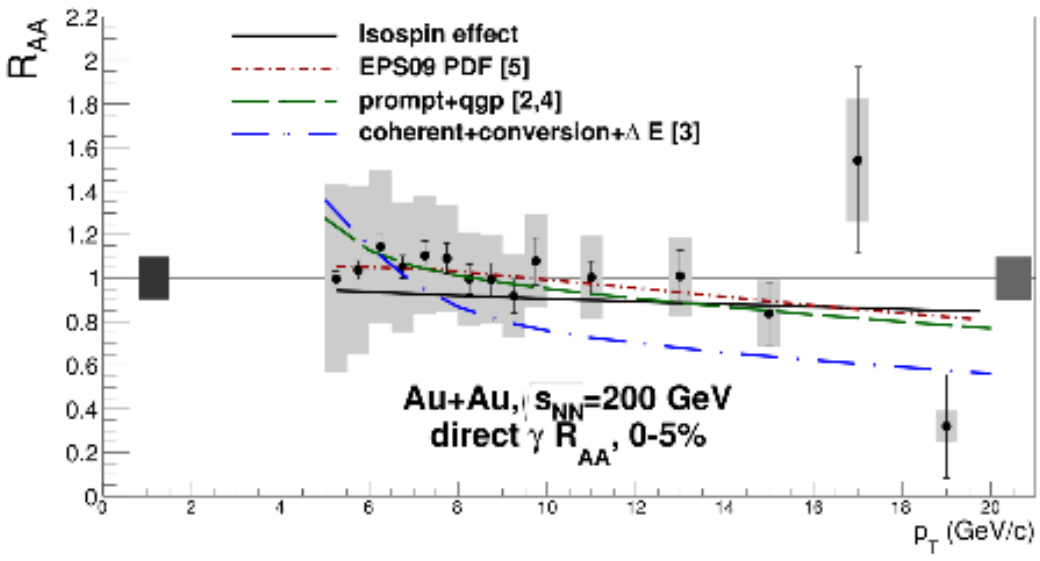

Figure 2.7: Direct photon R_{AA} versus p_T by PHENIX for central Au+Au collisions at $\sqrt{s_{NN}} = 200$ GeV [61].

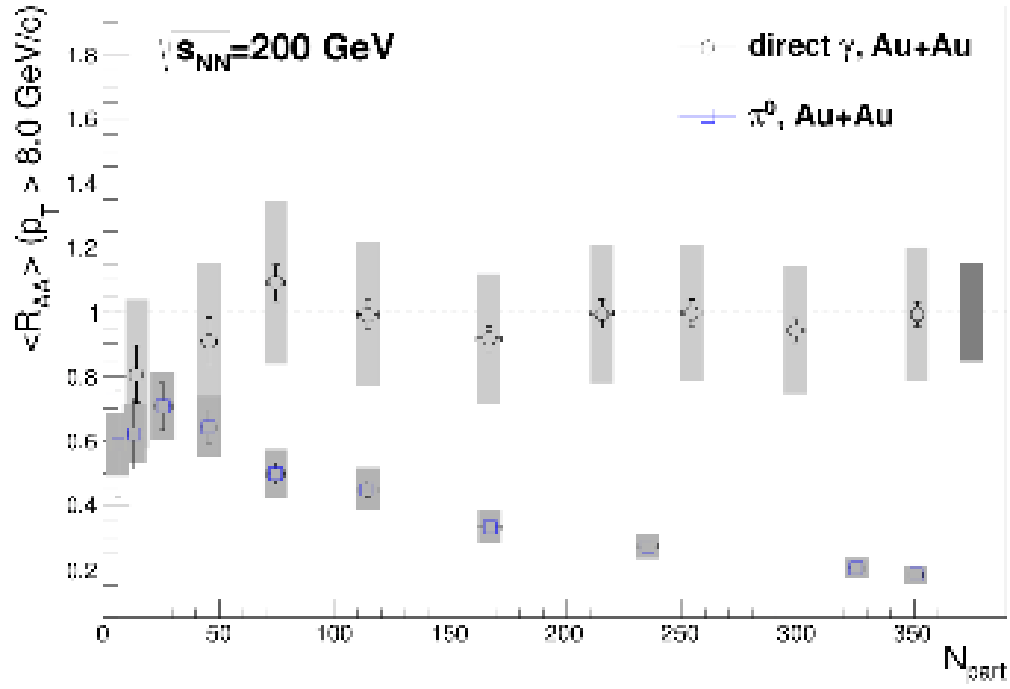

Figure 2.8: Direct photon R_{AA} versus N_{part} by PHENIX for central Au+Au collisions at $\sqrt{s_{NN}} = 200$ GeV [61].

of the thermal photons averaged over the space-time evolution of the collision [61], the temperature of QGP formation can be estimated [66]. Studies have indicated an inverse slope which is consistent with a temperature of around $T = 200 - 400$ GeV with large error bars [15, 57, 64], which is qualitatively consistent with various hydrodynamical models to within a factor of two [67] (also see reference within). Additionally, the p_T distributions of thermal photons can offer insight to the flow and chemical composition of the medium [57].

2.4 Hard Probes

Energetic particles are created early in the collision through hard parton scattering [68]. These particles live through the entire collision and can therefore be used as probes of the medium. Hard processes are characterized by large momentum transfers [69]. The products, heavy flavor hadrons and jets, act as hard probes [69]. The benefit is that their production can be calculated in pp collisions perturbatively and is expected to scale with N_{coll} in A+A collisions.

2.4.1 Jet quenching

An elastic $(2 \rightarrow 2)$ or inelastic $(2 \rightarrow 2 + X)$ scattering of two partons from each of the colliding nuclei results in the production of two or more partons in the final state. At high p_T, the outgoing particles have a large momenta transfer, Q, which gets reduced by subsequently radiating gluons or splitting into quark-antiquark pairs. At this point, the produced partons fragment non-perturbatively into a set of final-state hadrons. The collimated spray of hadrons formed from the fragmentation of an outgoing parton is called a "jet" [70].

When partons which form jets traverse the QGP, the partons interact with the medium and lose energy. This process of partonic energy loss is referred to as jet quenching [26, 71]. Jet quenching was one of the first proposed "smoking guns" of

QGP formation [70] because the energy loss provides fundamental information about the thermodynamical and transport properties of the medium [72]. This process is shown in Fig. 2.9 [70]. This is a diagram of a high energy head-on nucleus-nucleus collision. Initially two quarks undergo a hard scattering. One of them goes directly into the vacuum where it radiates a few gluons and hadronizes [70]. The other quark goes through the dense medium and suffers energy loss due to medium induced gluon radiation. It finally fragments outside the medium into a (quenched) jet [70]. By studying this phenomenon we can look into the dynamics of the medium [26], properties of the original parton, and the modification of their fragmentation process [71].

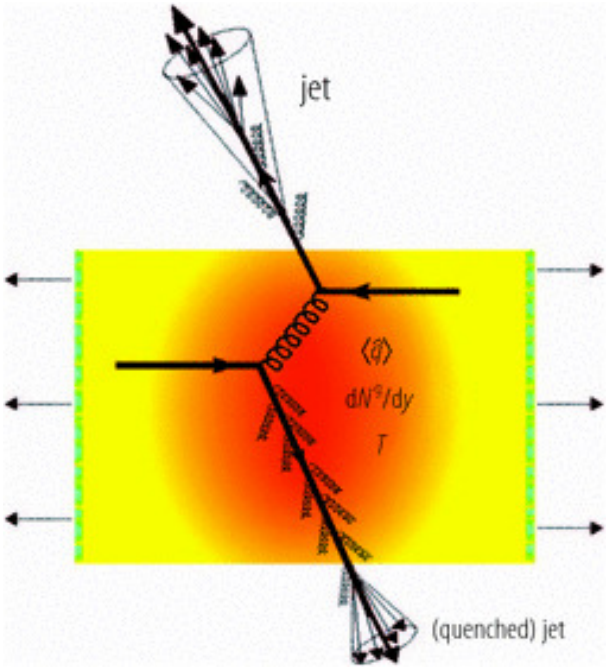

Figure 2.9: Jet quenching in a head-on A+A collision [70].

There are two primary ways a parton traversing the medium can lose energy. Energy is lost by partons as they undergo collisions and continue scattering. This mechanism dominates at low energy [68]. Gluon radiation can occur in the form of gluon bremsstrahlung [68]. This mechanism dominates at high energy [68] and can

be measured directly by reconstructing the jet structure in a heavy-ion collision [73]. A reduction in parton energy leads to a reduction of the yield at high-p_T [68]. The magnitude of energy loss is a characteristic of the density of the medium, the path length traveled, the energy of and particular type of particle in question. This is further discussed in Sec. 3.5.

2.4.2 Nuclear modification factor R_{AA}

The nuclear modifcation factor, R_{AA}, is an observable for quantifying medium effects in heavy-ion collisions. R_{AA} compares nucleus-nucleus collisions to proton-proton collisions. R_{AA} is given by:

$$R_{AA} = \frac{1}{N_{coll}} \frac{\sigma_{AA}}{\sigma_{pp}} = \frac{1}{N_{coll}} \frac{dN/dp_T|_{AA}}{dN/dp_T|_{pp}} \tag{2.5}$$

where σ_{AA} and σ_{pp} are the invariant cross sections and $dN/dp_T|_{AA}$ and $dN/dp_T|_{pp}$ are the p_T distributions for a given process in A+A collisions and pp collisions, respectively [74]. The average number of nucleon-nucleon collisions in the A+A collision is given by N_{coll}. A value of unity shows the yield of the process scales with the number of binary nucleion-nucleon collisions [68]. A value smaller (larger) than 1 indicates suppression (enhancement) [75]. Binary scaling can be broken because of initial state effects in nuclei or final state effects present in A+A collisions. This can occur through jet quenching or cold nuclear matter effects.

On the left panel of Fig. 2.10 are the charged hadron p_T spectrum for Pb–Pb collisions at $\sqrt{s_{NN}}$ =2.76 TeV for centralities of 0-5%, 20-40%, and 40-80% [74]. The shape of the Pb–Pb spectra are different from those in pp collisions. The right panel of Fig. 2.10 shows the nuclear modification factor, R_{AA}, as a function of p_T for charged particles in Pb–Pb collisions at $\sqrt{s_{NN}}$ =2.76 TeV for centralities of 0-5%, 20-40%, and 40-80% [74]. A large suppression can be seen. Above $p_T \approx 6$ GeV/c, R_{AA} is similar for all particles [35] indicating that the suppression may be a partonic effect

alone [76]. It appears that heavy quarks have a similar level of suppression to that of light and strange quarks [77, 78].

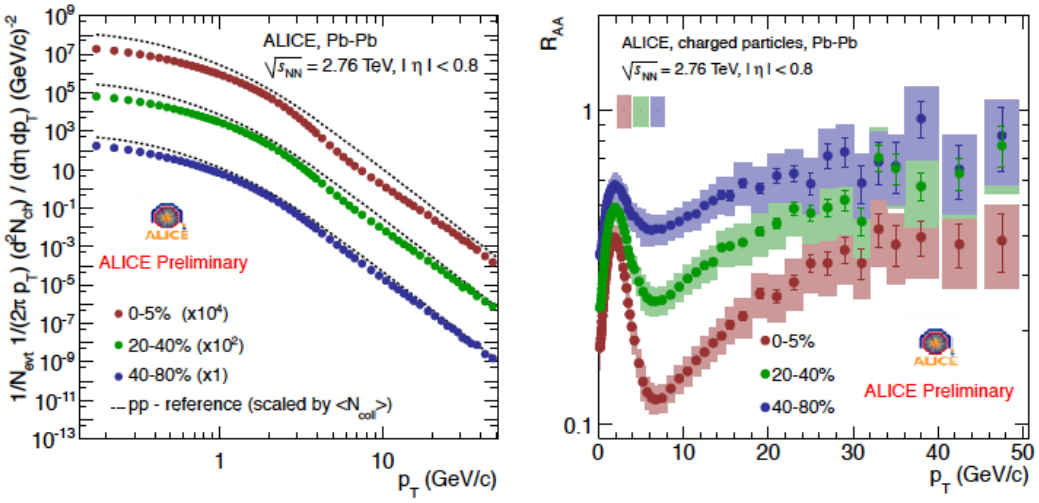

Figure 2.10: Left panel: Transverse momentum distributions of primary charged particles in Pb–Pb collisions at $\sqrt{s_{NN}}$ =2.76 TeV. Centrality selections of 0-5%, 20-40%, and 40-80% are shown for comparison. It should be noted, different centrality bins are scaled for easier viewing. Right panel: Nuclear modification factor R_{AA} for charged particles in Pb–Pb collisions at $\sqrt{s_{NN}}$ =2.76 TeV. Centrality selections of 0-5%, 20-40% and 40-80% are shown for comparison [74].

The hadron suppression factor, R_{AA}, was used to help constrain medium properties for the jet transport coefficient $\hat{q}$ which was calulated by the Jet Collaboration [79]. The jet transport coefficent is expressed such that:

$$\hat{q} = Q^2/L, \tag{2.6}$$

where Q is the momentum transfer in a hard process and L is the pathlength traversed and is used to help quantify partonic energy loss in the medium [79]. The jet transport coefficent quantifies the "stopping power" of the QGP. The Jet Collaboration determined that for a 10 GeV/c hadron, the jet transport coefficient is $\hat{q} = 1.9 \pm 0.7\ GeV^2/fm$ in Pb–Pb collisions at $\sqrt{s_{NN}}$ = 2.76 TeV and $\hat{q} = 1.2 \pm 0.3$ GeV^2/fm in Au–Au collisions at $\sqrt{s_{NN}}$ = 200 GeV.

2.4.3 Quarkonia

Quarkonia are excited states of a flavorless meson composed of a heavy quark (Q) and its own anti-quark ($\bar{Q}$). The J/Ψ meson (charm and anti-charm $c\bar{c}$ pair) and the Υ meson (bottom and anti-bottom $b\bar{b}$ pair) along with their excited states serve as the most common examples of quarkonia. When the quark pair moves around in the medium, the abundant amount of light quarks can result in Debye screening of the quark color charge [80]. When the radius of the screening drops below the binding radius of the quark system, the quarkonia can melt and the binding force can no longer hold the quarks together [80]. The melting process manifests itself via the suppression of quarkonia of various states in heavy-ion collisions when compared to that of proton-proton collisions. The suppression of states is determined by the deconfinement temperature T_c and their binding energies. This suppression of quarkonia states was seen by CMS [81] to be consistent with the sequential melting scenario as described by [82]. This is highlighted by Fig. 2.11, which shows the nuclear modifcation factors for $\Upsilon(1S)$, $\Upsilon(2S)$, and $\Upsilon(3S)$ meson production in Pb–Pb collisions as a function of centrality [81]. Charmonium states such as J/Ψ, however, experience less suppression and have other effects at play, such as regeneration and cold nuclear matter effects [80, 83, 84].

This Υ suppression serves as direct evidence of deconfinement since the binding potential between the constituents of the quarkonium state should experience color charge screening by the surrounding light quarks and gluons [81].

The free energy for heavy quark and anti-quark screening at finite temperatures is shown in Fig. 2.12. It shows that as the temperature is increased, the free energy begins to drop below the zero temperature case and as it is further increased, screening sets in at smaller radii. This means that quarkonia states which are loosely bound will melt at lower temperatures and as the states become more tightly bound, it will take a higher temperature for the melting to set in. This sequential pattern of the melting of quarkonia states serves as a very useful thermometer of the QGP [85, 86].

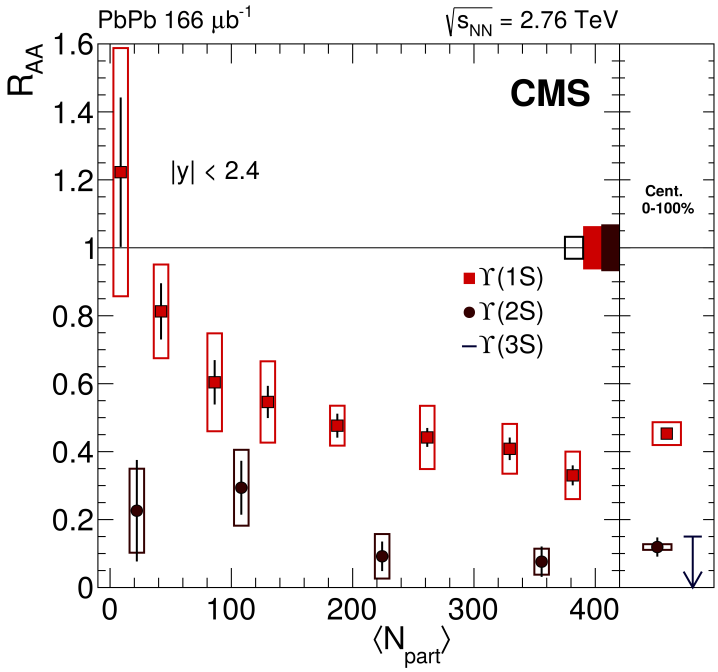

Figure 2.11: The nuclear modification factor vs centrality for the $\Upsilon(1S)$, $\Upsilon(2S)$, and $Upsilon(3S)$ quarkonium states in Pb–Pb collisions at $\sqrt{s_{NN}} = 2.76$ TeV measured by CMS [81].

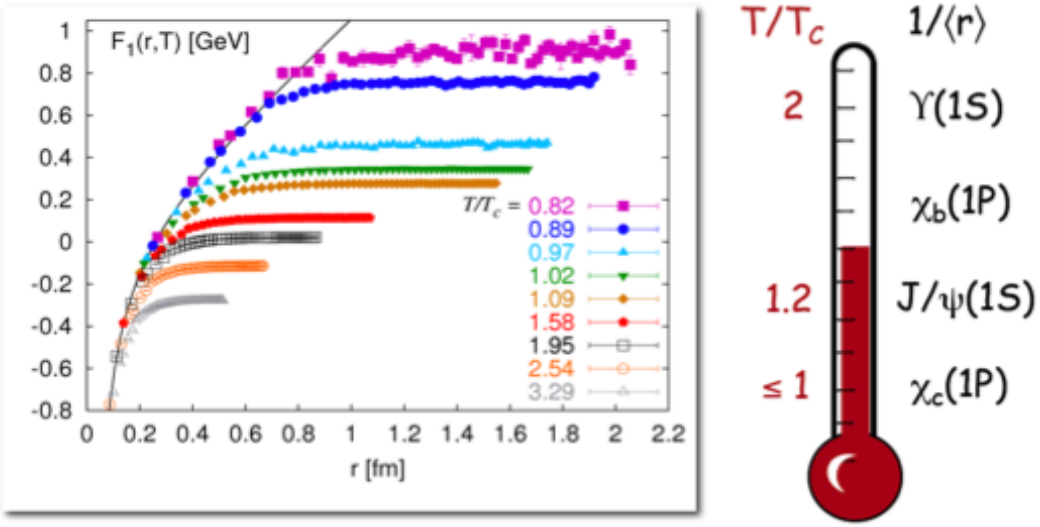

Figure 2.12: The quarkonium thermometer used to measure the QGP temperature. (Left) Heavy quark and anti-quark screening of the free energy for finite temperatures. (Right) Ordered melting of quarkonia states [85, 86].

Chapter 3

Jets

3.1 Overview

Jets are the experimental signatures of quarks and gluons. They are expected to reflect the kinematics and topology of the originating partons and are an ideal probe of the QGP since they are created early in the collision. By studying the suppression of the number of jets in A+A collisions to that of a baseline system (R_{AA} measurement) and by studying the modification of the p_T or angular distribution of jet fragments (correlation meaurement), we can learn valuable information about the QGP.

pQCD theory calculates properties of partons. Experiment measures the fragments of partons: tracks and deposits in calorimeter towers. Comparisons between theory and experiment require proper parameters for jet reconstruction, jet finding algorithms, and optimal ways of dealing with the fluctuations and background of heavy-ion collisions. This section will address the connection between theory and experimental measurement, explain how we define jets, list various jet-finding algorithms and discuss current jet results.

3.2 Jet Definitions

Qualitatively, we refer to jets as the collimated shower of hadrons produced during the hard scattering of partons [87]. To make quantitative measurements, we need a better method of assigning particles to the jet. A general jet definition amounts to a specific choice of a jet finding algorithm, its parameters, and a recombination scheme [88]. Ideally, properties of jets such as their energy and direction can be associated with that of the original partons produced during the hard scattering process.

Due to the high correlation of particles in the η-ϕ plane, a method for defining the geometry of the jet is needed. More details can be found in [89]. The invariant cone radius R of the jet is defined by:

$$R = \sqrt{\triangle\eta_{ij}^2 + \triangle\phi_{ij}^2}. \tag{3.1}$$

The optimal choice of R depends on what system we are looking at [90]. In pp collisions, most of the energy of the jet is enclosed in a cone radius of R=1 [91]. In the study of heavy-ion collisions, backgrounds and fluctuations of energy become important. At this point there is a tradeoff. We do not want to lose too much out-of-cone radiation but want to have a small background in the jet area [90]. In Pb–Pb collisions, a radius reduced to 0.3 for a 50 GeV/c jet, still measures roughly 80% of the jet energy and allows separation of jets from the immense background [91].

In pp collisions, jets are defined as a transverse energy excess of the underlying events (UE) background within a cone radius in the $\eta-\phi$ plane of R=1 [91]. However, during heavy-ion collisions, the total energy from the UE is over an order of magnitude larger than the jet we want to measure and fluctuates with an energy on the order of the jet energy [91]. Therefore a reduction in cone size is necessary. Background energy scales as R^2 and fluctutations as R, so the contributions of these can be reduced by reducing the cone size [91].

3.3 Factorization

Due to confinement, quarks and gluons (partons) cannot be observed directly. These partons fragment, leading to a collimated cone of hadrons called a jet [26, 92]. These resulting hadrons are measured by the detectors. Most of these jets are created in $2 \rightarrow 2$ hard parton scatterings from the incoming nuclei [26]. The incoming partons have momenta nearly parallel to the nuclei. Momentum conservation causes the scattered partons to be separated by roughly 180^{o} in azimuth [26]. The processes occuring in these high energy heavy-ion collisions can be broken down into the long distance quantities of the hadrons and the short distance quantities of the partons. The long distance quantities are not perturbatively calculable through pQCD [93], but are process independent [70]. On the other hand, the short distance quantities are process dependent, but perturbatively calculable [70]. There are certain high energy cross section calculations which contain both behaviors and thus require certain assumptions [94].

Jet cross sections are an example of a final state measurement which includes both of these behaviors. We assume we can compute jet cross sections by factorizing physical observables into calculable and non-calculable pieces [93]. It rests on the idea that we can separate the perturbative part and the universal non-perturbative fragmentation functions and parton distribution functions [90].

A sketch of dijet production and the pQCD factorization scheme in hadronic collisions is shown in Fig. 3.1. The jet cross section [90] in heavy-ion collisions is calculated using the factorization theorem expressed by Eqn. 3.2.

$$E\frac{d^3\sigma}{dp^3} \propto f_{a/A}(x_a, Q^2) \otimes f_{b/B}(x_b, Q^2) \otimes \frac{d\hat{\sigma}^{ab\rightarrow cd}}{dt} \otimes D_{h/c}(z_c, Q^2) \otimes D_{h/d}(z_d, Q^2) \quad (3.2)$$

The $\otimes$ denotes a convolution of functions. $f_{a/A}$ and $f_{b/B}$ are the parton distribution functions [90]. They are the probability for a parton a (b) to carry a fraction x_a (x_b)

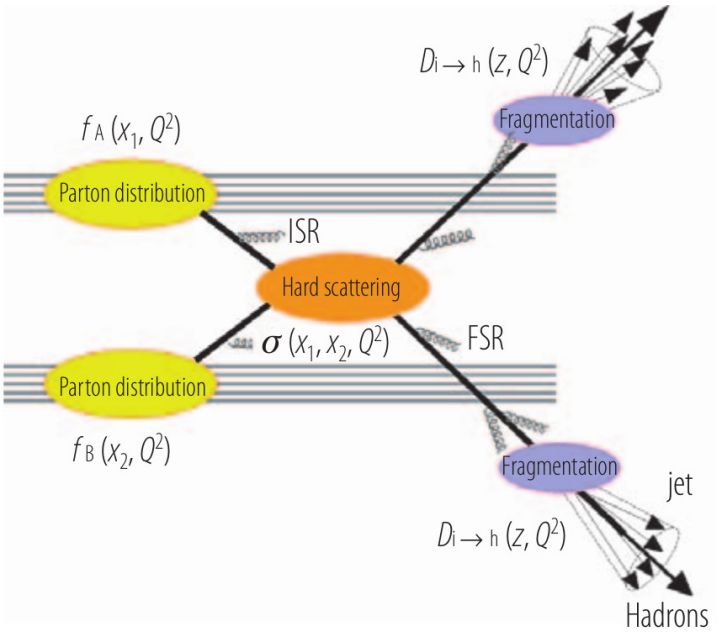

Figure 3.1: Cartoon diagram showing the dijet production and pQCD factorization scheme in hadronic collisions [70].

of the hadron momentum at scale Q [90]. They are assumed to be universal functions which are extracted from experimental data for one or more processes that can be calcuated via pQCD [90]. $d\hat{\sigma}^{ab\to cd}/dt$ is the parton cross section which is computed from pQCD [90, 94]. The resulting parton level cross section is not itself a prediction of QCD, but a prediction of the parton model [94]. The factorization theorem will make the connection between the two [94]. $D_{h/c}$ and $D_{h/d}$ are the fragmentation functions. They can be interpreted as the probability for finding a hadron h carrying a certain momentum fraction z_c (z_d) of the parent parton c (d) [93]. They are assumed to be universal in elementary processes [90, 93] and are extracted from experimental data in pp and e^+e^- collisions [90]. The fragmentation functions $D_{h/c}$ and $D_{h/d}$ can be modified by the QGP [95]. This can occur in the form of parton energy loss before fragmentation or modification to the fragmentation functions for partons that

fragment in the medium [26]. At high enough energies, the main source of this energy loss is thought to come from gluon radiation [73].

3.4 Jet-finding algorithms

Jet algorithms provide a set of rules for grouping final state particles into jets. Experimentally, final state particles are classified as either tracks or calorimeter towers. Jet algorithms can be broken down into two types; recombination/clustering algorithm and cone algorithms. Jet algorithms involve a restrictive parameter which indicates how close two particles should be to belong to the same jet.

An important decision is which algorithm to use. It is optimal to use a jet-finding algorithm which is both infrared and collinear safe. Collinear safety requires that during the collinear splitting of a single particle into two particles that the jets returned by the algorithm are unchanged. Infrared safety requires that the emission of a very soft particle will not change the jets returned by the algorithm. Algorithms which are not infrared and collinear safe lead to divergences in perturbation theory [88, 96].

A cone algorithm looks for particles in angular (η, ϕ) space. It defines them into a stable cone of invariant radius R, given by Eqn. 3.1. Depending on the particular cone algorithm, a list of proto-jets are formed above some energy seed [87]. Stable cones are found through an iterative process of starting with the highest energy seed, drawing a cone of radius R and calculating the energy weighted centroid [87]. They define a new cone at the centroid of radius R and continue iterating until the cones become stable [87]. This process is repeated until all proto-jets are put into a jet. If necessary, it may be required to split or merge jets if they overlap. The problem with seeded cone algorithms is they are not infrared or collinear safe [87].

The clustering/recombination algorithms define a distance measure d_{ij} between each pair of particles i and j:

$$d_{ij} = min(k_{ti}^{2p}, k_{tj}^{2p}) \frac{\triangle_{ij}^2}{R^2} d_{iB} = k_{ti}^{2p} \tag{3.3}$$

where $\triangle_{ij}^2 = (y_i - y_j)^2 + (\phi_i - \phi_j)^2$. k_{tj}, y_i, and ϕ_i are the transverse momentum, rapidity, and angle of azimuth of the i'th particle. The parameter p is used here to define the power of the energy versus geometrical ($\triangle_{ij}$) scales [97,98]. Setting $p = 1$ in Eqn. 3.3 refers to the inclusive k_t algorithm, $p = 0$ to the inclusive Cambridge/Aachen algorithm [99], and $p = -1$ to the anti-k_t jet-clustering algorithm [97, 98]. After defining the distance between each pair, the k_T algorithm groups soft objects first, while the anti-k_T algorithm groups hard objects first. It recombines the pair of particles which are closest, and then repeats until it reaches a set value of jets or finds all jets to be widely separated [97, 98].

ALICE uses the infrared-safe and collinear-safe anti-k_T algorithm which works within the Fastjet algorithm framework. The anti-k_T algorithm offers a computationally faster replacement to the older cone algorithms [100]. It also removes irregularities of the normal k_T algorithm by fixing the boundaries of the final jets due to soft radiation.

3.5 Why measure jets in heavy-ion collisions?

Jets are important probes of the QGP. Through jet reconstruction, we can access kinematics of the binary hard scatterings. Through comparison of near and away side jets, the parton energy loss can be characterized in the hot QCD medium [90]. Since energy loss depends on path length, studies of the mediums geometry can be performed. Fig. 3.2 highlights the idea of energy loss of a parton in the medium of a heavy-ion (Pb–Pb) collision compared to the case of a parton in a vacuum from a pp collision.

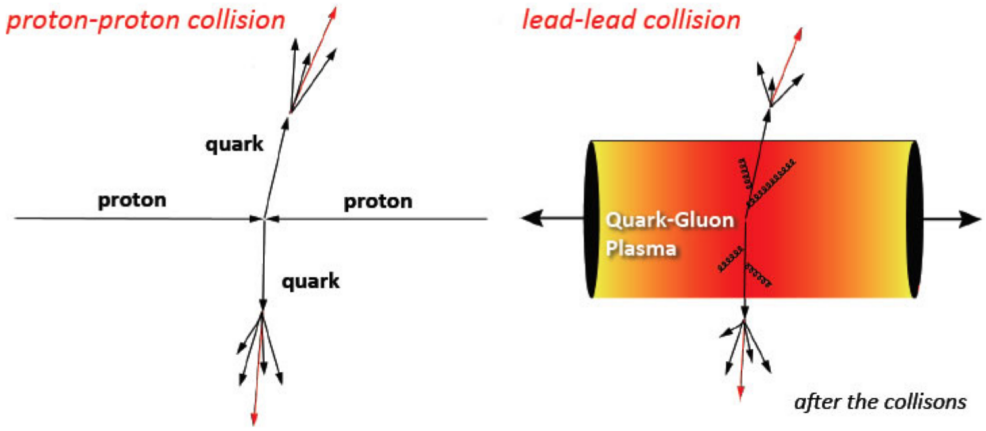

Figure 3.2: Energy loss of parton in QGP [101].

Energy loss models [102] tell us that we can describe the amount of energy loss experienced by a parton ΔE using the parton position l, path length L, scattering probability density $dP(l)/dl$ and mean free path λ by:

$$\Delta E = \int_0^L dl \frac{dP(l)}{dl} \lambda(l) \frac{dE(l,E)}{dl} \tag{3.4}$$

and

$$\frac{dP(l)}{dl} = \frac{1}{\lambda(l)} \exp\left(\frac{-l}{\lambda(l)}\right). \tag{3.5}$$

The primary mechanisms of energy loss consist of collisional energy loss and radiative energy loss. Collisional energy loss occurs when a parton loses energy by colliding with other constituent partons of the QGP. Radiative energy loss occurs when a particle radiates off gluons from bremsstrahlung. This is the dominating energy loss mechanism at LHC energies [101]. A general form of the total energy loss is usually expressed by:

$$\Delta E = \Delta E_{collisional} + \Delta E_{radiative}. \tag{3.6}$$

3.6 Ways of studying jets and using them to study the QGP

In the lab frame, particles are highly correlated in η and ϕ in a Lorentz-boosted jet. To conserve momentum, jets also tend to be oriented back-to-back [103] in azimuth and also have their E_T balanced. By using both the azimuthal distribution of pairs of high-p_T particles and analyzing the leading particles of jets via the p_T spectra of hadrons, one can gain a better understanding of the the effects a medium has on an energetic parton. Leading particle studies have limitations in extreme quenching scenarios. In these cases, particle emission occurs near the surface of the medium and there is very little sensitivty of R_{AA} to medium properties. [91]

Full jet reconstruction allows for an unbiased measurement of the original parton 4-momentum and the transverse and longitudinal shape of the jet. Through modifications of the jet structure, partonic energy loss and partonic shower mechanisms of the medium can be studied [104, 105]. This can be seen through changes in the number of particles carrying a large fraction z of the jet energy and through radiated energy which is shown by an increase in the number of particles with small z [91].

The internal jet structure is studied through jet shapes (radial profiles) and jet frargmentation functions (longitudinal profiles) [104]. The radial profile can be summarized by how momentum is distributed within the jet cone via Eqn.3.7:

$$\rho(r) = \frac{1}{\delta r}\frac{1}{N_{jet}}\sum_{jets}\frac{p_T(r-\delta r/2, r+\delta r/2)}{E_T^{jet}}, \tag{3.7}$$

where $r = \sqrt{(\eta-\eta_{jet})^2+(\varphi-\varphi_{jet})^2} \leq R^{jet}$ is the radial distance from a jet constituent to the jet axis [104]. This is defined by coordinates η_{jet} and φ_{jet}. The longitudinal profile is described by the jet fragmentation function $D(z)$, given by Eqn. 3.11, and further discussed in Sec. 3.7.4. The jet fragmentation function defines the probability for a jet constituent particle to carry a fraction z of the jet transverse momentum [104].

3.7 Current status in jet research

3.7.1 Partonic Energy Loss at RHIC

RHIC has shown clear evidence of partonic energy loss [91]. They found a strong suppression of high-p_T hadrons in central Au–Au collisions at $\sqrt{s_{NN}} = 200$ GeV. For $p_T > 5$ GeV/c, the R_{AA} for charged hadrons and neutral pions is suppressed by a factor of 5 in central Au–Au collisions relative to pp collisions. This same suppression is not observed in d+Au collisions at the same energy. This is indicative that the suppression in central Au–Au collisions is primarily due to final-state interactions of partons with the dense medium [91].

3.7.2 Jet Suppression at the LHC

As an alternative of comparing to pp collisions, a nuclear modification factor, R_{CP}, can be formed by comparing central collisions to peripheral collisions. This is usually done when no pp reference data are available or the pp reference has large statistical errors. With an interpretation similar to that of R_{AA}, R_{CP} is given [106] by:

$$R_{CP} = \frac{\frac{1}{N_{coll}^{cent}} E \frac{d^3 N^{cent}}{dp^3}}{\frac{1}{N_{coll}^{periph}} E \frac{d^3 N^{periph}}{dp^3}}. \tag{3.8}$$

Jets are defined by the anti-k_T clustering algorithm with distance parameters R=0.2, 0.3, 0.4 and 0.5 [107]. The algorithm takes input in the form of towers of calorimeter cells. Track jets are reconstructed from charged particles with $p_T > 4$ GeV/c. The average underlying event contribution (background) is subtracted from the jet candidates on an event-by-event basis [107, 108].

The results from ATLAS are shown in Fig. 3.3 [106]. On the left panel, R_{CP} is plotted on the y-axis versus jet p_T on the x-axis for R=0.4 anti-k_T jets in centrality bins of 0-10%, 10-20%, 30-40%, and 50-60%. Results indicate that R_{CP} is nearly independent of p_T. It can also be seen that $R_{CP} \sim 0.5$ in the most central collisions

while varying smoothly to more peripheral collisions. On the right panel, the R dependence of the suppression is shown. The effects of jet quenching are thought to cause a broadening of the parton shower [106]. This causes the jet's energy to be deposited outside the nominal jet cone. This radiation detected outside the cone can be recovered by increasing the radius of the jet [106]. The R_{CP} ratio is measured with a particular R value, R^R_{CP}, and divided by the corresponding value for R=0.2 jets. These results indicate a significant dependence of R_{CP} on jet radius in the most central collisions. For $p_T < 100$ GeV/c the $R^R_{CP}/R^{0.2}_{CP}$ values for both R=0.4 and R=0.5 differ from one beyond the statistical and systematic uncertainties. This is evidence of broadening of the jets in Pb–Pb collisions [106].

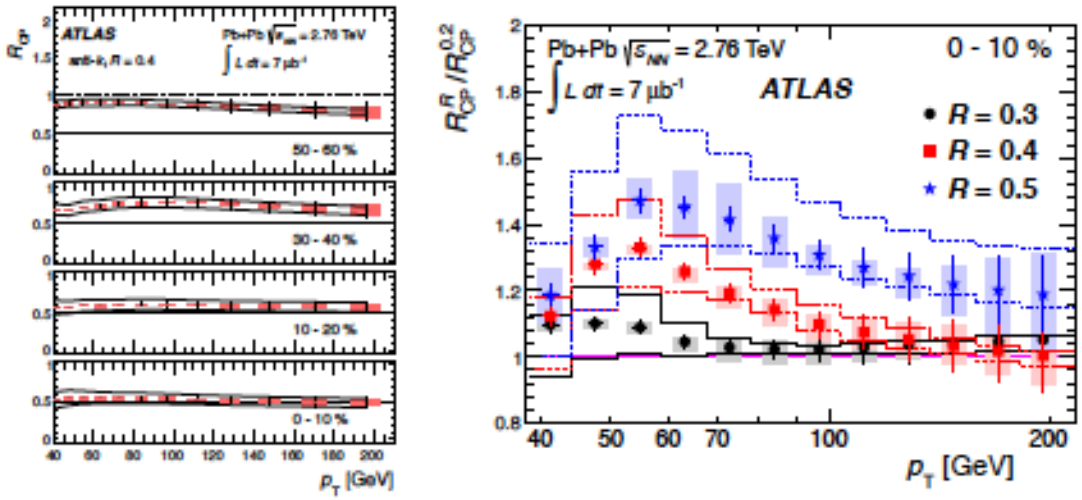

Figure 3.3: Left: R_{CP} as a function of jet p_T for R=0.4 anti-k_T jets in four bins of collisions centrality. Collisions were measured for Pb–Pb at $\sqrt{s_{NN}}$ = 2.76 TeV. The dotted lines represent R_{CP} = 0.5. Right: Ratios of R_{CP} values for R=0.3, 0.4, and 0.5 jets against reference R=0.2 as a function of p_T in the 0-10% centrality bin. Statistical uncertainties are show via error bars. The shaded boxes and solid lines indicate statistical, uncorrelated systematic and correlated systematic errors [106].

3.7.3 Dijet Asymmetries at the LHC

Measurements of dijet asymmetry and dijet correlations in Pb–Pb collisions at $\sqrt{s_{NN}} = 2.76$ TeV were made with the ATLAS detector [107]. They provided the first evidence of jet quenching at TeV energies [107]. The analysis was done in a similar style to the above mentioned by the ATLAS collaboration. Similar measurements were made by CMS [109] and STAR [110]

Pairs of jets called dijets are balanced in azimuth and transverse energy in pp collisions. Jet quenching can be studied by comparing the transverse energy of the two jets. The first jet was required to have $E_{T,1} > 100$ GeV and the second jet $E_{T,2} > 25$ GeV [107]. They can travel different path lengths if created in the medium. The resulting energy imbalance can be quantified using the asymmetry by:

$$A_J = (E_{T,1} - E_{T,2})/(E_{T,1} + E_{T,2}), \tag{3.9}$$

where $E_{T,1} > E_{T,2}$ are transverse energies of jets in a dijet system [107]. It was seen that one of the jets was clearly suppressed and measured at a lower energy [107].

Another way of understanding the large dijet asymmetry is by measuring the energy flow of the event [107]. This can be done by measuring the sum of transverse energy for a strip centered at the pseudorapidity position of the leading jet or sub-leading jet [107]. The results are shown in Fig. 3.4 [107]. Plotted on the y-axis is the sum of the transverse energy in the calorimeter towers ($\sum E_T^{tower}$) versus azimuthal angle $\triangle\phi$ on the x-axis. The left plot of shows the sum of transverse energy for three bins in the measured jet asymmetry. This asymmetry is clearly visible. The offset of the distribution is larger for jets with larger asymmetries. This is because they are occuring in more central collisions [107]. The CMS collaboration has seen similar results in their measurement of jet fragmentation into charged particles in pp and Pb–Pb collisions at $\sqrt{s_{NN}} = 2.76$ TeV [111]. This is a strong indication of jet quenching in heavy-ion collisions [107].

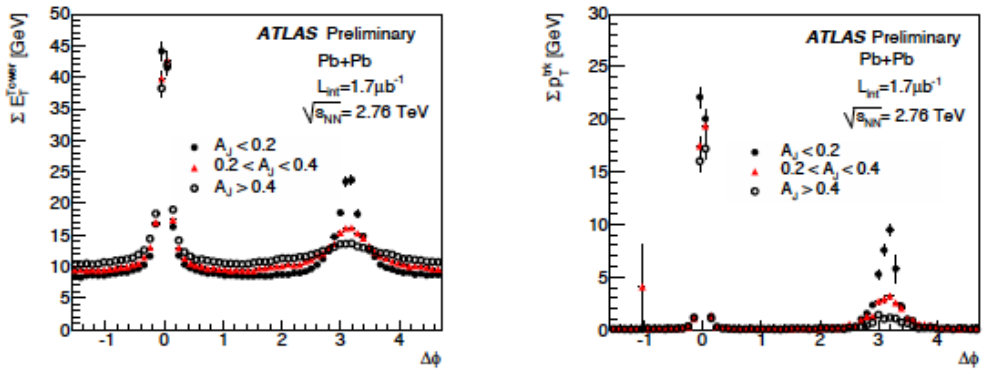

Figure 3.4: Energy flow measured using non-calibrated non-subtracted calorimeter towers (left) and tracks with $p_T > 4$ GeV/c (right) [107]. The transverse energy of towers or transverse momentum of tracks is summed over strips of size, $\triangle\eta \times \triangle\phi = 0.8 \times 0.1$, centered at the pseudorapidity position of the leading jet or sub-leading jet [107].

3.7.4 Modification to the Fragmentation Functions in different centralities

A modification of internal jet structure is predicted by various theoretical models [112]. By measuring the fragmentation functions, possible modifications to the parton showers due to a medium can be studied.

The centrality dependence of the fragmentation function for Pb–Pb collisions at $\sqrt{s_{NN}} = 2.76$ TeV with the ATLAS detector is shown in Fig. 3.3 [112, 113]. The analysis was done in a similar style to the above mentioned by the ATLAS collaboration. On the y-axis is $R_{D(z)}$ [113] given by:

$$R_{D(z)} \equiv D(z)_{cent}/D(z)_{peri}, \tag{3.10}$$

where D(z), given by Eqn. 3.11, is the fragmentation function, evaluated at corresponding centralities.

$$D(z)(p_T^{jet}) = \frac{1}{N_{jet}(p_T^{jet})} \frac{1}{\epsilon(p_T,\eta)} \left(\frac{\triangle N_{ch}(z, p_T^{jet})}{\triangle z} - \frac{\triangle N_{ch}^{UE}(z, p_T^{jet})}{\triangle z} \right) \tag{3.11}$$

The momentum fraction, z, on the x-axis is given by $z = p_T/p_T^{jet} \cos \triangle R$ [112, 113]. The ratio, $R_{D(z)}$, is evaluated at increasing centrality bins of 0-10%, 10-20%, 20-30%, 30-40%, 40-50%, and 50-60% compared to the most peripheral bin of 60-80%. An enhancement of $\sim$ 25% at low z, and thus low p_T^{had}, can clearly be seen for central collisions with respect to peripheral collisions [113]. There is a suppression of $\sim$ 15% at $z \approx 0.1$ [113]. No modifications are seen at high z within the systematic errors. In Fig. 3.5 [113], data are only shown for R=0.4. Similar results were found for R=0.2 and 0.3 jets [113]. These results show an increasing size of modification of the fragmentation functions with increasing centrality. This can be interpreted as a direct observation of medium modifications of the fragmentation functions in central Pb–Pb collisions [111]. These modifications from medium interactions are proof of energy loss, which is expected to be path length dependent. The path length dependence of energy loss is the primary focus of study for this thesis work through the use of jet-hadron correlations. The CMS collaboration performed a similar measurement in [114] and saw similar results. They took a Pb–Pb/pp ratio of the fragmentation function and saw the value rise to $\sim$ 1.5 in the most central collisions implying that the particles in the Pb–Pb jets have a softer particle spectrum compared to pp collisions [114]. This can be explained by changes occuring in the fraction of jets arising from either quarks or gluons, medium modified parton showers, or the presence of particles resulting from the medium response [114–119].

3.7.5 Jet-Hadron Correlations

Jet-hadron correlations are commonly defined as distributions in $\triangle\phi = \phi_{jet} - \phi_{assoc}$, where ϕ_{jet} is the azimuthal angle of the axis of the reconstructed (trigger) jet and

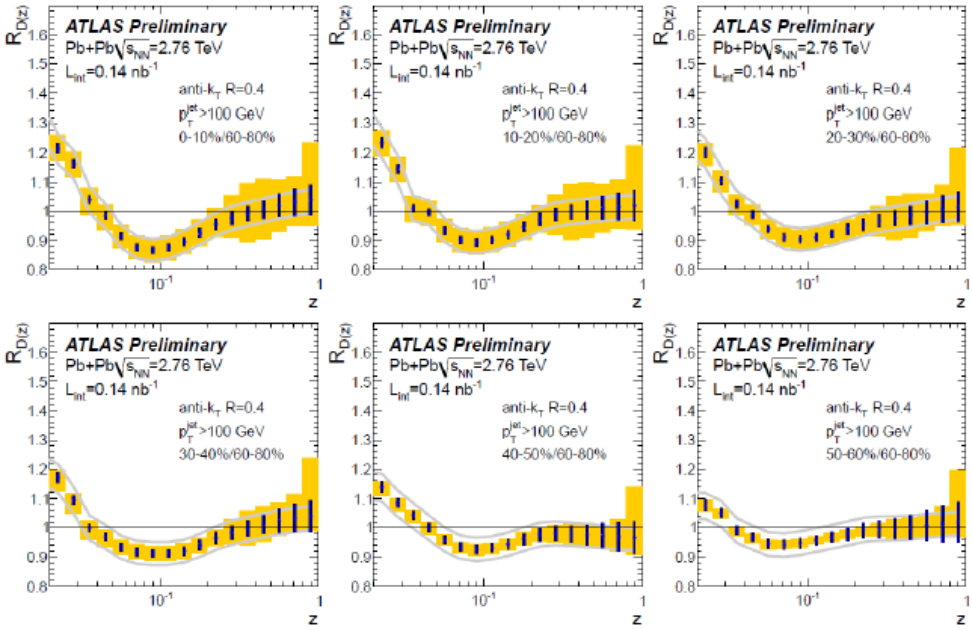

Figure 3.5: Fragmentation function modification as a function of centrality. The ratio, $R_{D(z)}$, is evaluated at increasing centrality bins of 0-10%, 10-20%, 20-30%, 30-40%, 40-50%, and 50-60% compared to the most peripheral bin of 60-80%. This ratio is shown as a function of momentum fraction z. An enhancement is clearly seen for low z, with a suppression near $z \sim 0.1$, and no modification at high z within the systematic errors [112].

all the assocated particles are all charged hadrons in the event [120]. In a jet-hadron correlation, what is referred to as the "near-side" is the side of the correlation where $\Delta\phi = 0$, corresponding to the azimuthal centroid placement of the trigger jet. This is used to position the trigger jet. Then, when charged particles are measured relative to the trigger jet, the "away-side" is used to refer to the opposite side in azimuth, where a recoil jet exists. This explanation is illustrated in Fig. 3.6, where the near-side and away-side from a jet-hadron correlation [121] seen in an event display are related to an actual correlation.

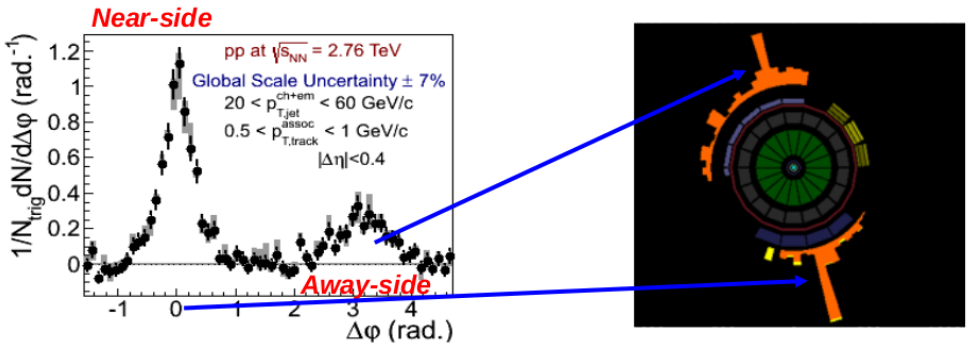

Figure 3.6: An example jet-hadron correlation compared to an event display used to define the near-side and away-side [121].

In a jet-hadron correlation, medium-induced modification effects can be quantified by the widths of the jets peaks, σ, the number of particles in the peaks and terms D_{AA} and $\sum D_{AA}$. D_{AA} is called energy balance. It is a measure of the p_T difference between A+A and pp in a given p_T^{assoc} bin with mean $\langle p_T^{assoc} \rangle$ and is given by:

$$D_{AA}(p_T^{assoc}) \equiv Y_{AuAu}(p_T^{assoc}) \cdot \langle p_T^{assoc} \rangle_{AuAu} - Y_{pp}(p_T^{assoc}) \cdot \langle p_T^{assoc} \rangle_{pp}. \tag{3.12}$$

$\sum D_{AA}$ measures the energy balance over the entire p_T^{assoc} range [120]:

$$\sum D_{AA} \equiv \sum_{p_T^{assoc}\ bins} D_{AA}(p_T^{assoc}). \tag{3.13}$$

$Y_{AA,pp}$ are the per-trigger associated yields in A+A,pp [122]. For identical fragmentation patterns of A+A and pp systems, $D_{AA} = 0$ for all p_T^{assoc} [120]. Any deviations from this value indicate modification of the jet.

STAR measured azimuthal angular correlations of charged hadrons with respect to a reconstructed (trigger) jet [120]. Jet quenching studies can be made by comparing the shapes of the associated hadron yields of jets in A+A with those in pp collisions. The measurement by STAR is done for pp and Au–Au collisions at $\sqrt{s_{NN}} = 200$ GeV [120]. Reconstruction is done using the anti-k_T algorithm with R=0.4 jets [120].

Figure 3.7 shows comparisons between the near-side and away-side D_{AA} versus the associated p_T of the jet [120]. The near-side jet is expected to have a surface bias. This makes it more likely that the recoil parton will travel a significant distance through the medium. This would enchance the partonic energy loss effects and quenching on the away-side. From Fig. 3.7 [120], we can see that the away-side D_{AA} exhibits suppression of high-p_T^{assoc} hadrons and enhancement of low-p_T^{assoc} jet fragments in Au–Au collisions. This indicates that the jet constituents in Au–Au are significantly softer than their counterparts in pp collisions. This STAR analysis [120] showed that the $\sum D_{AA}$ values indicate that the high-p_T^{assoc} suppression is balanced by the low-p_T^{assoc} enhancement. This is the first time that jet-hadron correlations were used to probe the modifications of the properties of partons which traversed the medium created in heavy-ion collisions.

The CMS Collaboration performed similar studies in [123]. CMS compared the yields of jet-hadron correlations from Pb–Pb collisions to that of pp collisions and saw that for the most peripheral events studied, there was a small excess at low-p_T compared to the pp reference. This excess, which extended out to large angles from the jet axis, had a similar Gaussian-like shape in δeta and $\delta\phi$ and grew with the centrality of the collision [123]. This observed excess descreases with increasing associated particle p_T [123]. These effects show that energy from high-p_T particle are redestributed into lower p_T particle from interactions with the medium [123]. This study gives a deeper evaluation of the medium effects on jet properties and provides

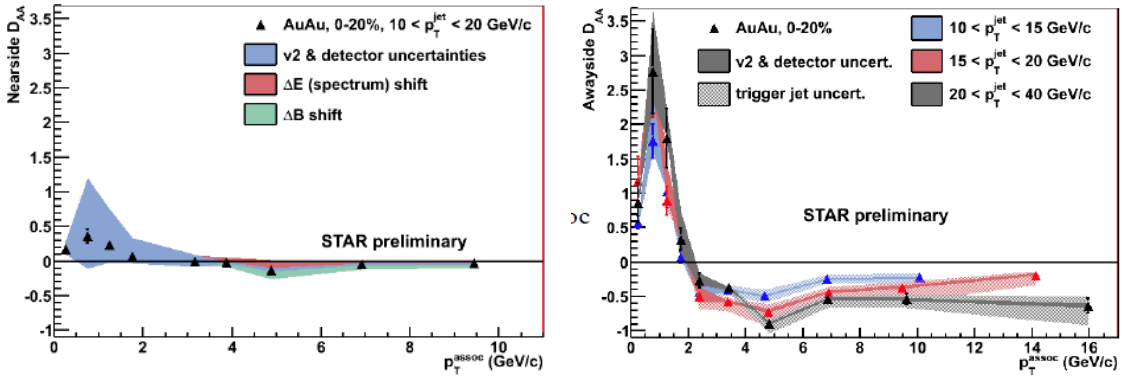

(a) figure a **(b)** figure b

Figure 3.7: Momentum difference D_{AA} is shown for data taken from Au+Au collisions at $\sqrt{s_{NN}} = 200$ GeV in the centrality range of 0-20%. Left: Near-side D_{AA} is shown for the range $p_T^{jet,rec}$: 10-20 GeV/c. Right: Away-side D_{AA} is show for three ranges of $p_T^{jet,rec}$: 10-15 GeV/c, 15-20 GeV/c, and 20-40 GeV/c. $p_T^{jet,rec}$ was calculated only from charged tracks and neutral towers with $p_T > 2$ GeV/c [120].

detailed information on the shapes of jet at large angles [123]. The conclusions of this measurement were also confirmed by CMS in [124].

Chapter 4

Experimental Setup

4.1 Large Hadron Collider (LHC)

The Large Hadron Collider (LHC) is in a 27 km circumference tunnel built 50-175 m underground at CERN, [125–127] and is the latest stage of the accelerator complex at CERN shown in Fig. 4.1. It is located on the French and Swiss borders near Geneva, Switzerland. The LHC consists of three main components: the magnet system to steer the particles, the accelerators to move them, and the beam pipes to hold them [128]. The beam pipes are kept at ultra-high vacuum in the accelerator. Inside the beamlines, particle beams travel in opposite directions at speeds very close to the speed of light until they collide. At full power, a center of mass energy of 13 TeV is reached with two beams of protons and 5.5 TeV per nucleon pair in Pb–Pb collisions [129]. Various detectors at specific locations observe, analyze, and interpret the collisions.

Before particles make it to the LHC accelerator ring, they must first start out elsewhere. CERN operators with 6 accelerators seen in Fig. 4.1. The pp collisions at the LHC start their life in a bottle of hydrogen, where the protons are extracted from the hydrogen [130]. They are first accelerated by the Linear Accelerator 2 (LINAC2) up to an energy of 50 MeV [130]. From there, they are then boosted by the Proton

Synchrotron Booster (PSB) to an energy of 1.4 GeV for the Proton Synchrotron (PS). In the PS, the oldest of the accelerators at CERN, they are accelerated up to 25 GeV [130]. The next stop for the beams is at the Super Proton Synchrotron (SPS), the second largest machine in CERN's accelerator complex. Here, they really begin to pick up speed, and reach 450 GeV. At this point, they are ready for their final destination at the LHC, where they will circulate in opposite directions before colliding head on in the various experimental set-ups.

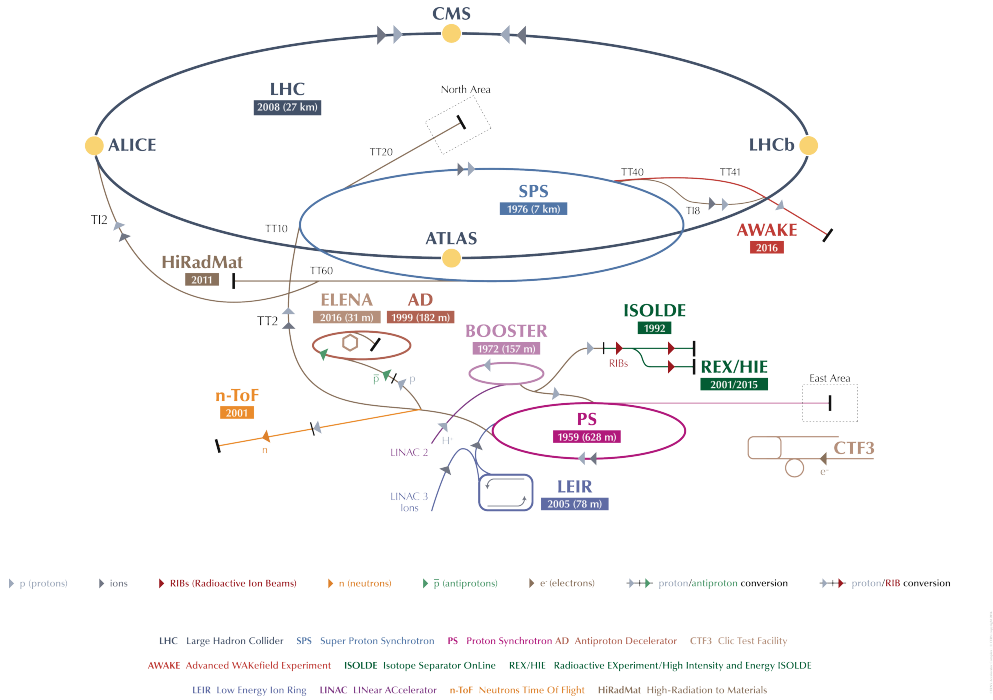

Figure 4.1: The CERN accelerator complex [131].

Pb–Pb collisions at the LHC start with highly purified lead ions which are heated to over 500°C. Electric currents are then applied in order to ionize the lead vapor [132]. The resulting ions are then accelerated up to 4.2 MeV per nucleon and then passed through foil made of carbon [132]. This interaction strips most of the ions into Pb54+ [132]. Once enough Pb54+ accumulates into a beam, it is accelerated up to 72 MeV per nucleon in the Lower Energy Ion Ring (LEIR) [130, 132] and sent off to the PS. At the PS, the ions will pass through another piece of carbon foil which strips

the them further down to Pb82+. The beam of ions will reach 5.9 GeV per nucleon in the PS before being transferred to the SPS [130, 132]. The SPS will then apply another boost up to 177 GeV per nucleon [132] before sending the lead ions off to the LHC to reach their final energy threshold and prepare for collisions.

4.2 A Large Ion Collider Experiment (ALICE)

A Large Ion Collider Experiment (ALICE) comprises approximately 1500 physicists and engineers from 154 universities and laboratories in 37 countries [133]. ALICE is an experiment [134] at CERN that studies proton-proton, proton-lead, and lead-lead collisions. Proton-proton and proton-lead collisions are used as reference data for the heavy-ion runs [134]. ALICE is dedicated to the the physics of strongly interacting matter at extreme values of temperature and energy density in nucleus-nucleus collisions [134].

The ALICE detector, shown in Fig. 4.2, [135] is roughly 50 m underground, weighs over 10,000 tons, and stands 16 m high, 16 m wide, and 26 m long [136]. The design of ALICE was motivated by the physics requirements and experimental conditions in Pb–Pb collisions [137]. It was designed for particle multiplicities up to $dN_{ch}/d\eta = 8000$ [91, 138] in heavy-ion collisions. The subdetectors of ALICE are optimized to provide high-momentum resolution and particle identication over a broad range of momenta [134].

The central barrel detectors cover $|\eta| < 0.9$ and mainly track and identify hadrons, electrons and photons [134]. A muon spectrometer located at small angles ($2^{o} - 9^{o}$, -4< η <-2.4) provides muon tracking down to zero transverse momentum. It is used primarily to measure the production of heavy-quark resonances [134]. In addition, ALICE has forward and trigger detectors to provide triggering information and global event characteristics for multiplicity, timing, and centrality [134].

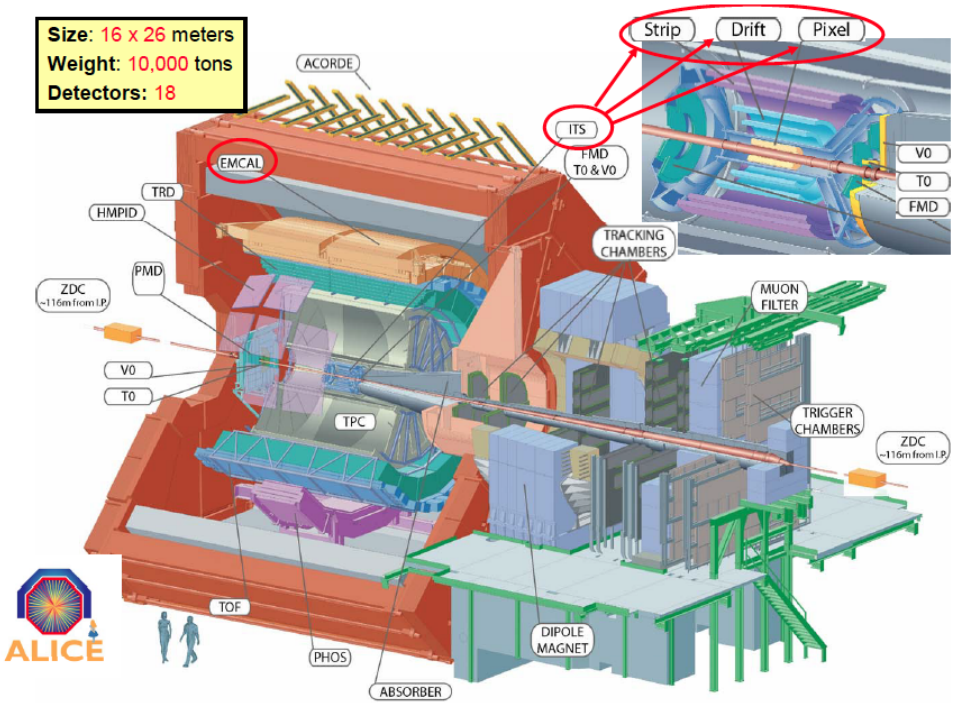

Figure 4.2: ALICE detector schematic. The 18 sub-detectors are shown along with the inset showing details of the ITS detector. The people shown at the bottom left are for scale comparison [135].

4.2.1 Inner Tracking System (ITS)

The Inner Track System (ITS) is located at the center of the main-barrel. The ITS is a cylindrical silicon detector made of six layers. The first two layers are the Silicon Pixel Detectors (SPD), followed by two layers of Silicon Drift Detectors (SDD), and two outer layers of Silicon Strip Detectors (SSD) [139]. The main goals of the inner tracker are to track and identify the low-p_T particles that do not reach the Time Projection Chamber, improve the momentum resolution for high-p_T particles, and aid in primary and secondary vertex reconstruction. The latter requires high resolution in order to detect open charm and beauty along with hyperons [137, 139]. The ITS can be used to identify low p_T particles via dE/dx measurements [137].

4.2.2 Time Projection Chamber (TPC)

The next detector surrounding the ITS is the Time Projection Chamber (TPC). The TPC is the main detector used for tracking in ALICE. It is filled with a gas mixture of Ne and CO_2. In the detector, high energy particles enter and ionize the gas. The electrons from ionization drift towards the end caps. The momentum and charge of the particles can be inferred from the curvature of the tracks. The TPC provides particle identification via dE/dx along with momentum measurements. The dE/dx distribution of the TPC in arbitrary units for 7 TeV pp collisions as a function of particle momentum is shown in Fig. 4.3 [140]. The TPC is able to identify individual particles below about 1 GeV/c and identify particles statistically in the relativistic rise region above 5 GeV/c [137].

4.2.3 VZERO detector system

The VZERO (V0) detector system consists of two scintillator arrays which are located asymmetrically on each side of the interaction point [141]. The VZERO-A covers the pseudorapidity range of $2.8 < \eta < 5.1$ and the VZER0-C covers the range of $-3.7 < \eta < -1.7$ [141, 142]. The VZERO serves the functions of providing a trigger

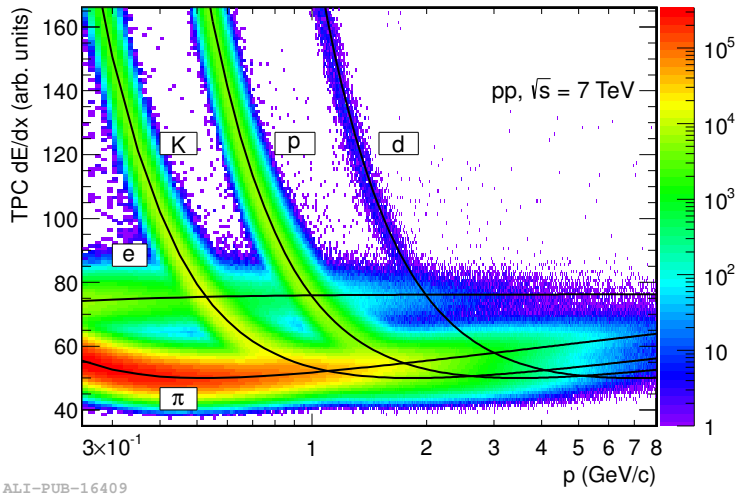

Figure 4.3: TPC dE/dx distribution in arbitrary units for $\sqrt{s}$=7 TeV pp collisions as a function of reconstructed charged particle momentum. This plot includes both positively and negatively charged particle contributions [140].

source, monitoring LHC beam conditions, rejecting beam-induced backgrounds, and also provides physics measurements of luminosity, particle multiplicity, centrality and event plane direction for nucleus-nucleus collisions [141]. In this work, the VZERO system is used for centrality and event plane measurement with the combined signal from both scintillators. A more thorough description of the VZERO system can be found in [141, 142].

An example of how centrality is attained from the combined VZERO signal amplitude is shown in Fig. 4.4. A Glauber Model fit is done to the event multiplicity distribution and the result is used to separate the events in centrality percentage bins. A "Glauber Model" in heavy-ion physics is used to calculate various geometric quantities used to describe a collision. They are expressed in terms of impact parameter (b), number of participating nucleons, N_{part} and number of binary nucleon-nucleon collisions (N_{coll}) [143].

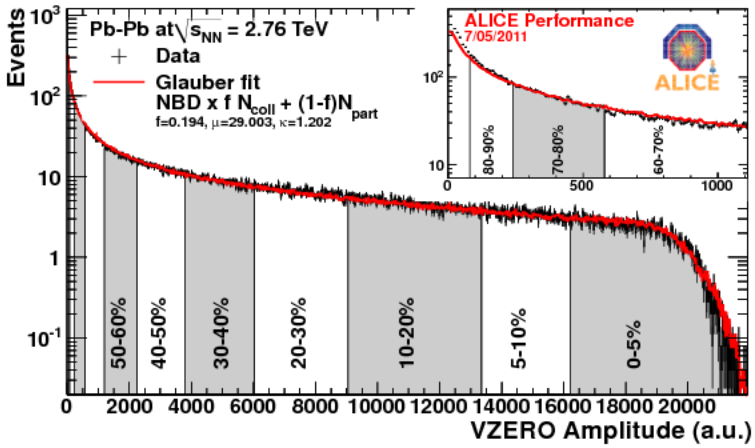

Figure 4.4: Total VZERO amplitude for Pb–Pb collisions at $\sqrt{s_{\rm NN}}$=2.76 TeV. The resulting distribution has a Glauber fit applied and is used to calculate centrality bins [144].

4.2.4 Electromagnetic Calorimeter (EMCal)

Electromagnetic Calorimeter (EMCal)

The Electromagnetic Calorimeter (EMCal) is a Pb-scintillator sampling calorimeter which has a low granularity and high energy resolution. It is optimized for measurements of jets and leptons from heavy flavor decays. The EMCal is capable of triggering on jets [145]. The EMCal covers $|\eta| \leq 0.7$ and $\triangle\phi = 107^{\rm o}$. It mainly measures photons and electrons from the decays of short-lived particles [137, 145].

Particle which traverse the EMCal produce electromagnetic showers from interaction with the scintillator while punching through. The showers contain photons, electrons, and positrons [146]. The photons come from decays and will be transported by fibers and collected by the Avalanche Photo Diode (APD). As the shower propagates through the EMCal, it will eventually deposit more and more of its energy. At some point it will either stop from losing enough energy or come out the other side. An electronic calorimeter is most sensitive to photons and electrons. If a high energy particle hits the nuclei in an atom inside the calorimeter it can also deposit energy this way. Therefore, there is sometimes contamination from a hadronic energy deposit

inside the EMCal. By taking the sum of the energy divided by the number of photons in the shower and multiplying by a sampling factor coming from the electronics, the energy of the incoming particle can be calculated.

Figure 4.5 shows the layout of the EMCal. The largest pieces are the super-module, which are the basic structural units of the calorimeter [147]. The EMCal, at the time of data-taking for this thesis had 10 full and 2 one-third super-modules. A super-module is made up of 24 strip-modules which each are in return made of 12 modules. A module is divided into 4 (2x2) "towers/cells" and is a self-contained detector unit. There are a total of 12,288 separate towers in the full detector. There are more now that the EMCal was been upgraded.

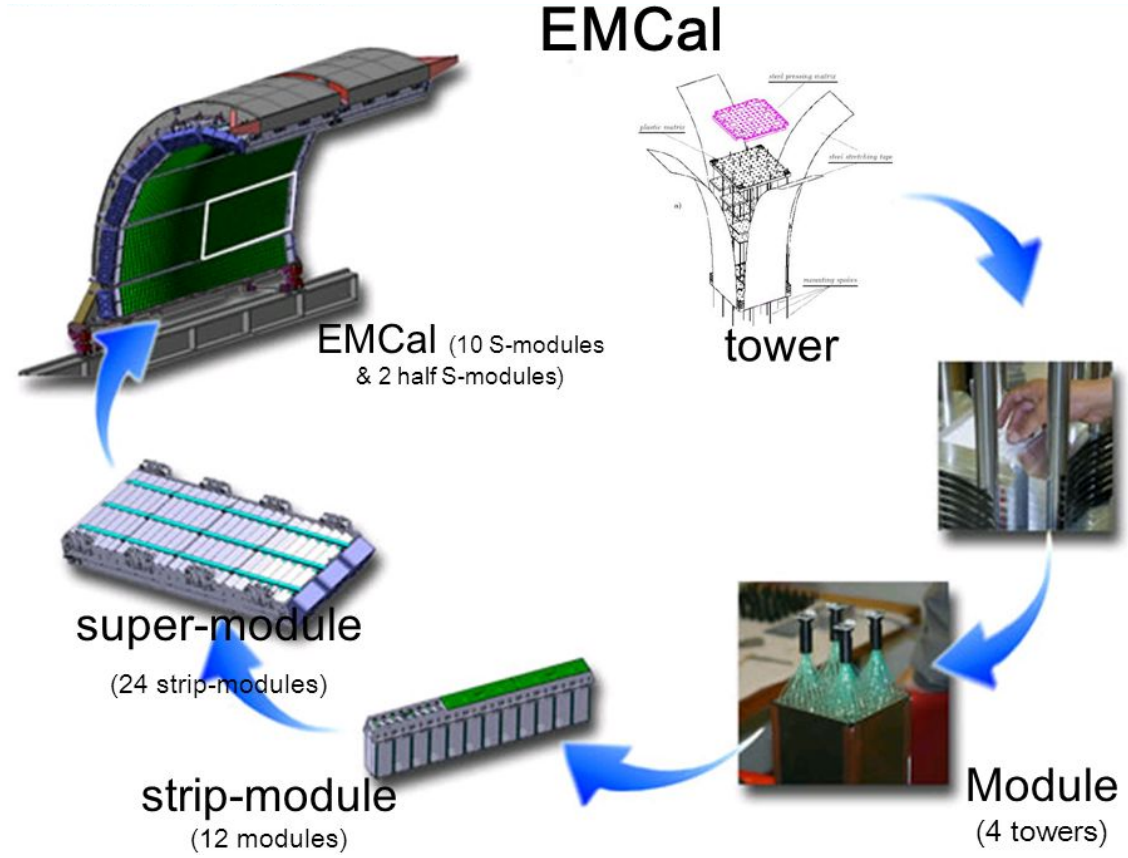

Figure 4.5: EMCal layout [148]. Shown is EMCal and the progression to smaller components that make it up.

The primary purpose of the EMCal in this analysis is to provide event triggers and the neutral component of the fully reconstructed jets from reconstructed clusters. The EMCal triggers are further discussed in [145, 147, 149] and the summarized EMCal trigger selection used in this thesis is given in Tab. 5.1. Combining the EMCal with the ALICE tracking detectors enables ALICE to reconstruct high transverse momentum jets. Most of the quantitative studies to date on jet quenching have relied on observables coming from high-p_T hadrons and their correlations (studied in this thesis) [147]. This allows for the calculation of the underlying event background coming from the heavy-ion collisions. However, it limits the study in the respect that the leading hadrons of the jets are preferentially from fragmentation of hard partons that interacted the least with the medium [147], meaning they were generated close to the surface. Full jet reconstruction in heavy-ion collisions is very important to overcome this bias and exploit fully the kinematic reach of the LHC [147]. This makes the EMCal very essential in making precise full jet measurements.

The physical characteristics of the EMCal and more extensive details can be found in [137, 147, 149]. In Sec. 5.4, more details of how the EMCal is used in this analysis are discussed.

Chapter 5

Analysis

Chapter 5 will give an introduction to the correlation measurement and give descriptions of the event, track, cluster and jet selections used in the analysis. Chapter 6 will discuss the correlation methods used. These include estimation of the reaction plane, event plane resolution calculation, description of the raw correlation and an explanation of the developed methods which were used to subtract the combinatorial background.

5.1 Introduction

Historically, the effects of the medium on high energy partons were studied by measuring the leading particles and studying the p_T distribution of pairs of high-p_T particles. Leading particle studies, however, have limitations in extreme quenching scenarios. In these cases, particle emission occurs near the surface of the medium and thus the sensitivity of the leading particles to the region of highest energy density is very limited. This consequently makes the nuclear modification factor insensitive to medium properties.

Correlations of charged tracks with full jets consisting of both EMCal clusters (neutral constituents) and charged particle tracks (charged constituents) using the anti-k_T algorithm from the FastJET package [150] are measured relative to the

reaction plane in Pb–Pb collisions at $\sqrt{s_{NN}} = 2.76$ TeV. This analysis expands upon earlier work on jet-hadron correlations [121] by introducting reaction plane dependence to study the path length dependence of energy loss.

In jet-hadron correlations, a reconstructed jet is used to define the coordinate system and the distribution of associated particles relative to that trigger jet is determined by

$$\frac{1}{N_{trig}} \frac{d^2 N_{assoc,jet}}{d\Delta\phi d\Delta\eta}, \tag{5.1}$$

where N_{trig} is the number of trigger jets in the sample, $N_{assoc,jet}$ is the number of associated particles, $\Delta\phi$ is the azimuthal angle of those trigger particles relative to the trigger jets, and $\Delta\eta$ is the difference between the pseudorapidities of the trigger jet and associated particle. The choice of normalization by the number of trigger jets is arbitrary but matches the conventions for most studies in the literature. The goals of this analysis are to study the conditional yield of associated particles, the width of the near- and away-side peaks (quantified using the RMS), and the suppression compared to pp collisions as a function of the angle of the jet relative to the reaction plane. The yield is calculated by

$$Y = \frac{1}{N_{trig}} \int_c^d \int_a^b \frac{d^2 N_{assoc,jet}}{d\Delta\phi d\Delta\eta} d\Delta\phi d\Delta\eta, \tag{5.2}$$

and I_{AA} by

$$I_{AA} = Y_{Pb-Pb}/Y_{pp}. \tag{5.3}$$

The choice of integration limits is somewhat arbitrary and their definition is considered part of the definition of the measurement. They are chosen based on practical considerations, including the detector acceptance and binning of histograms. More details of the the limits used when reporting these measurements can be found in Sec. 7.3. We report the truncated RMS

$$RMS = \sqrt{\int_a^b \frac{1}{Y N_{trig}} \frac{dN_{assoc,jet}}{d\Delta\phi} (\Delta\phi - \Delta\phi_0)^2 d\Delta\phi} \tag{5.4}$$

where $\Delta\phi_0 = 0$ for the near-side and π for the away-side rather than the RMS over all $\Delta\phi$ because integration over a wide range in $\Delta\phi$ increases the weight of statistical error bars without dramatically changing the result. The integration limits are the same as for Eqn. 5.2.

The measurement of the correlation function, discussed in Sec. 6, requires several corrections:

$$\frac{1}{N_{trig}} \frac{d^2 N_{assoc,jet}}{d\Delta\phi d\Delta\eta} = \frac{1}{N_{trig}} \frac{d^2}{d\Delta\phi d\Delta\eta} \frac{N_{meas} - N_{bkgd}}{\epsilon(p_T, \eta) a(\Delta\phi, \Delta\eta)} \tag{5.5}$$

where $\epsilon(p_T, \eta)$ is the single track reconstruction efficiency and acceptance, * $a(\Delta\phi, \Delta\eta)$ is the acceptance correction for track pairs, N_{meas} is the measured number of associated particles, and N_{bkgd} is the number of associated particles from the background. The single track reconstruction efficiency only accounts for the reconstruction of associated particles. Event selection is discussed in Sec. 5.2. The details of jet finding are discussed in Sec. 5.5. Since correlation functions are measured relative to the reaction plane, discussion of the measurement of the reaction plane is discussed in Sec. 6.1. The selection of tracks, the corresponding reconstruction efficiency, and the systematic uncertainty on that correction are discussed in Sec. 5.3. The pair acceptance correction and its uncertainty are discussed in Sec. 6.5. The background subtraction is primarily done using the Reaction Plane Fit method [151]. This correction and its uncertainty are discussed in Sec. 6.6.

*Acceptance effects such as gaps between sector boundaries are included in this correction, however, we refer to $\epsilon(p_T, \eta)$ as an efficiency correction in order to distinguish it from $a(\Delta\phi, \Delta\eta)$.

5.2 Event selection

The Pb–Pb data for this analysis were collected in 2011. It is sorted into Good and Semi-Good run lists, corresponding to the quality of the TPC throughout the runs. The Good TPC run list is used in this thesis for the analysis. The Semi-Good TPC run list corresponds to an inner readout chamber (IROC) being switched off within the TPC, causing a dip in the reconstruction efficiency of the TPC in ϕ [152]. The dip did not overlap with the acceptance of the EMCal and only amounted to roughly 10% of the total statistics. These Semi-Good TPC runs were dropped from the analysis, but are shown for comparison with the Good TPC runs in 5.3.1.

The physics selection filters used with the EMCal are given in Tab. 5.1. This analysis focuses on EMCal triggered events. Jet patch, gamma patch, and minimum bias triggered data sets are used. The jet patch trigger consists of deposits in 32x32 towers, while the gamma patch trigger consists of deposits in 4x4 towers. The energy thresholds are centrality dependent. But, when a threshold in a given patch region is met for a given event, that event passes the trigger requirement and the event is thus flagged as meeting that particular physics selection offered by the given trigger. The gamma trigger is the primary trigger. Jet patch triggered data were investigated, but was not be used for the final analysis. For a more details look at the trigger scheme and functionality of the ALICE EMCal triggers, please see [145, 147, 149]. The mixed event correction, which corrects for the limited acceptance range of the EMCal, mixes jets from gamma triggered events with charged hadrons from minimum bias events. The 0–80% most central events are studied to avoid the corrections required for electromagnetic interactions which contaminate the most peripheral collisions. We select events which have a reconstructed primary vertex $|V_z| < 10$ cm. Centrality selection is as in [153].

Table 5.1: EMCal trigger selection breakdown by clustering size of towers.

kEMCEJE	L1 jet trigger	deposit in 32x32 towers, sliding by 8 towers
kEMCEGA	L1 gamma trigger	deposit in 4x4 towers, sliding by 2 towers
kEMCE7, kEMCE1	L0 trigger	deposit in 4x4 towers, sliding by 2 towers, 3 exclusive regions per SM

5.3 Track reconstruction and selection

Track selection is as in [121, 152]. The charged jet component and the charged tracks which are used in the correlations are reconstructed using the ALICE central barrel tracking detectors. The ALICE central barrel tracking detectors consist of the Inner Tracking System (ITS) and the Time Projection Chamber (TPC). The track selection uses "hybrid tracks". Hybrid tracks use a combination of track classes in order to ensure uniform distributions in the (η, ψ) plane. The track quality cuts used to define the 2 track types are listed in Tab. 5.2. The difference between global constrained and global tracks for LHC11h data is that the global constrained tracks (also referred to as complementary tracks [152]) do not require SPD hits [154]. Instead, the complementary tracks are constrained to the primary vertex in order to improve the p_T resolution of the tracks [152, 154, 155]. Global tracks are used when available and global constrained tracks are used otherwise. In this analysis, only tracks which have $p_T > 150$ MeV/c are used.

5.3.1 Tracking Efficiency

The single track reconstruction efficiency is used for the determination of the number of associated particles. The tracking efficiency is defined as the ratio of the number of particles detected by the detector to the number of generated particles incident within

Table 5.2: Overview of the hybrid track cuts.

AliESDtrackCuts function	Value	Comment
Global and complementary tracks		
Min N clusters TPC p_T dep.	$70+30/20 p_T$, 20	Linear rise from 70 ($p_T = 0$) to 100 ($p_T = 20$ GeV/c), 100 for $p_T > 20$ GeV/c
Max χ^2 per cluster TPC	4	Maximum χ^2 per TPC cluster in the first iteration
Require TPC standalone	TRUE	Enable cut on TPC clusters in the first iteration
Accept kink daughters	FALSE	Reject Tracks with kink
Require TPC refit	TRUE	Require TPC refit
Max fraction shared TPC clusters	0.4	Maximum fraction of shared TPC clusters
Max DCA to vertex XY	2.4	Maximum Distance of Closest Approach (DCA) to the main vertex in transverse direction
Max DCA to vertex Z	3.2	Maximum DCA in longitudinal direction
DCA to vertex 2D	TRUE	Cut on the quadratic sum of DCA in XY- and Z-direction
Max χ^2 per cluster ITS	36	Maximum χ^2 per ITS cluster
Max χ^2 TPC constrained global	36	Maximum χ^2 between global and TPC constrained tracks
Require sigma to vertex	FALSE	No sigma cut to vertex
Eta range	-0.9, 0.9	Pseudorapidity cut
p_T range	0.15, 1E+15.	Minimum $p_T > 150$ MeV/c
Only for global tracks		
Cluster requirement ITS	ESD track cuts: kSPD, kAny	Require at least one hit in SPD
Require ITS refit	TRUE	Require ITS refit
Only for complementary tracks		
Require ITS refit	FALSE	No ITS refit

the relevant phase space. Monte-Carlo (MC) productions created using HIJING [156] are used to determine the number of generated particles.

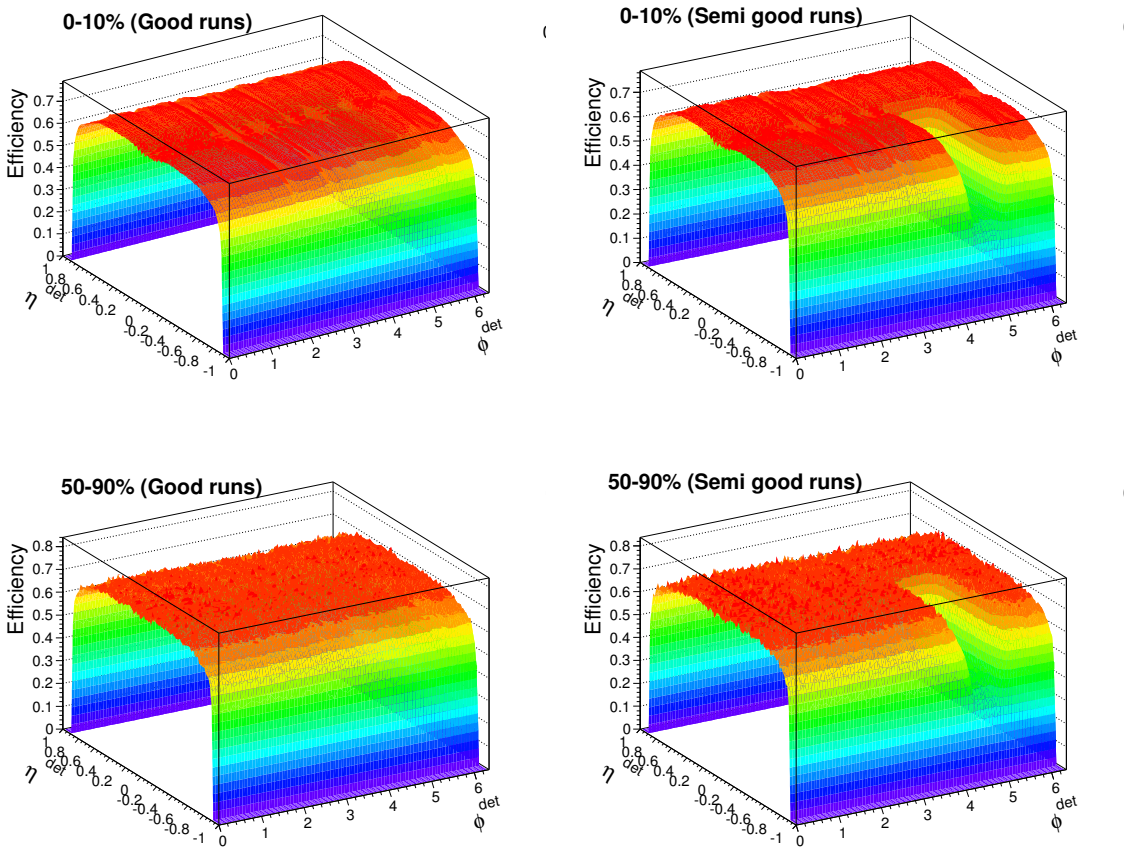

Figure 5.1: Tracking efficiency for 0-10% (top) and 50-90% (bottom) centrality classes as a function of ϕ and η for Good runs (left) and Semi-Good runs (right).

Figure 5.1 shows the tracking efficiency as a function of ϕ and η for 0-10% and 50-90% centrality classes for Good runs and Semi-Good runs. The efficiency is factorized into η-dependent and p_T dependent parts. The dip in Semi-Good runs is from the bad sector in the TPC. The efficiency is determined separately for various centralities and for Good runs and Semi-Good runs and fit simultaneously by

$$\epsilon^{Semi-Good}(p_T,\eta) = \begin{pmatrix} p_0\ e^{-(p_1/p_T)^{p_2}} + p_3\ p_T, & p_T < 2.9 \\ p_4 + p_5\ p_T + p_6\ p_{\mathrm{T}}^2, & p_T > 2.9 \end{pmatrix} \times \\ \begin{pmatrix} p_7\ e^{-(p_8/|\eta+0.91|)^{p_9}} + p_{10}\ \eta, & \eta < -0.07 \\ p_{11} + p_{12}\ \eta + p_{13}\ \eta^2, & -0.07 < \eta < 0.4 \\ \eta > 0.4) \times (p_{14}\ e^{-(p_{15}/|-\eta+0.91|)^{p_{16}}}, & \eta > 0.4 \end{pmatrix} \quad (5.6)$$

for Semi-Good runs and

$$\epsilon^{Good}(p_T,\eta) = \begin{pmatrix} p_0\ e^{-(p_1/p_T)^{p_2}} + p_3\ p_T, & p_T < 2.9 \\ p_4 + p_5\ p_T + p_6\ p_{\mathrm{T}}^2, & p_T > 2.9 \end{pmatrix} \times \\ \begin{pmatrix} p_7\ e^{-(p_8/|\eta+0.91|)^{p_9}} + p_{10}\ \eta, & \eta < 0.0 \\ p_{11} + p_{12}\ \eta + p_{13}\ \eta^2, & 0.0 < \eta < 4.0 \\ p_{14}\ e^{-(p_{15}/|-\eta+0.91|)^{p_{16}}}, & \eta > 0.4 \end{pmatrix} \quad (5.7)$$

for Good runs. The efficiencies, the difference between the fit and the efficiencies, and the ratio of the efficiencies to the fit are shown for several centrality bins in Fig. 5.2 for Semi-Good runs and in Fig. 5.3 for Good runs. The goal of the fit is to completely describe the shape of the efficiency to make analysis on the Worldwide LHC Computing Grid (WLCG) [157] easier. The fit function is empirical and as can be see in Fig. 5.2 and Fig. 5.3, this function describes the efficiency well. Fit parameters are given in Tab. 5.3.

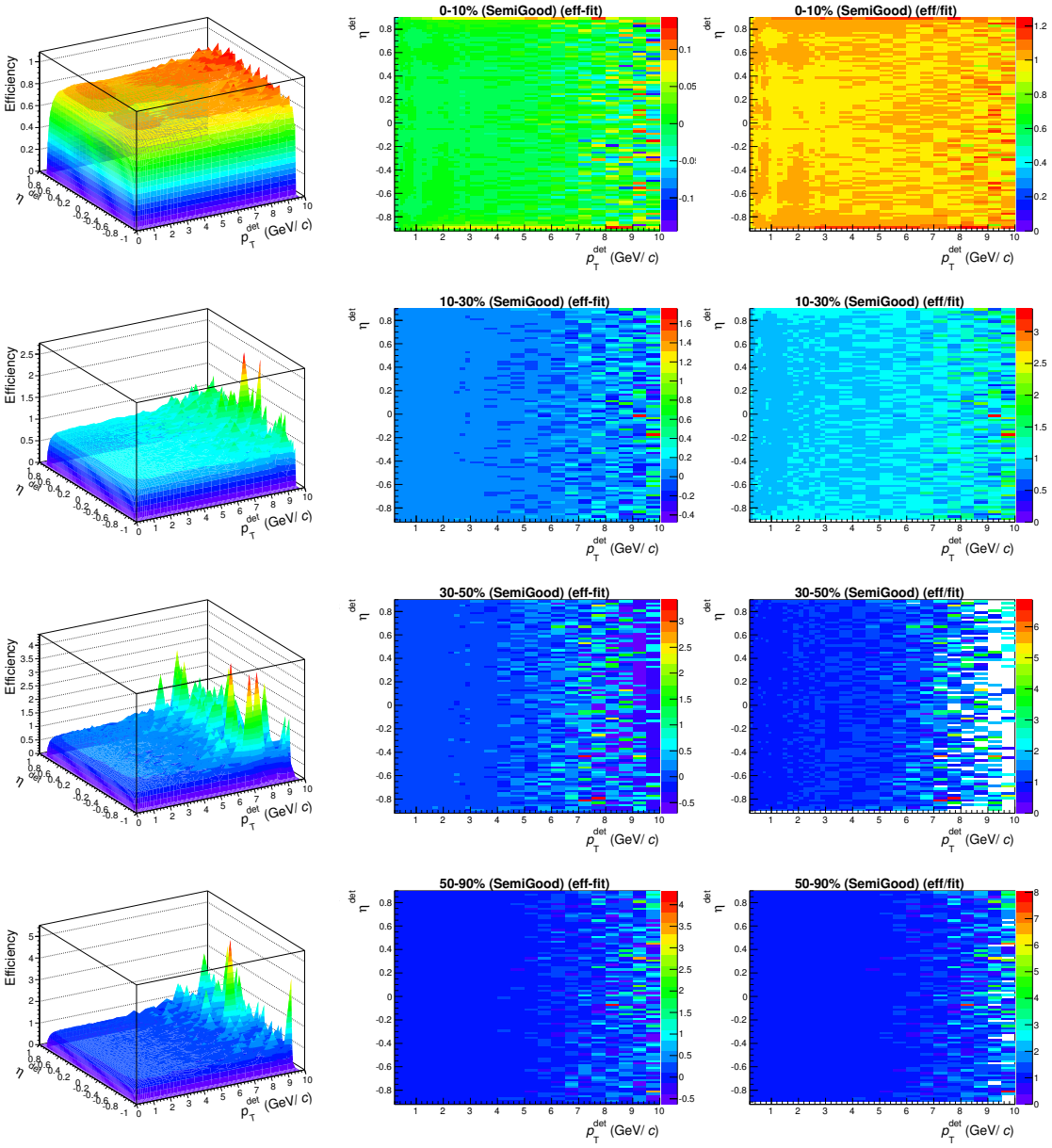

Figure 5.2: Efficiency (left), difference between efficiency and fit (middle), and ratio of efficiency and fit (right) for each centrality bin for Semi-Good runs.

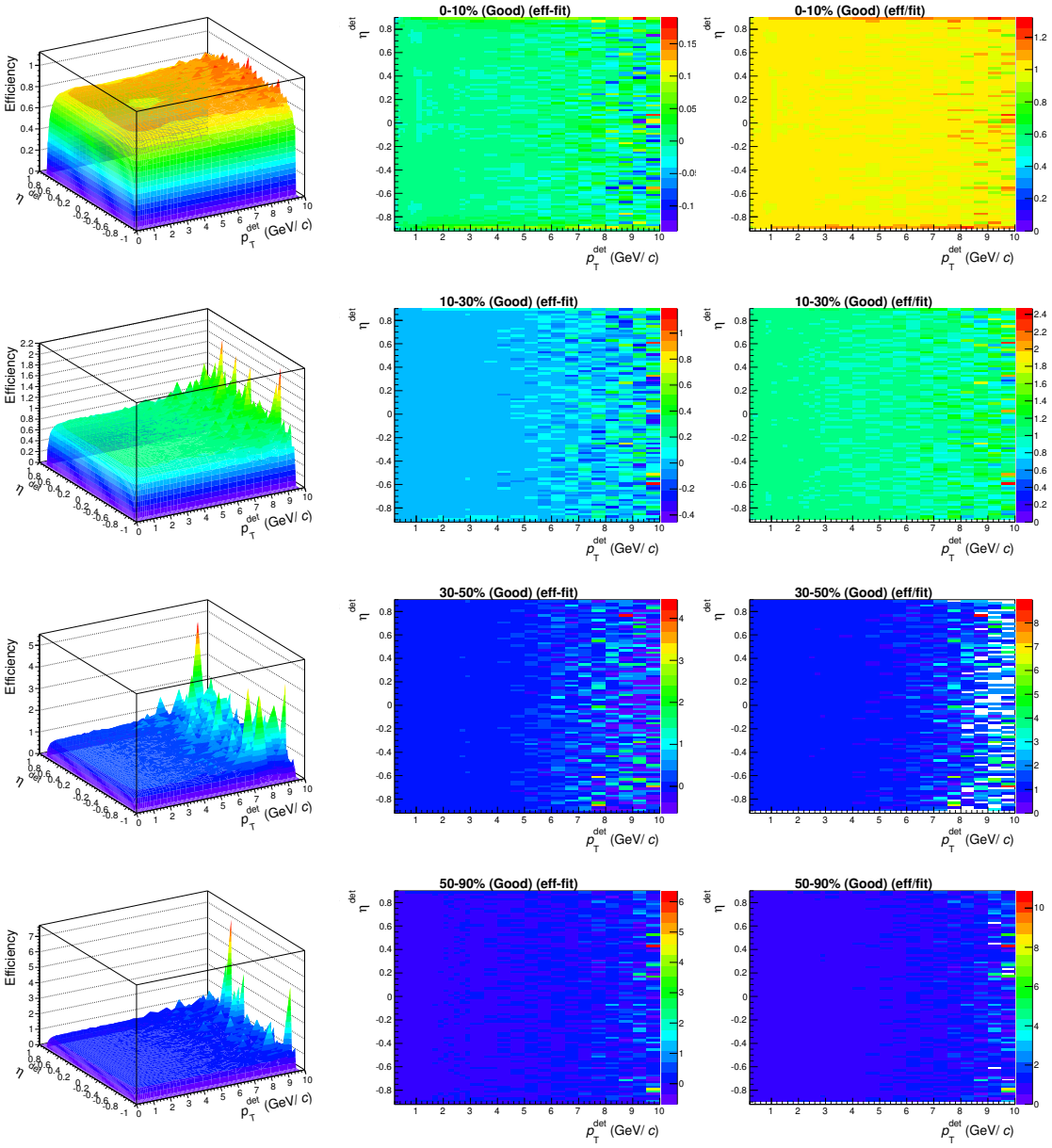

Figure 5.3: Efficiency (left), difference between efficiency and fit (middle), and ratio of efficiency and fit (right) for each centrality bin for Good runs.

Table 5.3: Efficiency fit parameters for Good and Semi-Good runs.

centrality	χ^2/NDF	p_0	p_1	p_2	p_3	p_4	p_5	p_6	p_7	p_8	p_8	p_{10}	p_{11}	p_{12}	p_{13}	p_{14}	p_{15}	p_{16}
Good Runs																		
0–10%	60327/2953	0.907	0.0754	1.12	-0.0233	0.795	0.0094	-0.00033	1.09	0.0107	0.443	-0.143	0.966	0.359	-0.581	1.07	0.0063	0.706
10–30%	3811.76/2953	0.908	0.0769	1.12	-0.0249	0.741	0.0361	-0.00368	1.10	0.0114	0.452	-0.133	0.981	0.358	-0.620	1.07	0.0056	0.753
30–50%	997.189/2761	0.959	0.0799	1.11	-0.0358	0.751	0.0608	-0.00930	0.99	0.0069	0.615	-0.048	0.968	0.322	-0.619	1.03	0.0065	0.799
50–90%	1638.97/2930	0.945	0.0807	1.13	-0.0325	0.666	0.0842	-0.00964	1.03	0.0067	0.550	-0.060	0.981	0.309	-0.619	1.05	0.0059	0.745
Semi-Good Runs																		
0–10%	87768.1/2953	0.972	0.0768	1.13	-0.0274	0.857	0.0054	0.00009	1.07	0.0110	0.447	-0.147	0.920	0.193	-0.269	1.00	0.0062	0.709
10–30%	5016.34/2953	0.979	0.0776	1.12	-0.0301	0.845	0.0135	-0.00123	1.08	0.0117	0.457	-0.133	0.931	0.174	-0.267	0.99	0.0057	0.765
30–50%	1159.74/2853	0.998	0.0817	1.14	-0.0354	0.752	0.0744	-0.01029	1.02	0.0071	0.572	-0.064	0.948	0.102	-0.195	1.00	0.0057	0.724
50–90%	2084.97/2947	0.970	0.0814	1.12	-0.0369	0.709	0.0702	-0.00784	1.06	0.0068	0.536	-0.070	0.983	0.095	-0.181	1.03	0.0058	0.738

Systematic uncertainties There was a 5% uncertainty used for track efficiency, along with a 1% uncertainty used for contamination from secondary particles. These estimates are based on various jet studies using the hybrid track selection [152, 158–160], summarized by Tab. 5.2. The tracking efficiency and contamination systematic uncertainties were added in quadrature with the mixed event normalization listed in Sec. 6.5 and the result was conservatively rounded up to give a 6% global scale uncertainty. This is listed on the final plots.

5.4 EMCal cluster selection

Cluster selection is as in [152, 159]. Clusters are found by using the V2 clustering algorithm, which combines cell towers of the calorimeter. The cell size is $\Delta\eta = 0.14$ and $\Delta\phi = 0.14$ per tower. The clustering algorithm takes all cells which have an energy deposit greater than 50 MeV and uses them as a seed for a cluster [146, 149]. A seed threshold is set at 100 MeV. The algorithm starts with the highest energy cell in the EMCal first. It adds all the cells meeting the threshold until there are none remaining. The center of energy of the cells is used to determine the cluster position [146]. Cells that become part of a cluster are removed from further clustering. To handle clusters which may be merged with another, the algorithm looks for a change in the derivative of the deposited energy as the cluster grows. If the cell in question has more energy than an adjacent cluster then it is neglected from being added and the algorithm haults [146, 149]. All clusters which then have an energy greater than 150 MeV are corrected for hadronic energy contamination and the clusters with greater than 300 MeV after correction are used for the analysis. More information on the hadronic correction can be found in [159].

5.4.1 EMCal timing

During Pb–Pb collisions at $\sqrt{s_{NN}} = 2.76$ GeV, the timing between bunch crossings was comparable to the timing resolution of the EMCal, so some clusters reconstructed in an event will come from the previous or next bunch crossing [152]. After timing calibrations, there are still clusters from events from out-of-time bunches. Clusters from out-of-time events should not be correlated with the measured event and should impact both the signal and the background [152]. The asymmetric dependence of the the timing distribution of cluster energies is not well understood, but the clusters which are in-time exhibit this behavior as well [152]. Therefore, the timing cuts about time $t = 0$ are also chosen to be asymmetric and for the data used in this analysis the cuts were chosen to be from -50×10^{-9} to 100×10^{-9}s.

5.4.2 Cluster-Track matching

A maximum distance of clusters and tracks matched is set at 0.1 radians. The propagation depth of 440 cm is used because it is the average depth of clusters in Pb–Pb events [152]. Electrons and positrons will leave a signature both in the tracking detectors and in the EMCal, as will some charged hadrons. The average energy deposited by a minimim ionizing particle (MIP) in the EMCal is approximately 280 MeV [152]. Additionally, charged hadrons may begin a hadronic shower, which will only be partially contained in the EMCal [152]. This can lead to double counting of the energy from these particles. However, due to the high occupancy of the EMCal in central events, clusters matched to tracks may be due to $e^{\pm}$, charged hadrons, the overlap of a charged track with a cluster due to a neutral particle, or a false match between a track and a cluster. Due to the finite single track reconstruction efficiency, some of the $e^{\pm}$ and charged hadrons which leave a deposit in the EMCal will not be matched to a track reconstructed in the tracking detectors.

The same approach as [152, 159] was used to remove energy which was deposited by charged particles. It is done to avoid the double counting of particles that deposit

energy in the EMCal as well as leave a track in the TPC. This is especially important during the jet-finding procedure. The correction of the cluster energy is given by $\Delta E_{corr} = E_{clust} - E_{corr}$. This correction is calcuated for each cluster that has tracks matched to it by [152]:

$$\Delta E_{corr} = \begin{cases} E_{clust} & \text{for } E_{clust} < f \times \sum_{matches} p \\ \\ f \times \sum_{matches} p & \text{for } E_{clust} > f \times \sum_{matches} p \end{cases} \tag{5.8}$$

where E_{clust} is the cluster energy and $\sum_{matches} p$ corresponding to the total momentum magnitude summed over all matching tracks. The cluster is corrected for by assigning new energy $E_{new} = E_{clust} - \Delta E_{corr}$ to the cluster. As for [121, 152], f is chosen to be 1. However, the cluster is discarded when the new energy is below the threshold 0.3 GeV.

5.5 Jet reconstruction

In this analysis, full jets are reconstructed. For full jet reconstruction, we combine the charged tracks of the ITS and TPC and the EMCal clusters. This reconstruction is done through the use of the FASTJET package [150]. This analysis uses the sequential recombination algorithms: anti-k_T and k_T. anti-k_T is used for signal jets while k_T is used for the underlying event estimation. Other than the momentum and energy thresholds used for jet reconstruction and subtraction of the background energy, both described in further detail below, this analysis follows the same procedure as [152].

In heavy-ion events, we have a large underlying event background and the jet signal is embedded beneath hundreds to thousands of particles resulting from various other processes. In order to reduce the influence of these background particles, this analysis uses tracks and clusters with $p_T > 3$ GeV/c as the constituents of the jet.

For full jets, the use of the EMCal for our clusters has the drawback of a limited acceptance range. The EMCal has coverage in pseudorapidity of $-0.7 < \eta < 0.7$ ($\Delta\eta = 1.4$) and coverage in azimuth of $80^{o} < \phi < 187^{o}$ ($\Delta\phi = 107^{o}$) [147]. We apply a fiducial cut based on the location of the jet centroid. This is given as:

$$|\eta_{jet}| < 0.7 - R, \;\; 1.4 + R < \phi_{jet} < 3.14 - R \tag{5.9}$$

Only jets with a resolution parameter $R = 0.2$ are used in this analysis. Additional cuts that are applied include a cut to the area in $\eta - \phi$ space to the jet. For the $R = 0.2$ jets, an area cut is applied to exclude jets that have an area below 0.08. This helps remove low momentum jets [160]. Jets which contain extremely high p_T tracks are rejected due to the likelihood that they are from misreconstructed tracks. The cutoff is set to 100 GeV/c.

5.5.1 Background energy density

The jets produced in heavy-ion collisions sit on top of a large amount of (soft) background. The variable most often used to quantify this background is ρ, which refers to the underlying event background density. The procedure for obtaining ρ follows from [152] and requires clustering all charged tracks in the event into groups using the k_T jet-finding algorithm provided by FastJet [150]. The two leading jets in the event are removed and the underlying event background density is expressed as the median of the remaining k_T clusters, by the ratio given in Eqn. 5.10.

$$\rho_{ch} = median\left(p^{ch}_{T,k_T jet}/A_{k_T jet}\right) \tag{5.10}$$

In Eqn. 5.10, $p^{ch}_{T,k_T jet}$ refers to the transverse momenta of the charged k_T jet and $A_{k_T jet}$ corresponds to the area of the jet. The charged background density scales with event multiplicity, N, such that: $\rho \sim N\langle p_T \rangle$. In order to include the neutral energy,

the underlying event charged background density is scaled by a centrality dependent scale factor. This is shown in Eqn. 5.11.

$$\rho_{scaled} = \rho_{ch} \times s_{EMC} \tag{5.11}$$

The scaled function, takes the form given by Eqn. 5.12, where A, B, and C are constants and x refers to the centrality dependence.

$$s_{EMC} = Ax^2 + Bx + C \tag{5.12}$$

Tab. 5.4 shows the parameter values of the scale function when a) using different hadronic corrections and b) different clusterizers.

Table 5.4: Charged background p_T density expressed in terms of event-by-event average and standard deviation for three different minimum particle p_T and two centrality bins [1].

clusterizer type	hadronic correction	C	B	A
2x2	2.0	1.765	-0.01160	0.000107
	1.7	1.817	-0.01501	0.000194
	1.3	1.905	-0.01698	0.000215
	0.0	2.042	-0.01579	0.000148
3x3	2.0	1.853	-0.01210	0.0001093
	0.0	2.136	-0.01652	0.0001428
GA trigger 2x2	2.0	1.812	-0.01055	0.0001455

The scaled background density for the particular constituent cuts used in this analysis is calculated as a cross check to demonstrate that background particles that end up in jets are negligible. This is especially true for track and cluster cuts above 3.0 GeV/c. Scaled background density vs centrality are shown in Sec. C.6 by Fig. C.11, C.12, and C.13 for 0.15, 1.0 and 2.0 GeV/c tracks. We see that ρ_{scaled} does not have any statistics to within the bin size for a 2.0 GeV/c track cut, suggesting how negligible the background becomes at that transverse momenta.

Chapter 6

Correlation methods

This section describes corrections required for the correct calculation of the correlation function described in Eqn. 5.5. It will describe the methods used to correct the correlation function relative to the event plane. These include estimating the reaction plane, event plane resolution calculation, mixed event correction, and modeling and subtraction of the combinatorial background.

6.1 Estimating the reaction plane

The reaction plane is the plane defined by the beam direction (z-axis) and the impact parameter (x-axis). We refer to the event plane as the experimental estimate of the reaction plane [161]. The nth order event plane can be calculated from the azimuthal distribution of charged particles by:

$$\varphi_n = \left(\arctan \frac{\sum_i w_i \sin(n\varphi_i)}{\sum_i w_i \cos(n\varphi_i)} \right) / n, \tag{6.1}$$

where the sum is over all particles in a given event. The ith particle has a weight, w_i, with a corresponding angle, φ_i. This analysis focuses on the use of the 2nd order event plane constructed from the combined VZERO signal, which we will denote as Ψ_{RP} in the following generalized equations. For the VZER0, the weights are equal

to the VZERO amplitude which is proportional to the multiplicity. When the TPC is split into different pseudorapidity regions, tracks are given an equal weight ($w_i = 1$) [162]. More details on the procedure can be found in [162].

The resulting azimuthal anistropy can be characterized by the Fourier decomposition of the azimuthal particle distribution with respect to the 2nd order reaction plane by:

$$\frac{dN}{d(\phi - \Psi_{RP})} = \frac{N_0}{2\pi}\left(1 + 2\sum_{n=1}^{\infty} v_n \cos[n(\phi - \Psi_{RP})]\right). \tag{6.2}$$

In Eqn. 6.2, which is the form of the background that gets modeled in this analysis, N_0 is the number of particles, ϕ describes the azimuthal angle of the particles, Ψ_{RP} describes the azimuthal angle of the true reaction plane determined by the beam axis and the impact parameter and v_n is the n-th harmonic coefficient. Since the 'true' reaction plane angle is not known experimentally, it is replaced by the reconstructed event plane angle. Due to the finite multiplicity of each event, there will be a difference between these two planes. It is corrected for by an event plane resolution, $\Re$, discussed in Sec. 6.2, which describes the accuracy in which the event plane reproduces the true reaction plane.

The n-th harmonic coefficient is expressed by $v_n = \langle\cos(n(\varphi - \psi_{RP}))\rangle$. The observed Fourier coefficients can be corrected if the event plane resolution is known. They are divided by the event plane resolution, $v_n = v_n^{obs}/\Re$ [141, 161]. Since an ideal event plane resolution is equal to 1, for non-ideal cases, the value of the coefficents will be raised by applying the correction.

The event plane is reconstructed by combining signals from both sides of the VZERO forward detector. It is possible to reduce the bias caused by highly energetic jets on the calculation of the event plane orientation since VZEROA and VZEROC cover different ranges of pseudo-rapidity and the probability for dijet pairs to hit both sides is low [162].

6.2 Event Plane Resolution

Due to the finite multiplicity of each event, there is a difference between the reconstructed event plane and the symmetry plane Ψ_n. The resulting limited resolution of measured coefficients need to be corrected up to what they would be relative to the real reaction plane [161]. This is done by introducing an event plane resolution $\Re$ factor. The event plane resolution factor is used in this analysis to correct the Fourier coefficients that are fit in the background of the correlations. This is discussed more in Sec. 6.6. The correlation of the event plane with the symmetry plane is expressed by $\Re$:

$$\Re = \langle \cos(n[\Psi_{EP} - \Psi_n]) \rangle. \tag{6.3}$$

This analysis has used the three sub-event method to calculate the event plane resolution, $\Re$. The three sub-events consisted of the VZERO signal, and both the positive and negative pseudo-rapidity regions of the TPC. Event plane resolution is most commonly expressed as a function of collision centrality. The centrality percentage bins used for the event plane resolution correction {0, 5, 10, 20, 30, 40, 50, 60, 70, 90} are different than the centrality percentage bins used in the analysis {0, 10, 20, 30, 50, 90}. Bins are corrected and then combined accordingly. By constructing the event plane in two different sub-events, the corresponding relation can be simplified. We can write the the correlation of two event planes by taking the product of two sub-events [161, 163]:

$$\langle \cos(n[\Psi^a_{EP} - \Psi^b_{EP}]) \rangle = \langle \cos(n[\Psi^a_{EP} - \Psi_n]) \rangle \langle \cos(n[\Psi^b_{EP} - \Psi_n]) \rangle = \Re^a_n \Re^b_n, \tag{6.4}$$

$$\langle \cos(n[\Psi^a_{EP} - \Psi^c_{EP}]) \rangle = \langle \cos(n[\Psi^a_{EP} - \Psi_n]) \rangle \langle \cos(n[\Psi^c_{EP} - \Psi_n]) \rangle = \Re^a_n \Re^c_n, \tag{6.5}$$

and

$$\langle \cos(n[\Psi^b_{EP} - \Psi^c_{EP}]) \rangle = \langle \cos(n[\Psi^b_{EP} - \Psi_n]) \rangle \langle \cos(n[\Psi^c_{EP} - \Psi_n]) \rangle = \Re^b_n \Re^c_n. \quad (6.6)$$

By combining Eqn. 6.4, 6.5, and 6.6 we can express the resolution of subevent a, b, and c by:

$$\Re^a_n = \langle \cos(n[\Psi^a_{EP} - \Psi_n]) \rangle = \sqrt{\frac{\langle \cos(n[\Psi^a_{EP} - \Psi^b_{EP}]) \rangle \langle \cos(n[\Psi^a_{EP} - \Psi^c_{EP}]) \rangle}{\langle \cos(n[\Psi^b_{EP} - \Psi^c_{EP}]) \rangle}}, \quad (6.7)$$

$$\Re^b_n = \langle \cos(n[\Psi^b_{EP} - \Psi_n]) \rangle = \sqrt{\frac{\langle \cos(n[\Psi^b_{EP} - \Psi^c_{EP}]) \rangle \langle \cos(n[\Psi^b_{EP} - \Psi^a_{EP}]) \rangle}{\langle \cos(n[\Psi^c_{EP} - \Psi^a_{EP}]) \rangle}}, \quad (6.8)$$

and

$$\Re^c_n = \langle \cos(n[\Psi^c_{EP} - \Psi_n]) \rangle = \sqrt{\frac{\langle \cos(n[\Psi^c_{EP} - \Psi^a_{EP}]) \rangle \langle \cos(n[\Psi^c_{EP} - \Psi^b_{EP}]) \rangle}{\langle \cos(n[\Psi^a_{EP} - \Psi^b_{EP}]) \rangle}}. \quad (6.9)$$

In this analysis, results are reported for 30-50% centrality by combining the 30-40% and 40-50% bins, using the number of events as a weight. It is noted that a simple average calculation differs from the weighted calculation by only 0.0049 for $R_2(\Psi_2)$ and 0.0061 for $R_4(\Psi_2)$.

The second (fourth) order VZERO event plane resolutions relative to the second order event plane as a function of collision centrality are shown in Fig. 6.1 and Fig. 6.2. Measured values for the event plane resolution are in good agreement with prior ALICE studies [164, 165]. The third and fifth order VZERO event plane resolutions relative to the second order event plane were also calculated, but not used in this analysis (and thus not shown) because the odd order event planes are negligibly

correlated with the 2nd order event plane [166–168]. When background calculations are done, fits are only done to fourth order of the Fourier coefficients. It is noted that different resolutions values can be extracted for the same detector using the two- or three- sub-event method due to fluctuations in flow and non-flow correlations [165]. The errors on the event plane resolution are very small, but as a conservative approach the systematic uncertainty for R_n was varied by 1%, and 2% with a negligible effect on the final $\Delta\phi$ correlations. The value used for the event plane resolution systematic uncertainty was 1%. A more detailed description can be found in Sec. C.4.

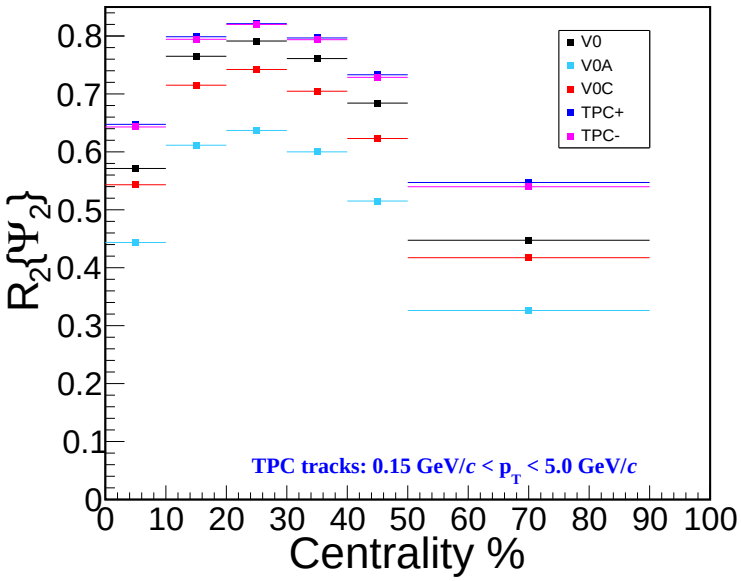

Figure 6.1: Event plane resolution: Second order harmonic relative to the second order event plane, $R_2(\Psi_2)$. The VZERO is used in this analysis, but comparison is shown for the other sub-detector events.

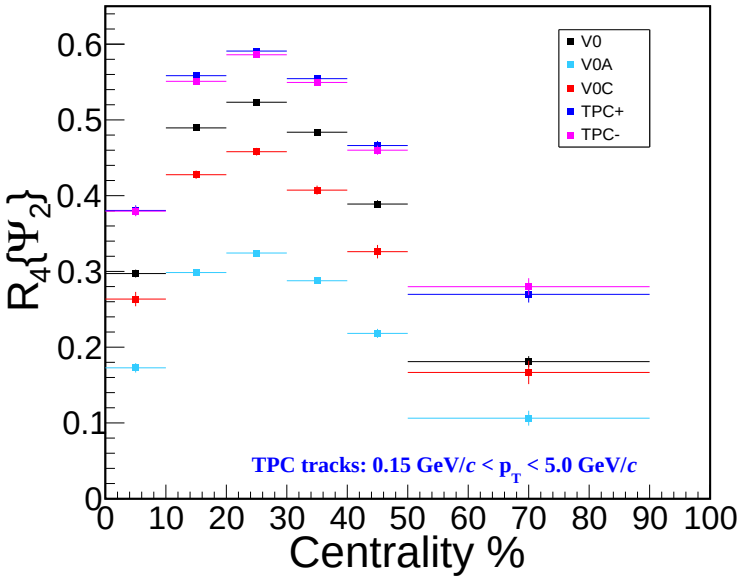

Figure 6.2: Event plane resolution: Fourth order harmonic relative to the second order event plane, $R_4(\Psi_2)$. The VZERO is used in this analysis, but comparison is shown for the other sub-detector events.

6.3 Restricting the trigger jet relative to reaction plane

The relative angle between the triggered jet candidate and the second order reaction plane defined using the combined VZER0 signal is expressed by:

$$\Delta\varphi = \varphi_{jet} - \varphi_{RP}. \tag{6.10}$$

By taking the absolute value of $\Delta\varphi$, we can then make a classification of the trigger jet candidate relative to the event plane. In this analysis we commonly make reference to in- mid- and out-of-plane. We define this by:

$$
\begin{aligned}
In\ Plane &: 0 < |\Delta\varphi| < \frac{\pi}{6} \\
Mid\ Plane &: \frac{\pi}{6} < |\Delta\varphi| < \frac{\pi}{3} \\
Out\ of\ Plane &: \frac{\pi}{3} < |\Delta\varphi| < \frac{\pi}{2}.
\end{aligned}
\tag{6.11}
$$

Using the cartoon picture of Fig. 6.3, we can see what this classification looks like. The reaction plane resolution impacts the flow modulated background for these correlations, as described in Sec. 6.6.

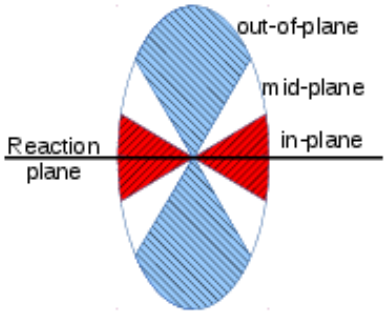

Figure 6.3: Event plane orientation classification used in this analysis [151].

In principle the finite reaction plane resolution also affects the signal because it will lead to some mixing of the bins defined above, however, these effects are less than the systematic uncertainty on the measurement so we neglect it here. There are two approaches to correcting the signal for the reaction plane resolution, unfolding or decomposition of the signal into its Fourier components. Unfolding is a complicated procedure requiring a resolution matrix and results in additional uncertainties. Additionally, since correlation functions are cyclic and the programs available for unfolding generally do not allow for the imposition of a cyclic boundary condition, substantial code development would be required. The signal can be Fourier decomposed, the Fourier components scaled by $\Re$ as described in Sec. 6.1, and the corrected Fourier coefficients summed. This approach is more straightforward,

however, also adds a systematic uncertainty. The impact of the reaction plane resolution on the signal will be greater if the signal has a greater dependence on the reaction plane angle. In the absence of a dependence of the signal on the reaction plane angle, the reaction plane resolution does not affect the signal. As is shown below, there is no dependence on the reaction plane within uncertainties.

6.4 Raw correlations

The correlation function is measured by:

$$\frac{1}{N_{trig}}\frac{d^2N_{assoc,jet}}{d\Delta\phi d\Delta\eta} = \frac{1}{N_{trig}}\frac{d^2}{d\Delta\phi d\Delta\eta}\frac{N_{meas}-N_{bkgd}}{\epsilon(p_T,\eta)a(\Delta\phi,\Delta\eta)} \tag{6.12}$$

where

$$a(\Delta\phi,\Delta\eta) = a_0\frac{d^2N_{pair}^{mixed}}{d\Delta\phi d\Delta\eta} \tag{6.13}$$

is normalized to be 1 at its maximum.

N_{meas} is the raw same event jet-track pairs. We define the $\epsilon(p_T,\eta)$ to be the single track acceptance times efficiency, discussed in Sec. 5.3, and refer to it simply as the efficiency to distinguish it from $a(\Delta\phi,\Delta\eta)$. $a(\Delta\phi,\Delta\eta)$ is the pair acceptance correction and is calculated from the raw pairs that we measure from a trigger jet associated with hadrons from mixed events, discussed in Sec. 6.5. The background correction N_{bkgd} is described in Sec. 6.6. The acceptance correction is applied in $\Delta\phi$ and $\Delta\eta$ before further analysis and background subtraction. Figure 6.4 shows an example of the raw correlations from same events pairs before applying a mixed event correction for the efficiency and acceptance of the EMCal. A plateau structure can be seen due to the finite acceptance of tracks and jets.

The correlations are determined in bins of centrality, reconstructed trigger jet transverse momentum ($p_T^{jet,rec}$), associated hadron transverse momentum (p_T^{assoc}), and bins of the trigger jet relative to the event plane (in, mid, out, all combined

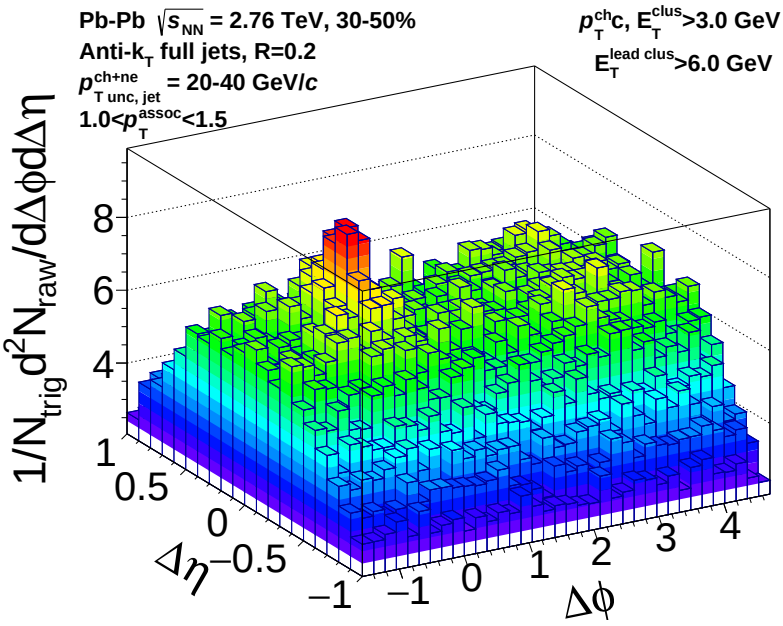

Figure 6.4: Example of a same pair correlation function distribution in 2 dimensions.

angles) defined in Sec. 6.3. The corrected correlation functions contain a large combinatorial background, N_{bkgd}, which must be subtracted. This subtraction procedure is described in Sec. 6.6.

6.5 Event mixing - acceptance correction

In this analysis, the full jet triggers are restricted to the limited EMCal acceptance given by Eqn. 5.9. The associated hadrons are from the full azimuthal acceptance and from $-0.9 < \eta < 0.9$ in pseudorapidity. This gives us a maximum $\Delta\eta$ between our trigger jet and associated hadrons of $-1.4 < \Delta\eta < 1.4$ for $R = 0.2$ jets. We apply a 2D mixed event correction to correct for this acceptance effect. The trigger jet is taken from one event and correlated with hadrons from other events, making sure to have the same cuts applied to both sets of pairs. Since the trigger jet and associated particles are from different events, they will be uncorrelated except through trivial

acceptance effects. A toy model calculation of the tent shaped plateau region in $\Delta\eta$ is shown in Fig. 6.5.

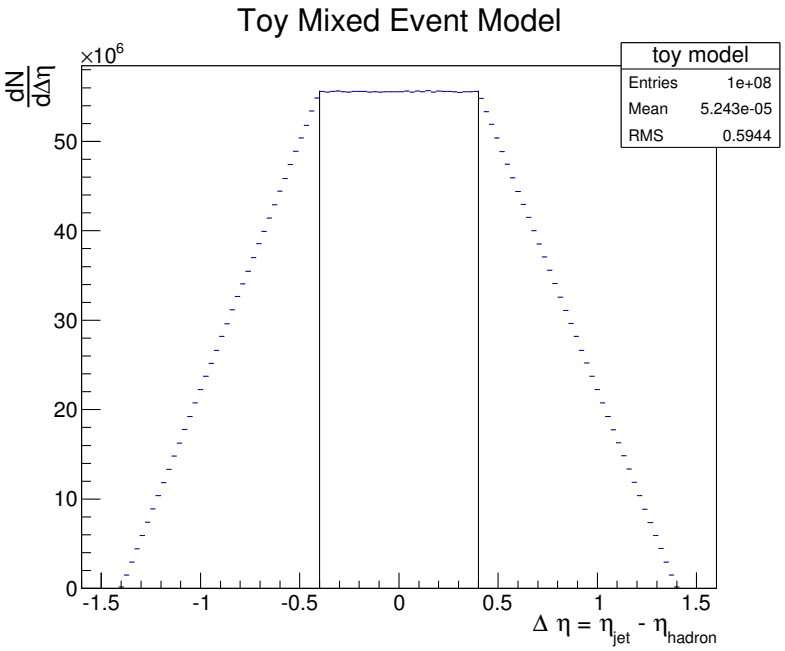

Figure 6.5: Toy model calculation showing the mixed event tent shaped plateau region spanning across pseudorapidity (η). This shows the ideal $\Delta\eta = \eta_{jet} - \eta_{assoc}$ acceptance for associated particles given $|\eta_{assoc}| < 0.9$ and $|\eta_{jet}| < 0.5$.

The reason for this structure is the difference of acceptance windows, $|\eta| < 0.9$ for charged tracks and $|\eta| < 0.5$ for R=0.2 full jets. It is noted that the mixed event procedure will also remove the trivial correlation due to an η dependence in the single particle and track distributions, however, since there is little η dependence in either tracks or jets within the acceptance used in this analysis, the dominant effect is the acceptance. In any analysis requiring mixed events, the ideal case of fine binning in all variables competes with the requirement for high statistics so that the precision of the final measurement is not limited by the mixed event statistics. The binning is optimized to focus on variables the acceptance is sensitive to and use wider bins in variables which the acceptance correction is not as sensitive to.

Event mixing is performed by using an event pool, which holds tracks to a depth of 50000. This depth refers to the number of tracks, or occupancy level, that a full event pool can contain. Other requirements were put on the minimum number of tracks and events to have in the event pool buffer before applying the mixing. The track requirement was set to 5000 and the event requirement was set to 1. In order to remove event-dependent geometry, the mixed pair are required to come from two events of similar collision geometry [169]. This means a similar centrality and collisions vertex (z-vertex), in order to avoid the change of z-vertex dependent acceptance and a single particle tracking efficiency which is multiplicity dependent [169]. The event pool is binned in 10% centrality and 2 cm z-vertex bins. Most ALICE analyses use 1% centrality bins. For this analysis, there is little dependence of the mixed events across large ranges in centrality as seen in Fig. 6.6 and also found by [170]. Mixed events are selected to have a trigger bit consisting of: $kMB + kCentral + kSemiCentral$, which is generally referred to as a "minimum bias" event. The idea is to select (trigger on) collisions with minimum detector activity in order to limit any biases of the event sample and use as close to an average collision as possible. This helps ensure that we are looking at a typical sample when calculating the acceptance effects. The mixed event distributions are weighted by $1/N_{mix\,events}$ in order to account for the number of events in the event pool.

The procedure is similar to [170]. The acceptance correction $a(\Delta\phi, \Delta\eta)$ is calculated as a function of centrality, the position of the collision vertex along the beam pipe (z_{vtx}), the momentum of the trigger jet p_T^{trig}, and the momentum of the associated particle p_T^{assoc}.

For the nominal method described here, the 2D distributions for same and mixed event pairs in Eqn. 6.12 are obtained by integrating over p_T^{trig}, p_T^{assoc}, z_{vtx}, and centrality before the division by the acceptance correction $a(\Delta\phi, \Delta\eta)$. The single pair correlations are binned in orienations of the trigger jet relative to the event plane while the mixed event correlations are not. A ratio is shown shown in Fig. 6.7 of the 2D mixed event distribution resulting from the ratio of in-plane to out-of-plane

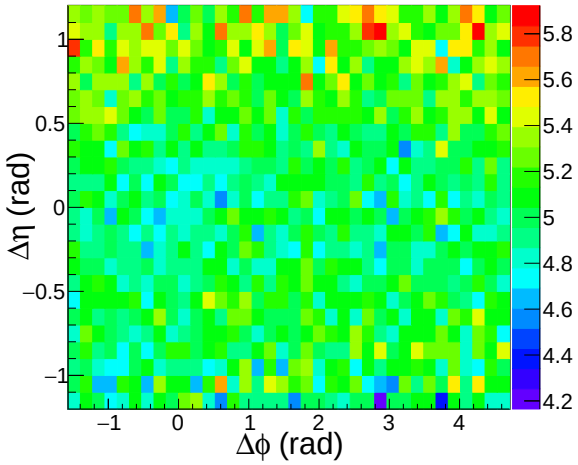

Figure 6.6: The ratio of the 2D mixed event distribution for mixed events from 20-30% over 30-50% centrality for p_T^{assoc} = 1.5-2.0 GeV/c tracks. This is for 20-40 GeV/c full jets. The ratio is shown over the ranges where the mixed events were used.

jets mixed with tracks of 1.0-1.5 GeV/c. This is shown for 20-40 GeV/c full jets from 30-50% central collisions and it can be seen that there are no shape differences. This allows us to simply use all combined orientations when the mixed event correction is performed.

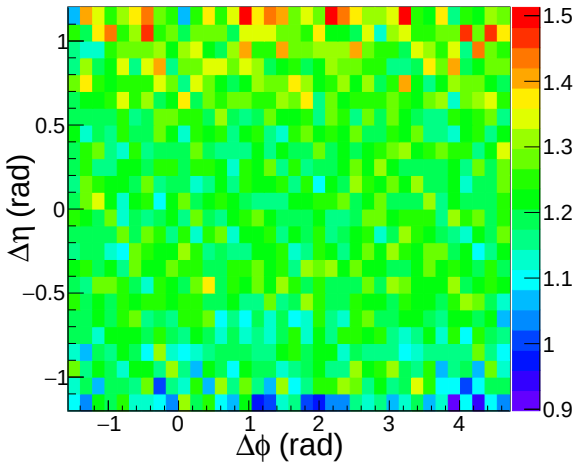

Figure 6.7: The ratio of the 2D mixed event distribution for mixed events of in-plane to out-of-plane jets mixed with 1.0-1.5 GeV/c tracks. This is for 20-40 GeV/c full jets from 30-50% central collisions. The ratio is shown over the ranges where the mixed events were used.

The normalization of the mixed events was determined using the region of approximately constant acceptance ($|\Delta\eta| < 0.4$). For each p_T^{assoc} bin, the precise region in ϕ was selected based on the region where the mixed event distribution was flat within statistical uncertainties and this region was fit with a constant to determine the normalization. The associated errors of the fits were used for the systematic error on the mixed event normalization, which is added in quadrature and reported as the scale uncertainty on the corrected correlation plots. This systematic uncertainty is under 0.5% in all p_T^{assoc} bins used for the reported results of 20-40 GeV/c jets in 30-50% centrality. This procedure suppresses the impact of statistical fluctuations on the normalization. Fig. 6.8 shows an example mixed event distribution from the correlations of full jets and charged hadrons from data which is used in this analysis. This example distribution is normalized.

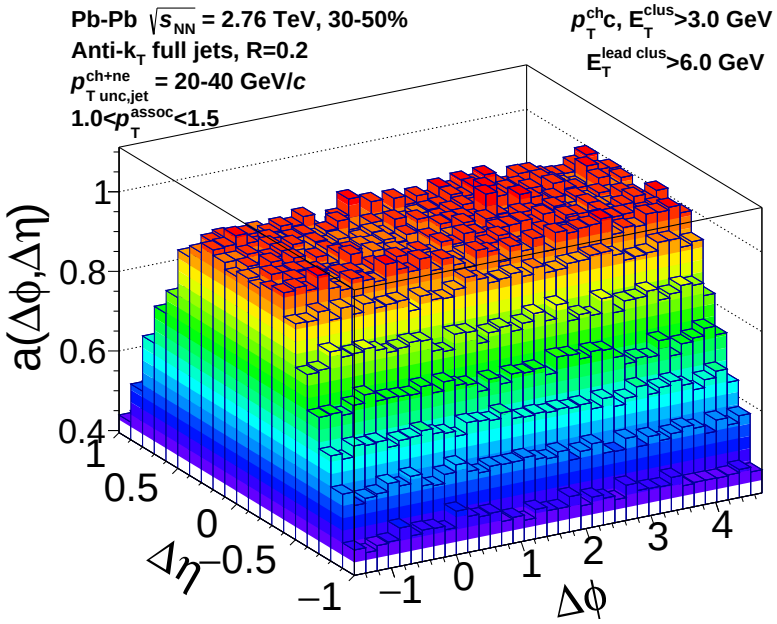

Figure 6.8: Example of a mixed event distribution in 2 dimensions. This shows the $\Delta\eta = \eta_{jet} - \eta_{assoc}$ acceptance for associated particles given $|\eta_{assoc}| < 0.9$ and $|\eta_{jet}| < 0.5$. Note: This example is already normalized.

The same acceptance correction is used for in-plane, mid-plane and out-of-plane trigger jets relative to the event plane. This procedure allows for larger statistics and

should have no adverse effect since $a(\Delta\phi, \Delta\eta)$ is dominated by the trivial acceptance for trigger jets and associated particles. In addition, due to the negligible p_T dependence of the mixed event distributions at high momenta, for p_T^{assoc} bins of 2 GeV/c and greater, the full range of 2.0-10.0 GeV/c for associated particles is used for the mixed event correction. A ratio is shown shown in Fig. 6.9 of the 2D mixed event distribution resulting from the ratio of 2.0-3.0 and 3.0-10.0 GeV/c tracks. This is shown for 20-40 GeV/c full jets from 30-50% central collisions and it can be seen that the dominant difference is purely statistical. Since high momentum tracks are nearly straight, the detector acceptance does not change significantly above $p_T > 2$ GeV/c.

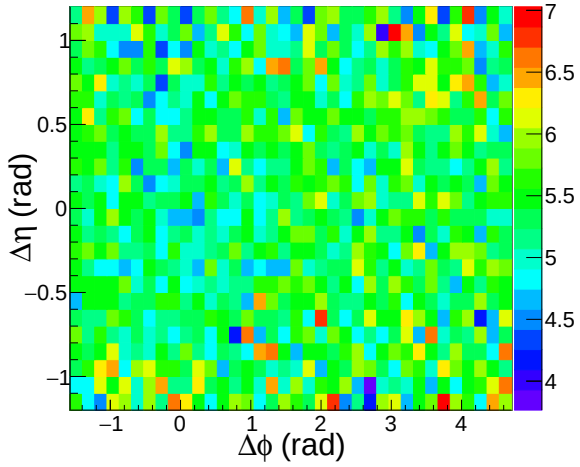

Figure 6.9: The ratio of the 2D mixed event distribution for mixed events of p_T^{assoc} = 2.0-3.0 GeV/c over 3.0-10.0 GeV/c. This is for 20-40 GeV/c full jets from 30-50% central collisions. The ratio is shown over the ranges where the mixed events were used.

Given high enough statistics, the acceptance correction in bins of z_{vtx} position in Eqn. 6.12 would be applied to the measured distribution before the correlations are added, as:

$$\frac{1}{N_{trig}} \frac{d^2 N_{assoc,jet}}{d\Delta\phi d\Delta\eta} = \frac{1}{N_{trig}} \sum_{i=0}^{N} \frac{d^2}{d\Delta\phi d\Delta\eta} \frac{N_i}{\epsilon(p_T, \eta) a_i(\Delta\phi, \Delta\eta)} \tag{6.14}$$

where i runs over the bins in z_{vtx} position, N_i is the single event distribution in z_{vtx} bin i, and $a_i(\Delta\phi, \Delta\eta)$ is the acceptance correction in z_{vtx} bin i. In practice, dividing the sample into several bins can exaggerate the impact of statistical fluctuations, which leads to a higher uncertainty in the normalization due to lower statistics in each bin, particularly at high z_{vtx}. Additionally, the uncertainty on the final correlation due to the normalization of the mixed events is hard to determine since it is different in each bin. However, the acceptance is known to be sensitive to z_{vtx}. The nominal measurement in this analysis does not use z_{vtx} as in Eqn. 6.14 (although mixed events are required to be close in z_{vtx}, as described above) and this is taken into account by a systematic error band on the shape, described below.

6.5.1 Method 2: weighted z-vertex Correlation function

As a cross check and to compare with prior studies, a second method of obtaining the acceptance corrected correlation function was used. The corrected correlation functions were obtained by calculating the ratio of signal to mixed event pairs in each z_{vtx} bin: [-10, -8], [-8,-6], [-6, -4], [-4, -2], [-2, 0], [0, 2], [2, 4], [4, 6], [6, 8], and [8, 10] cm ranges. The procedure used in this section is the same as Sec. 6.5, except it is calculated as in Eqn. 6.14.

When the z_{vtx} mixed event method is used, the normalization of the mixed event is performed by fitting a 1D function to the entire plateu region of the distribution defined by $-0.4 < \Delta\eta < 0.4$ and $-\pi/2 < \Delta\phi < 3\pi/2$ in order to suppress the impact of statistical fluctuations in the mixed events. For calculating various systematic uncertainties, when comparing the two mixed event methods, this same normalization is performed rather than the nominal approach in order to be consistent. The difference between this procedure and a proper normalization using only the constant region cancels out in the ratio as long as both the z_{vtx} binned correlations and the nominal correlations are normalized in the same way.

Scale systematic uncertainties There is a scale uncertainty on the background $\Delta\eta$ shape that will add to the background uncertainty, yield, RMS and correlation function. This uncertainty is from the differences between the nominal and z_{vtx} method for correcting the mixed events on the level of the background in the $0.8 < \Delta\eta < 1.2$ range and signal plus background in the $|\Delta\eta| < 0.6$ range. The large $\Delta\eta$ region is used to determine the background so any uncertainties in the level of the correlation function in this region lead to an uncertainty in the level of the background in the signal region. This is expressed as an additional scale band. Above $p_T^{assoc} > 3$ GeV/c, this uncertainty is negligible because the background is small.

To quantify this difference, the ratio of the integrated yields in the background dominated and signal plus background regions are calculated and compared between the 2 acceptance correction methods. The ratio of the integral in the signal plus background region and the background dominated region is given by:

$$A_{nom} = \frac{\int\int_{sig} Y_{nom} d\Delta\eta d\Delta\phi}{\int\int_{bkgd} Y_{nom} d\Delta\phi d\Delta\eta} \tag{6.15}$$

for the nominal method and

$$A_{zvtx} = \frac{\int\int_{sig} Y_{zvtx} d\Delta\phi d\Delta\eta}{\int\int_{bkgd} Y_{zvtx} d\Delta\phi d\Delta\eta} \tag{6.16}$$

for the weighted z_{vtx} method, where A is just a constant that is calculated for each p_T^{assoc} bin and the integral over $\Delta\phi$ covers full azimuth. Taking the ratio of the two methods gives:

$$\alpha = \frac{A_{nom}}{A_{zvtx}} = \frac{\frac{\int_{sig} Y_{nom} d\Delta\eta}{\int_{bkgd} Y_{nom} d\Delta\eta}}{\frac{\int_{sig} Y_{zvtx} d\Delta\eta}{\int_{bkgd} Y_{zvtx} d\Delta\eta}} = \frac{\int_{sig} Y_{nom} d\Delta\eta}{\int_{sig} Y_{zvtx} d\Delta\eta} \frac{\int_{bkgd} Y_{zvtx} d\Delta\eta}{\int_{bkgd} Y_{nom} d\Delta\eta}. \tag{6.17}$$

In Eqn. 6.17, α is a number of order 1 and would be 1 in the abscence of a scale uncertainty. The scale uncertainy band is then found by scaling the bin contents of

each $\Delta\phi$ bin by α and $2-\alpha$ to get the high and low edges accordingly. The values used for α for each p_T^{assoc} bin are shown in Tab. 6.1.

Table 6.1: Systematic scale uncertainty on the background. Calculated for each p_T^{assoc} bin for p_T^{jet} = 20-40 GeV/c, and 30-50% centrality collisions.

p_T^{assoc} GeV/c	α
0.15-0.5	1.00239
0.5-1.0	1.00459
1.0-1.5	1.00843
1.5-2.0	1.02001
2.0-3.0	1.03706
3.0-4.0	1.03034
4.0-5.0	1.05916
5.0-6.0	1.02901
6.0-10.0	1.00285

Shape systematic uncertainties If there were a shape uncertainty in $\Delta\phi$ due to the z_{vtx} binning, similar to that in $\Delta\eta$, this could lead to an additional shape uncertainty in the correlation functions. To test for this, the ratio of the 1D $\Delta\phi$ projection with the nominal z_{vtx} binning and the binning described above was calculated for each p_T^{jet}, p_T^{assoc}, and centrality bin. The variations about 1.0 are smaller than the statistical errors associated with the points. This uncertainty was therefore considered negligible.

6.6 Combinatorial background

The combinatorial background in azimuth in jet-hadron correlations has the form

$$\frac{dN}{\pi d\Delta\phi} = B(1 + \sum_{n=2}^{\infty} 2\tilde{v}_n^{\mathrm{t}}\tilde{v}_n^{\mathrm{a}}\cos(n\Delta\phi)), \tag{6.18}$$

where $\tilde{v}_n^{\mathrm{t}}$ ($\tilde{v}_n^{\mathrm{a}}$) are the Fourier coefficients of the trigger (associated) particles in the background [151,171]. The $\tilde{v}_n$ may arise due to hydrodynamical flow or jet quenching.

In heavy-ion collisions, collective particle flow plays a significant role to understanding the underlying event background. Fig. 6.10 depicts how collective particle flow looks for non-central collisons due to the pressure gradient built up in the overlap region [171]. The inclusive single particle distribution described in terms of ϕ and given with respect to the reaction plane Ψ_R is expressed as [171, 172]:

$$\frac{dN}{d(\phi - \Psi_R)} \propto (1 + \sum_{n=1}^{\infty} 2v_n \cos(n(\phi - \Psi_R))). \tag{6.19}$$

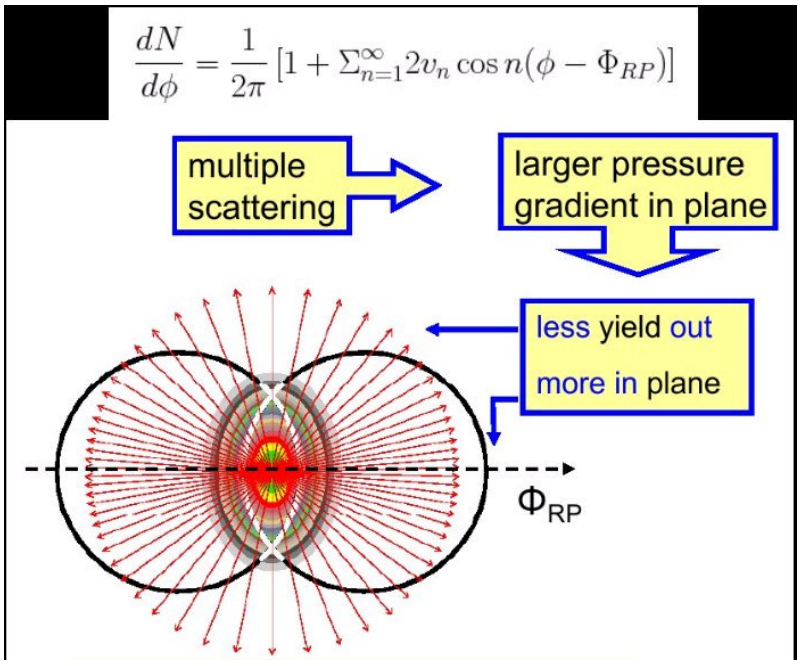

Figure 6.10: Cartoon image highlighting what happens for non-central collisions. The overlap region has a spatial anisotropy which leads to a pressure gradient in the direction of the reaction plane [173].

In order to analyze the jet-hadron correlation signal in Pb–Pb collisions, it is necessary to understand and subtract the large combinatoric background. With the aim of improving on prior studies, new methods were developed for subtracting the background in [151] and applied to STAR data in [174]. Two key methods were the near-side fit (NSF) discussed in 6.6.2 and the reaction plane fit (RPF) discussed in 6.6.3.

6.6.1 Zero-Yield-At-Minimum (ZYAM)

To isolate true jet yields from di-hadron aziumthal correlations, a flow modulated contribution needs to be subtracted [175]. ZYAM has been the historic background subtraction method of choice. ZYAM refers to Zero-Yield-At-Minimum [176, 177], with variations of ZYAM assuming zero yield at $\Delta\phi = 1$. Both the nominal case and its variations still assume that there is a region where the signal goes to zero. A large problem with this assumption is that there may be no region in azimuth where the jet-jet correlations goes to zero [151, 175]. In heavy-ion collisions, where the background is very large and the jet peaks can be modified by medium interactions, this assumption is even less reliable [151, 175]. ZYAM also relies on inclusive v_n measurements to quantify the flow contribution. It has been shown by [175] that ZYAM typically overestimates the background level and v_n may also be incorrectly extracted by conventional measurements. This results in incorrect jet yields and a distorted away-side peak, which led to the incorrect inference of "Mach cones" or "Mach shocks" [174, 175].

6.6.2 Near-Side Fit (NSF)

In heavy-ion collisions not only is there a large underlying event, but additionally collective flow is observed in the bulk particle production [151]. This can lead to correlations in the bulk which are similar to those of correlations from jet production [151]. Both of these effects contribute to correlations between particles making it complicated to disentangle the background. The flow mechanism is dominant at low transverse momenta. A partial solution is to look at jets with harder constituents. However, when gluons are radiated, the resulting gluons are generally softer than their parent partons [151]. As these gluons hadronize, their final-state hadrons tend to be softer than the final-state hadrons of the parent parton on average [178]. Therefore, the modifications that are seen to be concentrated at large angles from the parent parton and at lower momentum [151]. In order to perform precise jet measurements

and quantify the modifications in these p_T regions, a precise method for subtracting the background is desired.

While ZYAM has several assumptions and underestimates the background level, this work sought a method to produce a more accurate and reliable modeling of the background. The NSF method works under the assumption that the signal is negligible in the large $\Delta\eta$ and small $\Delta\phi$ region. This background dominated region is projected and fit to Eqn. 6.18 in the small $\Delta\phi$ region and extrapolated to the full range of $\Delta\phi$.

A toy model was set up to test the NSF method on both di-hadron and jet-hadron correlations. The di-hadron correlations were calculated using charged hadrons for both the trigger and associated particles and the jet-hadron correlations used gluons and quarks as a proxy for the fully reconstructed jets [151]. The signal used in the model was generated using PYTHIA events which followed the Perugia 2011 tune [151]. Acceptance cuts were implemented to follow the same cuts of this analysis. The study focused on associated hadrons of $1 < p_T^{assoc} < 2$ GeV/c, trigger hadrons with $8 < p_T^{trig} < 10$ GeV/c, and trigger partons with $20 < p_T^{trig} < 40$ GeV/c from 0-10% and 30-40% events.

The background is generated under the assumption that each trigger particle and corresponding associated particle are correlated with the reaction plane. The v_n used in modeling the background came from the available data in [179–182] and the exact choice does not impact the feasibility of the method [151]. Available data does not tightly constrain the higher order v_n terms, so as an upper bound, the approximation of $v_{n+2} = v_n/2$ was made [151]. Only v_2 is currently available for reconstructed jets [164, 179], so the assumption was made that higher order v_n corresponding to trigger jets were approximately the same as that of high-p_T hadrons [151]. PYTHIA events already include an underlying event, so it was subtracted off using the ZYAM method to give the used signal [151]. Background pairs are simulated by choosing the reaction plane angle to be zero in detector coordinates and throwing random trigger

jets or hadrons and associated particles according to Eqn. 6.19 [151]. Additional details can be found in [151].

The NSF method was compared to the ZYAM method in Fig. 6.11 for h-h correlations where the left panel shows the background fit and the right panel shows the extracted signal. The NSF method was then compared to the ZYAM method in Fig. 6.12 for j-h correlations where the left panel shows the background fit and the right panel shows the extracted signal. The NSF method improves upon the ZYAM method by making fewer assumptions and having smaller errors when calculating the extracted signal while not requiring independent measurements of v_n. While this method works, the fits were not stable to the fit region in $\Delta\phi$. Results of the application of the NSF method in a toy model can be found in [151].

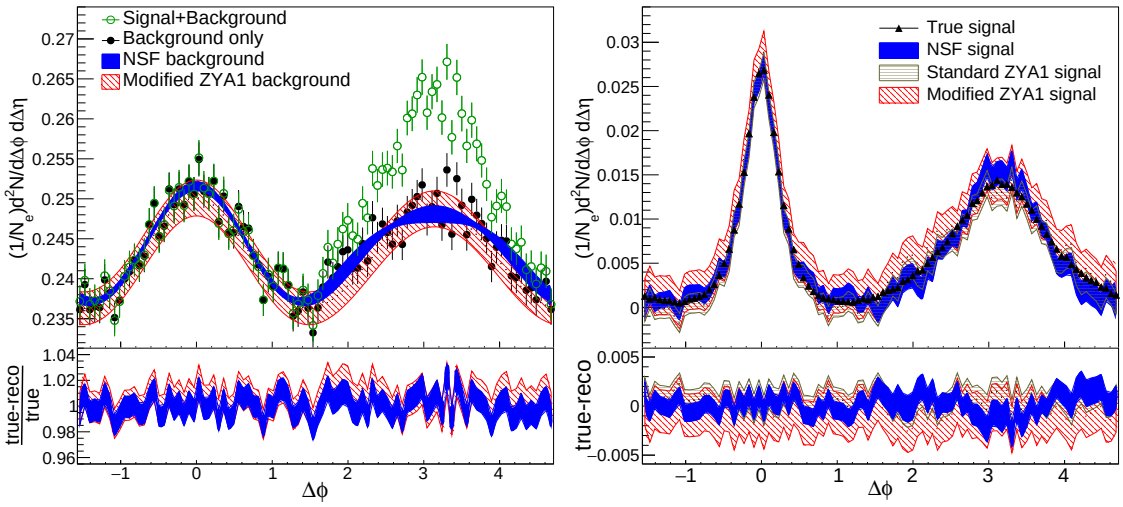

Figure 6.11: (left) Signal+background for di-hadron correlations in 30-40% Pb–Pb collisions at $\sqrt{s_{NN}} = 2.76$ TeV. Comparison is made to true background, background from ZYA1 method and background from NSF method. (bottom left) Ratio of NSF and ZYA1 backgrounds to true background [151]. (right) The extracted true signal compared to that from NSF and that from 2 variations of ZYA1. (bottom right) Difference between true signal and extracted signals from NSF and the ZYA1 methods.

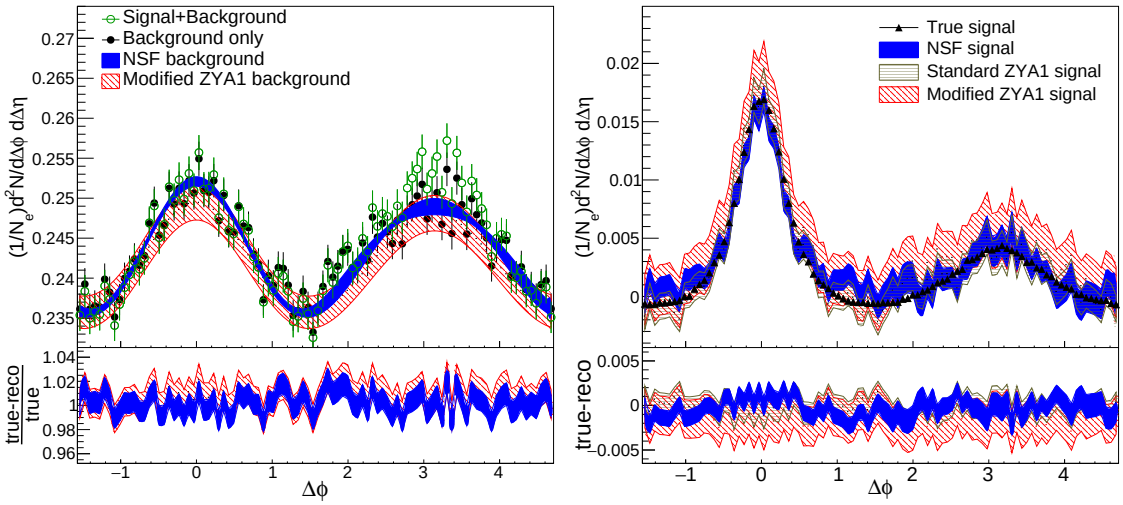

Figure 6.12: (left) Signal+background for jet-hadron correlations in 30-40% Pb–Pb collisions at $\sqrt{s_{NN}} = 2.76$ TeV. Comparison is made to true background, background from ZYA1 method and background from NSF method. (bottom left) Ratio of NSF and ZYA1 backgrounds to true background [151]. (right) The extracted true signal compared to that from NSF and that from 2 variations of ZYA1. (bottom right) Difference between true signal and extracted signals from NSF and the ZYA1 methods.

6.6.3 Reaction plane dependent background

In this analysis, the trigger jet was restricted relative to the event plane into three equal sized slices in $\Delta\varphi$, defined in Sec. 6.3. When fixing a trigger (jet) relative to the event plane, the level of the background and effective v_n^t are modified [171]. The even v_n^t are given by Eqn. 6.20 [151, 171].

$$\tilde{v}_n^{\Re,t} = \frac{v_n + \cos(n\phi_s)\frac{\sin(nc)}{nc}\Re_n + \sum_{k=2,4,6,..}(v_{k+n} + v_{|k-n|})\cos(k\phi_s)\frac{\sin(kc)}{kc}\Re_n}{1 + \sum_{k=2,4,6,..} 2v_k\cos(k\phi_s)\frac{\sin(kc)}{kc}\Re_n} \tag{6.20}$$

and the effective background level by [171]:

$$\tilde{\beta^R} = 1 + \sum_{k=2,4,6...} 2v_k\cos(k\phi_S)\frac{\sin(kc)}{kc}R_n \tag{6.21}$$

where ϕ_s is the center of the range, while kc is the width of the range. Combining Eqns. 6.20 and 6.21 allows the modified background to be expressed by [151]:

$$b(\Delta\phi,\psi^t) = \frac{dN^{pairs}}{\pi\Delta\phi} = \tilde{\beta}^{\Re}(1 + \sum_{n=1} = 2\tilde{v}_n^{R,t}\tilde{v}_n^a\cos(n\Delta\phi)). \tag{6.22}$$

Since $\tilde{\beta^R}$ and $\tilde{v}$ depend on the reaction plane, the reaction plane dependence can be used to determine the background. When using the $n = 2$ event plane, all odd n terms are given by $\tilde{v}_n^{\Re,t} = \tilde{v}_n^t$, since the odd n event planes are not correlated with the n=2 plane [151]. The four width and center regions of the range defined for the binning of this analysis are given by:

- All;
- In-plane: $\phi_S = 0$, c=$\pi/6$;
- Mid-plane: $\phi_S = \pi/4$ and $\phi_S = 3\pi/4$, c=$\pi/12$;
- Out-of-plane: $\phi_S = \pi/2$, c=$\pi/6$.

The RPF method is an extension to NSF to handle background in reaction plane dependent analyses such as this one and to help stabilize the fits. The range used to

define the signal plus background region in data is $|\Delta\eta| < 0.6$ and $0.8 < |\Delta\eta| < 1.2$ was used to define the background dominated region where the signal was assumed to be negligible. While the full range in $|\Delta\eta|$ extends to 1.4, the edge bins were not used due to low statistics that caused large fluctuations in the acceptance correction.

The projections are done for in-plane, mid-plane, out-of-plane and all angles combined. A simulataneous fit is performed on the in-plane, mid-plane, and out-of-plane data. The correlation for all angles combined is not used since it would lead to double counting. The fit with Eqn. 6.22 is restricted to $|\Delta\phi| < \pi/2$ for each orientation and extended up to n=4 (n=3 for p_T^{assoc} bins > 2.0 GeV/c) for $|\Delta\phi| < \pi/2$, while being extrapolated over the full range of $\Delta\phi$. The resulting errors on the fit are a result of the parameter errors. The errors are non-trivially correlated point-to-point.

By default a χ^2 (least-square) fit is performed on the histogram. This method excludes bins with zero error from the fit. Statistics are limited at higher p_T^{assoc}. There are empty entries for the 4.0-5.0, 5.0-6.0, and 6.0-10.0 GeV/c p_T^{assoc} ranges. The log likelihood fit option, "L", works best for low statistics, but it resulted in much higher uncertainties than the standard χ^2 minimization at low p_T^{assoc}, where there is no problem with statistics. For the 5.0-6.0 and 6.0-10.0 p_T^{assoc} range, the use of the log likelihood fit option is best because for p_T^{assoc}=5.0-6.0 GeV/c, there are only 32 of 54 fit bins that are non-empty. For p_T^{assoc}=6.0-10.0 GeV/c, 27 of 54 fit bins are non-empty. For p_T^{assoc}=4.0-5.0 GeV/c, the fit is worse with the log likelihood fit and this bin has enough statistics to get a good fit without doing it.

Figure 6.13 shows an example of the data in the signal plus background region, $|\Delta\eta| < 0.6$, the projection of the background dominated region, $0.8 < |\Delta\eta| < 1.2$, and the fit to the background with associated errors coming from the errors on the parameter of the fit given as the blue band.

For more method details on the background subtraction methods and their application to a re-analysis of STAR data, please see [151] and [174].

Systematic uncertainties: background fit In general the uncertainty σ on a function f with parameters p_i for i=0..N is given by

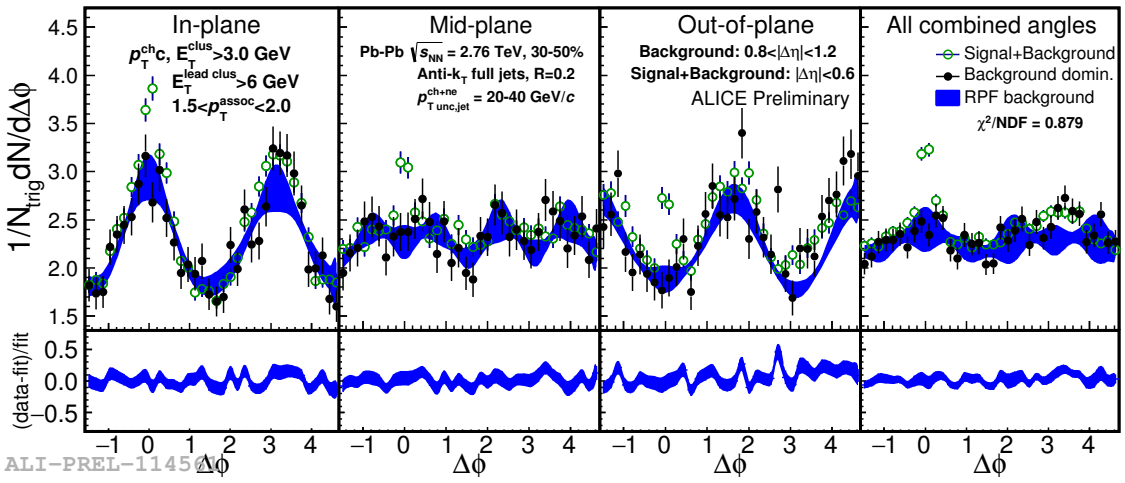

Figure 6.13: The fit to the $\Delta\phi$ distribution of jet-hadron correlations for 20-40 GeV/c jets correlated with 1.5-2.0 GeV/c hadrons from 30-50% centrality events. There is a 6 GeV cluster bias requirement and it is made sure the cluster is matched to a firing trigger patch in the EMCal.

$$\sigma^2 = \sum_{i=0}^{N}\sum_{j=0}^{N} \frac{\partial f}{\partial p_i}\frac{\partial f}{\partial p_j}\sigma_{ij} \tag{6.23}$$

where σ_{ij} is the covariance between parameter i and j. In the specific case of f given by Eqn. 6.22, the parameters are B, $\tilde{v_2^a}$, $\tilde{v_2^t}$, $\tilde{v_3^a}\tilde{v_3^t}$, $\tilde{v_4^a}$ and $\tilde{v_4^t}$. For the correlation functions, this is done for each bin in $\Delta\phi$.

The background uncertainties come from the errors on the parameters from the fit and are non-trivially correlated point-to-point. They are shown as a grey band in the background subtracted correlations, yield plots, and RMS calculation.

Extracted background level and Fourier coefficients from RPF fits

Figures 6.14, 6.15, 6.16, 6.17, 6.18, and 6.19 show the fit parameters for the RPF method as a function of p_T^{assoc} for 20-40 GeV/c jets in 30-50% centrality collisions. The v_4^{jet} and v_4^{assoc} parameters were only used in the background fits for the [0.15-0.50, 0.5-1.0, 1.0-1.5, 1.5-2.0] GeV/c p_T^{assoc} bins. At higher p_T^{assoc}, the statistics were limited. Reducing the number of parameters helps the fit converge and since the background

is smaller at high p_T, it does not substantially increase the uncertainties. Tables corresponding to the RPF fits showing the χ^2, NDF, parameters, and parameter errors for each p_T^{assoc} bin can be found in App. A.

Figure 6.15 shows a comparison to the previously released charged jet v_2 measurement [164] from the same centrality bin used in this analysis, but from two different jet transverse momentum bins. The event selection and jet parameters are also different, but this comparison is mainly drawn as a cross check. Fig. 6.16 shows a comparison to various methods [181] of calculating v_2 of charged hadrons. The results are comparable despite different methods, event selection, and track cuts.

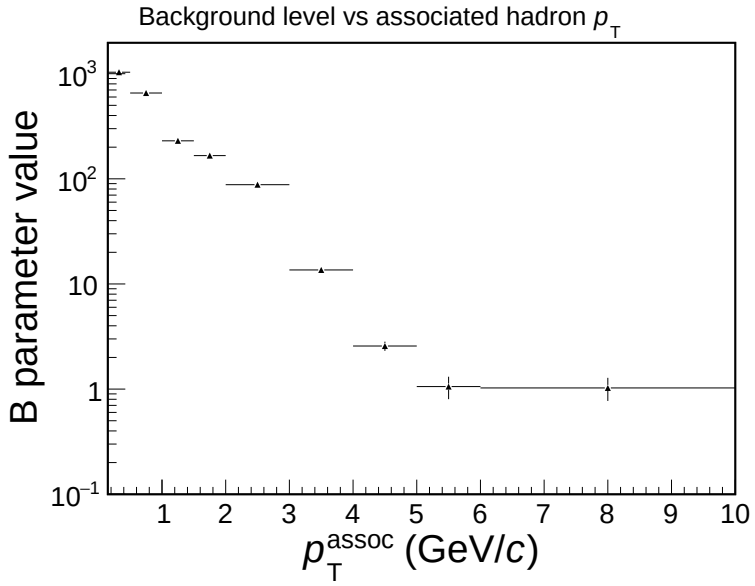

Figure 6.14: The background level, B, extracted from the RPF fits vs p_T^{assoc}. Shown is the case of 20-40 GeV/c full jets in 30-50% central collisions.

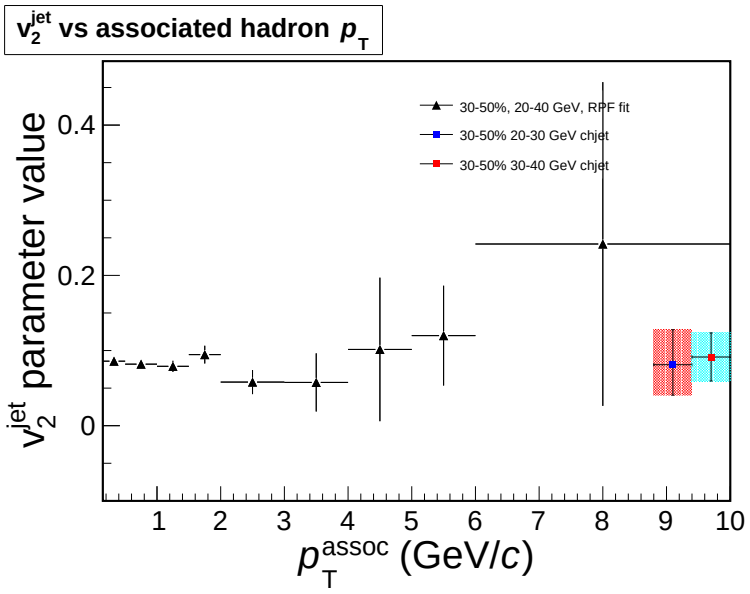

Figure 6.15: The v_2^{jet}, extracted from the RPF fits vs p_T^{assoc} for 20-40 GeV/c full jets in 30-50% central collisions are compared to the results from the charged v_2^{jet} measurement in [164].

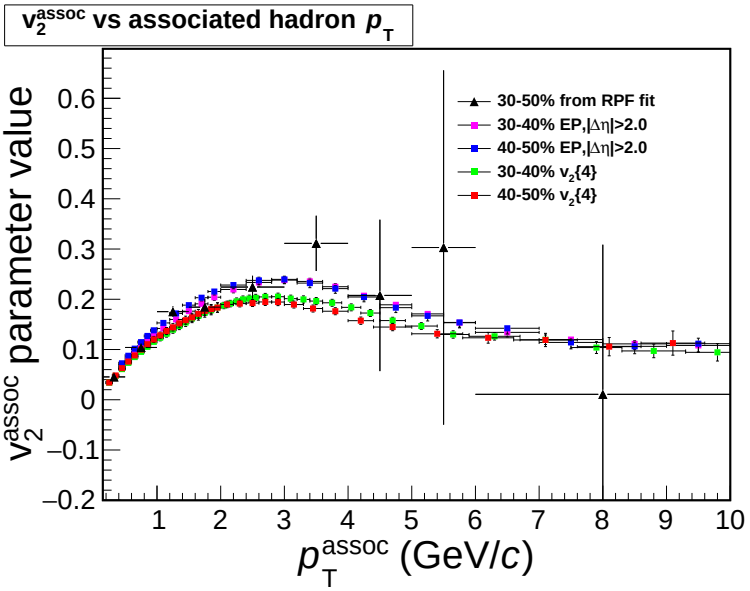

Figure 6.16: The v_2^{assoc}, extracted from the RPF fits vs p_T^{assoc} for 20-40 GeV/c full jets in 30-50% central collisions are compared to the charged hadron v_2 measurement in [181] for 2 different methods.

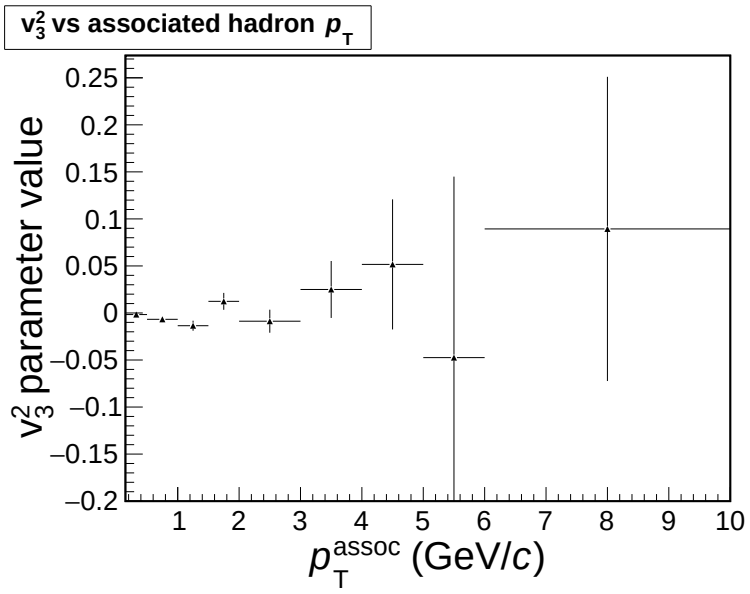

Figure 6.17: The v_3^2, extracted from the RPF fits vs p_T^{assoc} for 20-40 GeV/c full jets in 30-50% central collisions.

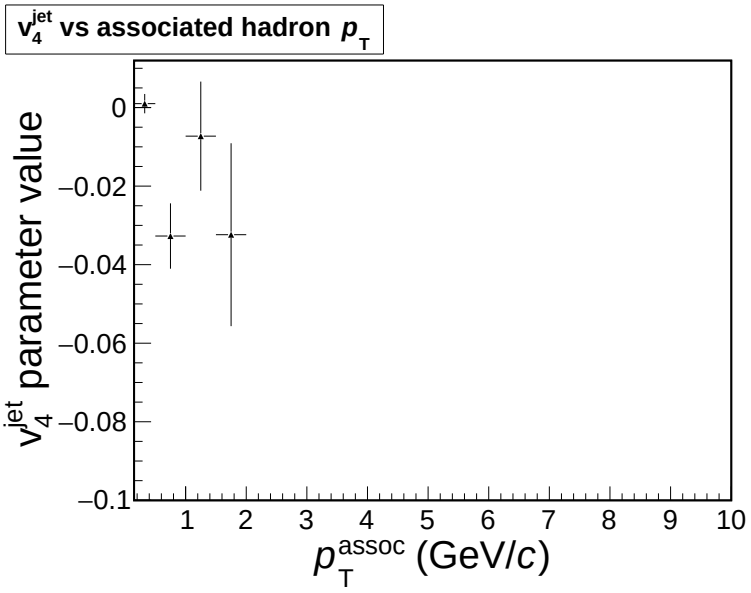

Figure 6.18: The v_4^{jet}, extracted from the RPF fits vs p_T^{assoc} for 20-40 GeV/c full jets in 30-50% central collisions.

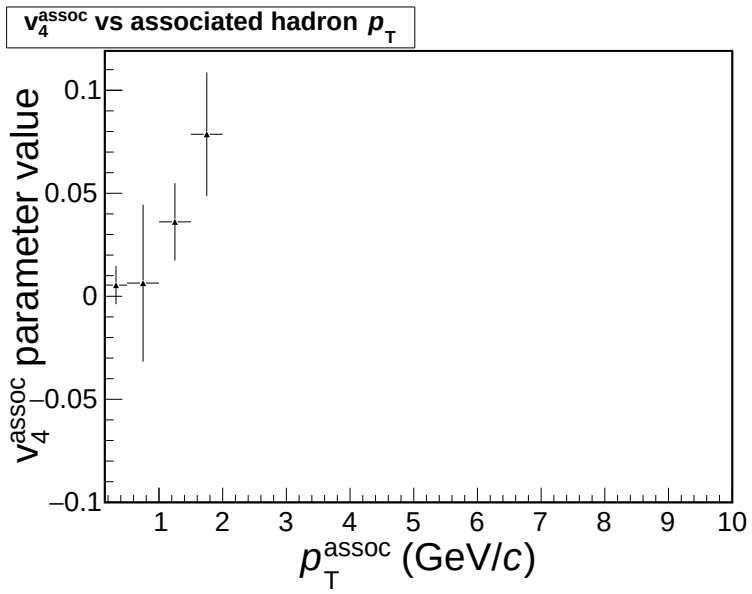

Figure 6.19: The v_4^{assoc}, extracted from the RPF fits vs p_T^{assoc} for 20-40 GeV/c full jets in 30-50% central collisions.

Chapter 7

Results

Following the method procedures presented in Ch. 6, the corrected results of this jet-hadron correlations analysis relative to the event plane are presented in this chapter. Ch. 6 discussed the corrections to the raw correlations, ending with the newly developed background subtraction methods which were applied in this analysis. This chapter will present the primary results of corrected jet-hadron $\Delta\phi$ correlations relative to the event plane in Sec. 7.1, followed by the extracted yields and truncated RMS calculation, shown in Sec. 7.3. To better quantify the effects seen from the event plane depedence of the yields, ratios of the yield for taken to compare out-of-plane to in-plane and mid-plane to in-plane yields, and shown in Sec. 7.5. Correlations are also shown for the most central collisions (0-10%), in Sec. 7.2 with the same methods applied, as well as yields and RMS. However ratios were not taken at this time. The central data are harder interpret as it comes with large uncertainties and poor reaction plane resolutions.

7.1 Correlation results: 20-40 GeV/c jets, 30-50% centrality

Figures 7.1, 7.2, 7.3, 7.4, 7.5, 7.6, 7.7, and 7.8 show the background subtracted $\Delta\phi$ jet-hadron correlations for p_T^{assoc} bins corresponding to [0.5-1.0, 1.0-1.5, 1.5-2.0, 2.0-3.0, 3.0-4.0, 4.0-5.0, 5.0-6.0, 6.0-10.0] GeV/c for 20-40 GeV/c fully reconstructed jets from the 30-50% central most events. App. A shows the spectra of jets used for these correlations, the raw acceptance corrected correlations, the RPF fit to the background, and a breakdown of the fit parameters and uncertainties to the fit. The plots are shown for in-plane, mid-plane, out-of-plane and all combined angles of the trigger jet. The signal+background region is defined to be $|\Delta\eta| < 0.6$.

The uncertainties of the correlations consist of statistical (points), correlated uncertainty on the scale (blue band) in $\Delta\eta$ due to background being taken from large $\Delta\eta$ range of the mixed events, and background uncertainty on the shape in $\Delta\phi$ due to the RPF fit on the background. The background uncertainty is non-trivally correlated point-to-point, so the uncertainties can not simply be added by eye or in quadrature. There is an additional 6% global scale uncertainty on the correlations. The sources of this scale uncertainty are summarized in Tab. 7.9.

For the lowest p_T^{assoc} bins, the uncertainties are statistics-limited. The uncertainty due to the background parametrization, the statistical errors on the data points, and the scale uncertainty due to the mixed event correction can be reduced with additional statistics At $p_T^{assoc} = 2.0\text{-}3.0$ GeV/c, the away-side is clearly there and suppressed. Due to the diminishing background for $p_T^{assoc} > 3.0$ GeV/c, the correlated scale uncertainty and uncertainty from the background fit become negligible.

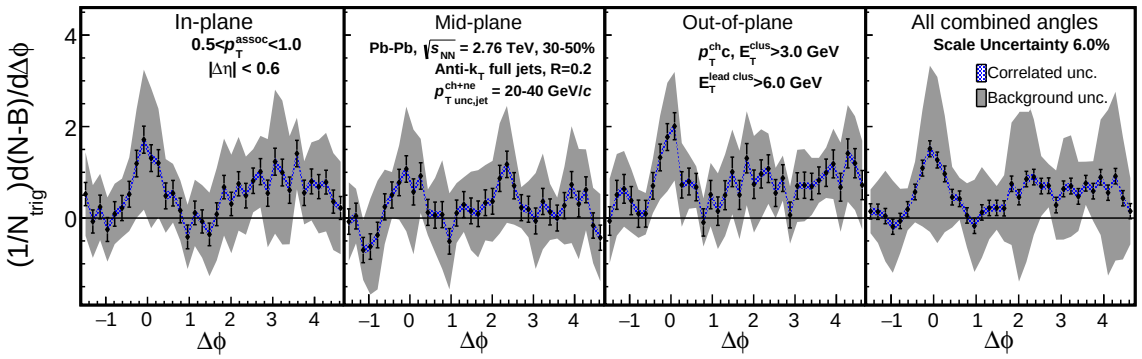

Figure 7.1: The background subtracted $\Delta\phi$ correlations for associated hadrons of 0.5-1.0 GeV/c.

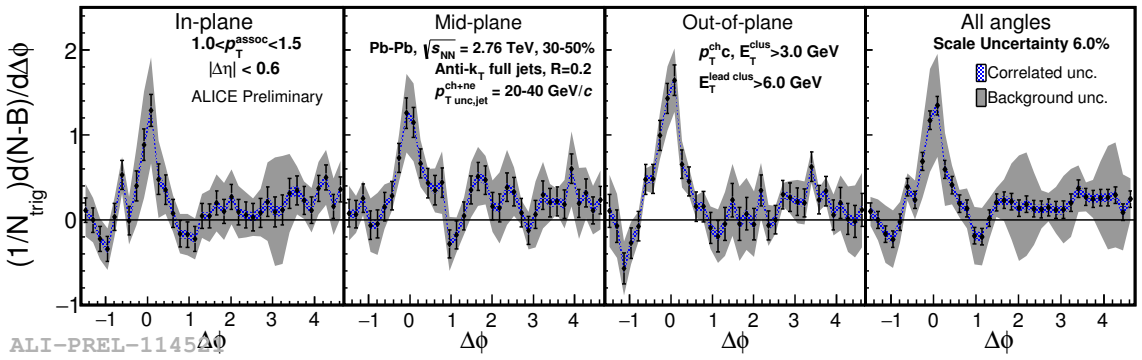

Figure 7.2: The background subtracted $\Delta\phi$ correlations for associated hadrons of 1.0-1.5 GeV/c.

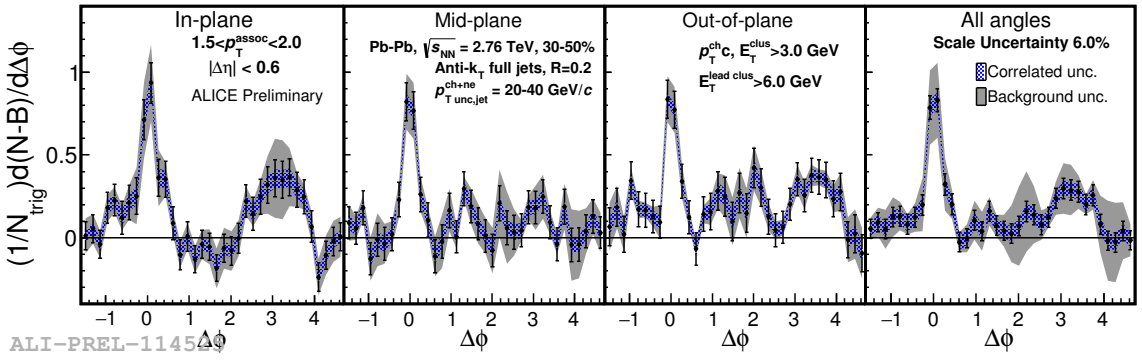

Figure 7.3: The background subtracted $\Delta\phi$ correlations for associated hadrons of 1.5-2.0 GeV/c.

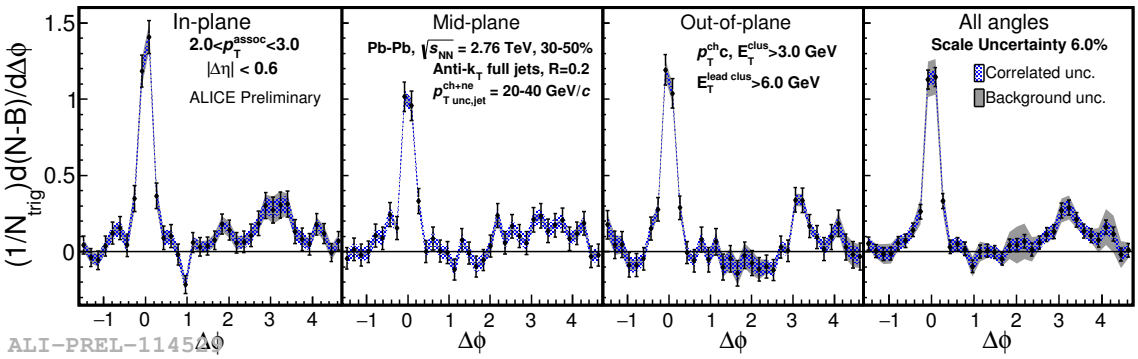

Figure 7.4: The background subtracted $\Delta\phi$ correlations for associated hadrons of 2.0-3.0 GeV/c.

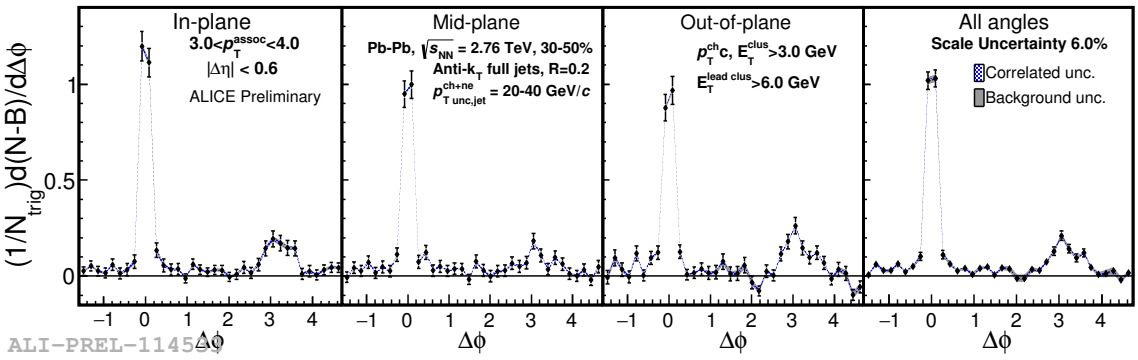

Figure 7.5: The background subtracted $\Delta\phi$ correlations for associated hadrons of 3.0-4.0 GeV/c.

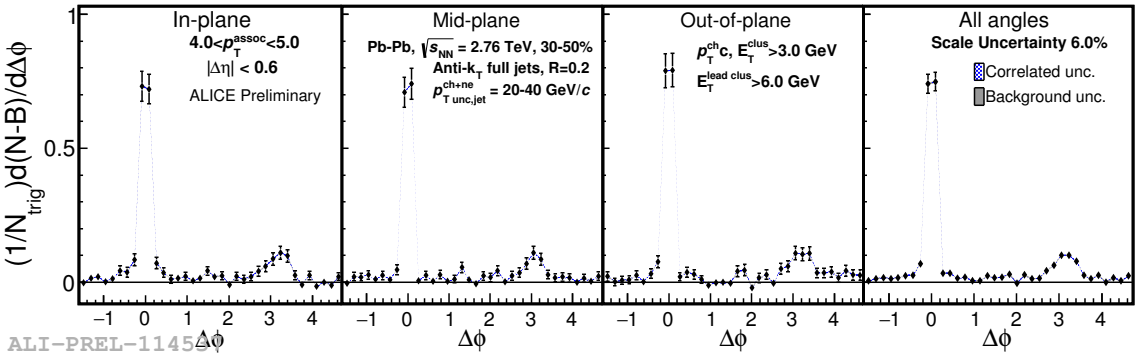

Figure 7.6: The background subtracted $\Delta\phi$ correlations for associated hadrons of 4.0-5.0 GeV/c.

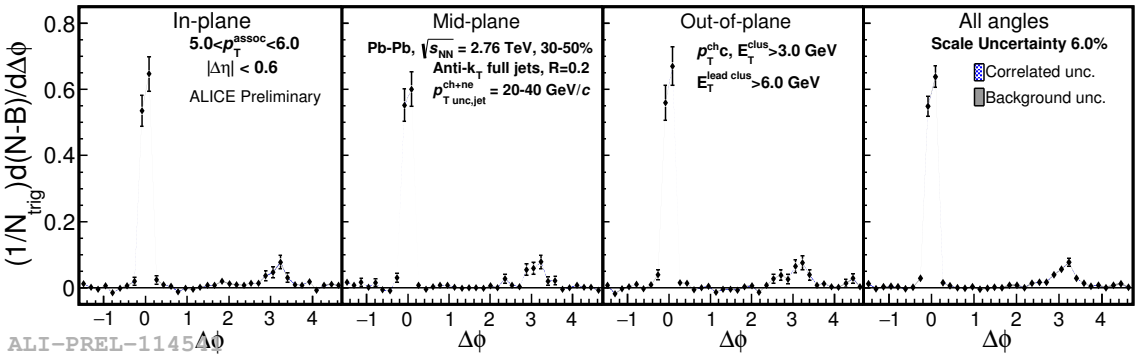

Figure 7.7: The background subtracted $\Delta\phi$ correlations for associated hadrons of 5.0-6.0 GeV/c.

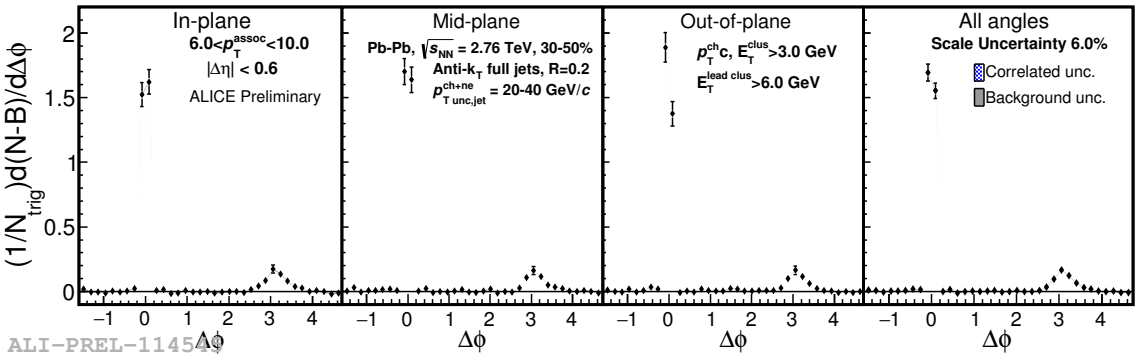

Figure 7.8: The background subtracted $\Delta\phi$ correlations for associated hadrons of 6.0-10.0 GeV/c.

7.2 Correlation results: 20-40 GeV/c jets, 0-10% centrality

Figures 7.9, 7.10, 7.11, 7.12, 7.13, 7.14, 7.15, and 7.16 show the background subtracted $\Delta\phi$ jet-hadron correlations for p_T^{assoc} bins corresponding to [0.5-1.0, 1.0-1.5, 1.5-2.0, 2.0-3.0, 3.0-4.0, 4.0-5.0, 5.0-6.0, 6.0-10.0] GeV/c for 20-40 GeV/c fully reconstructed jets from the 30-50% central most events. App. B shows the spectra of jets used for these correlations, the raw acceptance corrected correlations, the RPF fit to the background, and a breakdown of the fit parameters and uncertainties to the fit. The plots are shown for in-plane, mid-plane, out-of-plane and all combined angles of the trigger jet.

Due the very large background in the 0-10% centrality events and a poor event plane resolution, the uncertainties on the extracted signals are very large. Reasonable away-side jet peaks are clearly seen until $p_T^{assoc} > 3.0$ GeV/c.

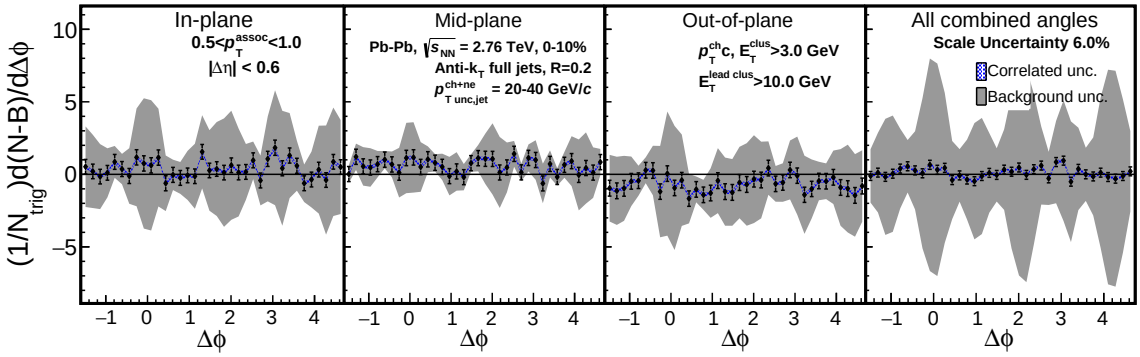

Figure 7.9: The background subtracted $\Delta\phi$ correlations for associated hadrons of 0.5-1.0 GeV/c.

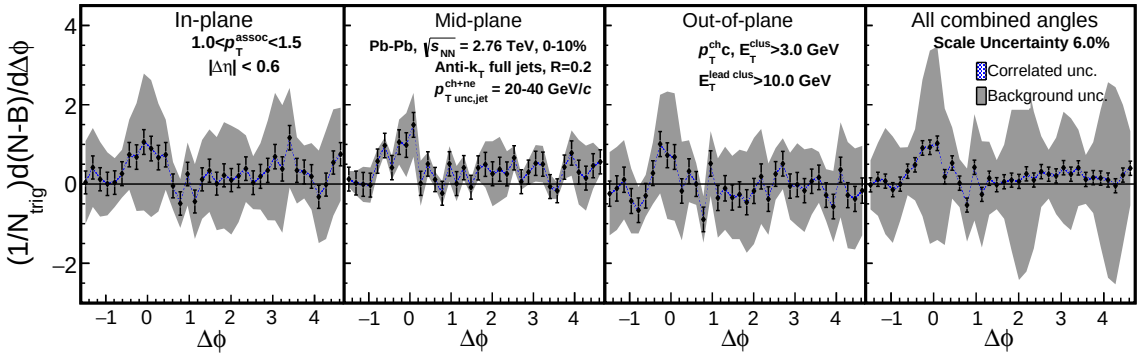

Figure 7.10: The background subtracted $\Delta\phi$ correlations for associated hadrons of 1.0-1.5 GeV/c.

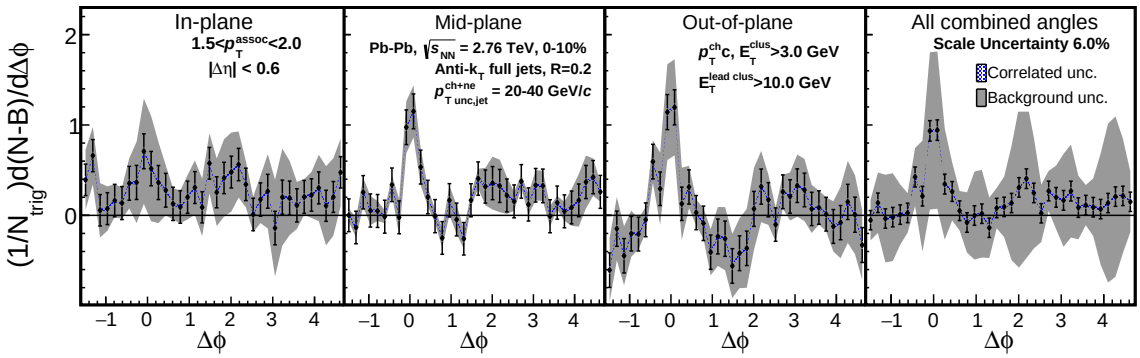

Figure 7.11: The background subtracted $\Delta\phi$ correlations for associated hadrons of 1.5-2.0 GeV/c.

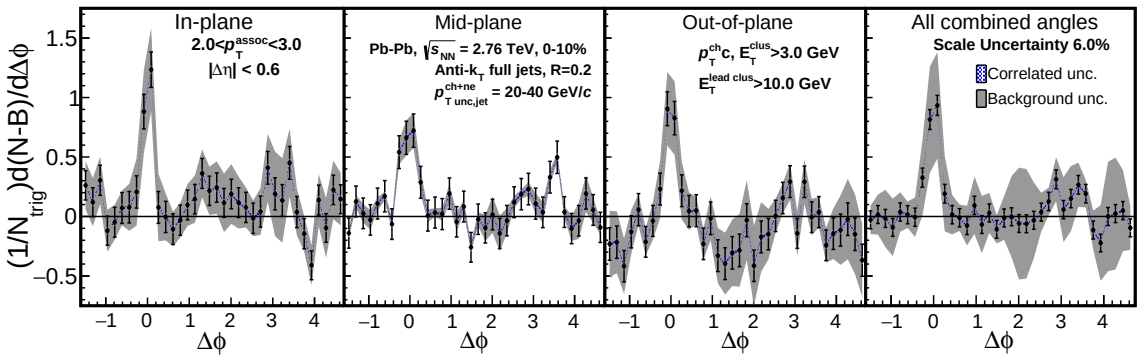

Figure 7.12: The background subtracted $\Delta\phi$ correlations for associated hadrons of 2.0-3.0 GeV/c.

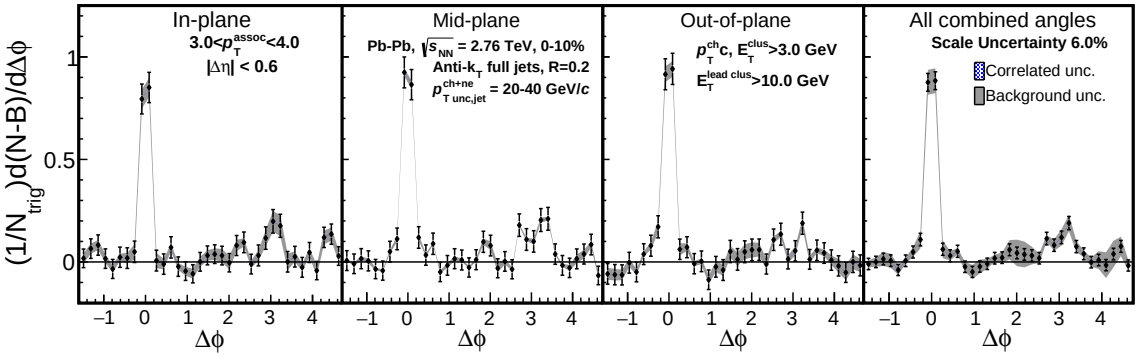

Figure 7.13: The background subtracted $\Delta\phi$ correlations for associated hadrons of 3.0-4.0 GeV/c.

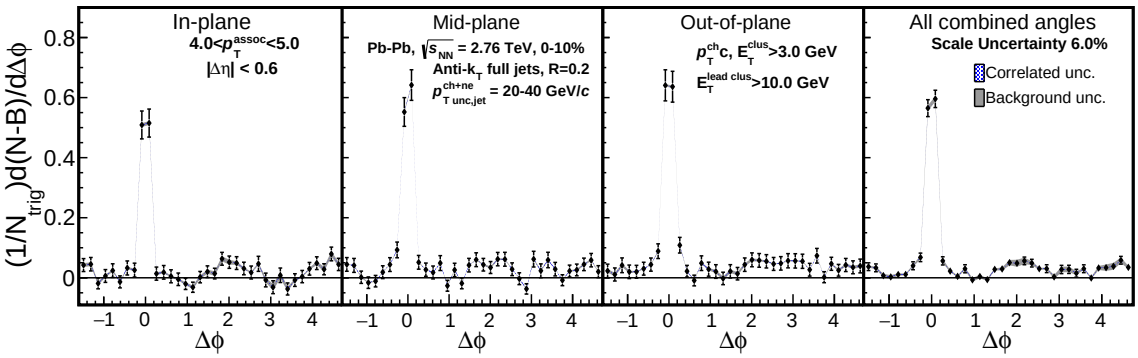

Figure 7.14: The background subtracted $\Delta\phi$ correlations for associated hadrons of 4.0-5.0 GeV/c.

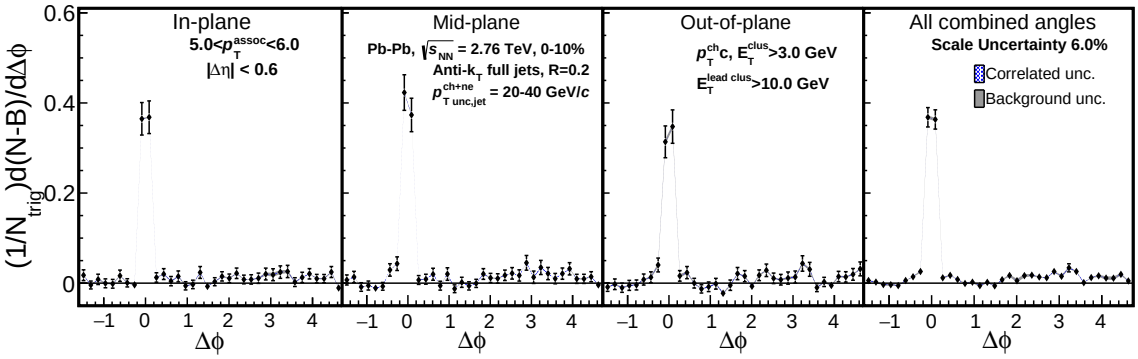

Figure 7.15: The background subtracted $\Delta\phi$ correlations for associated hadrons of 5.0-6.0 GeV/c.

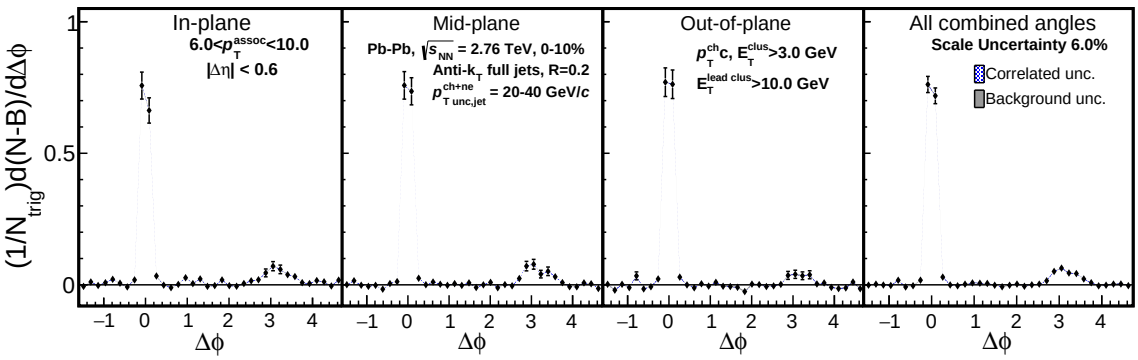

Figure 7.16: The background subtracted $\Delta\phi$ correlations for associated hadrons of 6.0-10.0 GeV/c.

7.3 Yield and RMS results

The yield is calculated by

$$Y = \frac{1}{N_{trig}} \int_c^d \int_a^b \frac{d(N_{meas} - N_{bkgd})}{d\Delta\phi} d\Delta\phi d\Delta\eta. \tag{7.1}$$

The background and signal are included explicitly in order to make propagation of the uncertainties more transparent. The choice of integration limits is somewhat arbitrary and their definition is considered part of the definition of the measurement. They are chosen based on practical considerations, including the detector acceptance and convenient histogram binning. The integration limits in $\Delta\phi$ for the near-side are $a = -1.047$ and $b = 1.047$, while for the away-side, we have $a = 2.094$ and $b = 4.189$. The integration limits in $\Delta\eta$ are the same for both the near-side and away-side, $c = -0.6$ and $d = 0.6$.

Propagation of uncertainties For the propagation of the uncertainties, we note that the background is independent of $\Delta\phi$ and therefore we rewrite Eqn. 7.1 as

$$Y = \int_a^b \frac{d(s_{meas} - b_{bkgd})}{d\Delta\phi} d\Delta\phi. \tag{7.2}$$

where the normalization by the number of triggers and the $\Delta\phi$ integration is included in the definition of

$$s_{meas} = \frac{1}{N_{trig}} \int_c^d \frac{dN_{meas}}{d\Delta\eta} d\Delta\eta \tag{7.3}$$

and

$$b_{bkgd} = \frac{1}{N_{trig}} \int_c^d \frac{dN_{bkgd}}{d\Delta\eta} d\Delta\eta \tag{7.4}$$

and b_{bkgd} is given by Eqn. 6.22. Integrating

$$Y_{All} = \int_a^b \frac{ds_{meas}}{d\Delta\phi} d\Delta\phi. \tag{7.5}$$

is straightforward because s_{meas} contains only statistical uncertainties. Integrating

$$Y_{Bkgd} = \int_a^b \frac{db_{bkgd}}{d\Delta\phi} d\Delta\phi = \int_a^b \tilde{B}^{\Re}(1 + \sum_{n=1}^{4} \tilde{v}_n^t \tilde{v}_n^a \cos(n\Delta\phi)) d\Delta\phi. \tag{7.6}$$

requires propagation of the uncertainties using the covariance matrix following Eqn. 6.23 where

$$f = \int_a^b \tilde{B}^{\Re}(1 + \sum_{n=1}^{4} \tilde{v}_n^t \tilde{v}_n^a \cos(n\Delta\phi)) d\Delta\phi \tag{7.7}$$

and the parameters are B, $\tilde{v_2^a}$, $\tilde{v_2^t}$, $\tilde{v_3^a v_3^t}$, $\tilde{v_4^a}$ and $\tilde{v_4^t}$. The uncertainties on the yield due to the background (Y_{Bkgd}) and the statistical uncertainties on Y_{All} are reported separately.

Figure 7.17 and 7.18 show the near-side and away-side jet yields vs p_T^{assoc} for 20-40 GeV/c full jets in 30-50% centrality collisions. Tab. The yields are compared for each orientation of the trigger jet restricted relative to the event plane (in/mid/out). Tab. 7.1 and Tab. 7.2 summarize the yield results with the uncertainties broken down.

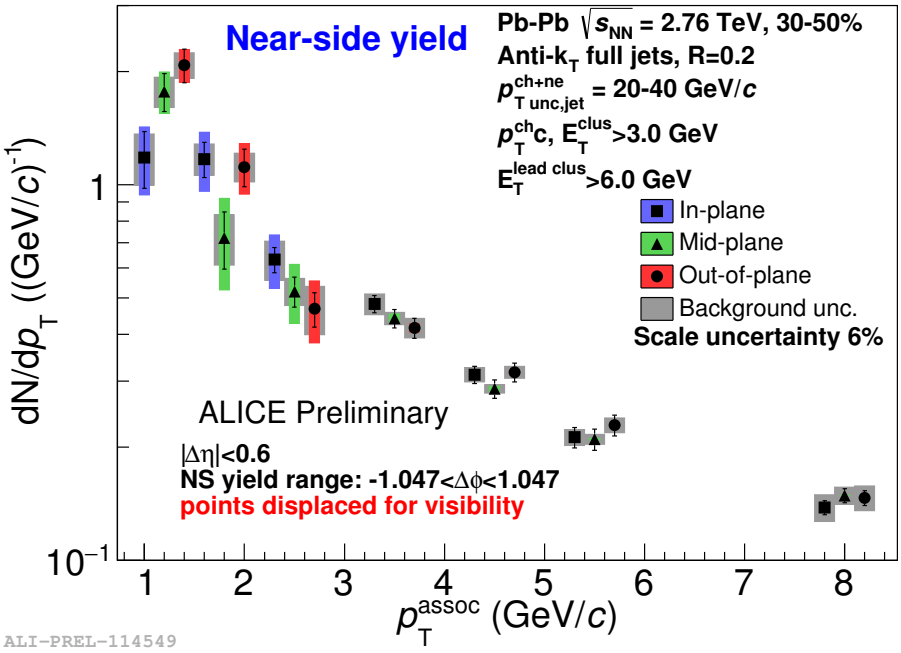

Figure 7.17: Near-side jet yield vs p_T^{assoc} for 20-40 GeV/c full jets in 30-50% centrality collisions. The grey bands are the systematic uncertainties of the background fits, the errors are non-trivially correlated point-to-point. The colored bands are the scale uncertainties from the mixed events. There is an additional 6% global scale uncertainty.

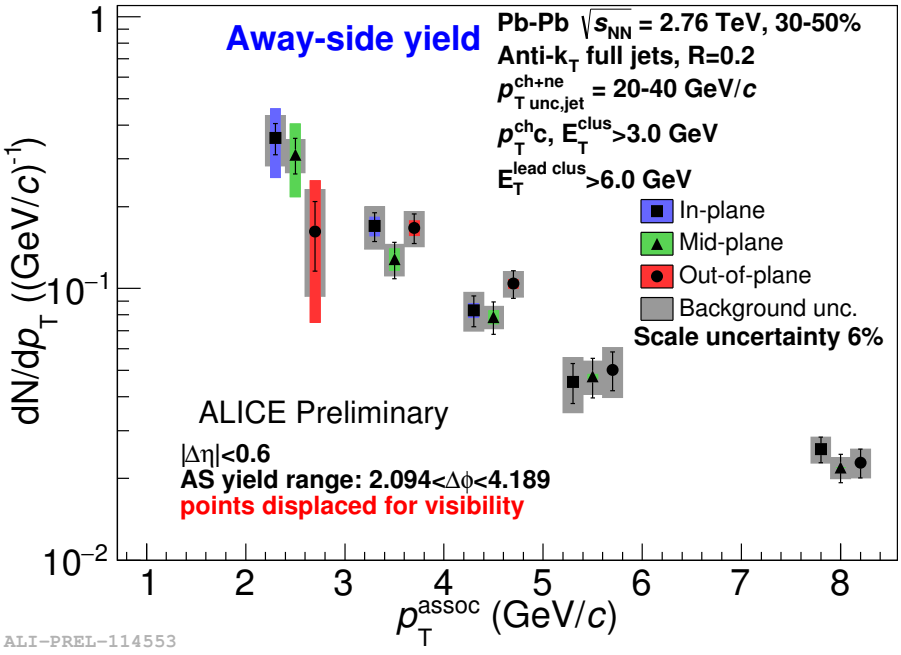

Figure 7.18: Away-side jet yield vs p_T^{assoc} for 20-40 GeV/c full jets in 30-50% centrality collisions. The grey bands are the systematic uncertainties of the background fits, the errors are non-trivially correlated point-to-point. The colored bands are the scale uncertainties from the mixed events. There is an additional 6% global scale uncertainty.

Table 7.1: Yield with uncertainties for Jets 20-40 GeV/c in 30-50% centrality events: in/mid/out-of-plane orientations for both the near-side and away-side. Included are the statistical, scale, and background uncertainties.

p_T GeV/c		Near-Side Yield	Away-Side Yield
1.0-1.5	In-plane	1.181 ± 0.204 (st) ± 0.241 (sc) ± 0.369 (bg)	0.732 ± 0.201 (st) ± 0.241 (sc) ± 0.369 (bg)
	Mid-plane	1.772 ± 0.207 (st) ± 0.225 (sc) ± 0.329 (bg)	0.902 ± 0.203 (st) ± 0.225 (sc) ± 0.329 (bg)
	Out-of-plane	2.082 ± 0.212 (st) ± 0.207 (sc) ± 0.328 (bg)	0.937 ± 0.207 (st) ± 0.207 (sc) ± 0.328 (bg)
1.5-2.0	In-plane	1.171 ± 0.126 (st) ± 0.209 (sc) ± 0.224 (bg)	0.829 ± 0.124 (st) ± 0.209 (sc) ± 0.224 (bg)
	Mid-plane	0.721 ± 0.125 (st) ± 0.197 (sc) ± 0.220 (bg)	0.390 ± 0.123 (st) ± 0.197 (sc) ± 0.220 (bg)
	Out-of-plane	1.115 ± 0.127 (st) ± 0.171 (sc) ± 0.198 (bg)	1.025 ± 0.126 (st) ± 0.171 (sc) ± 0.198 (bg)
2.0-3.0	In-plane	0.632 ± 0.049 (st) ± 0.102 (sc) ± 0.076 (bg)	0.358 ± 0.047 (st) ± 0.102 (sc) ± 0.076 (bg)
	Mid-plane	0.520 ± 0.048 (st) ± 0.093 (sc) ± 0.044 (bg)	0.310 ± 0.046 (st) ± 0.093 (sc) ± 0.044 (bg)
	Out-of-plane	0.467 ± 0.049 (st) ± 0.087 (sc) ± 0.069 (bg)	0.162 ± 0.047 (st) ± 0.087 (sc) ± 0.069 (bg)
3.0-4.0	In-plane	0.481 ± 0.025 (st) ± 0.013 (sc) ± 0.030 (bg)	0.170 ± 0.021 (st) ± 0.013 (sc) ± 0.030 (bg)
	Mid-plane	0.440 ± 0.025 (st) ± 0.012 (sc) ± 0.017 (bg)	0.128 ± 0.020 (st) ± 0.012 (sc) ± 0.017 (bg)
	Out-of-plane	0.416 ± 0.025 (st) ± 0.011 (sc) ± 0.025 (bg)	0.167 ± 0.021 (st) ± 0.011 (sc) ± 0.025 (bg)
4.0-5.0	In-plane	0.312 ± 0.017 (st) ± 0.005 (sc) ± 0.014 (bg)	0.083 ± 0.011 (st) ± 0.005 (sc) ± 0.014 (bg)
	Mid-plane	0.286 ± 0.016 (st) ± 0.004 (sc) ± 0.007 (bg)	0.079 ± 0.011 (st) ± 0.004 (sc) ± 0.007 (bg)
	Out-of-plane	0.317 ± 0.018 (st) ± 0.004 (sc) ± 0.011 (bg)	0.104 ± 0.012 (st) ± 0.004 (sc) ± 0.011 (bg)
5.0-6.0	In-plane	0.213 ± 0.013 (st) ± 0.001 (sc) ± 0.010 (bg)	0.045 ± 0.008 (st) ± 0.001 (sc) ± 0.010 (bg)
	Mid-plane	0.210 ± 0.014 (st) ± 0.001 (sc) ± 0.007 (bg)	0.047 ± 0.008 (st) ± 0.001 (sc) ± 0.007 (bg)
	Out-of-plane	0.229 ± 0.015 (st) ± 0.001 (sc) ± 0.010 (bg)	0.050 ± 0.008 (st) ± 0.001 (sc) ± 0.010 (bg)
6.0-10.0	In-plane	0.138 ± 0.006 (st) ± 0.000 (sc) ± 0.003 (bg)	0.026 ± 0.003 (st) ± 0.000 (sc) ± 0.003 (bg)
	Mid-plane	0.149 ± 0.006 (st) ± 0.000 (sc) ± 0.002 (bg)	0.022 ± 0.003 (st) ± 0.000 (sc) ± 0.002 (bg)
	Out-of-plane	0.147 ± 0.007 (st) ± 0.000 (sc) ± 0.003 (bg)	0.023 ± 0.003 (st) ± 0.000 (sc) ± 0.003 (bg)

Table 7.2: Yield with uncertainties for Jets 20-40 GeV/c in 30-50% centrality events from all event plane orientations for both the near-side and away-side. Included are the statistical, scale, and background uncertainties.

p_T GeV/c	Near-Side Yield	Away-Side Yield
1.0-1.5	1.648 ± 0.124 (st) ± 0.226 (sc) ± 0.202 (bg)	0.850 ± 0.121 (st) ± 0.226 (sc) ± 0.202 (bg)
1.5-2.0	1.003 ± 0.076 (st) ± 0.194 (sc) ± 0.123 (bg)	0.739 ± 0.074 (st) ± 0.194 (sc) ± 0.123 (bg)
2.0-3.0	0.545 ± 0.029 (st) ± 0.094 (sc) ± 0.045 (bg)	0.284 ± 0.028 (st) ± 0.094 (sc) ± 0.045 (bg)
3.0-4.0	0.448 ± 0.015 (st) ± 0.012 (sc) ± 0.018 (bg)	0.155 ± 0.012 (st) ± 0.012 (sc) ± 0.018 (bg)
4.0-5.0	0.305 ± 0.010 (st) ± 0.004 (sc) ± 0.008 (bg)	0.088 ± 0.006 (st) ± 0.004 (sc) ± 0.008 (bg)
5.0-6.0	0.216 ± 0.008 (st) ± 0.001 (sc) ± 0.007 (bg)	0.047 ± 0.005 (st) ± 0.001 (sc) ± 0.007 (bg)
6.0-10.0	0.144 ± 0.004 (st) ± 0.000 (sc) ± 0.002 (bg)	0.024 ± 0.002 (st) ± 0.000 (sc) ± 0.002 (bg)

Figure 7.19 and 7.20 show the near-side and away-side jet yields vs p_T^{assoc} for 20-40 GeV/c full jets in 0-10% centrality collisions. The yields are compared for each orientation of the trigger jet restricted relative to the event plane (in/mid/out). Tab. 7.3 and Tab. 7.4 summarize the results with the uncertainties broken down.

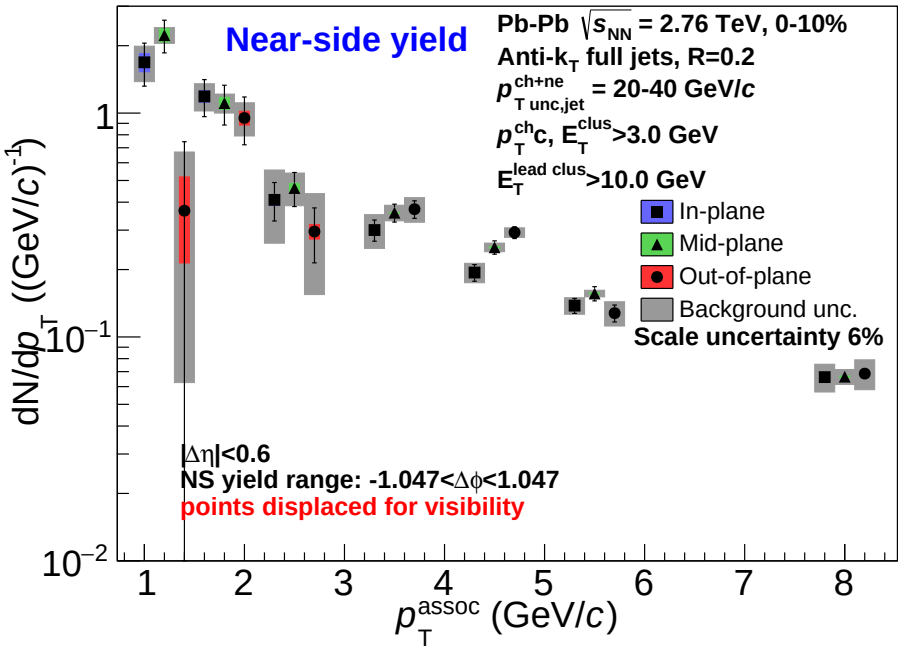

Figure 7.19: Near-side jet yield vs p_T^{assoc} for 20-40 GeV/c full jets in 0-10% centrality collisions. The grey bands are the systematic uncertainties of the background fits, the errors are non-trivially correlated point-to-point. The colored bands are the scale uncertainties from the mixed events. There is an additional 6% global scale uncertainty.

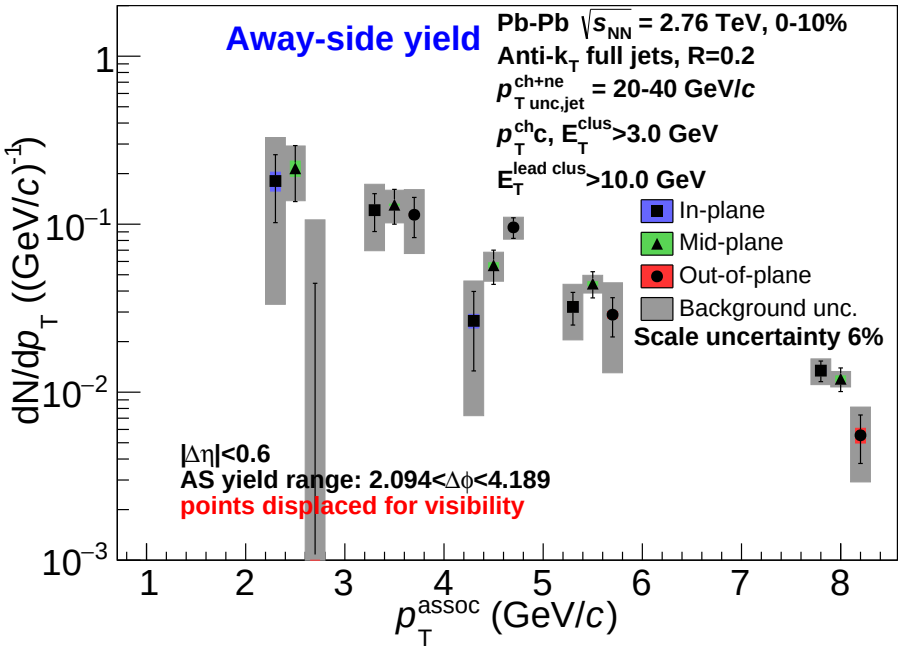

Figure 7.20: Away-side jet yield vs p_T^{assoc} for 20-40 GeV/c full jets in 0-10% centrality collisions. The grey bands are the systematic uncertainties of the background fits, the errors are non-trivially correlated point-to-point. The colored bands are the scale uncertainties from the mixed events. There is an additional 6% global scale uncertainty.

Table 7.3: Yield with uncertainties for Jets 20-40 GeV/c in 0-10% centrality events: in/mid/out-of-plane orientations for both the near-side and away-side. Included are the statistical, scale, and background uncertainties.

p_T GeV/c		Near-Side Yield	Away-Side Yield
1.0-1.5	In-plane	1.686 ± 0.367 (st) ± 0.157 (sc) ± 0.609 (bg)	1.380 ± 0.364 (st) ± 0.157 (sc) ± 0.609 (bg)
	Mid-plane	2.228 ± 0.371 (st) ± 0.153 (sc) ± 0.361 (bg)	1.378 ± 0.367 (st) ± 0.153 (sc) ± 0.361 (bg)
	Out-of-plane	0.366 ± 0.379 (st) ± 0.152 (sc) ± 0.608 (bg)	0.022 ± 0.375 (st) ± 0.152 (sc) ± 0.608 (bg)
1.5-2.0	In-plane	1.187 ± 0.223 (st) ± 0.070 (sc) ± 0.331 (bg)	0.863 ± 0.221 (st) ± 0.070 (sc) ± 0.331 (bg)
	Mid-plane	1.108 ± 0.224 (st) ± 0.068 (sc) ± 0.216 (bg)	0.798 ± 0.221 (st) ± 0.068 (sc) ± 0.216 (bg)
	Out-of-plane	0.951 ± 0.229 (st) ± 0.067 (sc) ± 0.322 (bg)	0.494 ± 0.226 (st) ± 0.067 (sc) ± 0.322 (bg)
2.0-3.0	In-plane	0.410 ± 0.080 (st) ± 0.023 (sc) ± 0.147 (bg)	0.181 ± 0.079 (st) ± 0.023 (sc) ± 0.147 (bg)
	Mid-plane	0.463 ± 0.080 (st) ± 0.022 (sc) ± 0.077 (bg)	0.215 ± 0.079 (st) ± 0.022 (sc) ± 0.077 (bg)
	Out-of-plane	0.296 ± 0.081 (st) ± 0.022 (sc) ± 0.141 (bg)	-0.035 ± 0.079 (st) ± 0.022 (sc) ± 0.141 (bg)
3.0-4.0	In-plane	0.300 ± 0.033 (st) ± 0.001 (sc) ± 0.052 (bg)	0.121 ± 0.031 (st) ± 0.001 (sc) ± 0.052 (bg)
	Mid-plane	0.359 ± 0.033 (st) ± 0.001 (sc) ± 0.029 (bg)	0.131 ± 0.031 (st) ± 0.001 (sc) ± 0.029 (bg)
	Out-of-plane	0.372 ± 0.033 (st) ± 0.001 (sc) ± 0.047 (bg)	0.114 ± 0.031 (st) ± 0.001 (sc) ± 0.047 (bg)
4.0-5.0	In-plane	0.194 ± 0.017 (st) ± 0.002 (sc) ± 0.019 (bg)	0.027 ± 0.013 (st) ± 0.002 (sc) ± 0.019 (bg)
	Mid-plane	0.251 ± 0.017 (st) ± 0.002 (sc) ± 0.011 (bg)	0.057 ± 0.013 (st) ± 0.002 (sc) ± 0.011 (bg)
	Out-of-plane	0.293 ± 0.018 (st) ± 0.002 (sc) ± 0.014 (bg)	0.096 ± 0.013 (st) ± 0.002 (sc) ± 0.014 (bg)
5.0-6.0	In-plane	0.138 ± 0.011 (st) ± 0.001 (sc) ± 0.012 (bg)	0.032 ± 0.007 (st) ± 0.001 (sc) ± 0.012 (bg)
	Mid-plane	0.156 ± 0.011 (st) ± 0.001 (sc) ± 0.005 (bg)	0.044 ± 0.008 (st) ± 0.001 (sc) ± 0.005 (bg)
	Out-of-plane	0.128 ± 0.011 (st) ± 0.001 (sc) ± 0.016 (bg)	0.029 ± 0.008 (st) ± 0.001 (sc) ± 0.016 (bg)
6.0-10.0	In-plane	0.066 ± 0.003 (st) ± 0.000 (sc) ± 0.002 (bg)	0.013 ± 0.002 (st) ± 0.000 (sc) ± 0.002 (bg)
	Mid-plane	0.066 ± 0.003 (st) ± 0.000 (sc) ± 0.001 (bg)	0.012 ± 0.002 (st) ± 0.000 (sc) ± 0.001 (bg)
	Out-of-plane	0.069 ± 0.004 (st) ± 0.001 (sc) ± 0.003 (bg)	0.006 ± 0.002 (st) ± 0.001 (sc) ± 0.003 (bg)

Table 7.4: Yield with uncertainties for Jets 20-40 GeV/c in 0-10% centrality events from all event plane orientations for both the near-side and away-side. Included are the statistical, scale, and background uncertainties.

p_T GeV/c	Near-Side Yield	Away-Side Yield
1.0-1.5	1.452 ± 0.219 (st) ± 0.154 (sc) ± 0.364 (bg)	0.951 ± 0.217 (st) ± 0.154 (sc) ± 0.364 (bg)
1.5-2.0	1.086 ± 0.132 (st) ± 0.069 (sc) ± 0.218 (bg)	0.725 ± 0.131 (st) ± 0.069 (sc) ± 0.218 (bg)
2.0-3.0	0.391 ± 0.047 (st) ± 0.023 (sc) ± 0.078 (bg)	0.124 ± 0.046 (st) ± 0.023 (sc) ± 0.078 (bg)
3.0-4.0	0.343 ± 0.019 (st) ± 0.001 (sc) ± 0.029 (bg)	0.122 ± 0.018 (st) ± 0.001 (sc) ± 0.029 (bg)
4.0-5.0	0.244 ± 0.010 (st) ± 0.002 (sc) ± 0.011 (bg)	0.059 ± 0.008 (st) ± 0.002 (sc) ± 0.011 (bg)
5.0-6.0	0.141 ± 0.006 (st) ± 0.001 (sc) ± 0.005 (bg)	0.035 ± 0.004 (st) ± 0.001 (sc) ± 0.005 (bg)
6.0-10.0	0.067 ± 0.002 (st) ± 0.000 (sc) ± 0.001 (bg)	0.010 ± 0.001 (st) ± 0.000 (sc) ± 0.001 (bg)

The truncated RMS is reported as:

$$RMS = \sqrt{\int_a^b \frac{1}{Y} \frac{d(s_{meas} - b_{bkgd})}{d\Delta\phi} (\Delta\phi - \Delta\phi_0)^2 d\Delta\phi} = \frac{1}{\sqrt{Y}} \sqrt{\alpha - \beta} \tag{7.8}$$

where $\Delta\phi_0 = 0$ for the near-side and π for the away-side rather than the RMS over all $\Delta\phi$ because integration over a wide range in $\Delta\phi$ increases the weight of statistical error bars without dramatically changing the result,

$$\alpha = \int_a^b \frac{ds_{meas}}{d\Delta\phi} (\Delta\phi - \Delta\phi_0)^2 d\Delta\phi \tag{7.9}$$

and

$$\beta = \int_a^b \frac{db_{bkgd}}{d\Delta\phi} (\Delta\phi - \Delta\phi_0)^2 d\Delta\phi. \tag{7.10}$$

Again, separation of the statistical uncertainties from the correlated uncertainties is done. The total uncertainty σ_{RMS} is given by

$$\sigma_{RMS}^2 = \left(\frac{\partial RMS}{\partial \alpha} \sigma_\alpha \right)^2 + \left(\frac{\partial RMS}{\partial \beta} \sigma_\beta \right)^2 = \frac{1}{2RMS^2} (\sigma_\alpha^2 + \sigma_\beta^2). \tag{7.11}$$

The uncertainties on α and β are calculated as for the yield, with σ_α from statistical uncertainties only and σ_β having correlated uncertainties calculated using Eqn. 6.23. The bin center was used as the position of $\Delta\phi$ for the calculation of α and σ_α.

Figure 7.21 and Fig. 7.22 show the near-side and away-side truncated jet RMS vs p_T^{assoc} for 20-40 GeV/c full jets in 30-50% centrality collisions. The truncated jet RMS are compared for each orientation of the trigger jet restricted relative to the event plane (in/mid/out). The integration limits are the same as for Eqn. 7.2. Tab. 7.5 and Tab. 7.6 summarize the RMS results with the uncertainties broken down.

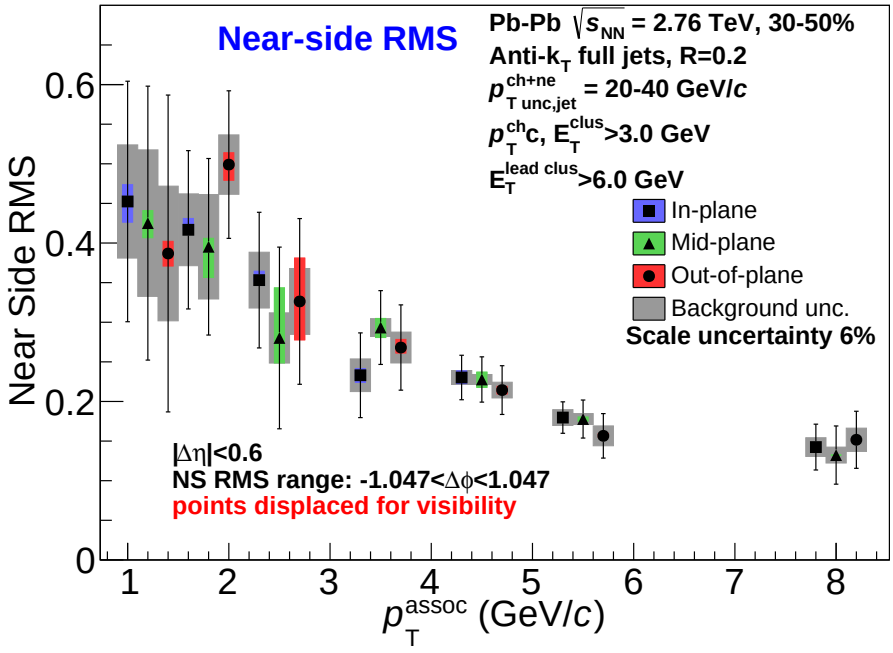

Figure 7.21: Truncated RMS of near-side vs p_T^{assoc} for 20-40 GeV/c full jets in 30-50% centrality collisions. The error bars on the data points include the uncertainties from the background fits and the statistical uncertainties. The background uncertainties are non-trivially correlated point-to-point. The colored bands are the scale uncertainties from the mixed events. There is an additional 6% global scale uncertainty.

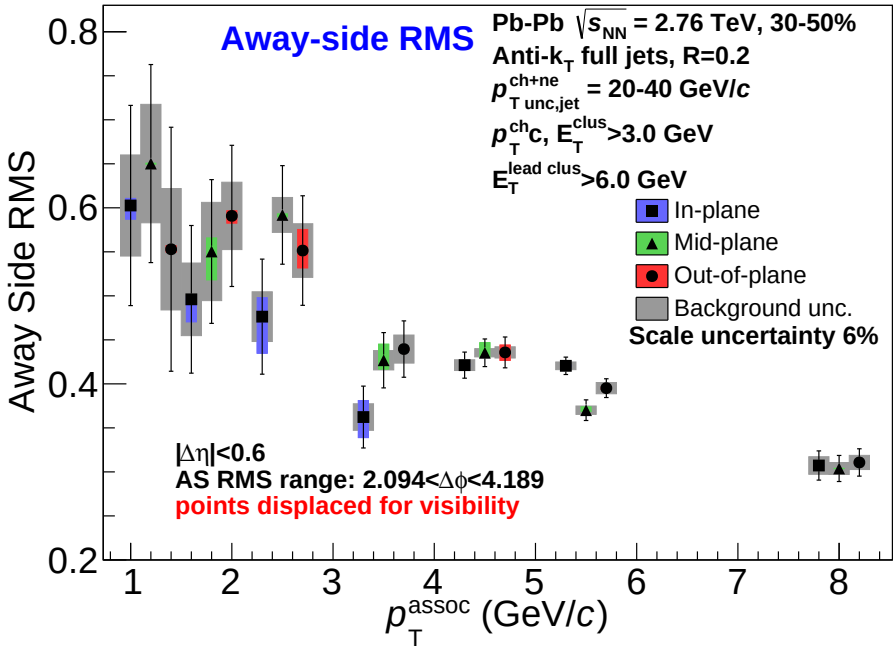

Figure 7.22: Truncated RMS of away-side vs p_T^{assoc} for 20-40 GeV/c full jets in 30-50% centrality collisions. The error bars on the data points include the uncertainties from the background fits and the statistical uncertainties. The background uncertainties are non-trivially correlated point-to-point. The colored bands are the scale uncertainties from the mixed events. There is an additional 6% global scale uncertainty.

Table 7.5: Truncated RMS with uncertainties for Jets 20-40 GeV/c in 30-50% centrality events: in/mid/out-of-plane orientation for both the near-side and away-side. Included are the statistical, scale, and background uncertainties.

p_T GeV/c		Near-Side RMS	Away-Side RMS
1.0-1.5	In-plane	$0.452^{+0.021}_{-0.026}$ (sc) $\pm$ 0.152 (st) $\pm$ 0.071 (bg)	$0.603^{+0.008}_{-0.016}$ (sc) $\pm$ 0.114 (st) $\pm$ 0.057 (bg)
	Mid-plane	$0.425^{+0.016}_{-0.019}$ (sc) $\pm$ 0.173 (st) $\pm$ 0.092 (bg)	$0.650^{+0.000}_{-0.001}$ (sc) $\pm$ 0.113 (st) $\pm$ 0.067 (bg)
	Out-of-plane	$0.387^{+0.015}_{-0.016}$ (sc) $\pm$ 0.200 (st) $\pm$ 0.085 (bg)	$0.553^{+0.004}_{-0.003}$ (sc) $\pm$ 0.139 (st) $\pm$ 0.069 (bg)
1.5-2.0	In-plane	$0.417^{+0.014}_{-0.000}$ (sc) $\pm$ 0.100 (st) $\pm$ 0.045 (bg)	$0.496^{+0.003}_{-0.026}$ (sc) $\pm$ 0.084 (st) $\pm$ 0.041 (bg)
	Mid-plane	$0.395^{+0.011}_{-0.039}$ (sc) $\pm$ 0.111 (st) $\pm$ 0.066 (bg)	$0.550^{+0.015}_{-0.032}$ (sc) $\pm$ 0.082 (st) $\pm$ 0.056 (bg)
	Out-of-plane	$0.499^{+0.015}_{-0.020}$ (sc) $\pm$ 0.093 (st) $\pm$ 0.037 (bg)	$0.591^{+0.006}_{-0.008}$ (sc) $\pm$ 0.080 (st) $\pm$ 0.038 (bg)
2.0-3.0	In-plane	$0.353^{+0.011}_{-0.002}$ (sc) $\pm$ 0.086 (st) $\pm$ 0.035 (bg)	$0.476^{+0.022}_{-0.042}$ (sc) $\pm$ 0.065 (st) $\pm$ 0.028 (bg)
	Mid-plane	$0.280^{+0.063}_{-0.031}$ (sc) $\pm$ 0.115 (st) $\pm$ 0.032 (bg)	$0.592^{+0.001}_{-0.002}$ (sc) $\pm$ 0.056 (st) $\pm$ 0.020 (bg)
	Out-of-plane	$0.326^{+0.055}_{-0.048}$ (sc) $\pm$ 0.105 (st) $\pm$ 0.042 (bg)	$0.551^{+0.024}_{-0.020}$ (sc) $\pm$ 0.062 (st) $\pm$ 0.030 (bg)
3.0-4.0	In-plane	$0.233^{+0.008}_{-0.009}$ (sc) $\pm$ 0.053 (st) $\pm$ 0.021 (bg)	$0.362^{+0.019}_{-0.023}$ (sc) $\pm$ 0.035 (st) $\pm$ 0.015 (bg)
	Mid-plane	$0.293^{+0.011}_{-0.013}$ (sc) $\pm$ 0.047 (st) $\pm$ 0.011 (bg)	$0.427^{+0.018}_{-0.010}$ (sc) $\pm$ 0.031 (st) $\pm$ 0.011 (bg)
	Out-of-plane	$0.268^{+0.010}_{-0.007}$ (sc) $\pm$ 0.054 (st) $\pm$ 0.020 (bg)	$0.440^{+0.000}_{-0.001}$ (sc) $\pm$ 0.032 (st) $\pm$ 0.016 (bg)
4.0-5.0	In-plane	$0.230^{+0.008}_{-0.008}$ (sc) $\pm$ 0.028 (st) $\pm$ 0.009 (bg)	$0.421^{+0.002}_{-0.002}$ (sc) $\pm$ 0.015 (st) $\pm$ 0.006 (bg)
	Mid-plane	$0.228^{+0.009}_{-0.010}$ (sc) $\pm$ 0.029 (st) $\pm$ 0.006 (bg)	$0.435^{+0.011}_{-0.005}$ (sc) $\pm$ 0.016 (st) $\pm$ 0.005 (bg)
	Out-of-plane	$0.214^{+0.005}_{-0.005}$ (sc) $\pm$ 0.031 (st) $\pm$ 0.010 (bg)	$0.436^{+0.008}_{-0.009}$ (sc) $\pm$ 0.018 (st) $\pm$ 0.006 (bg)
5.0-6.0	In-plane	$0.180^{+0.001}_{-0.001}$ (sc) $\pm$ 0.020 (st) $\pm$ 0.010 (bg)	$0.421^{+0.001}_{-0.001}$ (sc) $\pm$ 0.010 (st) $\pm$ 0.004 (bg)
	Mid-plane	$0.178^{+0.003}_{-0.003}$ (sc) $\pm$ 0.024 (st) $\pm$ 0.007 (bg)	$0.370^{+0.004}_{-0.002}$ (sc) $\pm$ 0.012 (st) $\pm$ 0.005 (bg)
	Out-of-plane	$0.157^{+0.003}_{-0.002}$ (sc) $\pm$ 0.028 (st) $\pm$ 0.013 (bg)	$0.395^{+0.001}_{-0.002}$ (sc) $\pm$ 0.011 (st) $\pm$ 0.006 (bg)
6.0-10.0	In-plane	$0.142^{+0.000}_{-0.000}$ (sc) $\pm$ 0.029 (st) $\pm$ 0.012 (bg)	$0.307^{+0.000}_{-0.000}$ (sc) $\pm$ 0.017 (st) $\pm$ 0.010 (bg)
	Mid-plane	$0.132^{+0.000}_{-0.000}$ (sc) $\pm$ 0.037 (st) $\pm$ 0.010 (bg)	$0.304^{+0.000}_{-0.000}$ (sc) $\pm$ 0.015 (st) $\pm$ 0.007 (bg)
	Out-of-plane	$0.152^{+0.000}_{-0.000}$ (sc) $\pm$ 0.036 (st) $\pm$ 0.015 (bg)	$0.311^{+0.000}_{-0.000}$ (sc) $\pm$ 0.016 (st) $\pm$ 0.008 (bg)

Table 7.6: Truncated RMS with uncertainties for Jets 20-40 GeV/c in 30-50% centrality events from all event plane orientations for both the near-side and away-side. Included are the statistical, scale, and background uncertainties.

p_T GeV/c	Near-Side RMS	Away-Side RMS
1.0-1.5	$0.407^{+0.012}_{-0.019}$ (sc) $\pm$ 0.107 (st) $\pm$ 0.050 (bg)	$0.610^{+0.003}_{-0.006}$ (sc) $\pm$ 0.071 (st) $\pm$ 0.045 (bg)
1.5-2.0	$0.389^{+0.035}_{-0.026}$ (sc) $\pm$ 0.067 (st) $\pm$ 0.031 (bg)	$0.493^{+0.015}_{-0.003}$ (sc) $\pm$ 0.054 (st) $\pm$ 0.035 (bg)
2.0-3.0	$0.291^{+0.024}_{-0.017}$ (sc) $\pm$ 0.065 (st) $\pm$ 0.031 (bg)	$0.496^{+0.027}_{-0.034}$ (sc) $\pm$ 0.039 (st) $\pm$ 0.024 (bg)
3.0-4.0	$0.257^{+0.014}_{-0.016}$ (sc) $\pm$ 0.030 (st) $\pm$ 0.013 (bg)	$0.379^{+0.009}_{-0.010}$ (sc) $\pm$ 0.020 (st) $\pm$ 0.013 (bg)
4.0-5.0	$0.218^{+0.009}_{-0.010}$ (sc) $\pm$ 0.017 (st) $\pm$ 0.007 (bg)	$0.408^{+0.010}_{-0.005}$ (sc) $\pm$ 0.010 (st) $\pm$ 0.005 (bg)
5.0-6.0	$0.135^{+0.003}_{-0.003}$ (sc) $\pm$ 0.017 (st) $\pm$ 0.009 (bg)	$0.349^{+0.000}_{-0.001}$ (sc) $\pm$ 0.007 (st) $\pm$ 0.005 (bg)
6.0-10.0	$0.119^{+0.000}_{-0.000}$ (sc) $\pm$ 0.024 (st) $\pm$ 0.011 (bg)	$0.267^{+0.000}_{-0.000}$ (sc) $\pm$ 0.010 (st) $\pm$ 0.008 (bg)

Figure 7.23 and Fig. 7.24 show the near-side and away-side truncated jet RMS vs p_T^{assoc} for 20-40 GeV/c full jets in 0-10% centrality collisions. The truncated jet RMS are compared for each orientation of the trigger jet restricted relative to the event plane (in/mid/out). The integration limits are the same as for Eqn. 7.2. Tab. 7.7 and Tab. 7.8 summarize the RMS results with the uncertainties broken down.

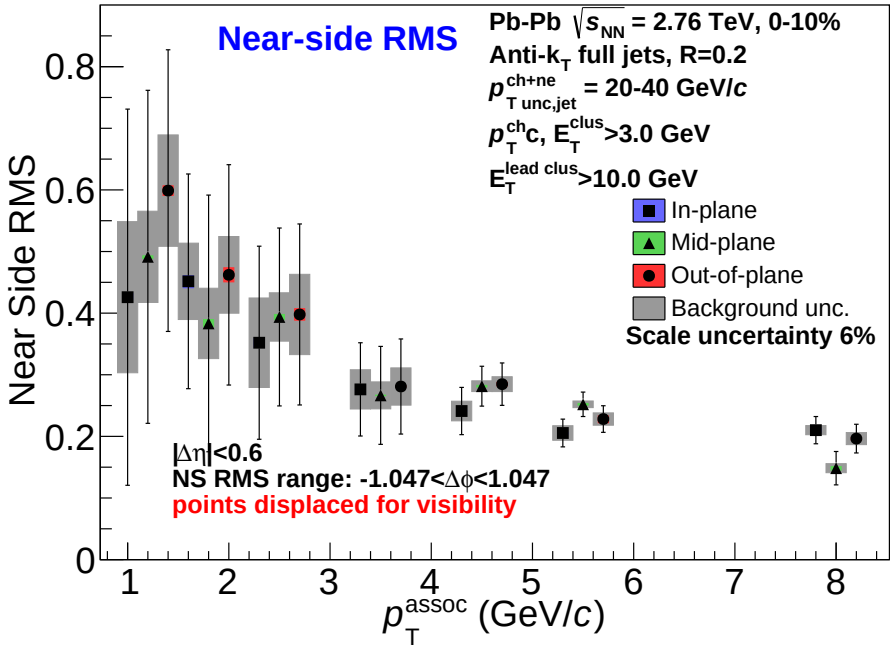

Figure 7.23: Truncated RMS of near-side vs p_T^{assoc} for 20-40 GeV/c full jets in 0-10% centrality collisions. The error bars on the data points include the uncertainties from the background fits and the statistical uncertainties. The background uncertainties are non-trivially correlated point-to-point. The colored bands are the scale uncertainties from the mixed events. There is an additional 6% global scale uncertainty.

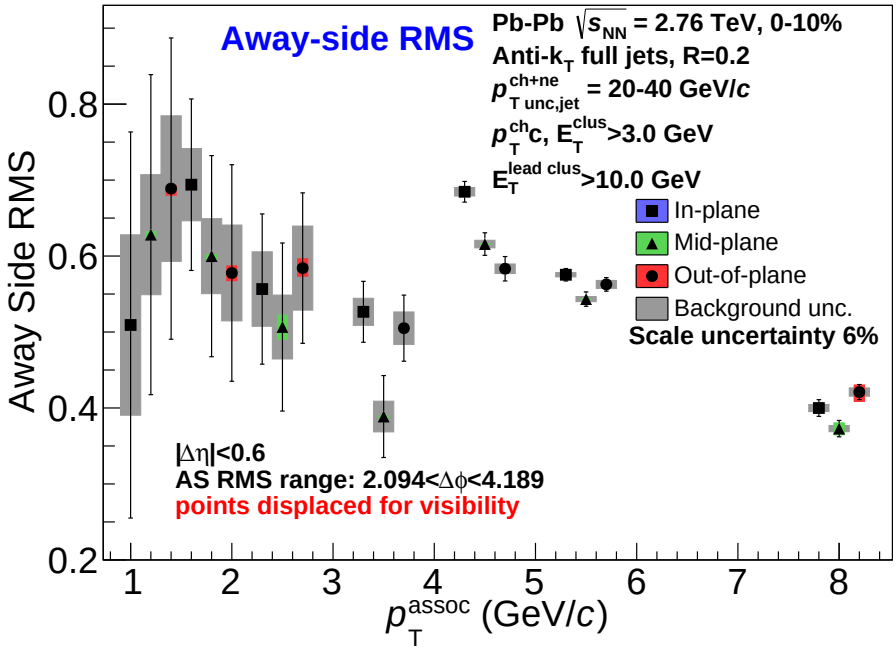

Figure 7.24: Truncated RMS of away-side vs p_T^{assoc} for 20-40 GeV/c full jets in 0-10% centrality collisions. The error bars on the data points include the uncertainties from the background fits and the statistical uncertainties. The background uncertainties are non-trivially correlated point-to-point. The colored bands are the scale uncertainties from the mixed events. There is an additional 6% global scale uncertainty.

Table 7.7: Truncated RMS with uncertainties for Jets 20-40 GeV/c in 0-10% centrality events: in/mid/out-of-plane orientation for both the near-side and away-side. Included are the statistical, scale, and background uncertainties.

p_T GeV/c		Near-Side RMS	Away-Side RMS
1.0-1.5	In-plane	$0.426^{+0.006}_{-0.003}$ (sc) $\pm$ 0.305 (st) $\pm$ 0.123 (bg)	$0.509^{+0.001}_{-0.001}$ (sc) $\pm$ 0.254 (st) $\pm$ 0.119 (bg)
	Mid-plane	$0.491^{+0.002}_{-0.003}$ (sc) $\pm$ 0.270 (st) $\pm$ 0.074 (bg)	$0.628^{+0.004}_{-0.005}$ (sc) $\pm$ 0.211 (st) $\pm$ 0.079 (bg)
	Out-of-plane	$0.599^{+0.008}_{-0.008}$ (sc) $\pm$ 0.229 (st) $\pm$ 0.090 (bg)	$0.689^{+0.004}_{-0.009}$ (sc) $\pm$ 0.198 (st) $\pm$ 0.096 (bg)
1.5-2.0	In-plane	$0.452^{+0.009}_{-0.011}$ (sc) $\pm$ 0.174 (st) $\pm$ 0.062 (bg)	$0.694^{+0.003}_{-0.002}$ (sc) $\pm$ 0.113 (st) $\pm$ 0.048 (bg)
	Mid-plane	$0.383^{+0.006}_{-0.005}$ (sc) $\pm$ 0.208 (st) $\pm$ 0.057 (bg)	$0.600^{+0.002}_{-0.004}$ (sc) $\pm$ 0.132 (st) $\pm$ 0.049 (bg)
	Out-of-plane	$0.462^{+0.012}_{-0.011}$ (sc) $\pm$ 0.179 (st) $\pm$ 0.062 (bg)	$0.578^{+0.009}_{-0.010}$ (sc) $\pm$ 0.143 (st) $\pm$ 0.063 (bg)
2.0-3.0	In-plane	$0.352^{+0.006}_{-0.007}$ (sc) $\pm$ 0.157 (st) $\pm$ 0.073 (bg)	$0.557^{+0.002}_{-0.002}$ (sc) $\pm$ 0.099 (st) $\pm$ 0.049 (bg)
	Mid-plane	$0.394^{+0.004}_{-0.004}$ (sc) $\pm$ 0.144 (st) $\pm$ 0.039 (bg)	$0.507^{+0.016}_{-0.016}$ (sc) $\pm$ 0.111 (st) $\pm$ 0.042 (bg)
	Out-of-plane	$0.398^{+0.009}_{-0.009}$ (sc) $\pm$ 0.147 (st) $\pm$ 0.065 (bg)	$0.584^{+0.012}_{-0.011}$ (sc) $\pm$ 0.099 (st) $\pm$ 0.055 (bg)
3.0-4.0	In-plane	$0.276^{+0.000}_{-0.000}$ (sc) $\pm$ 0.076 (st) $\pm$ 0.032 (bg)	$0.527^{+0.000}_{-0.000}$ (sc) $\pm$ 0.040 (st) $\pm$ 0.018 (bg)
	Mid-plane	$0.267^{+0.000}_{-0.000}$ (sc) $\pm$ 0.079 (st) $\pm$ 0.022 (bg)	$0.389^{+0.001}_{-0.001}$ (sc) $\pm$ 0.054 (st) $\pm$ 0.020 (bg)
	Out-of-plane	$0.281^{+0.001}_{-0.001}$ (sc) $\pm$ 0.077 (st) $\pm$ 0.030 (bg)	$0.505^{+0.001}_{-0.001}$ (sc) $\pm$ 0.044 (st) $\pm$ 0.021 (bg)
4.0-5.0	In-plane	$0.241^{+0.000}_{-0.000}$ (sc) $\pm$ 0.038 (st) $\pm$ 0.016 (bg)	$0.685^{+0.004}_{-0.004}$ (sc) $\pm$ 0.014 (st) $\pm$ 0.006 (bg)
	Mid-plane	$0.281^{+0.001}_{-0.001}$ (sc) $\pm$ 0.032 (st) $\pm$ 0.009 (bg)	$0.616^{+0.001}_{-0.001}$ (sc) $\pm$ 0.015 (st) $\pm$ 0.005 (bg)
	Out-of-plane	$0.285^{+0.003}_{-0.003}$ (sc) $\pm$ 0.034 (st) $\pm$ 0.012 (bg)	$0.583^{+0.000}_{-0.000}$ (sc) $\pm$ 0.016 (st) $\pm$ 0.006 (bg)
5.0-6.0	In-plane	$0.205^{+0.001}_{-0.002}$ (sc) $\pm$ 0.023 (st) $\pm$ 0.012 (bg)	$0.575^{+0.001}_{-0.001}$ (sc) $\pm$ 0.008 (st) $\pm$ 0.003 (bg)
	Mid-plane	$0.252^{+0.001}_{-0.001}$ (sc) $\pm$ 0.020 (st) $\pm$ 0.005 (bg)	$0.543^{+0.000}_{-0.000}$ (sc) $\pm$ 0.009 (st) $\pm$ 0.003 (bg)
	Out-of-plane	$0.228^{+0.005}_{-0.006}$ (sc) $\pm$ 0.022 (st) $\pm$ 0.010 (bg)	$0.563^{+0.001}_{-0.001}$ (sc) $\pm$ 0.009 (st) $\pm$ 0.005 (bg)
6.0-10.0	In-plane	$0.210^{+0.003}_{-0.003}$ (sc) $\pm$ 0.022 (st) $\pm$ 0.007 (bg)	$0.400^{+0.003}_{-0.003}$ (sc) $\pm$ 0.011 (st) $\pm$ 0.005 (bg)
	Mid-plane	$0.148^{+0.003}_{-0.003}$ (sc) $\pm$ 0.027 (st) $\pm$ 0.007 (bg)	$0.373^{+0.007}_{-0.008}$ (sc) $\pm$ 0.011 (st) $\pm$ 0.004 (bg)
	Out-of-plane	$0.196^{+0.002}_{-0.003}$ (sc) $\pm$ 0.023 (st) $\pm$ 0.010 (bg)	$0.421^{+0.009}_{-0.012}$ (sc) $\pm$ 0.010 (st) $\pm$ 0.005 (bg)

Table 7.8: Truncated RMS with uncertainties for Jets 20-40 GeV/c in 0-10% centrality events from all event plane orientations for both the near-side and away-side. Included are the statistical, scale, and background uncertainties.

p_T GeV/c	Near-Side RMS	Away-Side RMS
1.0-1.5	$0.479^{+0.004}_{-0.010}$ (sc) $\pm$ 0.163 (st) $\pm$ 0.077 (bg)	$0.535^{+0.010}_{-0.014}$ (sc) $\pm$ 0.146 (st) $\pm$ 0.093 (bg)
1.5-2.0	$0.294^{+0.003}_{-0.014}$ (sc) $\pm$ 0.160 (st) $\pm$ 0.075 (bg)	$0.634^{+0.003}_{-0.003}$ (sc) $\pm$ 0.074 (st) $\pm$ 0.047 (bg)
2.0-3.0	$0.341^{+0.002}_{-0.002}$ (sc) $\pm$ 0.097 (st) $\pm$ 0.046 (bg)	$0.486^{+0.012}_{-0.021}$ (sc) $\pm$ 0.068 (st) $\pm$ 0.044 (bg)
3.0-4.0	$0.263^{+0.000}_{-0.000}$ (sc) $\pm$ 0.047 (st) $\pm$ 0.022 (bg)	$0.409^{+0.000}_{-0.000}$ (sc) $\pm$ 0.030 (st) $\pm$ 0.019 (bg)
4.0-5.0	$0.222^{+0.003}_{-0.003}$ (sc) $\pm$ 0.024 (st) $\pm$ 0.011 (bg)	$0.685^{+0.004}_{-0.004}$ (sc) $\pm$ 0.008 (st) $\pm$ 0.005 (bg)
5.0-6.0	$0.185^{+0.001}_{-0.001}$ (sc) $\pm$ 0.015 (st) $\pm$ 0.007 (bg)	$0.558^{+0.000}_{-0.000}$ (sc) $\pm$ 0.005 (st) $\pm$ 0.003 (bg)
6.0-10.0	$0.162^{+0.001}_{-0.000}$ (sc) $\pm$ 0.016 (st) $\pm$ 0.007 (bg)	$0.322^{+0.007}_{-0.013}$ (sc) $\pm$ 0.008 (st) $\pm$ 0.005 (bg)

7.4 Systematic uncertainty summary

Table 7.9 and 7.10 summarize the key systematic uncertainty sources for the main analysis of this thesis, the 30-50% centrality full jets with p_T = 20-40 GeV/c. Tab. 7.9 includes the uncertainties coming from the single particle reconstruction efficiency, contamination, mixed event shape uncertainty of $\Delta\phi$, mixed event normalization factor, and event plane resolution. These are listed as percent uncertainties. These sources sum in quadrature and round up to a 6% global scale uncertainty which is written on the final plots. Tab. 7.10 lists the mixed event scale uncertainty in $\Delta\eta$ for both the yield and RMS calculation on the near-side and away-side for each orientation of the trigger jet relative to the event plane. Tab. 7.9 also lists the uncertainties from the background fits for both the yield and RMS calcuation on the near-side and away-side for each orientation of the trigger jet relative to the event plane. These uncertainties are listed as percent error. The uncertainties of the mixed event scale and background fit are p_T dependent and thus are listed as a range from smallest to largest for a given orientation. Both of these systematic uncertainties are given as error bands on the final results for the yields and RMS.

Table 7.9: Systematic uncertainty summary for p_T^{jet} = 20-40 GeV/c, and 30-50% centrality collisions.

Source	% Uncertainty
Single particle reconstruction efficiency	5
Contamination	1
Mixed event (shape $\Delta\phi$)	negligible
Mixed event normalization	< 0.5
Event plane resolution	negligible

Table 7.10: Systematic uncertainty summary for source varying with event plane orienation bins. Given for p_T^{jet} = 20-40 GeV/c, and 30-50% centrality collisions. The following uncertainties have a p_T^{assoc} dependence and are thus expressed as a range from the smallest to largest.

Source	Result type	Orientation	Near-side	Away-side
Mixed event (scale $\Delta\eta$)	Yield	in-plane	0.2-20.4	0.1-33
		mid-plane	0.2-27.4	0.2-50.7
		out-of-plane	0.3-18.7	0.2-53.7
	RMS	in-plane	$^{+0.01-4.7}_{-0.01-5.8}$	$^{+0.02-5.2}_{-0.03-8.7}$
		mid-plane	$^{+0.01-22.5}_{-0.1-11.2}$	$^{+0.07-4.3}_{-0.1-5.9}$
		out-of-plane	$^{+0.05-16.8}_{-0.07-14.8}$	$^{+0.09-1.9}_{-0.4-3.6}$
Background fit	Yield	in-plane	4.4-15.6	11.6-50.4
		mid-plane	2.6-15.3	9.5-56.6
		out-of-plane	3.6-10.9	10.9-35
	RMS	in-plane	3.8-15.8	1.1-9.5
		mid-plane	2.2-10.5	1.1-10.3
		out-of-plane	3.1-13	1.5-12.5

7.5 Yield ratio

To better quantify and examine the event plane dependence of the yields, ratios were taken of mid-plane yields relative in-plane yields and out-of-plane yields relative to in-plane yields. Fig. 7.25, 7.26 show the ratios for the near-side yield ratio of out-of-plane/in-plane and mid-plane/in-plane.

The propagation of uncertainties was done similarly to that of Sec. 6.6.3. The yield ratio is given by following the notation from Sec. 6.6.3, this is shown by Eqn. 7.12:

$$R = \frac{Y_A}{Y_B} = \frac{s^A_{meas} - b^A_{bkgd}}{s^B_{meas} - b^B_{bkgrd}}, \tag{7.12}$$

where A and B just denote the event plane orientaiton of the yield being used. The statistical errors, coming only from the terms, s^A_{meas} and s^B_{meas}, which were completely uncorrelated were calculated by Eqn. 7.13:

$$\sigma_R^{stat} = \left|\frac{1}{R}\right| \sqrt{\left(\frac{\sigma_A}{Y_A}\right)^2 + \left(\frac{\sigma_B}{Y_B}\right)^2}. \tag{7.13}$$

The scale uncertainties, displayed as colored bands on the yield and rms plots, completely cancelled in the ratio because they came from the same mixed event distribution. To calculate the uncertainties from the background fit, Eqn. 6.23, the covariance matrix is used from the background fit, but now on Eqn. 7.12, which includes correlated background equations in the numerator and denominator of the ratio. The correlated background uncertainties are now given by Eqn. 7.14:

$$\sigma_R^{bkgd} = \sqrt{\sum_{i=0}^{N}\sum_{j=0}^{N} \frac{\partial R}{\partial p_i}\frac{\partial R}{\partial p_j}\sigma_{ij}}. \tag{7.14}$$

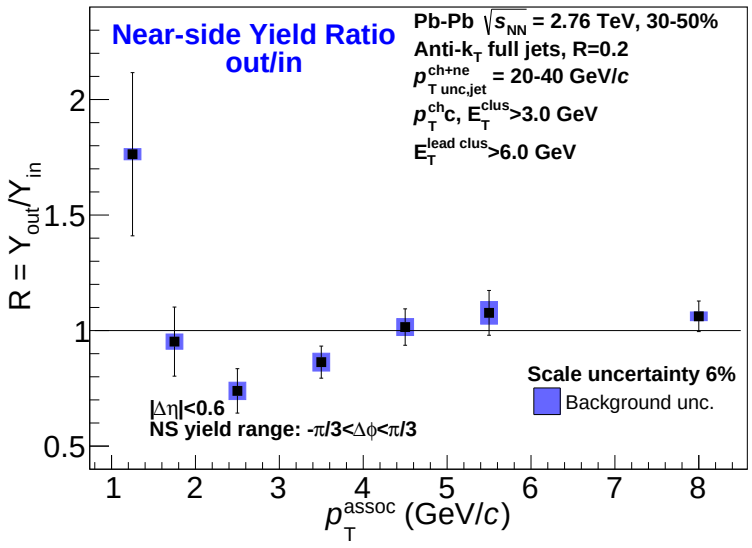

Figure 7.25: Near-side jet yield vs p_T^{assoc} for 20-40 GeV/c full jets in 30-50% centrality collisions. The grey bands are the systematic uncertainties of the background fits, the errors are non-trivially correlated point-to-point. The colored bands are the scale uncertainties from the mixed events. There is an additional 6% global scale uncertainty.

Figure 7.27, 7.28 show the ratios for the away-side yield ratio of out-of-plane/in-plane and mid-plane/in-plane.

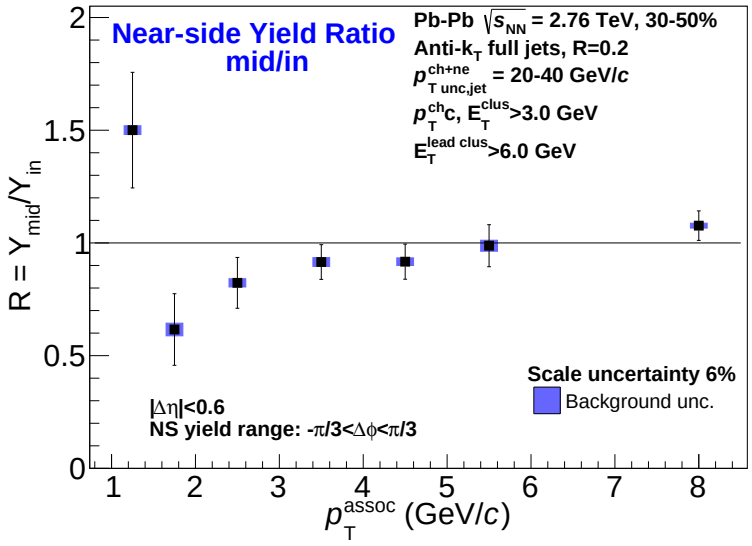

Figure 7.26: Near-side jet yield vs p_T^{assoc} for 20-40 GeV/c full jets in 30-50% centrality collisions. The grey bands are the systematic uncertainties of the background fits, the errors are non-trivially correlated point-to-point. The colored bands are the scale uncertainties from the mixed events. There is an additional 6% global scale uncertainty.

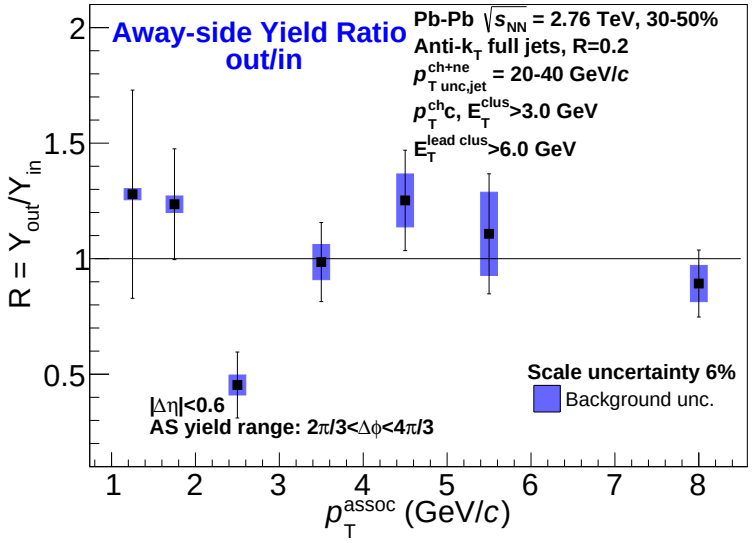

Figure 7.27: Near-side jet yield vs p_T^{assoc} for 20-40 GeV/c full jets in 30-50% centrality collisions. The grey bands are the systematic uncertainties of the background fits, the errors are non-trivially correlated point-to-point. The colored bands are the scale uncertainties from the mixed events. There is an additional 6% global scale uncertainty.

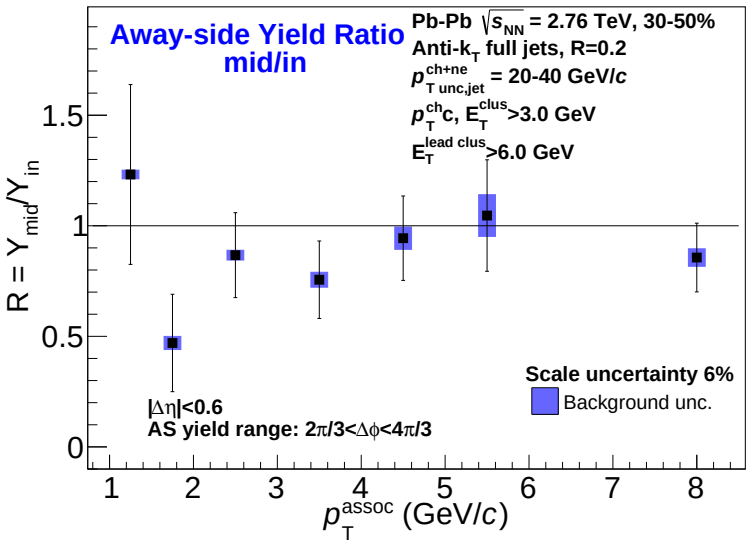

Figure 7.28: Near-side jet yield vs p_T^{assoc} for 20-40 GeV/c full jets in 30-50% centrality collisions. The grey bands are the systematic uncertainties of the background fits, the errors are non-trivially correlated point-to-point. The colored bands are the scale uncertainties from the mixed events. There is an additional 6% global scale uncertainty.

Chapter 8

Conclusion and outlook

This chapter will discuss the various biases involved in these measurements and the implications they may have on the results. Interpretation of the results and outlook moving forward will be discussed. Because this analysis does not have a reference in pp collisions, statements cannot be made at this time about modifications relative to correlations in pp collisions.

8.1 Discussion

There are various potential biases involved when making a jet measurement in a heavy-ion collision. The exact implications, as of yet, are unknown, but should be considered as a factor when interpreting the data. In order to reduce the contribution that the background has on the reconstructed jet, constituents tracks and clusters greater than 3.0 GeV/c are used in this analysis. In addition, there is a threshold requirement that the jet contains a cluster that is matched to a firing trigger patch in the EMCal and that for 30-50% centrality has an $E_T > 6$ GeV and for 0-10% centrality has an $E_T > 10.0$ GeV. This matched cluster imposes a survivor bias on the jet candidates being studied. The requirement of a highly energetic cluster biases the jet candidate to have originated from the initial hard-scattering. Quark jets are generally harder and more collimated then gluon jets [183]. This generally results in

quark jets meeting the trigger threshold more easily then gluon jets. In the RHIC kinematic range, the parton type bias of triggering on a quark translates into the away-side parton being a gluon [183].

It was shown by [183] that imposing a leading track or cluster requirement or increasing the constituent cut of a reconstructed jet can lead to surface bias. This effects the trigger jet on the near-side. This can create a systematic offset between the experiment jet energy and the underlying parton energy [183]. For this measurement, we are not as concerned with a potential surface bias because the goal is to determine the path length dependence and thus the away-side serves as a viable measurement to explore this.

There is no clear event plane dependence within the current uncertainties on the yields across the studied p_T^{assoc} range of 0.5-10.0 GeV/c. The near-side can be hard to interpret due to the autocorrelation occuring above 3.0 GeV/c from particles included in the jet-finding. The flow has been subtracted from the correlations, so any remaining effects should be based on path length dependence or in-medium interactions.

The effects seen in the jet-hadron correlations relative to the event plane using the RPF method indicate that medium-induced modifications to the associated particles of a jet are much more subtle than prior results which used the ZYAM background subtraction and neglected odd v_n terms [184]. There are competing effects happening across the studied p_T^{assoc} range. The effects include, but are not limited to gluon bremsstrahlung and jet quenching. The yield is expected to decrease going from in-plane to out-of-plane from the effect of quenching. However, gluon radiation would cause the yield to increase from in-plane to out-of-plane at low p_T. Any combination of these effects could end up canceling out each other.

When the ratio was taken of the out-of-plane to in-plane and mid-plane to in-plane yields in Fig. 7.25 and 7.26, it was seen that there was an enhancement both out-of-plane and mid-plane relative to in-plane at low p_T^{assoc}, although the effect is only 2

sigma. This can be explained by the additional induced gluon radiation that out-of-plane and mid-plane jets will experience relative to in-plane jets. This occurs due to the longer path-length traversed by jets that are not in-plane. This is seen on both the near-side and away-side. The effect is more pronounced on the near-side. More soft particles are seen due to more potential interactions with the medium. ALICE is well suited to perform PID and make precision tracking measurements [147] in this low transverse momentum region, an interesting direction for future studies considering theories which propose that the hadronization mechanism may be different in the medium. Deviations of the yield ratios from 1.0 are not statistically significant on the away-side. A suppression is seen in-plane relative to both mid-plane and out-of plane on both the near-side and the away-side. It occurs for p_T^{assoc}=2.0-3.0 GeV/c for out/in, but shifts down to p_T^{assoc}=1.5-2.0 GeV/c for mid/in. The suppression in-plane to both out-of-plane and mid-plane is roughly $\sim$ 0.5. The suppression is expected to occur at a higher momentum fraction, z, of the jet. On the away-side, the effects are favoring a redistribution of energy. However, the away-side measurement is not sensitive enough to the potential effects because the uncertainties associated with the result are dominated by statistics.

With the current statistics, the yields and yield ratios show that the path length dependence of the energy loss is a secondary effect relative to statistical and energy loss fluctuations in the medium because there is no significant deviations of the ratios from 1.0. This is also seen in a di-jet asymmetry measurement relative to the event plane [185]. They reported that not only energy loss fluctuations, but also hard fluctuations which did not arise from jet-medium interactions played a more important role than path length dependence [185].

There is ongoing work on understanding the jet energy scale quantitatively so that preparation of an appropriate reference from pp collisions can be done. Because the final results are statistically limited, much more precise measurements can be performed on future datasets. At this point the significant improvement of the precision of the measurement using the improved background subtraction method is

demonstrated by these plots. Even in the 0-10% most central events, the uncertainties are not unreasonable considering how poor the event plane resolution is. The lack of event plane dependence was seen in jet-hadron and h-h correlations by [174]. Another possible explanation is the decorrelation between high/low p_T event planes [186].

8.2 Outlook

A currently proposed study is to create an analog to the energy balance observable in Eqn. 3.12 by defining a similar observable as in Eqn. 8.1:

$$D_{AA}^{EP}(p_T^{assoc}) = Y_{PbPb}^{out}(p_T^{assoc}) \times \langle p_T^{assoc} \rangle - Y_{PbPb}^{in}(p_T^{assoc}) \times \langle p_T^{assoc} \rangle. \tag{8.1}$$

Here, Y_{PbPb}^{out} (Y_{PbPb}^{in}) correspond to the out-of-plane (in-plane) yields from Pb–Pb collisions taken in a given p_T^{assoc} bin with average transverse momentum given by $\langle p_T^{assoc} \rangle$. The study would look at the p_T^{assoc} dependence to see where the energy lost at high-p_T^{assoc} goes.

Studies of performing particle identification (PID) on the associated hadrons within the jet-hadron correlations has already been underway. The goal is to conduct a measurement of the particle ratio in and out of the jets. Answering the question "Is enhancement in p/π ratio correlated with jet production?" can be answered by identifying associated hadrons. Theoretical predictions of modified fragmentation functions in heavy-ion collisions [187] predict that jet which fragment in the medium as opposed to the vacuum may have a higher production of baryons and strange particles.

Bibliography

[1] B. Abelev *et al.*, "Measurement of Event Background Fluctuations for Charged Particle Jet Reconstruction in Pb-Pb collisions at $\sqrt{s_{NN}} = 2.76$ TeV," *JHEP*, vol. 1203, p. 053, 2012. xii, 69

[2] N. Serra, "Standard Model," 2015 (accessed June 21, 2016). http://www.physik.uzh.ch/groups/serra/StandardModel.html. 2

[3] E. Drexler, "Summary of interactions betweeen particles described by the Standard Model.," 2014 (accessed June 23, 2016). https://commons.wikimedia.org/w/index.php?curid=32230766. 2, 3

[4] D. J. Griffiths, *Introduction to elementary particles; 2nd rev. version*. Physics textbook, New York, NY: Wiley, 2008. 3

[5] "A Modern Indroduction to Nuclear Physics," 201X (accessed June 23, 2016). http://www.physics.umd.edu/courses/Phys741/xji/chapter1.pdf. 4, 5

[6] H. D. Politzer, "Reliable perturbative results for strong interactions?," *Phys. Rev. Lett.*, vol. 30, pp. 1346–1349, Jun 1973. 4

[7] D. J. Gross and F. Wilczek, "Ultraviolet behavior of non-abelian gauge theories," *Phys. Rev. Lett.*, vol. 30, pp. 1343–1346, Jun 1973. 4

[8] B. Z. Kopeliovich and A. H. Rezaeian, "Applied High Energy QCD," *Int. J. Mod. Phys.*, vol. E18, pp. 1629–1696, 2009. [,51(2008)]. 4, 5

[9] "String Theory," 201X (accessed June 24, 2016). https://www.learner.org/courses/physics/unit/text.html?unit=4&secNum=3. 5, 6

[10] F. L. H. Wolfs, "Evolution of the universe." University Lecture, 1999. 6

[11] "Duke physics." https://www.phy.duke.edu/research/NPTheory/QGP/index.php, 2012. Visited January 2013. 6

[12] E. Shuryak, "A "little bang" arrives at the lhc," *Physics*, vol. 3, p. 105, Dec 2010. 6

[13] C. Nattrass, "The little bang: understanding the quark gluon plasma." Colorado State University Colloquium Lecture, November 2012. 7, 12, 13

[14] H. Caines, "The RHIC Beam Energy Scan: STAR'S Perspective," pp. 375–378, 2009. 7

[15] J. Adam *et al.*, "Direct photon production in Pb-Pb collisions at $\sqrt{s_{NN}} = 2.76$ TeV," *Phys. Lett.*, vol. B754, pp. 235–248, 2016. 7, 22

[16] N. Cabibbo and G. Parisi, "Exponential hadronic spectrum and quark liberation," *Physics Letters B*, vol. 59, no. 1, pp. 67 – 69, 1975. 8

[17] E. M. Richardson, *Elliptic flow at forward rapidity in* $\sqrt{s_{NN}} = 200$ *GeV Au+Au collisions*. PhD thesis, Maryland U., 2012. 8

[18] A. Bazavov *et al.*, "Equation of state in (2+1)-flavor QCD," *Phys. Rev.*, vol. D90, p. 094503, 2014. 8

[19] F. Karsch, *Lattice QCD at High Temperature and Density*, pp. 209–249. Berlin, Heidelberg: Springer Berlin Heidelberg, 2002. 8

[20] C. Nonaka and M. Asakawa, "Modeling a Realistic Dynamical Model for High Energy Heavy Ion Collisions," *PTEP*, vol. 2012, p. 01A208, 2012. 8, 9

[21] M. Verweij, *Modelling and measurement of jet quenching in relativistic heavy-ion collisions at the LHC*. Phd dissertation, Utrecht University, 2013. 8, 9

[22] R. Thomas, *Energy Loss of Quarks by Gluon Radiation in Deconfined Matter*. PhD thesis, Technical University of Dresden, November 2003. 8

[23] H. A. Grunder, C. W. Leemann, and F. B. Selph, "Relativistic Heavy Ion Accelerators," in *Proceedings, 10th International Conference on High-Energy*

Accelerators, HEACC 1977, v.1-2: Protvino, USSR, July 11–17, 1977, pp. 321–338, 1977. 11

[24] G. Baym, "RHIC: From dreams to beams in two decades," *Nucl. Phys.*, vol. A698, pp. XXIII–XXXII, 2002. 11

[25] J. Klein, *Jet Physics with A Large Ion Collider Experiement at the Large Hadron Collider*. PhD thesis, Ruperto-Carola University of Heidelberg, 2014. 11

[26] C. Nattrass, *System, energy, and flavor dependence of jets through di-hadron correlations in heavy-ion collisions*. PhD thesis, Yale University, December 2009. 11, 22, 23, 30, 32

[27] K. Adcox *et al.*, "Formation of dense partonic matter in relativistic nucleus-nucleus collisions at RHIC: Experimental evaluation by the PHENIX collaboration," *Nucl. Phys.*, vol. A757, pp. 184–283, 2005. 12, 14, 15

[28] J. Adams *et al.*, "Experimental and theoretical challenges in the search for the quark gluon plasma: The STAR collaboration's critical assessment of the evidence from RHIC collisions," *Nucl. Phys.*, vol. A757, pp. 102–183, 2005. 12

[29] B. B. Back *et al.*, "The PHOBOS perspective on discoveries at RHIC," *Nucl. Phys.*, vol. A757, pp. 28–101, 2005. 12

[30] I. Arsene *et al.*, "Quark Gluon Plasma an Color Glass Condensate at RHIC? The perspective from the BRAHMS experiment," *Nucl. Phys.*, vol. A757, pp. 1–27, 2005. 12

[31] R. Snellings, "Elliptic Flow: A Brief Review," *New J.Phys.*, vol. 13, p. 055008, 2011. 12, 13, 14

[32] "Taking a closer look at LHC - detectors." http://www.lhc-closer.es/php/index.php?i=1&s=5&p=8&e=0, 2010. Visited January 2013. 12

[33] I. P. Lokhtin, L. V. Malinina, S. V. Petrushanko, A. M. Snigirev, I. Arsene, and K. Tywoniuk, "HYDJET++ heavy ion event generator and its applications for RHIC and LHC," *PoS*, vol. High-pT physics09, p. 023, 2009. 12

[34] K. Aamodt *et al.*, "Elliptic flow of charged particles in Pb-Pb collisions at 2.76 TeV," *Phys.Rev.Lett.*, vol. 105, p. 252302, 2010. 12, 13, 14

[35] M. Leeuwen, "Latest results on heavy ion physics from ALICE." May 2012. 13, 24

[36] R. Vernet, "Soft Probes of the Quark-Gluon Plasma with ALICE at LHC," 2009. 13

[37] A. Taranenko, "PHENIX studies of the scaling properties of elliptic flow at LHC energies." Conference Lecture, November 2006. 13, 15

[38] E. Simili, *Elliptic Flow Measurement at ALICE*. PhD thesis, Utrecht University, June 2008. 13

[39] M. Donadelli, "Overview of ATLAS heavy ions results." Conference Lecture, 2012. 13

[40] A. Zichichi, *How and Where to Go Beyond the Standard Model: Proceedings of the International School of Subnuclear Physics*. Subnuclear series, World Scientific, 2007. 13

[41] R. Yang, "Discovery of quark gluon plasma at rhic," 5 2006. Available at http://guava.physics.uiuc.edu/~nigel/courses/569/Essays_Spring2006/files/yang.pdf. 13

[42] U. Wiedemann, "Heavy ion collisions at RHIC and at the LHC: Physics challenges," in *Particles and Nuclei* (P. D. Barnes *et al.*, eds.), Seventeenth International Conference on Particle and Nuclei, American Institute of Physics, November 2004. 14

[43] M. Elnimr, *Dihadron Fragmentation Functions in Proton Proton Collisions at the Relativistic Heavy Ion Collider (RHIC).* PhD thesis, Wayne State University, 2010. 14

[44] D. T. Son and A. O. Starinets, "Viscosity, Black Holes, and Quantum Field Theory," *Ann. Rev. Nucl. Part. Sci.*, vol. 57, pp. 95–118, 2007. 14

[45] P. K. Kovtun, D. T. Son, and A. O. Starinets, "Viscosity in strongly interacting quantum field theories from black hole physics," *Phys. Rev. Lett.*, vol. 94, p. 111601, Mar 2005. 14

[46] P. Genzer and K. Walsh, "Tiny drops of early universe 'perfect' fluid." Newsroom: Media and Communications Office, 2015. 15

[47] W. A. Zajc, "AdS/CFT intersects nuclear beams at columbia." University Lecture, October 2007. 15

[48] M. Nasim, L. Kumar, P. K. Netrakanti, and B. Mohanty, "Energy dependence of elliptic flow from heavy-ion collision models," *Phys.Rev.*, vol. C82, p. 054908, 2010. 15

[49] A. Adare *et al.*, "Deviation from quark-number scaling of the anisotropy parameter v_2 of pions, kaons, and protons in Au+Au collisions at $\sqrt{s_{NN}} = 200$ GeV," *Phys. Rev.*, vol. C85, p. 064914, 2012. 15

[50] M. Veldhoen, "p/pi Ratio in Di-Hadron Correlations," 2012. 16

[51] A. O. Velasquez, "p/π ratio, Pb-Pb and pp at 7 tev." https://aliceinfo.cern.ch/Figure/node/3603, August 2012. Visited January 2013. 16

[52] J. Rafelski, "Strangeness production and quark gluon plasma properties." Conference Lecture, September 2011. 16

[53] G. T. Sanchez, "Some aspects on hadronization by dynamical quark recombination." Workshop Lecture, April 2011. 16

[54] B. Hippolyte, "Bulk matter physics and its future at the Large Hadron Collider," *Eur. Phys. J.*, vol. C62, pp. 237–242, 2009. 16, 17

[55] J. Adam *et al.*, "Measurement of transverse energy at midrapidity in Pb-Pb collisions at $\sqrt{s_{\rm NN}} = 2.76$ TeV," 2016. 17, 18, 19

[56] J. D. Bjorken, "Highly relativistic nucleus-nucleus collisions: The central rapidity region," *Phys. Rev. D*, vol. 27, pp. 140–151, Jan 1983. 18, 19

[57] Y. Akiba, "Quest for the quark gluon plasma hard and electromagnetic probes," *Progress of Theoretical and Experimental Physics*, vol. 2015, no. 3, 2015. 19, 20, 22

[58] E. L. Bratkovskaya, O. Linnyk, and W. Cassing, "Electromagnetic probes of the QGP," *EPJ Web Conf.*, vol. 95, p. 01002, 2015. 20

[59] M. M. Aggarwal *et al.*, "Observation of direct photons in central 158-A-GeV Pb-208 + Pb-208 collisions," *Phys. Rev. Lett.*, vol. 85, pp. 3595–3599, 2000. 20

[60] S. S. Adler *et al.*, "Mid-rapidity direct-photon production in p^+p collisions at $\sqrt{s} = 200$-GeV," *Phys. Rev.*, vol. D71, p. 071102, 2005. 20

[61] I. Tserruya, "Photons and low-mass dileptons: results from PHENIX," *Nucl. Phys.*, vol. A904-905, pp. 225c–232c, 2013. 20, 21, 22

[62] S. Chatrchyan *et al.*, "Measurement of isolated photon production in *pp* and PbPb collisions at $\sqrt{s_{NN}} = 2.76$ TeV," *Phys. Lett.*, vol. B710, pp. 256–277, 2012. 20

[63] G. David, "Direct Photons at RHIC," in *Proceedings, 34th International Conference on High Energy Physics (ICHEP 2008)*, 2008. 20

[64] A. Adare *et al.*, "Enhanced production of direct photons in Au+Au collisions at $\sqrt{s_{NN}} = 200$ GeV and implications for the initial temperature," *Phys. Rev. Lett.*, vol. 104, p. 132301, 2010. 20, 22

[65] A. Monnai, *Relativistic Dissipative Hydrodynamic Description of the Quark-Gluon Plasma*. Springer Theses, Springer Japan, 2014. 20

[66] P. Sorensen, "Highlights from Heavy Ion Collisions at RHIC and the Acoustics of the Little Bangs," 2012. 22

[67] S. Turbide, R. Rapp, and C. Gale, "Hadronic production of thermal photons," *Phys. Rev.*, vol. C69, p. 014903, 2004. 22

[68] R. Arnaldi, "Hard probes (experiment)." University Lecture, March 2011. 22, 23, 24

[69] M. Elnimr, *Dihadron Fragmentation Functions in Proton Proton Collisions at the Relativistic Heavy Ion Collider*. PhD thesis, Wayne State University, 2010. 22

[70] J. Schaffner-Bielich, *Relativistic Heavy Ion Physics*, vol. 23 of *Landolt-Bornstein: Numerical Data and Functional Relationships in Science and Technology - New Series*. Springer Berlin Heidelberg, 2010. 22, 23, 30, 31

[71] C. Klein-Bosing, "Jet reconstruction and jet background classification with the ALICE experiment in PbPb collisions at the LHC," *J.Phys.*, vol. G38, p. 124088, 2011. 22, 23

[72] J. Casalderrey-Solana and C. A. Salgado, "Introductory lectures on jet quenching in heavy ion collisions," *Acta Phys. Polon.*, vol. B38, pp. 3731–3794, 2007. 23

[73] C. A. Salgado, "Heavy ions theory review," *Acta Phys.Polon.*, vol. B38, pp. 975–986, 2007. 24, 32

[74] M. van Leeuwen, "High-p_T results from ALICE," 2012. 24, 25

[75] A. Adare *et al.*, "Nuclear-Modification Factor for Open-Heavy-Flavor Production at Forward Rapidity in Cu+Cu Collisions at $\sqrt{s_{NN}}$ = 200 GeV," *Phys.Rev.*, vol. C86, p. 024909, 2012. 24

[76] A. Morreale, "Production of π^0, $K^{\pm}$ and η mesons in Pb-Pb and pp collisions at $\sqrt{s_{\rm NN}}$ =2.76 TeV measured with the ALICE detector at the LHC," in *16th International Conference on Strangeness in Quark Matter (SQM 2016) Berkeley, California, United States, June 27-July 1, 2016*, 2016. 25

[77] A. Dainese, "Suppression of high-p_T heavy-flavour particles in Pb-Pb collisions at the LHC, measured with the ALICE detector," *PoS*, vol. ICHEP2012, p. 417, 2013. 25

[78] A. Adare *et al.*, "System-size dependence of open-heavy-flavor production in nucleus-nucleus collisions at $\sqrt{s_{NN}}$=200 GeV," *Phys. Rev.*, vol. C90, no. 3, p. 034903, 2014. 25

[79] K. M. Burke *et al.*, "Extracting the jet transport coefficient from jet quenching in high-energy heavy-ion collisions," *Phys.Rev.*, vol. C90, no. 1, p. 014909, 2014. 25

[80] T. Matsui and H. Satz, "J/ψ Suppression by Quark-Gluon Plasma Formation," *Phys. Lett.*, vol. B178, pp. 416–422, 1986. 26

[81] V. Khachatryan *et al.*, "Suppression of $\Upsilon(1S)$, $\Upsilon(2S)$ and $\Upsilon(3S)$ production in PbPb collisions at $\sqrt{s}_{NN}$ = 2.76 TeV," 2016. 26, 27

[82] A. Emerick, X. Zhao, and R. Rapp, "Bottomonia in the Quark-Gluon Plasma and their Production at RHIC and LHC," *Eur. Phys. J.*, vol. A48, p. 72, 2012. 26

[83] S. Chatrchyan *et al.*, "Observation of sequential Upsilon suppression in PbPb collisions," *Phys. Rev. Lett.*, vol. 109, p. 222301, 2012. 26

[84] Y. Liu, C. M. Ko, and T. Song, "Hot medium effects on J/ψ production in $p + Pb$ collisions at $\sqrt{s_{NN}} = 5.02$ TeV," *Phys. Lett.*, vol. B728, pp. 437–442, 2014. 26

[85] A. Mocsy and P. Petreczky, "Color screening melts quarkonium," *Phys. Rev. Lett.*, vol. 99, p. 211602, 2007. 26, 27

[86] A. Mocsy and P. Petreczky, "Quarkonia correlators above deconfinement," *Phys. Rev.*, vol. D73, p. 074007, 2006. 26, 27

[87] K. Perez, "Choice of jet algorithms in atlas." 2009. 29, 32

[88] M. Cacciari, "Recent Progress in Jet Algorithms and Their Impact in Underlying Event Studies," pp. 42–49, 2009. 29, 32

[89] G. P. Salam, "Towards Jetography," *Eur.Phys.J.*, vol. C67, pp. 637–686, 2010. 29

[90] E. Bruna, "Jet analysis in heavy ion collisons." University Lecture, March 2011. 29, 30, 31, 33

[91] M. L. Noriega, "Jet physics in alice.," *European Physical Journal C – Particles & Fields*, vol. 49, no. 1, pp. 315 – 319, 2007. 29, 35, 36, 47

[92] S.-L. Blyth, "Jet Study in Ultra-Relativistic Heavy-Ion Collisions with the ALICE Detectors at the LHC," 2006. 30

[93] M. Stratmann, "Lectures on perturbative QCD or from basic principles to current applications." July 2005. 30, 31

[94] J. C. Collins, D. E. Soper, and G. F. Sterman, "Factorization of Hard Processes in QCD," *Adv.Ser.Direct.High Energy Phys.*, vol. 5, pp. 1–91, 1988. 30, 31

[95] F. Arleo, "(Medium-modified) Fragmentation Functions," *Eur. Phys. J.*, vol. C61, pp. 603–627, 2009. 31

[96] S. Salur, "Searching for Jets in Heavy Ion Collisions," 2008. 32

[97] G. P. Salam, "Infrared safe definition of jet flavour," pp. 391–394, 2006. 33

[98] M. Cacciari, G. P. Salam, and G. Soyez, "The anti- k t jet clustering algorithm," *Journal of High Energy Physics*, vol. 2008, no. 04, p. 063, 2008. 33

[99] Y. L. Dokshitzer, G. D. Leder, S. Moretti, and B. R. Webber, "Better jet clustering algorithms," *JHEP*, vol. 08, p. 001, 1997. 33

[100] M. Cacciari, G. P. Salam, and G. Soyez, "The Anti-k(t) jet clustering algorithm," *JHEP*, vol. 04, p. 063, 2008. 33

[101] D. Watanabe, *Measurements of π^0-jet correlations in $\sqrt{s}$=7 TeV pp collisions and in $\sqrt{s_{NN}}$ = 2.76 TeV central Pb–Pb collisions at ALICE experiment.* PhD thesis, University of Tsukuba, 2016. 34

[102] I. P. Lokhtin and A. M. Snigirev, "A Model of jet quenching in ultrarelativistic heavy ion collisions and high-p(T) hadron spectra at RHIC," *Eur. Phys. J.*, vol. C45, pp. 211–217, 2006. 34

[103] M. S. Daughertiy, *Two-particle correlations in ultra-relativistic heavy ion collisions.* PhD thesis, University of Texas-Austin, 2008. 35

[104] I. P. Lokhtin, A. A. Alkin, and A. M. Snigirev, "On jet structure in heavy ion collisions," *Eur. Phys. J.*, vol. C75, no. 9, p. 452, 2015. 35

[105] S. Chatrchyan *et al.*, "Modification of jet shapes in PbPb collisions at $\sqrt{s_{NN}}$ = 2.76 TeV," *Phys. Lett.*, vol. B730, pp. 243–263, 2014. 35

[106] A. Angerami, "Measurements of Jet Suppression with ATLAS," 2012. 36, 37

[107] M. Spousta, "Jet Reconstruction and Jet Quenching in Heavy Ion Collisions at ATLAS," 2011. 36, 38, 39

[108] M. Spousta, "Jets in ATLAS." Quark Matter Lecture, August 2012. 36

[109] S. Chatrchyan *et al.*, "Observation and studies of jet quenching in PbPb collisions at nucleon-nucleon center-of-mass energy = 2.76 TeV," *Phys. Rev.*, vol. C84, p. 024906, 2011. 38

[110] L. Adamczyk *et al.*, "Di-Jet Imbalance Measurements at $\sqrt{s_{NN}} = 200$ GeV at STAR," 2016. 38

[111] S. Chatrchyan *et al.*, "Measurement of jet fragmentation into charged particles in *pp* and PbPb collisions at $\sqrt{s_{NN}} = 2.76$ TeV," *JHEP*, vol. 1210, p. 087, 2012. 38, 40

[112] M. Rybar, "Jets fragmentation and jet properties in $\sqrt{s_{NN}} = 2.76$ TeV PbPb collisions using the ATLAS detector at the LHC." Quark Matter Lecture, August 2012. 39, 40, 41

[113] B. Wosiek, "Recent results for Pb-Pb collisions with the ATLAS detector." Quark Matter Lecture, August 2012. 39, 40

[114] S. Chatrchyan *et al.*, "Measurement of jet fragmentation in pbpb and *pp* collisions at $\sqrt{s_{NN}} = 2.76$ tev," *Phys. Rev. C*, vol. 90, p. 024908, Aug 2014. 40

[115] X.-N. Wang and X. Guo, "Multiple parton scattering in nuclei: parton energy loss," *Nuclear Physics A*, vol. 696, no. 3, pp. 788 – 832, 2001. 40

[116] T. Renk, "Parton shower evolution in a 3d hydrodynamical medium," *Phys. Rev. C*, vol. 78, p. 034908, Sep 2008. 40

[117] T. Renk, "Comparison study of medium-modified qcd shower evolution scenarios," *Phys. Rev. C*, vol. 79, p. 054906, May 2009. 40

[118] N. Armesto, L. Cunqueiro, and C. A. Salgado, "Q-pythia: a medium-modified implementation of final state radiation," *The European Physical Journal C*, vol. 63, no. 4, p. 679, 2009. 40

[119] W.-T. Deng and X.-N. Wang, "Multiple parton scattering in nuclei: Modified dokshitzer-gribov-lipatov-altarelli-parisi (dglap) evolution for fragmentation functions," *Phys. Rev. C*, vol. 81, p. 024902, Feb 2010. 40

[120] L. Adamczyk *et al.*, "Jet-Hadron Correlations in $\sqrt{s_{NN}}$ = 200 GeV Au+Au and p+p Collisions," 2013. 42, 43, 44

[121] M. Connors, "Jet-hadron correlations in pp and pb-pb collisions with alice," *Journal of Physics: Conference Series*, vol. 446, no. 1, p. 012009, 2013. 42, 55, 58, 67

[122] J. Kapitan, "Jet studies with STAR at RHIC: jet algorithms, jet shapes, jets in AA," 2011. 43

[123] V. Khachatryan *et al.*, "Correlations between jets and charged particles in PbPb and pp collisions at $\sqrt{s_{\rm NN}}$ = 2.76 TeV," *JHEP*, vol. 02, p. 156, 2016. 43, 44

[124] V. Khachatryan *et al.*, "Decomposing transverse momentum balance contributions for quenched jets in PbPb collisions at sqrt(s[NN]) = 2.76 TeV," 2016. 44

[125] "LHC machine outreach." http://lhc-machine-outreach.web.cern.ch/lhc-machine-outreach/, 2012. Visited January 2013. 45

[126] "CERN - the LHC experiments." http://public.web.cern.ch/public/en/lhc/LHCExperiments-en.html, 2008. Visited January 2013. 45

[127] "CERN - LHC: Facts and figures." http://public.web.cern.ch/public/en/lhc/Facts-en.html, 2008. Visited January 2013. 45

[128] M. Strassler, "Introduction to the LHC." http://profmattstrassler.com/articles-and-posts/largehadroncolliderfaq/introduction-to-the-large-hadron-collider/, April 2009. Visited January 2013. 45

[129] M. C. Llatas, "New world record, - first pp collisions at 8 TeV." http://cms.web.cern.ch/news/new-world-record-first-pp-collisions-8-tev, April 2012. Visited January 2013. 45

[130] L. portal, "Cern accelerator complex." http://www.stfc.ac.uk/research/particle-physics-and-particle-astrophysics/large-hadron-collider/cern-accelerator-complex/, 2016. 45, 46, 47

[131] C. De Melis, "The CERN accelerator complex. Complexe des accélérateurs du CERN," Jul 2016. General Photo. 46

[132] Science and T. F. Council, "Accleration." http://www.lhcportal.com/Portal/Info/accelerators.htm, 2016. 46, 47

[133] A. Collaboration, "Alice - a large ion collider experiment." http://aliceinfo.cern.ch/Public/Welcome.html, 2008. 47

[134] T. A. Collaboration, K. Aamodt, *et al.*, "The alice experiment at the cern lhc," *Journal of Instrumentation*, vol. 3, no. 08, p. S08002, 2008. 47

[135] P. Christiansen, "High pt identified particle production in ALICE," 2012. 47, 48

[136] "ALICE." http://www.uslhc.us/LHC_Science/Experiments/ALICE, 2008. Visited January 2013. 47

[137] Breskin, Amos and Voss, Rudiger, *The CERN Large Hadron Collider: Accelerator and Experiments*. Geneva: CERN, 2009. 47, 49, 51, 53

[138] T. Bird, "An overview of the ALICE experiment," tech. rep., University of Southhampton, January 2010. 47

[139] C. Guarnaccia, *The Time Of Flight system for A Large Ion Collider Experiement (ALICE) at CERN: a high performance detector for particle identification*. PhD thesis, University of Salerno, 2008. 49

[140] B. Abelev *et al.*, "Measurement of electrons from semileptonic heavy-flavor hadron decays in *pp* collisions at $\sqrt{s}$=7 TeV," *Phys. Rev. D*, vol. 86, p. 112007, Dec 2012. 49, 50

[141] E. Abbas *et al.*, "Performance of the ALICE VZERO system," *JINST*, vol. 8, p. P10016, 2013. 49, 50, 71

[142] P. Cortese *et al.*, "ALICE technical design report on forward detectors: FMD, T0 and V0," 2004. 49, 50

[143] M. L. Miller, K. Reygers, S. J. Sanders, and P. Steinberg, "Glauber modeling in high energy nuclear collisions," *Ann. Rev. Nucl. Part. Sci.*, vol. 57, pp. 205–243, 2007. 50

[144] A. Toia, "Bulk Properties of Pb-Pb collisions at $\sqrt{s_{NN}}$ = 2.76 TeV measured by ALICE," *J. Phys.*, vol. G38, p. 124007, 2011. 51

[145] J. Kral, "Level 0 trigger for ALICE EMCal." https://indico.cern.ch/getFile.py/access?contribId=471&sessionId=65&resId=0&materialId=poster&confId=30248, 2008. Visited January 2013. 51, 53, 57

[146] H. Zhang, "Neutral Pion Production in pp Collisions at $\sqrt{s}$ = 2.76 TeV at the LHC with the ALICE Detector usig the Electromagnetic Calorimeter," Master's thesis, Central China Normal University, China, 2015. 51, 65

[147] U. Abeysekara *et al.*, "ALICE EMCal Physics Performance Report," 2010. 52, 53, 57, 68, 133

[148] G. Bourdaud, "γ-jet physics with the emcal calorimeter of the alice experiment at lhc," 2014 (accessed October 4, 2016). 52

[149] J. Kral, *Intrinsic Transverse Momentum Distribution of Jet Constituents in p-Pb Collisions at ALICE*. PhD thesis, Jyvaskyla U., 2014-07-10. 53, 57, 65

[150] M. Cacciari, G. P. Salam, and G. Soyez, "FastJet User Manual," *Eur.Phys.J.*, vol. C72, p. 1896, 2012. 54, 67, 68

[151] N. Sharma, J. Mazer, M. Stuart, and C. Nattrass, "Background subtraction methods for precision measurements of di-hadron and jet-hadron correlations in heavy ion collisions," *Phys. Rev.*, vol. C93, no. 4, p. 044915, 2016. 56, 76, 86, 87, 88, 89, 90, 91, 92, 93

[152] J. Adam *et al.*, "Measurement of jet suppression in central Pb-Pb collisions at $\sqrt{s_{\rm NN}} = 2.76$ TeV," *Phys. Lett.*, vol. B746, pp. 1–14, 2015. 57, 58, 65, 66, 67, 68

[153] B. Abelev *et al.*, "Centrality determination of Pb-Pb collisions at $\sqrt{s_{NN}} = 2.76$ TeV with ALICE," *Phys.Rev.*, vol. C88, no. 4, p. 044909, 2013. 57

[154] R. Ma, "QA: Charged Tracks," 2012 (accessed April 15, 2016). https://twiki.cern.ch/twiki/bin/view/Main/QA:ChargedTracks. 58

[155] M. V. Leeuwen, "Hybrid Tracks," 2015 (accessed April 15, 2016). https://twiki.cern.ch/twiki/bin/view/ALICE/HybridTracks. 58

[156] M. Gyulassy and X.-N. Wang, "HIJING 1.0: A Monte Carlo program for parton and particle production in high-energy hadronic and nuclear collisions," *Comput. Phys. Commun.*, vol. 83, p. 307, 1994. 60

[157] J. Andreeva, P. Dhara, A. D. Girolamo, A. Kakkar, M. Litmaath, N. Magini, G. Negri, S. Ramachandran, S. Roiser, P. Saiz, M. D. S. Santos, B. Sarkar, J. Schovancova, A. Sciabà, and A. Wakankar, "New solutions for large scale functional tests in the wlcg infrastructure with sam/nagios: the experiments experience," *Journal of Physics: Conference Series*, vol. 396, no. 3, p. 032100, 2012. 61

[158] J. Adam *et al.*, "Jet-like correlations with neutral pion triggers in pp and central Pb–Pb collisions at 2.76 TeV," *Phys. Lett.*, vol. B763, pp. 238–250, 2016. 65

[159] B. Abelev *et al.*, "Measurement of the inclusive differential jet cross section in *pp* collisions at $\sqrt{s} = 2.76$ TeV," *Phys. Lett.*, vol. B722, pp. 262–272, 2013. 65, 66

[160] B. Abelev *et al.*, "Measurement of charged jet suppression in Pb-Pb collisions at $\sqrt{s_{NN}} = 2.76$ TeV," *JHEP*, vol. 1403, p. 013, 2014. 65, 68

[161] A. M. Poskanzer and S. Voloshin, "Methods for analyzing anisotropic flow in relativistic nuclear collisions," *Phys.Rev.*, vol. C58, pp. 1671–1678, 1998. 70, 71, 72

[162] R. Bertens, "Azimuthal anisotropy of R=0.2 charged jet production in $\sqrt{s_{NN}}$=2.76 TeV Pb–Pb collisions," September 2015. Internal ALICE Analysis Note ANA-2014-1539, https://aliceinfo.cern.ch/Notes/node/297. 71

[163] J. Barrette *et al.*, "Energy and charged particle flow in a 10.8-A/GeV/c Au + Au collisions," *Phys.Rev.*, vol. C55, pp. 1420–1430, 1997. 72

[164] J. Adam *et al.*, "Azimuthal anisotropy of charged jet production in $\sqrt{s_{\rm NN}} =$ 2.76 TeV Pb-Pb collisions," *Phys. Lett.*, vol. B753, pp. 511–525, 2016. 73, 89, 95, 96

[165] B. B. Abelev *et al.*, "Performance of the ALICE Experiment at the CERN LHC," *Int. J. Mod. Phys.*, vol. A29, p. 1430044, 2014. 73, 74

[166] Z. Qiu and U. Heinz, "Hydrodynamic event-plane correlations in Pb+Pb collisions at $\sqrt{s} = 2.76$ATeV," *Phys. Lett.*, vol. B717, pp. 261–265, 2012. 74

[167] J. Qian and U. Heinz, "Hydrodynamic flow amplitude correlations in event-by-event fluctuating heavy-ion collisions," *Phys. Rev.*, vol. C94, no. 2, p. 024910, 2016. 74

[168] G. Aad *et al.*, "Measurement of event-plane correlations in $\sqrt{s_{NN}} = 2.76$ TeV lead-lead collisions with the ATLAS detector," *Phys. Rev.*, vol. C90, no. 2, p. 024905, 2014. 74

[169] H. Pei, I. S. U. Physics, and Astronomy, *A Study of Jet Energy Loss in Heavy-ion Collisions at PHENIX-RHIC, Via 2-particle and "2+1" Correlations, and Future Upgrade*. Iowa State University, 2008. 80

[170] J. F. Grosse-Oetringhaus, M. Kofarago, and A. Morsch, "Jet-like near-side peak shapes," January 2016. Internal ALICE Analysis Note ANA-56, https://aliceinfo.cern.ch/Notes/node/33. 80

[171] J. Bielcikova, S. Esumi, K. Filimonov, S. Voloshin, and J. Wurm, "Elliptic flow contribution to two particle correlations at different orientations to the reaction plane," *Phys.Rev.*, vol. C69, p. 021901, 2004. 86, 87, 92

[172] S. Voloshin and Y. Zhang, "Flow study in relativistic nuclear collisions by Fourier expansion of Azimuthal particle distributions," *Z.Phys.*, vol. C70, pp. 665–672, 1996. 87

[173] J. Rak, "Collective hydrodynamic flow in the qgp," 2015. http://puma.uio.no/trine/ALICE-Oslo/flow_pattern.html. 87

[174] C. Nattrass, N. Sharma, J. Mazer, M. Stuart, and A. Bejnood, "Disappearance of the Mach Cone in heavy ion collisions," *Phys. Rev.*, vol. C94, no. 1, p. 011901, 2016. 87, 88, 93, 134

[175] T. A. Trainor, "Zero yield at minimum (ZYAM) method and v2: Underestimating jet yields from dihadron azimuth correlations," *Phys. Rev.*, vol. C81, p. 014905, 2010. 88

[176] S. S. Adler *et al.*, "Jet structure from dihadron correlations in d+Au collisions at s(NN)**(1/2) = 200-GeV," *Phys. Rev.*, vol. C73, p. 054903, 2006. 88

[177] J. Adams *et al.*, "Direct observation of dijets in central Au + Au collisions at $\sqrt{s_{NN}} = 200$ GeV," *Phys. Rev. Lett.*, vol. 97, p. 162301, Oct 2006. 88

[178] I. Vitev, S. Wicks, and B.-W. Zhang, "A Theory of jet shapes and cross sections: From hadrons to nuclei," *JHEP*, vol. 11, p. 093, 2008. 88

[179] G. Aad *et al.*, "Measurement of the Azimuthal Angle Dependence of Inclusive Jet Yields in Pb+Pb Collisions at $\sqrt{s_{NN}} = 2.76$ TeV with the ATLAS detector," *Phys. Rev. Lett.*, vol. 111, no. 15, p. 152301, 2013. 89

[180] S. Chatrchyan *et al.*, "Studies of azimuthal dihadron correlations in ultra-central PbPb collisions at $\sqrt{s_{NN}} = 2.76$ TeV," *JHEP*, vol. 02, p. 088, 2014. 89

[181] B. Abelev *et al.*, "Anisotropic flow of charged hadrons, pions and (anti-)protons measured at high transverse momentum in Pb-Pb collisions at $\sqrt{s_{NN}}$=2.76 TeV," *Phys. Lett.*, vol. B719, pp. 18–28, 2013. 89, 95, 96

[182] K. Aamodt *et al.*, "Higher harmonic anisotropic flow measurements of charged particles in Pb-Pb collisions at $\sqrt{s_{NN}}$=2.76 TeV," *Phys. Rev. Lett.*, vol. 107, p. 032301, 2011. 89

[183] T. Renk, "Theoretical assessment of jet-hadron correlations," *Phys. Rev.*, vol. C87, no. 2, p. 024905, 2013. 131, 132

[184] H. Agakishiev *et al.*, "Measurements of Dihadron Correlations Relative to the Event Plane in Au+Au Collisions at $\sqrt{s_{NN}} = 200$ GeV," 2010. 132

[185] J. G. Milhano and K. C. Zapp, "Origins of the di-jet asymmetry in heavy ion collisions," *Eur. Phys. J.*, vol. C76, no. 5, p. 288, 2016. 133

[186] J. Jia, "Azimuthal anisotropy in a jet absorption model with fluctuating initial geometry in heavy ion collisions," *Phys. Rev.*, vol. C87, no. 6, p. 061901, 2013. 134

[187] S. Sapeta and U. A. Wiedemann, "Jet hadrochemistry as a characteristics of jet quenching," *Eur. Phys. J.*, vol. C55, pp. 293–302, 2008. 134

Appendix

Appendix A

Results: 30-50% centrality

A.1 Trigger Spectra: 20-40 GeV/c jets

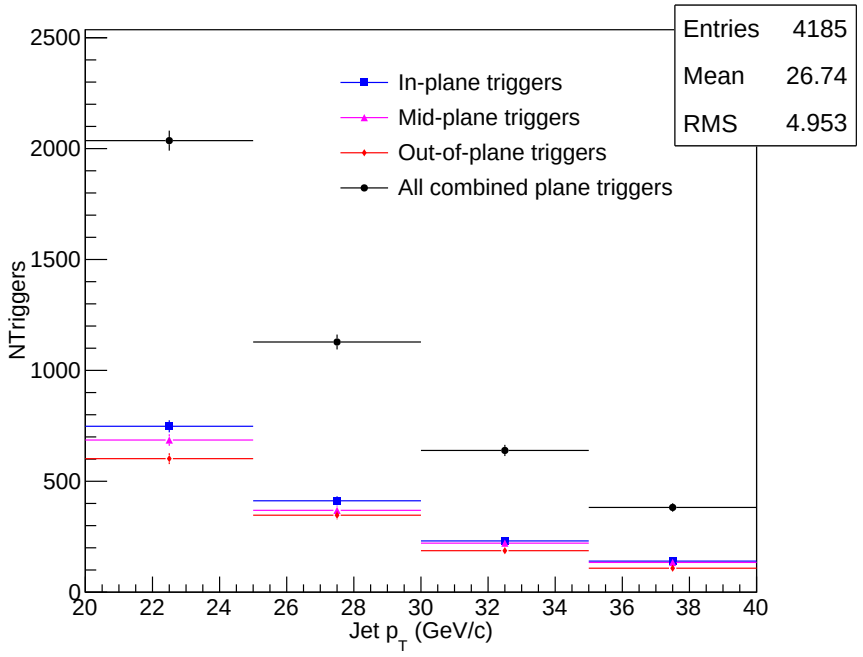

Figure A.1: Jet (triggers) spectra for 20-40 GeV/c jets in 30-50% centrality events. There is a 6 GeV cluster bias requirement and it is made sure the cluster is matched to a firing trigger patch in the EMCal. Comparison for the orientations of the trigger jet relative to the event plane is shown.

A.2 Acceptance corrected and background fit correlations

A.2.1 20-40 GeV/c jets, 30-50% centrality, 0.5-1.0 GeV/c associated hadrons

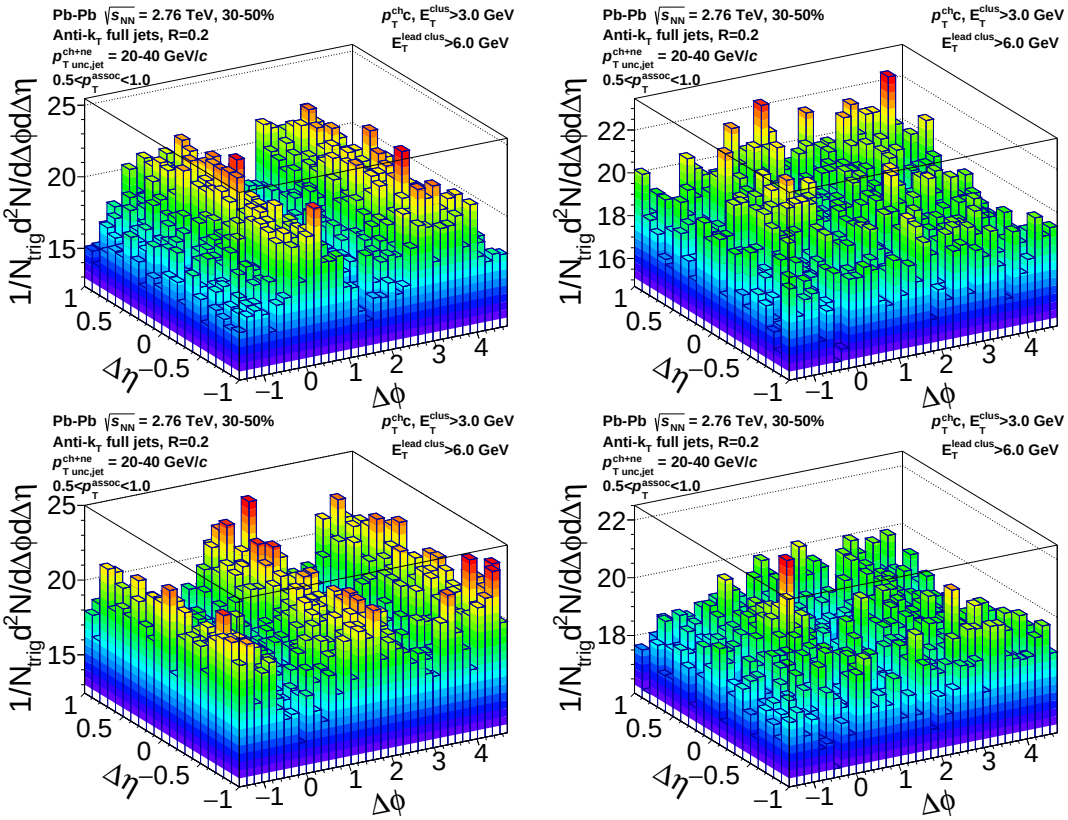

Figure A.2: Raw acceptance corrected correlations from the 30-50% most central events for 20-40 GeV/c full jets, associated hadrons of 0.5-1.0 GeV/c. Top left: in-plane, top right: mid-plane, bottom left: out-of-plane, bottom right: all angles of the trigger jet relative to the event plane.

Table A.1: RPF fit details for Jets 20-40 GeV, associated hadrons 0.5-1.0 GeV, and 30-50% centrality

$\chi^2 = 61.165$ NDF $= 48$ $\chi^2/NDF = 1.274$				
NAME	VALUE		ERROR	% ERROR
B	1.3115e+03	+/-	5.9209e+00	0.451
v_2^{jet}	8.1703e-02	+/-	4.3570e-03	5.333
v_2^{assoc}	1.0381e-01	+/-	6.4176e-03	6.182
v_3^2	-6.6132e-03	+/-	3.2462e-03	49.087
v_4^{jet}	-3.2710e-02	+/-	7.8555e-03	24.015
v_4^{assoc}	5.2227e-03	+/-	6.4330e-02	1231.734

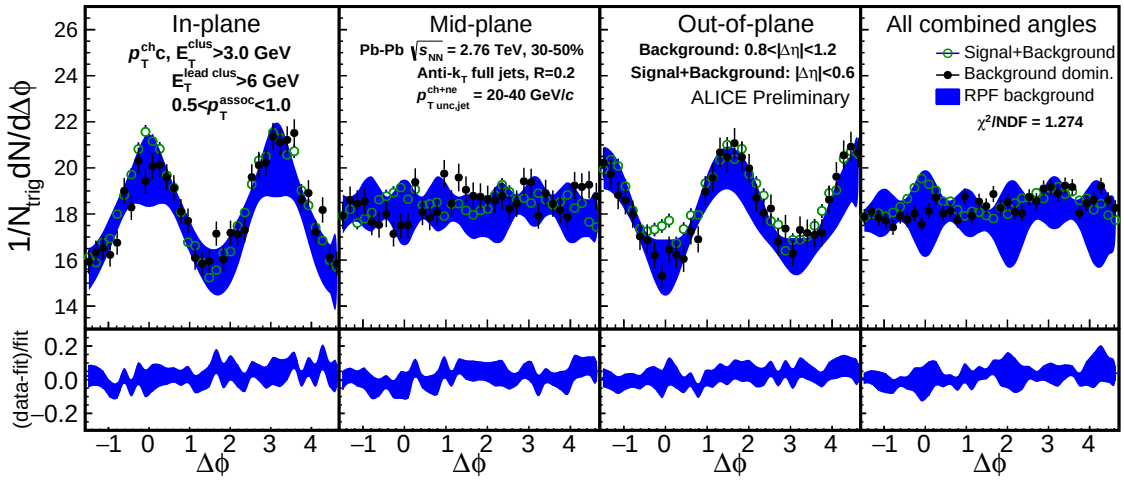

Figure A.3: The signal+background region, $|\Delta\eta| < 0.6$ (green points), background dominated region, $0.8 < |\Delta\eta| < 1.2$ (black points), and the RPF fit (blue band) to the background dominated region for 20-40 GeV/c full jets correlated with 0.5-1.0 GeV/c hadrons from 30-50% centrality collisions on the top panel. The bottom panel shows the quality of the RPF fit to the background dominiated region, (data - fit) / fit.

A.2.2 20-40 GeV/c jets, 30-50% centrality, 1.0-1.5 GeV/c associated hadrons

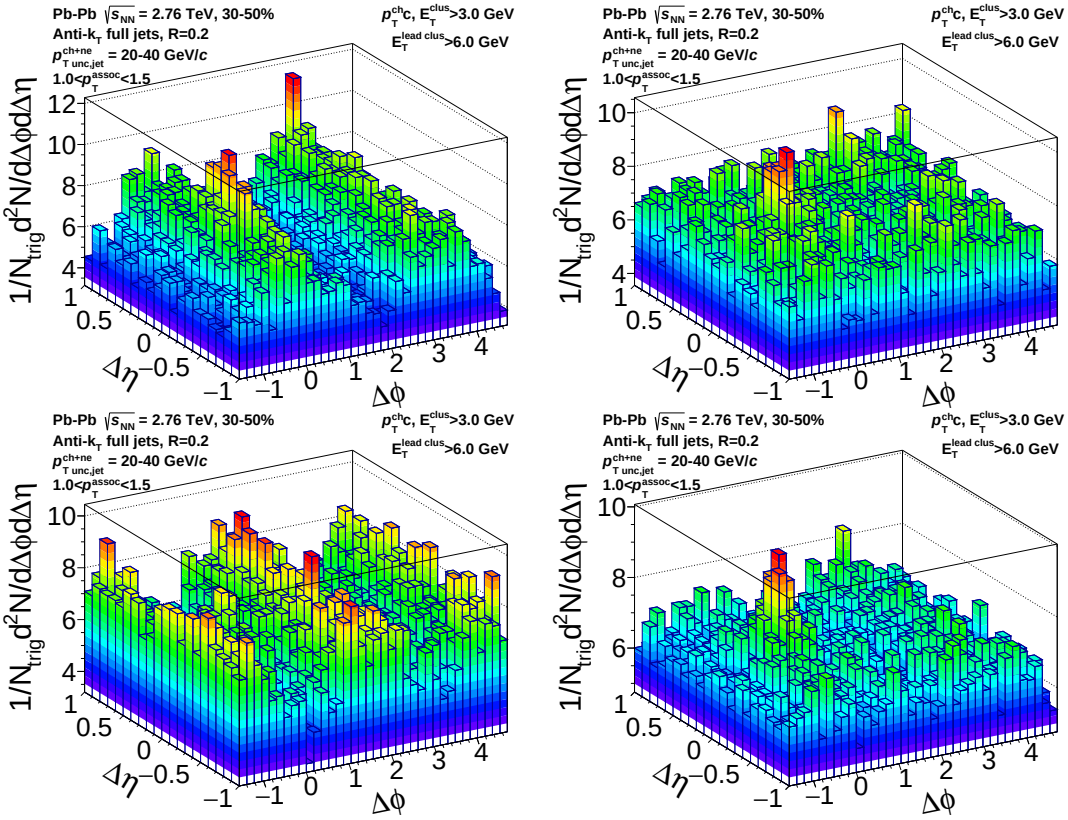

Figure A.4: Raw acceptance corrected correlations from the 30-50% most central events for 20-40 GeV/c full jets, associated hadrons of 1.0-1.5 GeV/c. Top left: in-plane, top right: mid-plane, bottom left: out-of-plane, bottom right: all angles of the trigger jet relative to the event plane.

Table A.2: RPF fit details for Jets 20-40 GeV, associated hadrons 1.0-1.5 GeV, and 30-50% centrality

$\chi^2 = 59.596$ NDF $= 48$ $\chi^2/NDF = 1.242$				
NAME	VALUE		ERROR	% ERROR
B	4.6151e+02	+/-	3.4599e+00	0.750
v_2^{jet}	7.8724e-02	+/-	6.9714e-03	8.856
v_2^{assoc}	1.7371e-01	+/-	1.0355e-02	5.961
v_3^2	-1.3027e-02	+/-	5.3395e-03	40.989
v_4^{jet}	-8.1285e-03	+/-	1.2999e-02	159.923
v_4^{assoc}	3.8967e-02	+/-	1.8743e-02	48.100

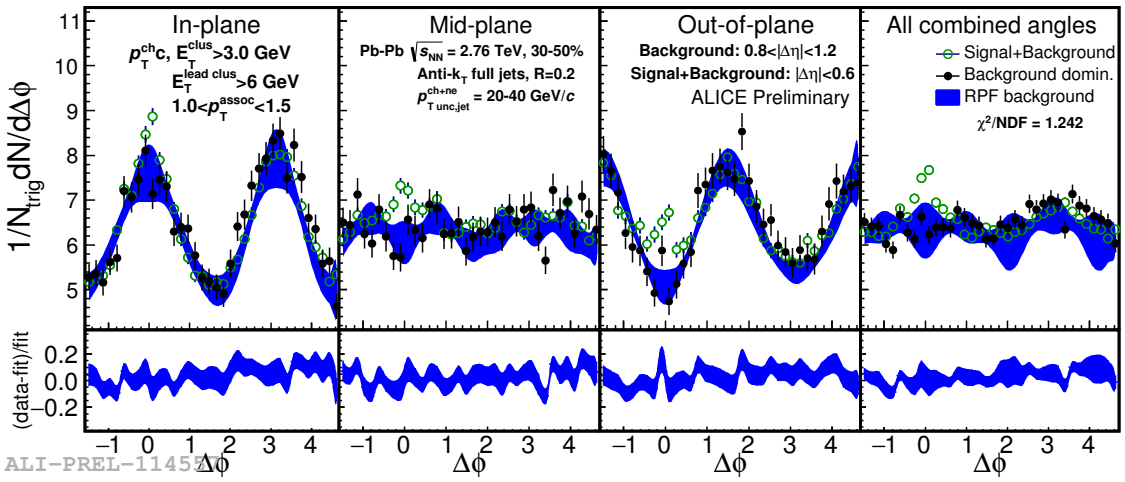

Figure A.5: The signal+background region, $|\Delta\eta| < 0.6$ (green points), background dominated region, $0.8 < |\Delta\eta| < 1.2$ (black points), and the RPF fit (blue band) to the background dominated region for 20-40 GeV/c full jets correlated with 1.0-1.5 GeV/c hadrons from 30-50% centrality collisions on the top panel. The bottom panel shows the quality of the RPF fit to the background dominiated region, (data - fit)/fit.

A.2.3 20-40 GeV/c jets, 30-50% centrality, 1.5-2.0 GeV/c associated hadrons

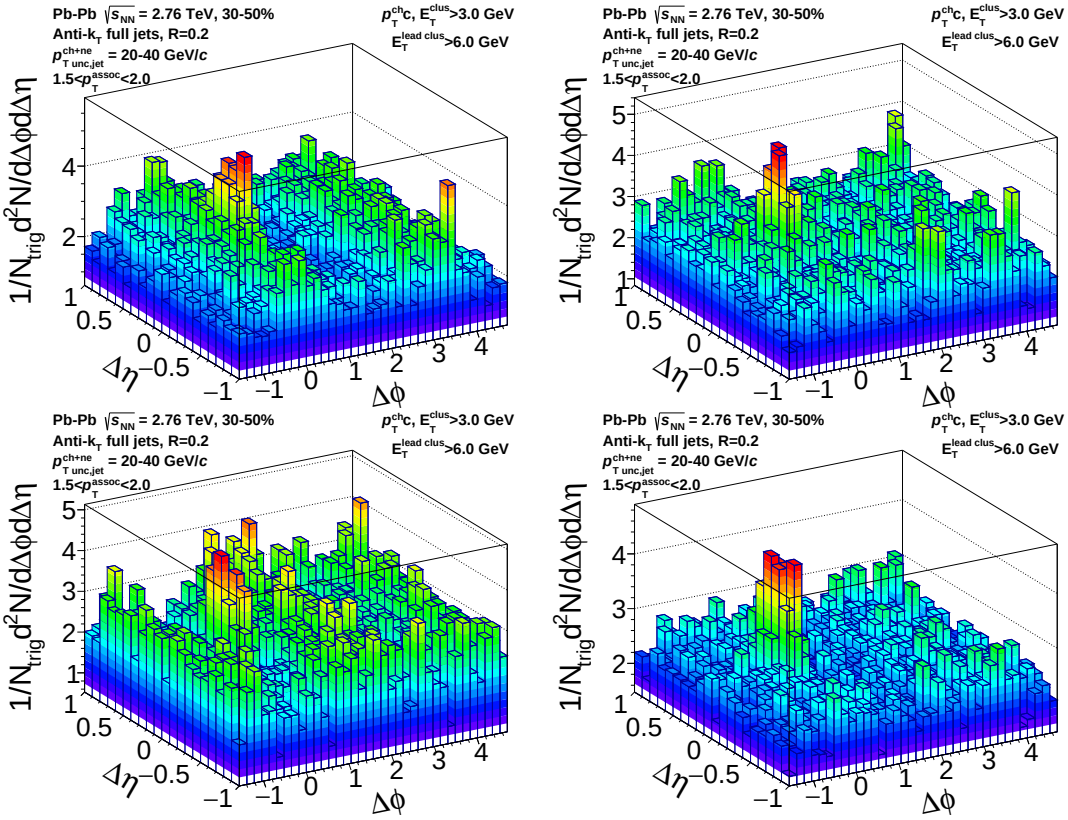

Figure A.6: Raw acceptance corrected correlations from the 30-50% most central events for 20-40 GeV/c full jets, associated hadrons of 1.5-2.0 GeV/c. Top left: in-plane, top right: mid-plane, bottom left: out-of-plane, bottom right: all angles of the trigger jet relative to the event plane.

Table A.3: RPF fit details for Jets 20-40 GeV, associated hadrons 1.5-2.0 GeV, and 30-50% centrality

$\chi^2 = 42.188$ NDF $= 48$ $\chi^2/NDF = 0.879$				
NAME	VALUE		ERROR	% ERROR
B	1.6627e+02	+/-	2.0812e+00	1.252
v_2^{jet}	9.4581e-02	+/-	1.1808e-02	12.484
v_2^{assoc}	1.8430e-01	+/-	1.7015e-02	9.232
v_3^2	1.2367e-02	+/-	8.9790e-03	72.606
v_4^{jet}	-3.2372e-02	+/-	2.3286e-02	71.933
v_4^{assoc}	7.8648e-02	+/-	3.0008e-02	38.154

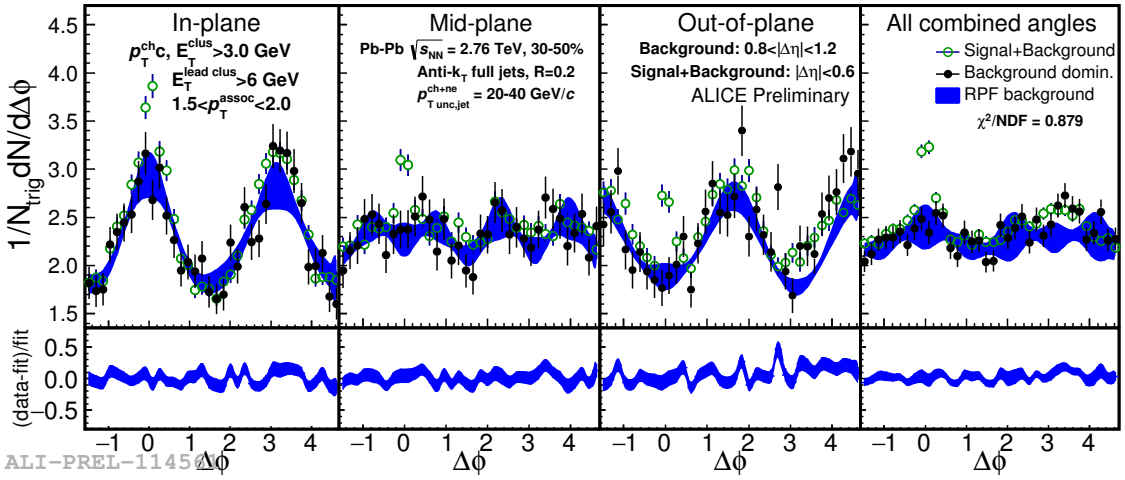

Figure A.7: The signal+background region, $|\Delta\eta| < 0.6$ (green points), background dominated region, $0.8 < |\Delta\eta| < 1.2$ (black points), and the RPF fit (blue band) to the background dominated region for 20-40 GeV/c full jets correlated with 1.5-2.0 GeV/c hadrons from 30-50% centrality collisions on the top panel. The bottom panel shows the quality of the RPF fit to the background dominiated region, (data - fit)/fit.

A.2.4 20-40 GeV/c jets, 30-50% centrality, 2.0-3.0 GeV/c associated hadrons

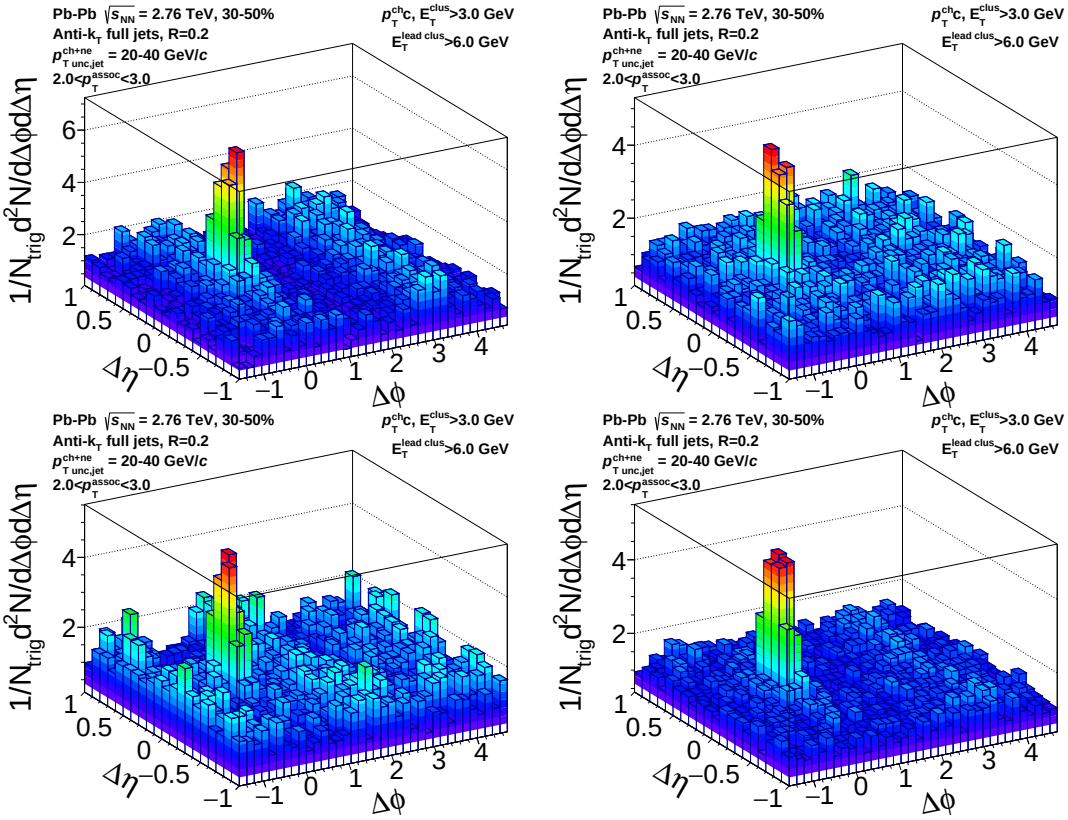

Figure A.8: Raw acceptance corrected correlations from the 30-50% most central events for 20-40 GeV/c full jets, associated hadrons of 2.0-3.0 GeV/c. Top left: in-plane, top right: mid-plane, bottom left: out-of-plane, bottom right: all angles of the trigger jet relative to the event plane.

Table A.4: RPF fit details for Jets 20-40 GeV, associated hadrons 2.0-3.0 GeV, and 30-50% centrality

$\chi^2 = 41.460$ NDF $= 50$ $\chi^2/NDF = 0.829$				
NAME	VALUE		ERROR	% ERROR
B	8.7927e+01	+/-	1.5254e+00	1.735
v_2^{jet}	5.8046e-02	+/-	1.6010e-02	27.582
v_2^{assoc}	2.2431e-01	+/-	2.2469e-02	10.017
v_3^2	-8.7493e-03	+/-	1.2253e-02	140.040

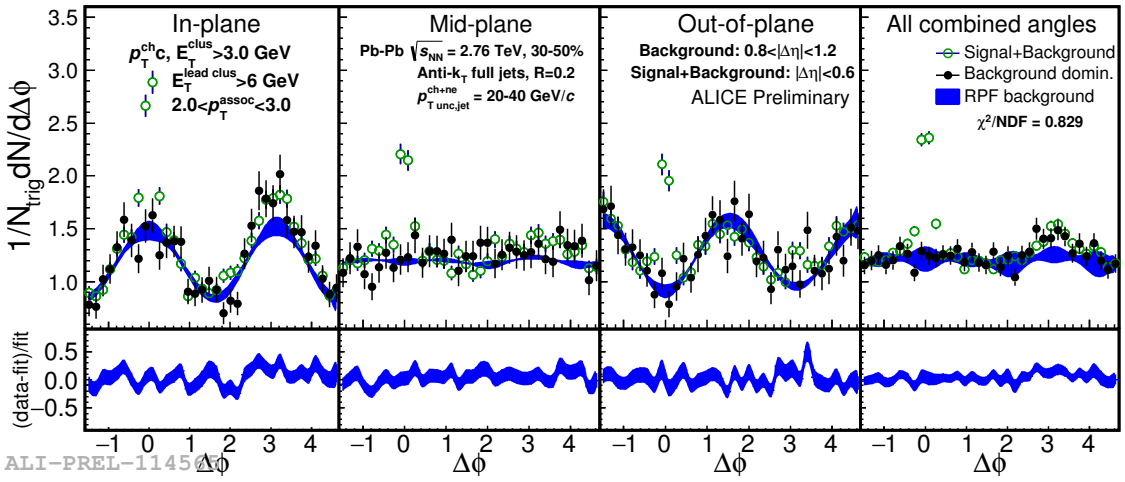

Figure A.9: The signal+background region, $|\Delta\eta| < 0.6$ (green points), background dominated region, $0.8 < |\Delta\eta| < 1.2$ (black points), and the RPF fit (blue band) to the background dominated region for 20-40 GeV/c full jets correlated with 2.0-3.0 GeV/c hadrons from 30-50% centrality collisions on the top panel. The bottom panel shows the quality of the RPF fit to the background dominiated region, (data - fit)/fit.

A.2.5 20-40 GeV/c jets, 30-50% centrality, 3.0-4.0 GeV/c associated hadrons

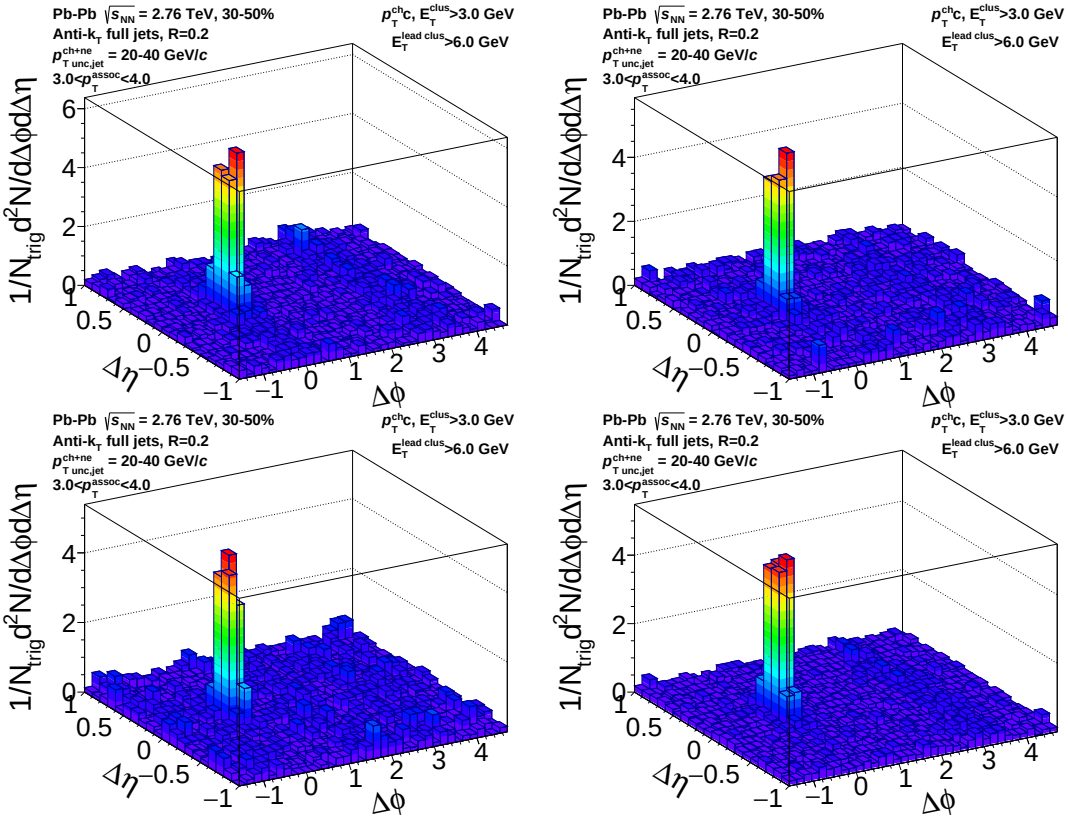

Figure A.10: Raw acceptance corrected correlations from the 30-50% most central events for 20-40 GeV/c full jets, associated hadrons of 3.0-4.0 GeV/c. Top left: in-plane, top right: mid-plane, bottom left: out-of-plane, bottom right: all angles of the trigger jet relative to the event plane.

Table A.5: RPF fit details for Jets 20-40 GeV, associated hadrons 3.0-4.0 GeV, and 30-50% centrality

$\chi^2 = 42.056$ NDF $= 50$ $\chi^2/NDF = 0.841$				
NAME	VALUE		ERROR	% ERROR
B	1.3591e+01	+/-	5.9595e-01	4.385
v_2^{jet}	5.7588e-02	+/-	3.8697e-02	67.196
v_2^{assoc}	3.1128e-01	+/-	5.5029e-02	17.678
v_3^2	2.4980e-02	+/-	3.0274e-02	121.191

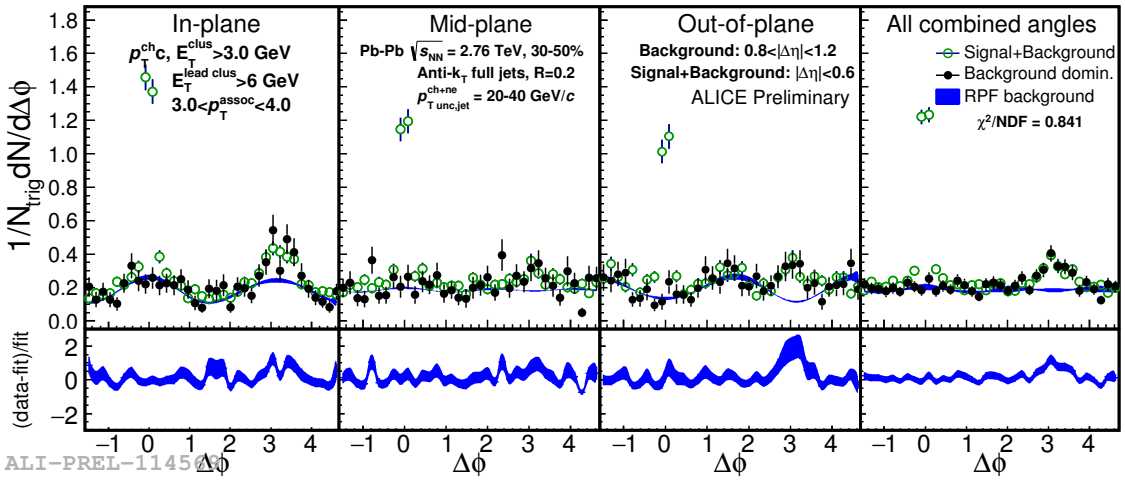

Figure A.11: The signal+background region, $|\Delta\eta| < 0.6$ (green points), background dominated region, $0.8 < |\Delta\eta| < 1.2$ (black points), and the RPF fit (blue band) to the background dominated region for 20-40 GeV/c full jets correlated with 3.0-4.0 GeV/c hadrons from 30-50% centrality collisions on the top panel. The bottom panel shows the quality of the RPF fit to the background dominiated region, (data - fit)/fit.

A.2.6 20-40 GeV/c jets, 30-50% centrality, 4.0-5.0 GeV/c associated hadrons

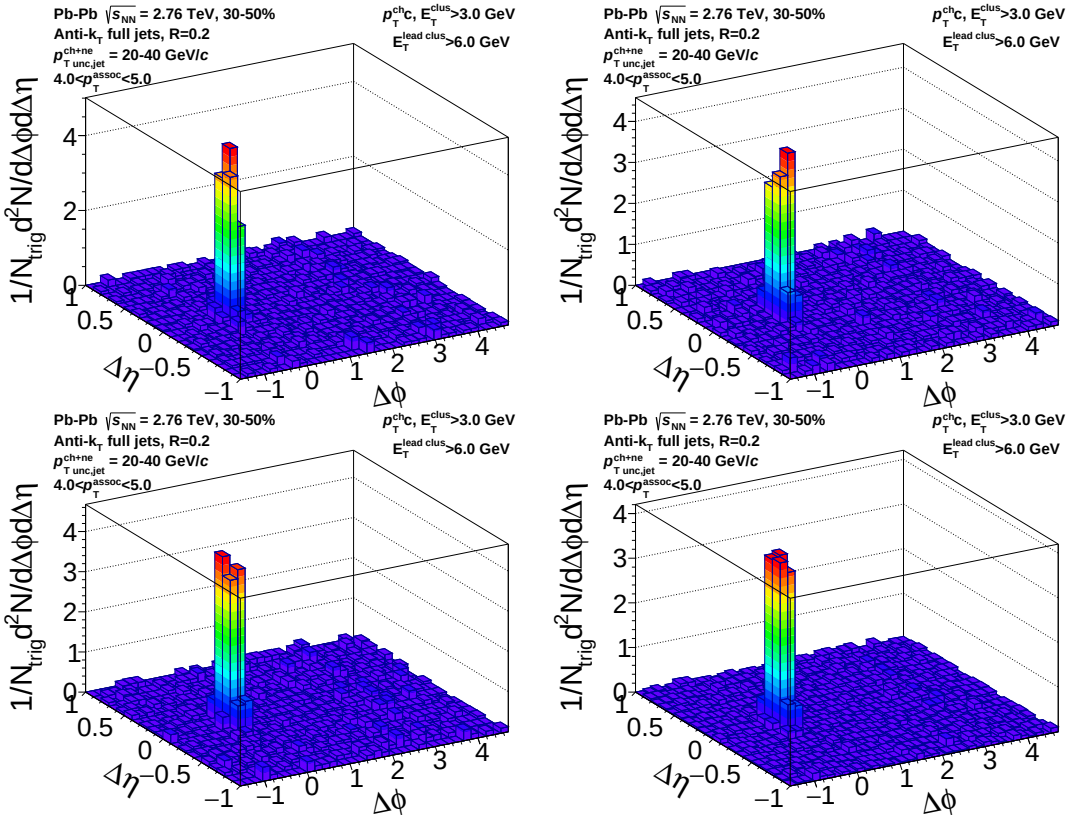

Figure A.12: Raw acceptance corrected correlations from the 30-50% most central events for 20-40 GeV/c full jets, associated hadrons of 4.0-5.0 GeV/c. Top left: in-plane, top right: mid-plane, bottom left: out-of-plane, bottom right: all angles of the trigger jet relative to the event plane.

Table A.6: RPF fit details for Jets 20-40 GeV, associated hadrons 4.0-5.0 GeV, and 30-50% centrality

$\chi^2 = 48.504$ NDF $= 48$ $\chi^2/NDF = 1.010$				
NAME	VALUE		ERROR	% ERROR
B	2.5688e+00	+/-	2.5833e-01	10.056
v_2^{jet}	1.0148e-01	+/-	9.5505e-02	94.110
v_2^{assoc}	2.0770e-01	+/-	1.5071e-01	72.560
v_3^2	5.1641e-02	+/-	6.9144e-02	133.895

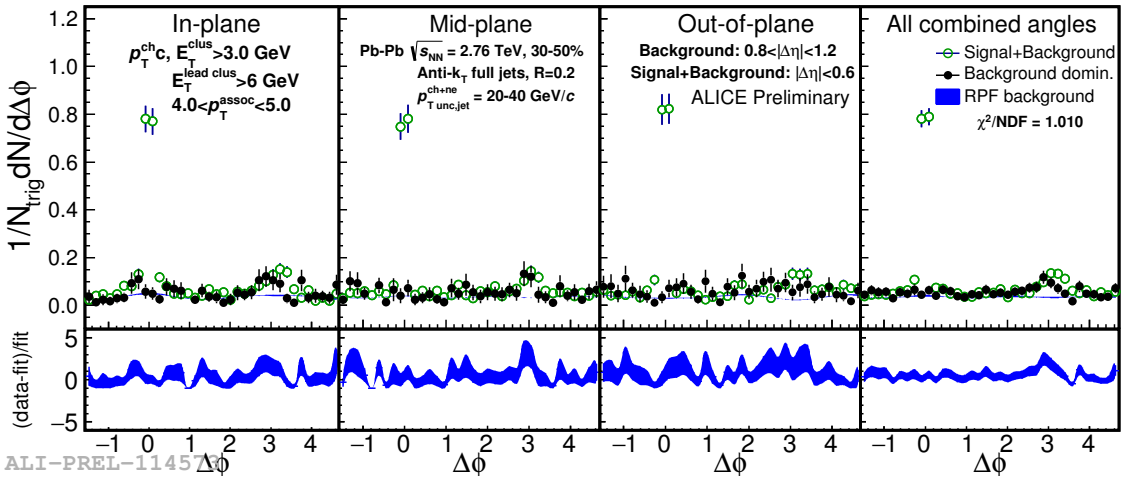

Figure A.13: The signal+background region, $|\Delta\eta| < 0.6$ (green points), background dominated region, $0.8 < |\Delta\eta| < 1.2$ (black points), and the RPF fit (blue band) to the background dominated region for 20-40 GeV/c full jets correlated with 4.0-5.0 GeV/c hadrons from 30-50% centrality collisions on the top panel. The bottom panel shows the quality of the RPF fit to the background dominiated region, (data - fit)/fit.

A.2.7 20-40 GeV/c jets, 30-50% centrality, 5.0-6.0 GeV/c associated hadrons

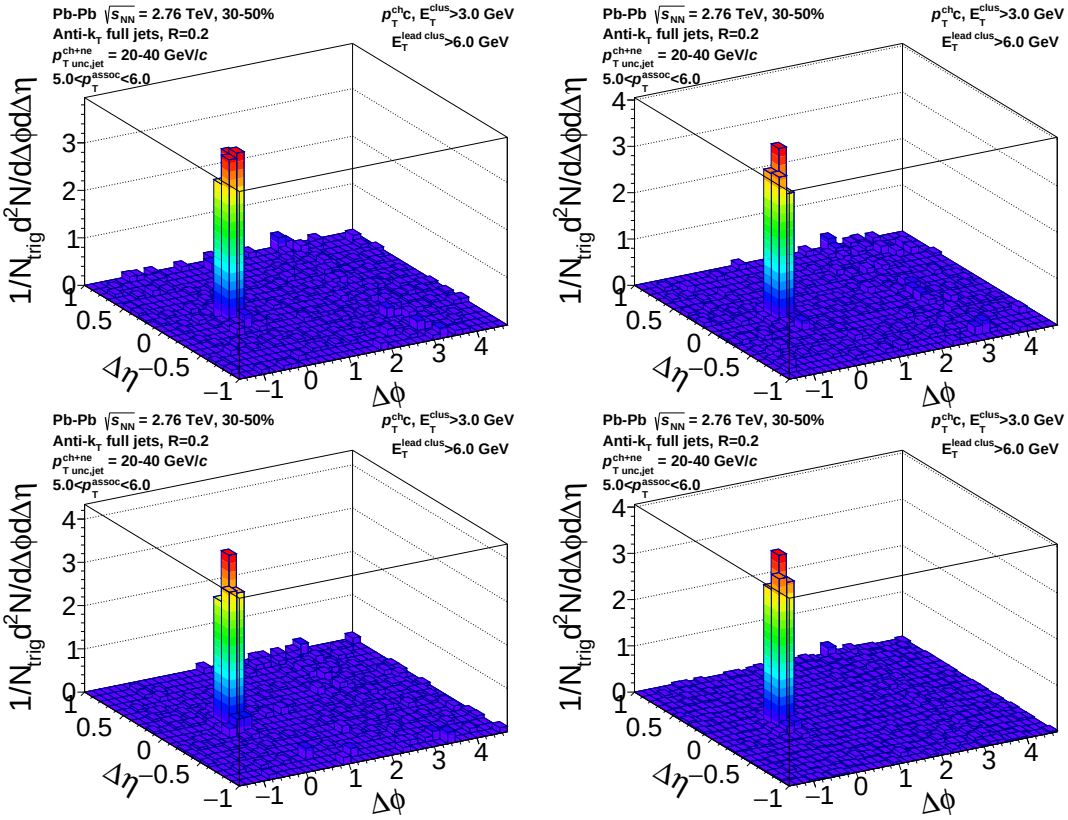

Figure A.14: Raw acceptance corrected correlations from the 30-50% most central events for 20-40 GeV/c full jets, associated hadrons of 5.0-6.0 GeV/c. Top left: in-plane, top right: mid-plane, bottom left: out-of-plane, bottom right: all angles of the trigger jet relative to the event plane.

Table A.7: RPF fit details for Jets 20-40 GeV, associated hadrons 5.0-6.0 GeV, and 30-50% centrality

$\chi^2 = 13.305$ NDF $= 50$ $\chi^2/NDF = 0.266$				
NAME	VALUE		ERROR	% ERROR
B	1.0566e+00	+/-	2.5462e-01	24.098
v_2^{jet}	1.1986e-01	+/-	6.6391e-02	55.390
v_2^{assoc}	3.0300e-01	+/-	3.5261e-01	116.372
v_3^2	-4.7459e-02	+/-	1.9241e-01	405.425

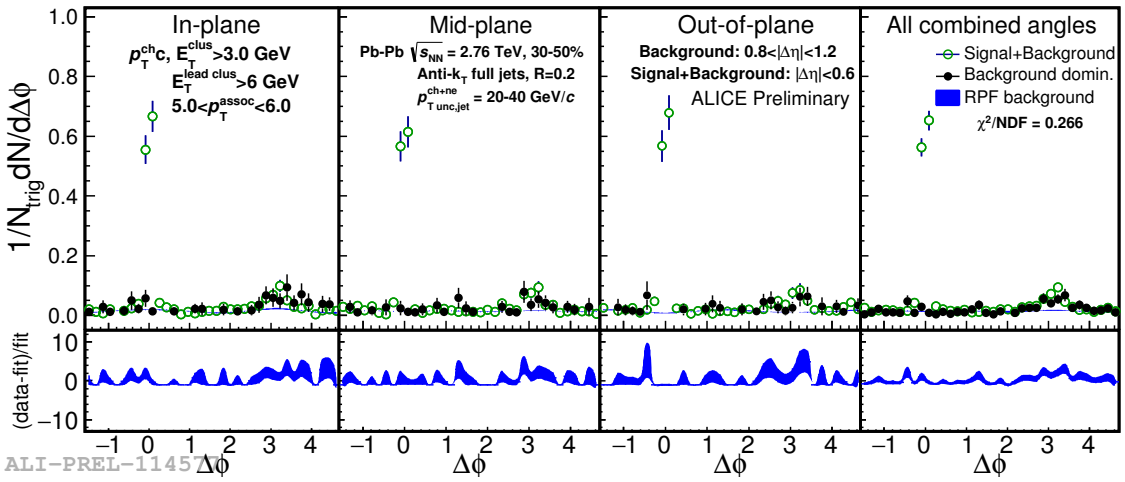

Figure A.15: The signal+background region, $|\Delta\eta| < 0.6$ (green points), background dominated region, $0.8 < |\Delta\eta| < 1.2$ (black points), and the RPF fit (blue band) to the background dominated region for 20-40 GeV/c full jets correlated with 5.0-6.0 GeV/c hadrons from 30-50% centrality collisions on the top panel. The bottom panel shows the quality of the RPF fit to the background dominiated region, (data - fit)/fit. A log likelihood fit is used due to low statistics which include empty bins.

A.2.8 20-40 GeV/c jets, 30-50% centrality, 6.0-10.0 GeV/c associated hadrons

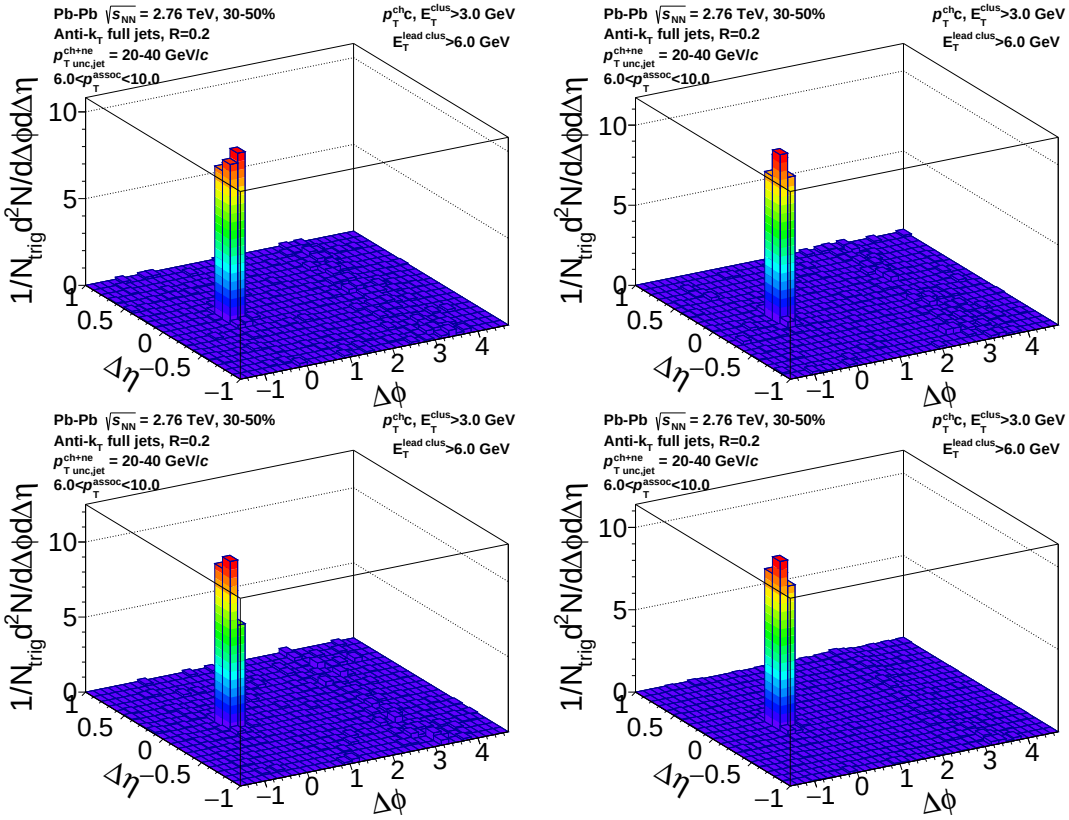

Figure A.16: Raw acceptance corrected correlations from the 30-50% most central events for 20-40 GeV/c full jets, associated hadrons of 6.0-10.0 GeV/c. Top left: in-plane, top right: mid-plane, bottom left: out-of-plane, bottom right: all angles of the trigger jet relative to the event plane.

Table A.8: RPF fit details for Jets 20-40 GeV, associated hadrons 6.0-10.0 GeV, and 30-50% centrality

$\chi^2 = 14.910$ NDF $= 50$ $\chi^2/NDF = 0.298$				
NAME	VALUE		ERROR	% ERROR
B	1.0256e+00	+/-	2.5439e-01	24.805
v_2^{jet}	2.4176e-01	+/-	2.1537e-01	89.083
v_2^{assoc}	1.0802e-02	+/-	2.9782e-01	2757.030
v_3^2	8.9351e-02	+/-	1.6169e-01	180.962

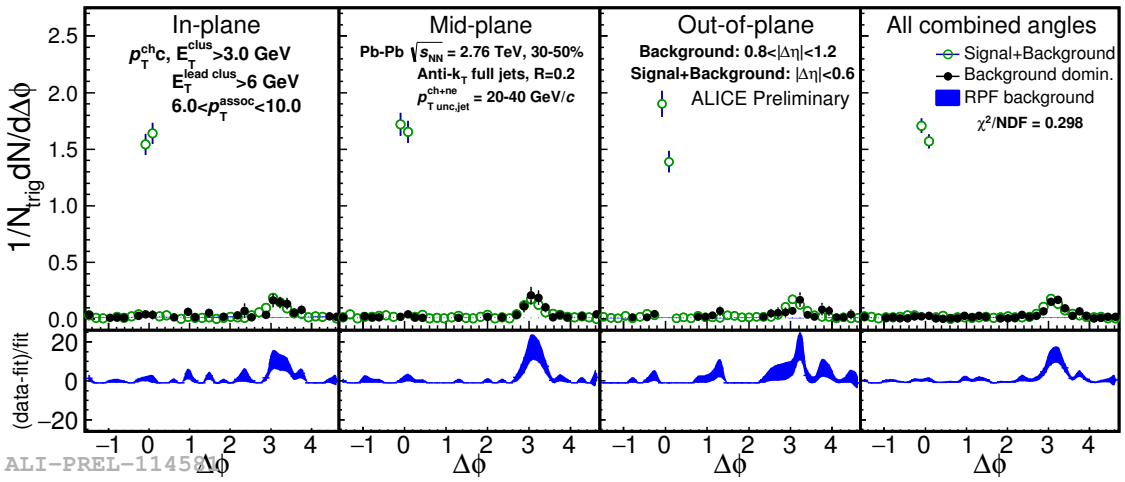

Figure A.17: The signal+background region, $|\Delta\eta| < 0.6$ (green points), background dominated region, $0.8 < |\Delta\eta| < 1.2$ (black points), and the RPF fit (blue band) to the background dominated region for 20-40 GeV/c full jets correlated with 6.0-10.0 GeV/c hadrons from 30-50% centrality collisions on the top panel. The bottom panel shows the quality of the RPF fit to the background dominiated region, (data - fit)/fit. A log likelihood fit is used due to low statistics which include empty bins.

Appendix B

Results: 0-10% centrality

B.1 Trigger Spectra: 20-40 GeV/c jets

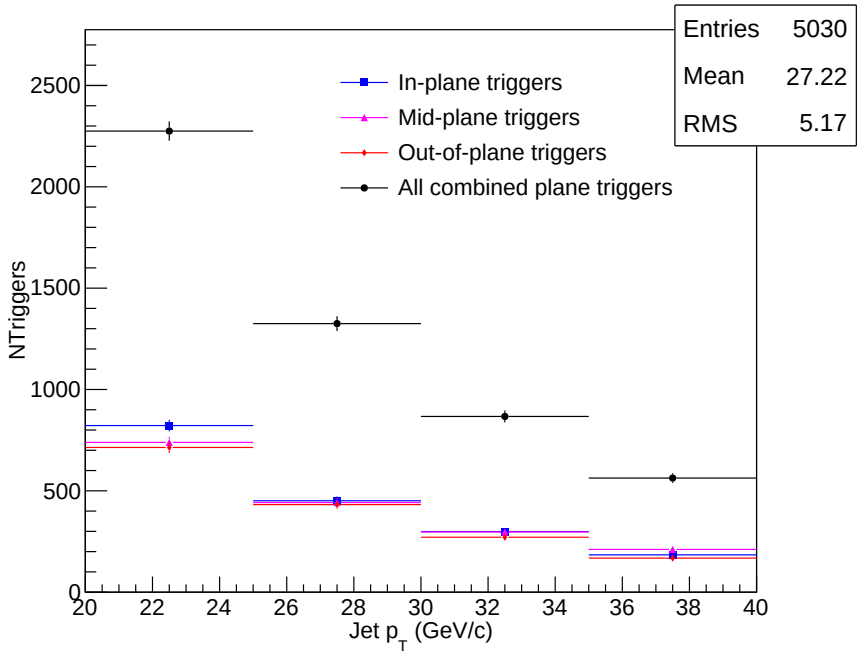

Figure B.1: Jet (triggers) spectra for 20-40 GeV/c jets in 0-10% centrality events. There is a 10 GeV cluster bias requirement and it is made sure the cluster is matched to a firing trigger patch in the EMCal. Comparison for the orientations of the trigger jet relative to the event plane is shown.

B.2 Acceptance corrected and background fit correlations

B.2.1 20-40 GeV/c jets, 0-10% centrality, 0.5-1.0 GeV/c associated hadrons

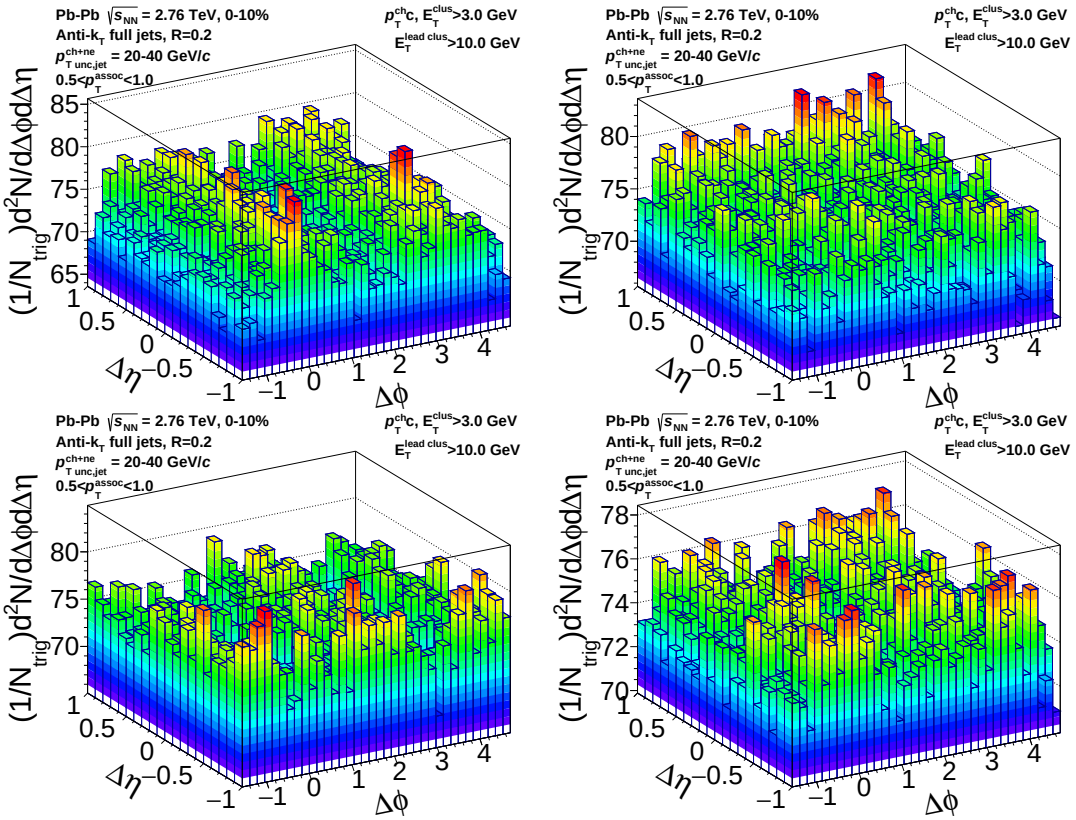

Figure B.2: Raw acceptance corrected correlations from the 0-10% most central events for 20-40 GeV/c full jets, associated hadrons of 0.5-1.0 GeV/c. Top left: in-plane, top right: mid-plane, bottom left: out-of-plane, bottom right: all angles of the trigger jet relative to the event plane.

Table B.1: RPF fit details for Jets 20-40 GeV, associated hadrons 0.5-1.0 GeV, and 0-10% centrality

$\chi^2 = 58.384$ NDF $= 50$ $\chi^2/NDF = 1.168$				
NAME	VALUE		ERROR	% ERROR
B	6.4580e+03	+/-	1.3178e+01	0.204
v_2^{jet}	4.6550e-02	+/-	1.0142e-03	2.179
v_2^{assoc}	3.6869e-02	+/-	3.6060e-03	9.781
v_3^2	1.0181e-03	+/-	1.4474e-03	142.160

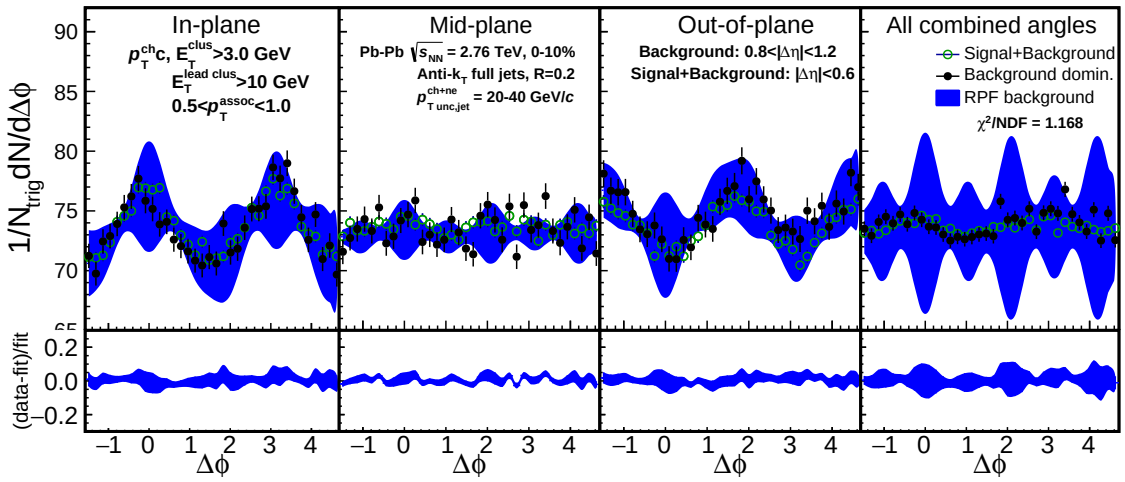

Figure B.3: The signal+background region, $|\Delta\eta| < 0.6$ (green points), background dominated region, $0.8 < |\Delta\eta| < 1.2$ (black points), and the RPF fit (blue band) to the background dominated region for 20-40 GeV/c full jets correlated with 0.5-1.0 GeV/c hadrons from 0-10% centrality collisions on the top panel. The bottom panel shows the quality of the RPF fit to the background dominiated region, (data - fit) / fit.

B.2.2 20-40 GeV/c jets, 0-10% centrality, 1.0-1.5 GeV/c associated hadrons

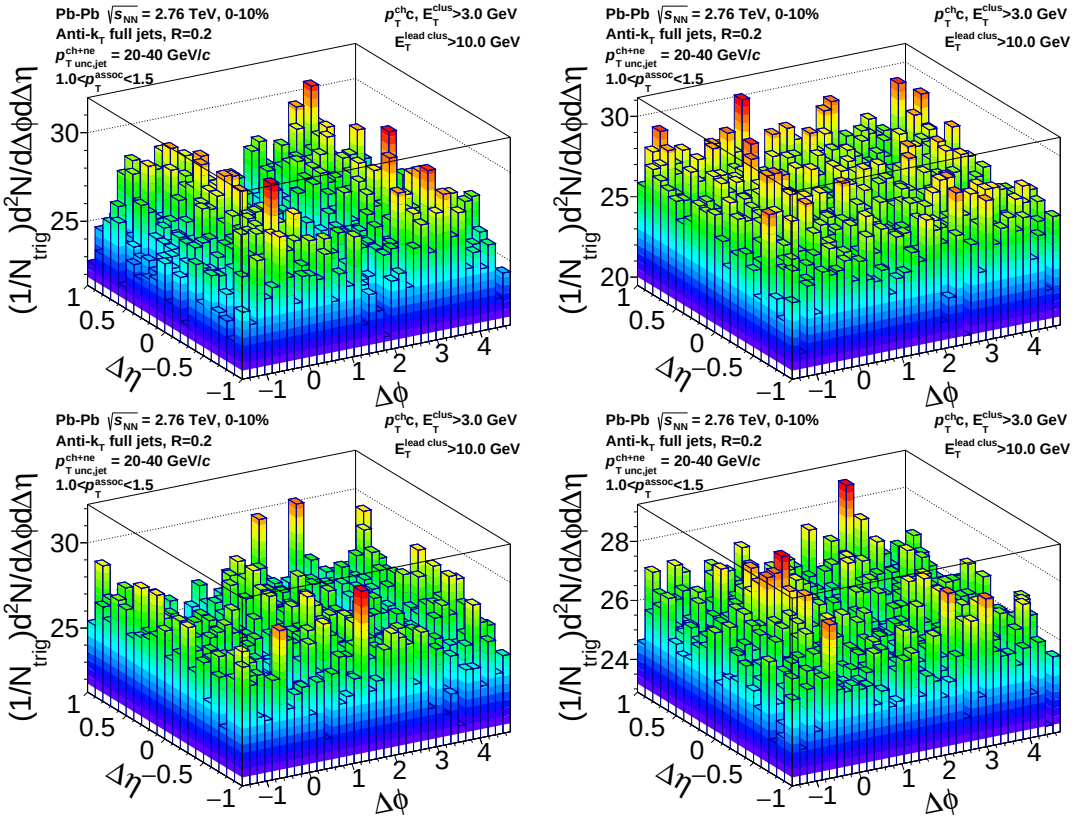

Figure B.4: Raw acceptance corrected correlations from the 0-10% most central events for 20-40 GeV/c full jets, associated hadrons of 1.0-1.5 GeV/c. Top left: in-plane, top right: mid-plane, bottom left: out-of-plane, bottom right: all angles of the trigger jet relative to the event plane.

Table B.2: RPF fit details for Jets 20-40 GeV, associated hadrons 1.0-1.5 GeV, and 0-10% centrality

$\chi^2 = 46.339$ NDF $= 50$ $\chi^2/NDF = 0.927$				
NAME	VALUE		ERROR	% ERROR
B	2.2428e+03	+/-	7.6011e+00	0.339
v_2^{jet}	4.7378e-02	+/-	4.1276e-03	8.712
v_2^{assoc}	5.1369e-02	+/-	5.7707e-03	11.234
v_3^2	-3.0638e-04	+/-	2.4104e-03	786.712

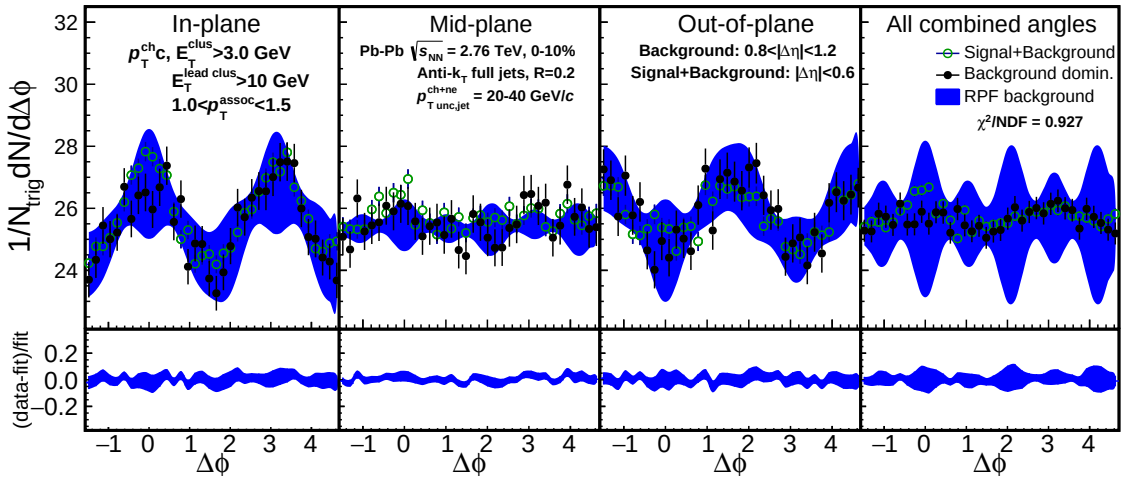

Figure B.5: The signal+background region, $|\Delta\eta| < 0.6$ (green points), background dominated region, $0.8 < |\Delta\eta| < 1.2$ (black points), and the RPF fit (blue band) to the background dominated region for 20-40 GeV/c full jets correlated with 1.0-1.5 GeV/c hadrons from 0-10% centrality collisions on the top panel. The bottom panel shows the quality of the RPF fit to the background dominiated region, (data - fit)/fit.

B.2.3 20-40 GeV/c jets, 0-10% centrality, 1.5-2.0 GeV/c associated hadrons

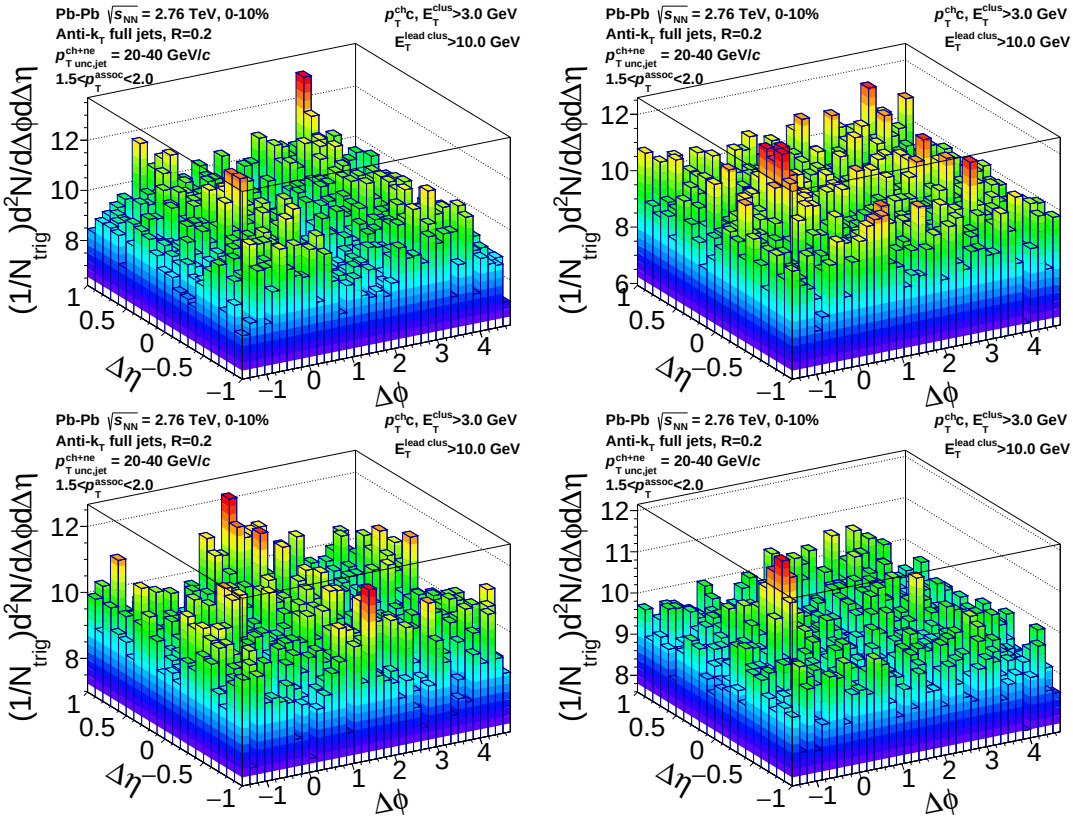

Figure B.6: Raw acceptance corrected correlations from the 0-10% most central events for 20-40 GeV/c full jets, associated hadrons of 1.5-2.0 GeV/c. Top left: in-plane, top right: mid-plane, bottom left: out-of-plane, bottom right: all angles of the trigger jet relative to the event plane.

Table B.3: RPF fit details for Jets 20-40 GeV, associated hadrons 1.5-2.0 GeV, and 0-10% centrality

$\chi^2 = 44.498$ NDF $= 50$ $\chi^2/NDF = 0.890$				
NAME	VALUE		ERROR	% ERROR
B	8.1019e+02	+/-	4.5461e+00	0.561
v_2^{jet}	4.0275e-02	+/-	5.2409e-03	13.013
v_2^{assoc}	9.0614e-02	+/-	9.7212e-03	10.728
v_3^2	-5.8120e-03	+/-	4.0077e-03	68.956

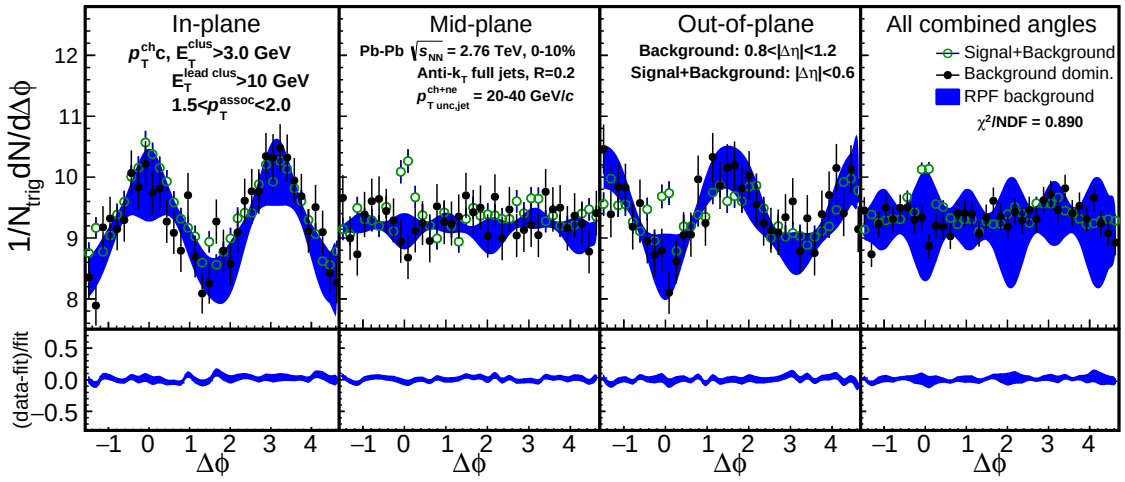

Figure B.7: The signal+background region, $|\Delta\eta| < 0.6$ (green points), background dominated region, $0.8 < |\Delta\eta| < 1.2$ (black points), and the RPF fit (blue band) to the background dominated region for 20-40 GeV/c full jets correlated with 1.5-2.0 GeV/c hadrons from 0-10% centrality collisions on the top panel. The bottom panel shows the quality of the RPF fit to the background dominiated region, (data - fit)/fit.

B.2.4 20-40 GeV/c jets, 0-10% centrality, 2.0-3.0 GeV/c associated hadrons

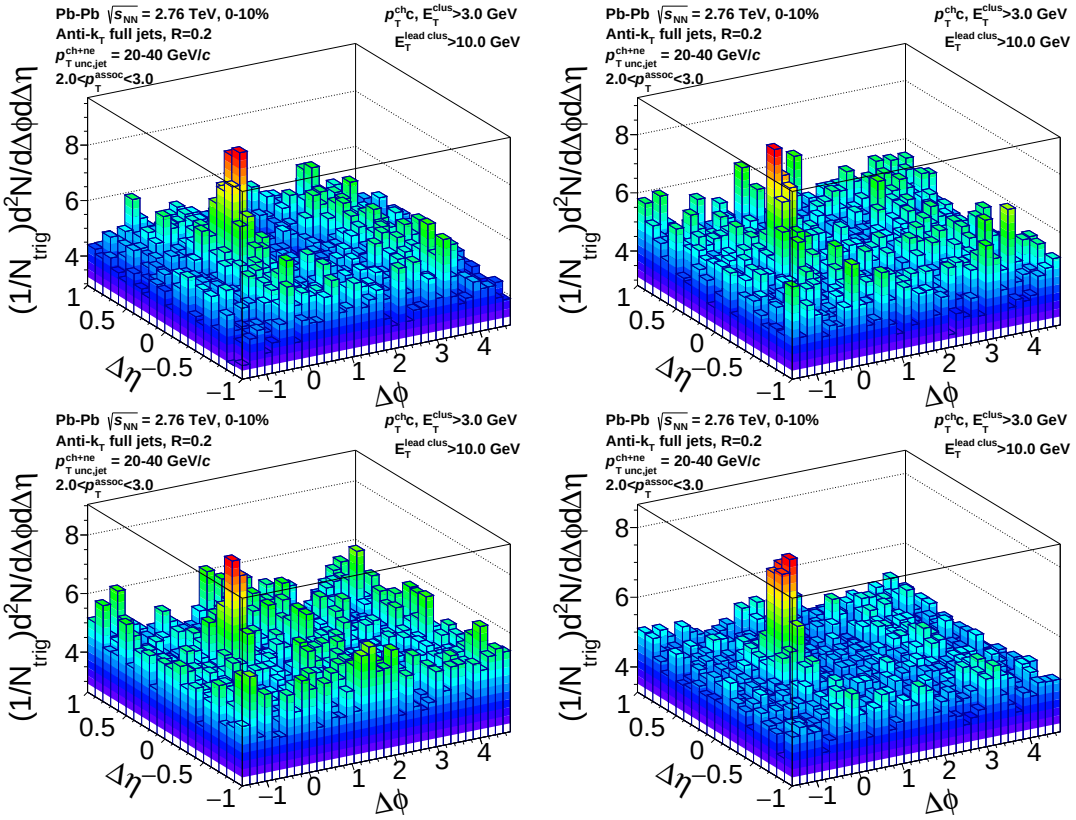

Figure B.8: Raw acceptance corrected correlations from the 0-10% most central events for 20-40 GeV/c full jets, associated hadrons of 2.0-3.0 GeV/c. Top left: in-plane, top right: mid-plane, bottom left: out-of-plane, bottom right: all angles of the trigger jet relative to the event plane.

Table B.4: RPF fit details for Jets 20-40 GeV, associated hadrons 2.0-3.0 GeV, and 0-10% centrality

$\chi^2 = 47.701$ NDF $= 50$ $\chi^2/NDF = 0.954$				
NAME	VALUE		ERROR	% ERROR
B	4.0686e+02	+/-	3.2446e+00	0.797
v_2^{jet}	4.1424e-02	+/-	1.2043e-02	29.074
v_2^{assoc}	1.0340e-01	+/-	1.3839e-02	13.384
v_3^2	1.5240e-03	+/-	5.6951e-03	373.689

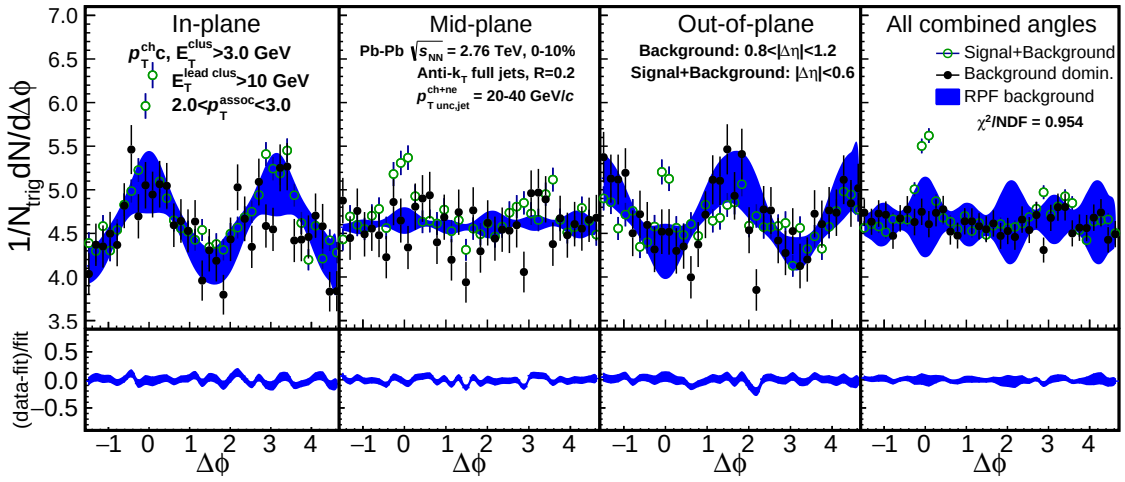

Figure B.9: The signal+background region, $|\Delta\eta| < 0.6$ (green points), background dominated region, $0.8 < |\Delta\eta| < 1.2$ (black points), and the RPF fit (blue band) to the background dominated region for 20-40 GeV/c full jets correlated with 2.0-3.0 GeV/c hadrons from 0-10% centrality collisions on the top panel. The bottom panel shows the quality of the RPF fit to the background dominiated region, (data - fit)/fit.

B.2.5 20-40 GeV/c jets, 0-10% centrality, 3.0-4.0 GeV/c associated hadrons

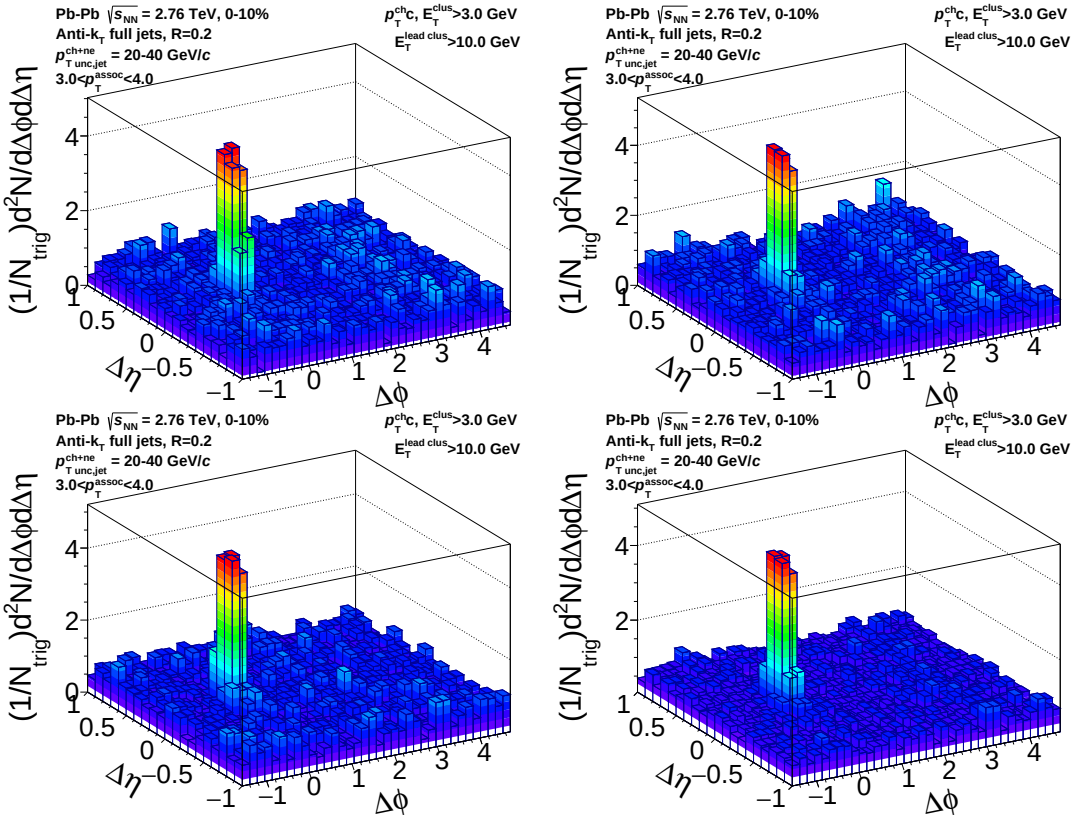

Figure B.10: Raw acceptance corrected correlations from the 0-10% most central events for 20-40 GeV/c full jets, associated hadrons of 3.0-4.0 GeV/c. Top left: in-plane, top right: mid-plane, bottom left: out-of-plane, bottom right: all angles of the trigger jet relative to the event plane.

Table B.5: RPF fit details for Jets 20-40 GeV, associated hadrons 3.0-4.0 GeV, and 0-10% centrality

$\chi^2 = 56.332$ NDF $= 50$ $\chi^2/NDF = 1.127$				
NAME	VALUE		ERROR	% ERROR
B	5.6849e+01	+/-	1.2067e+00	2.123
v_2^{jet}	6.3603e-02	+/-	2.5620e-02	40.281
v_2^{assoc}	1.2372e-01	+/-	3.3740e-02	27.272
v_3^2	-7.6654e-03	+/-	1.5219e-02	198.543

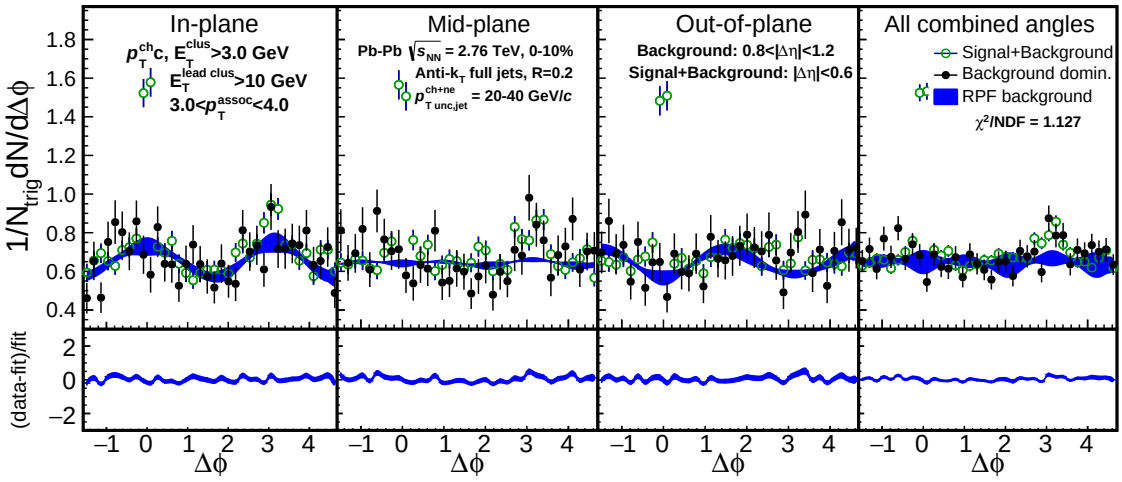

Figure B.11: The signal+background region, $|\Delta\eta| < 0.6$ (green points), background dominated region, $0.8 < |\Delta\eta| < 1.2$ (black points), and the RPF fit (blue band) to the background dominated region for 20-40 GeV/c full jets correlated with 3.0-4.0 GeV/c hadrons from 0-10% centrality collisions on the top panel. The bottom panel shows the quality of the RPF fit to the background dominiated region, (data - fit)/fit.

B.2.6 20-40 GeV/c jets, 0-10% centrality, 4.0-5.0 GeV/c associated hadrons

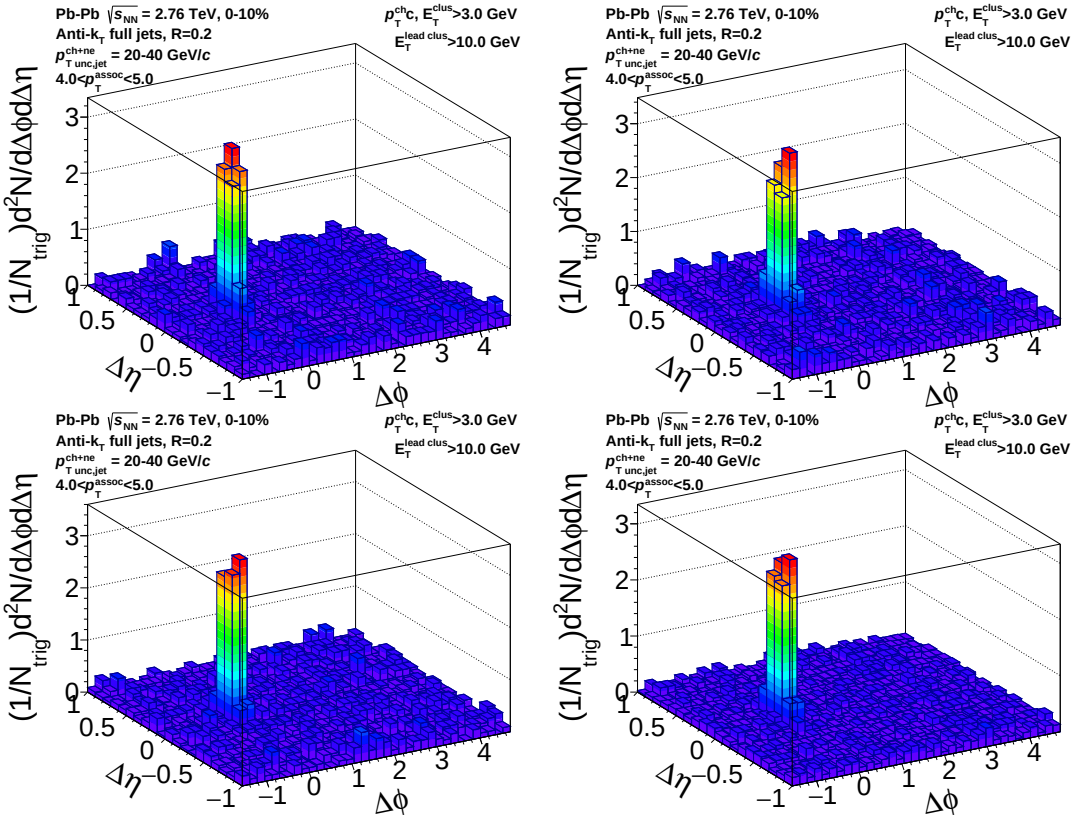

Figure B.12: Raw acceptance corrected correlations from the 0-10% most central events for 20-40 GeV/c full jets, associated hadrons of 4.0-5.0 GeV/c. Top left: in-plane, top right: mid-plane, bottom left: out-of-plane, bottom right: all angles of the trigger jet relative to the event plane.

Table B.6: RPF fit details for Jets 20-40 GeV, associated hadrons 4.0-5.0 GeV, and 0-10% centrality

$\chi^2 = 64.751$ NDF $= 50$ $\chi^2/NDF = 1.295$				
NAME	VALUE		ERROR	% ERROR
B	8.9929e+00	+/-	4.6510e-01	5.172
v_2^{jet}	1.7219e-01	+/-	6.3426e-02	36.835
v_2^{assoc}	2.3353e-01	+/-	9.9603e-02	42.651
v_3^2	-9.8750e-02	+/-	4.2167e-02	42.700

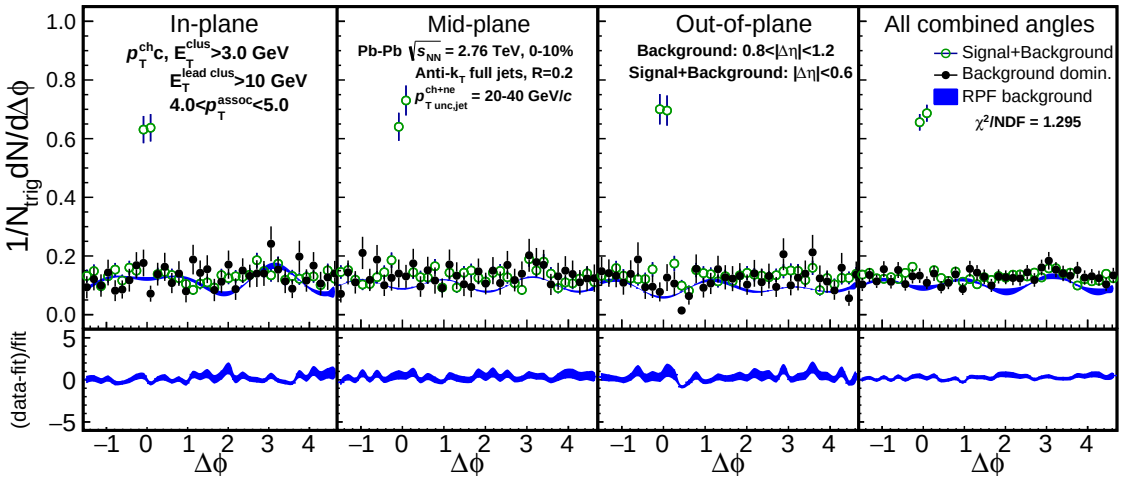

Figure B.13: The signal+background region, $|\Delta\eta| < 0.6$ (green points), background dominated region, $0.8 < |\Delta\eta| < 1.2$ (black points), and the RPF fit (blue band) to the background dominated region for 20-40 GeV/c full jets correlated with 4.0-5.0 GeV/c hadrons from 0-10% centrality collisions on the top panel. The bottom panel shows the quality of the RPF fit to the background dominiated region, (data - fit)/fit.

B.2.7 20-40 GeV/c jets, 0-10% centrality, 5.0-6.0 GeV/c associated hadrons

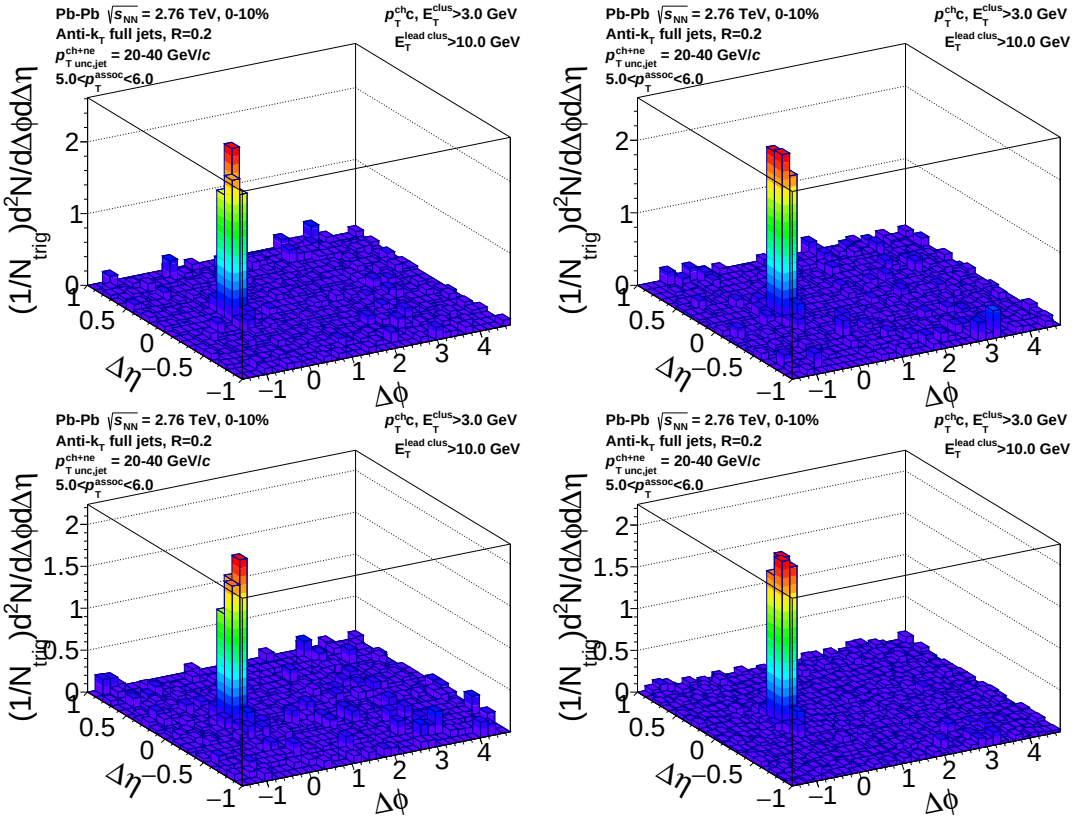

Figure B.14: Raw acceptance corrected correlations from the 0-10% most central events for 20-40 GeV/c full jets, associated hadrons of 5.0-6.0 GeV/c. Top left: in-plane, top right: mid-plane, bottom left: out-of-plane, bottom right: all angles of the trigger jet relative to the event plane.

Table B.7: RPF fit details for Jets 20-40 GeV, associated hadrons 5.0-6.0 GeV, and 0-10% centrality

$\chi^2 = 50.877$ NDF $= 50$ $\chi^2/NDF = 1.018$				
NAME	VALUE		ERROR	% ERROR
B	2.3182e+00	+/-	3.6490e-01	15.741
v_2^{jet}	-5.0814e-02	+/-	1.9927e-01	392.146
v_2^{assoc}	8.7694e-02	+/-	2.8354e-01	323.329
v_3^2	-1.4367e-01	+/-	1.1632e-01	80.964

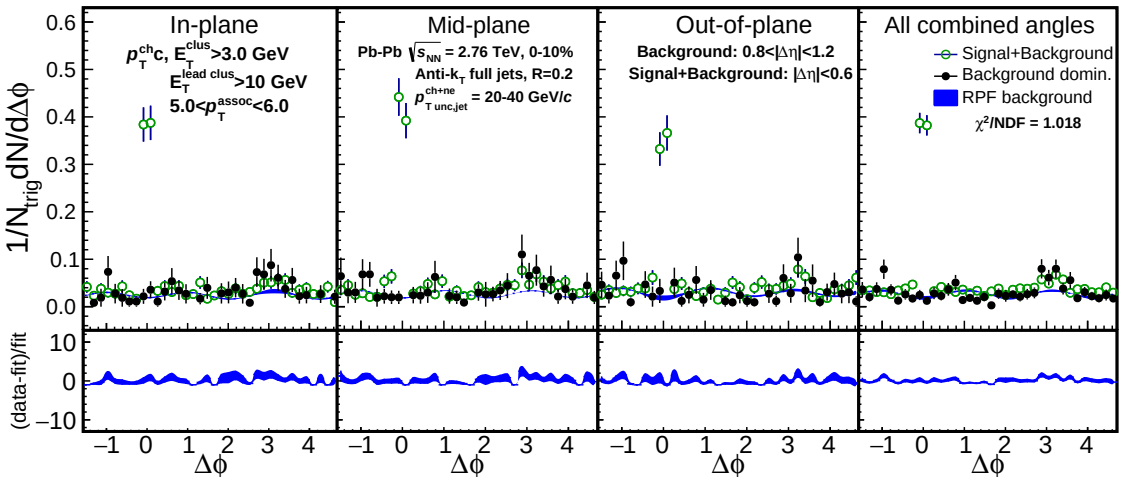

Figure B.15: The signal+background region, $|\Delta\eta| < 0.6$ (green points), background dominated region, $0.8 < |\Delta\eta| < 1.2$ (black points), and the RPF fit (blue band) to the background dominated region for 20-40 GeV/c full jets correlated with 5.0-6.0 GeV/c hadrons from 0-10% centrality collisions on the top panel. The bottom panel shows the quality of the RPF fit to the background dominiated region, (data - fit)/fit. A log likelihood fit is used due to low statistics which include empty bins.

B.2.8 20-40 GeV/c jets, 0-10% centrality, 6.0-10.0 GeV/c associated hadrons

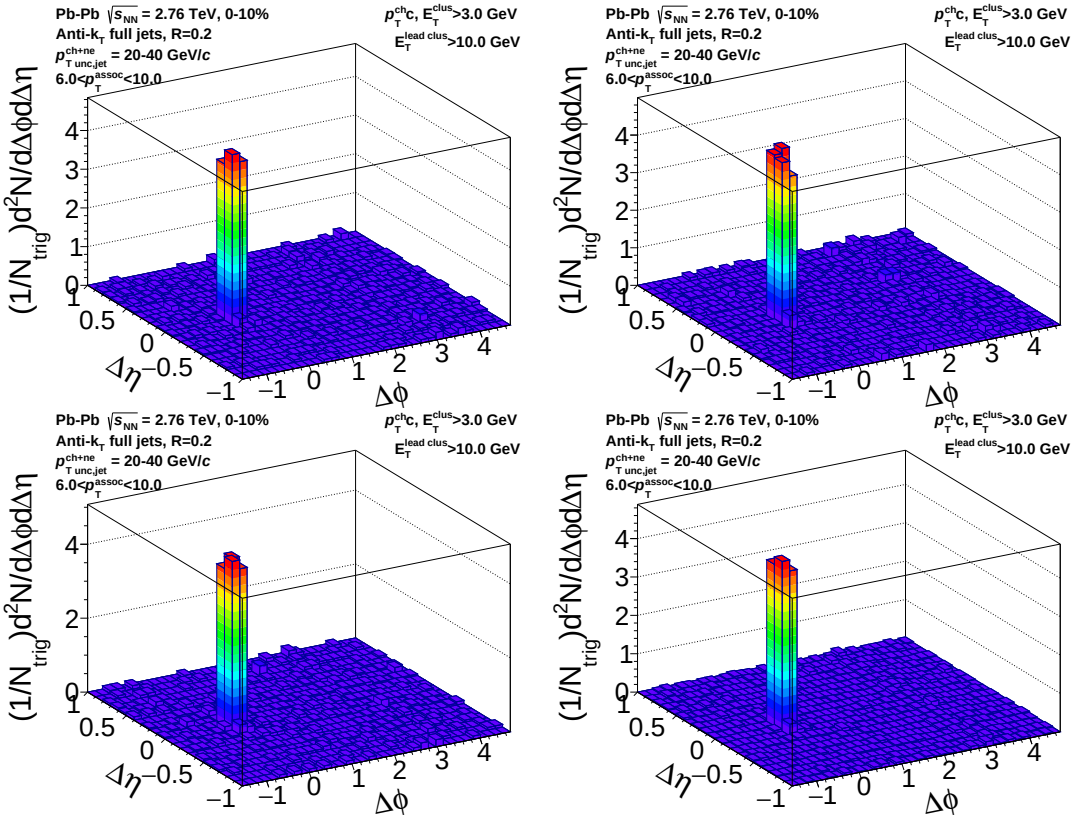

Figure B.16: Raw acceptance corrected correlations from the 0-10% most central events for 20-40 GeV/c full jets, associated hadrons of 6.0-10.0 GeV/c. Top left: in-plane, top right: mid-plane, bottom left: out-of-plane, bottom right: all angles of the trigger jet relative to the event plane.

Table B.8: RPF fit details for Jets 20-40 GeV, associated hadrons 6.0-10.0 GeV, and 0-10% centrality

$\chi^2 = 37.614$ NDF $= 50$ $\chi^2/NDF = 0.752$				
NAME	VALUE		ERROR	% ERROR
B	2.0765e+00	+/-	3.6106e-01	17.388
v_2^{jet}	-8.8691e-02	+/-	2.0555e-01	231.758
v_2^{assoc}	6.9298e-02	+/-	2.9276e-01	422.463
v_3^2	2.3334e-02	+/-	1.3062e-01	559.773

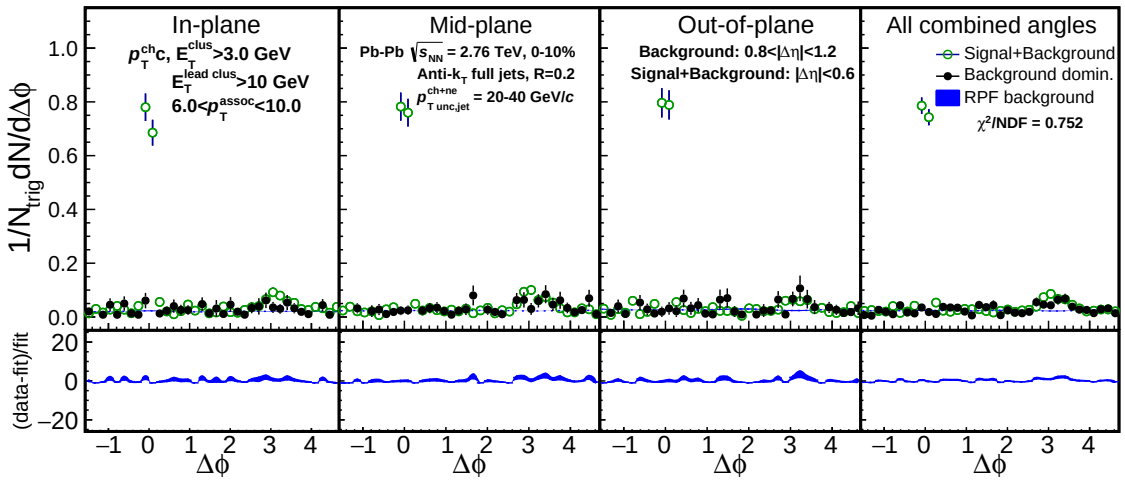

Figure B.17: The signal+background region, $|\Delta\eta| < 0.6$ (green points), background dominated region, $0.8 < |\Delta\eta| < 1.2$ (black points), and the RPF fit (blue band) to the background dominated region for 20-40 GeV/c full jets correlated with 6.0-10.0 GeV/c hadrons from 0-10% centrality collisions on the top panel. The bottom panel shows the quality of the RPF fit to the background dominiated region, (data - fit)/fit. A log likelihood fit is used due to low statistics which include empty bins.

Appendix C

Cross checks

C.1 Cross-check event plane dependence of triggered events

Below are the combined VZERO event plane for Min-Bias and EMCal gamma triggered events. The specific cuts are slightly differnt than those used in this analysis.

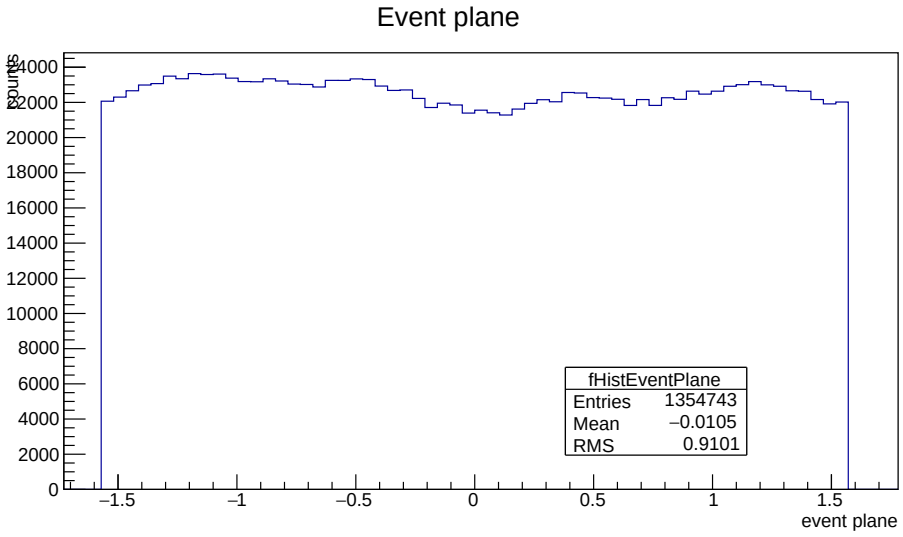

Figure C.1: Event plane from combined VZERO vs azimuthal angle for all Min-Bias (MB) events. Note: this doesn't have the specific cuts on the event used in the analysis. It was generated quickly in response to AN questions.

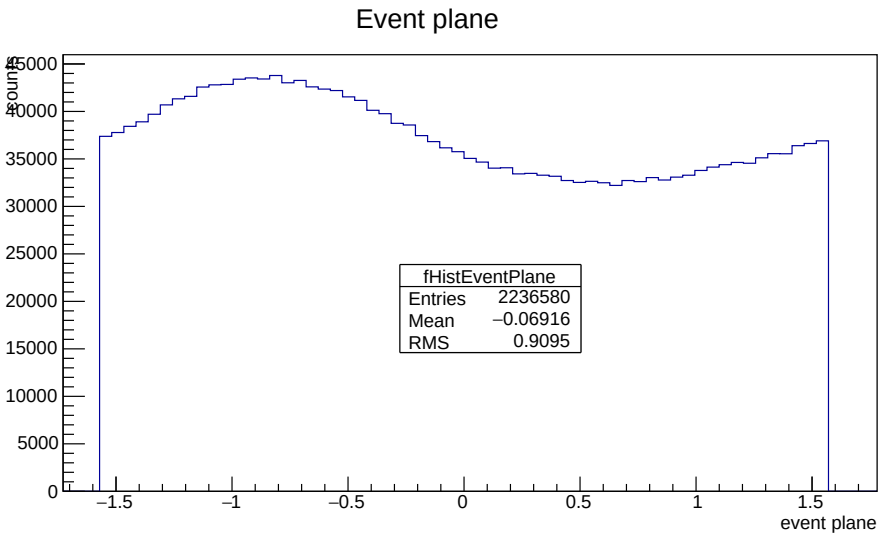

Figure C.2: Event plane from combined VZERO vs azimuthal angle for all EMCGA (Gamma) events. Note: this doesn't have the specific cuts on the event used in the analysis. It was generated quickly in response to AN questions.

C.2 Cross-check: projection of mixed event ratios in $\Delta\eta$ and $\Delta\phi$

Below are some added requests (cross checks) to show the $\Delta\eta$ and $\Delta\phi$ projections for the mixed event ratios of: 1) centrality and 2) transverse momenta.

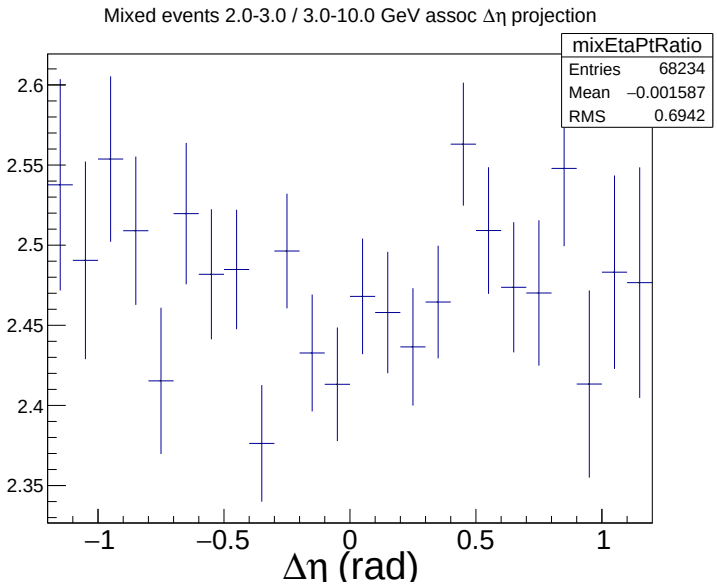

Figure C.3: $\Delta\eta$ projection of the transverse momenta (2.0-3.0 / 3.0-10.0 GeV/c) ratio of mixed events. Normalization is done to scale as binwidth / width.

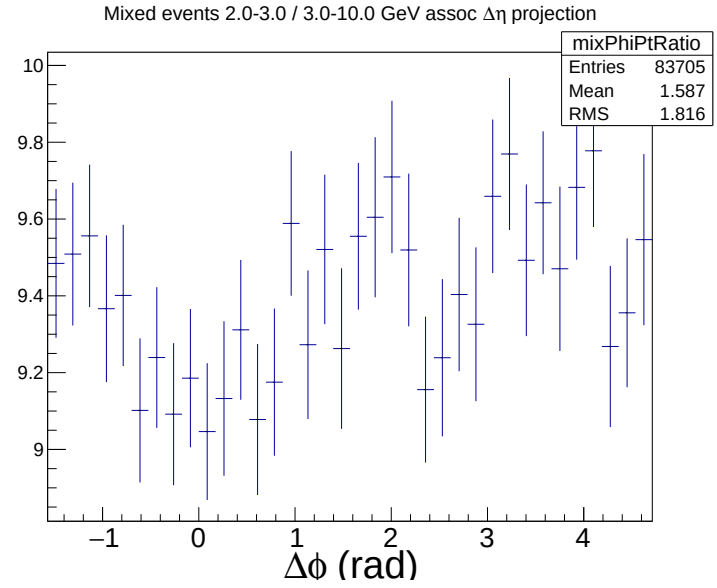

Figure C.4: $\Delta\phi$ projection of the transverse momenta (2.0-3.0 / 3.0-10.0 GeV/c) ratio of mixed events. Normalization is done to scale as binwidth / width.

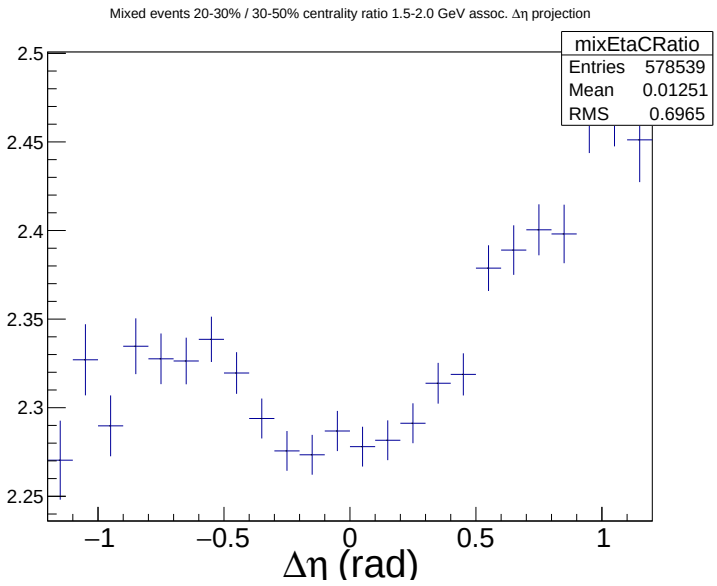

Figure C.5: $\Delta\eta$ projection of the centrality ratio (20-30% / 30-50%) of mixed events. Normalization is done to scale as binwidth / width.

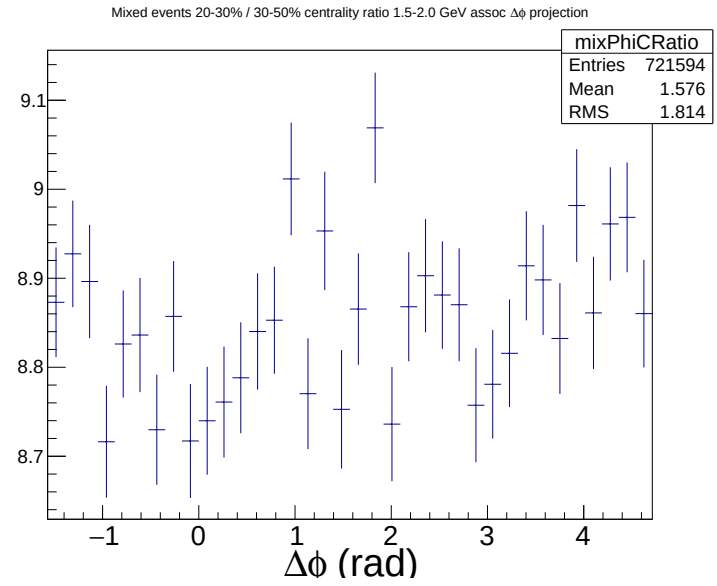

Figure C.6: $\Delta\phi$ projection of the centrality ratio (20-30% / 30-50%) of mixed events. Normalization is done to scale as binwidth / width.

C.3 Cross-check: mixed events $\Delta\phi$ projections for different p_T^{assoc} bins

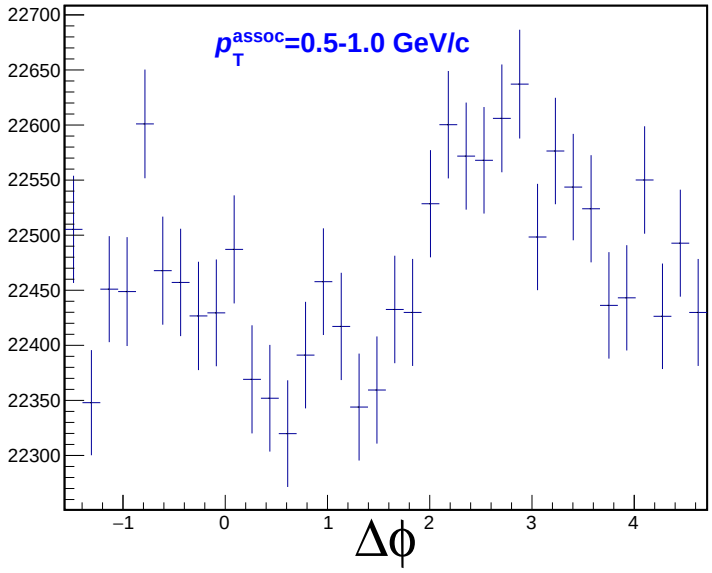

Figure C.7: $\Delta\phi$ projection of the mixed events for p_T^{assoc}=0.5-1.0 GeV/c tracks.

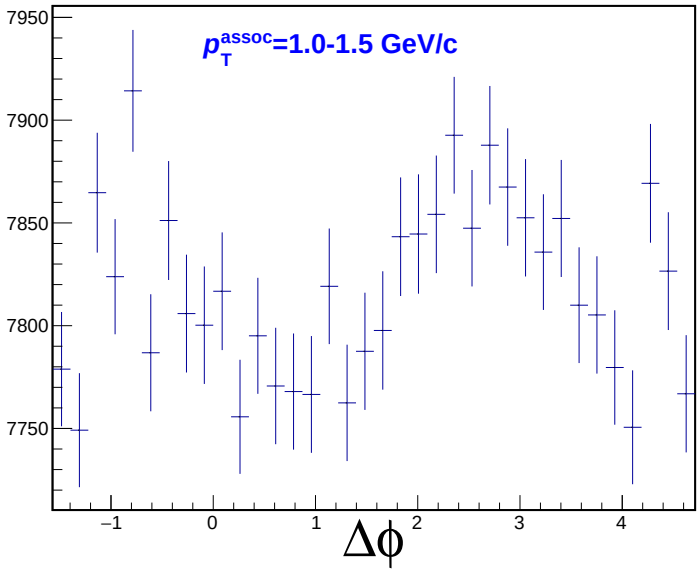

Figure C.8: $\Delta\phi$ projection of the mixed events for p_T^{assoc}=1.0-1.5 GeV/c tracks.

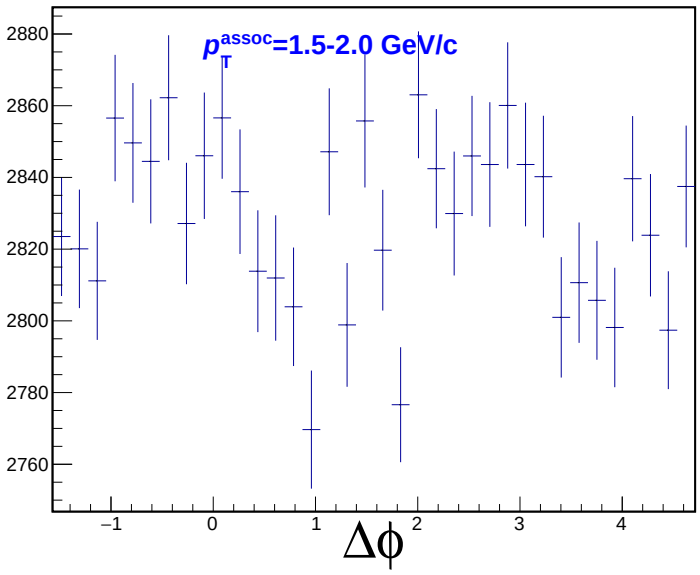

Figure C.9: $\Delta\phi$ projection of the mixed events for p_T^{assoc}=1.5-2.0 GeV/c tracks.

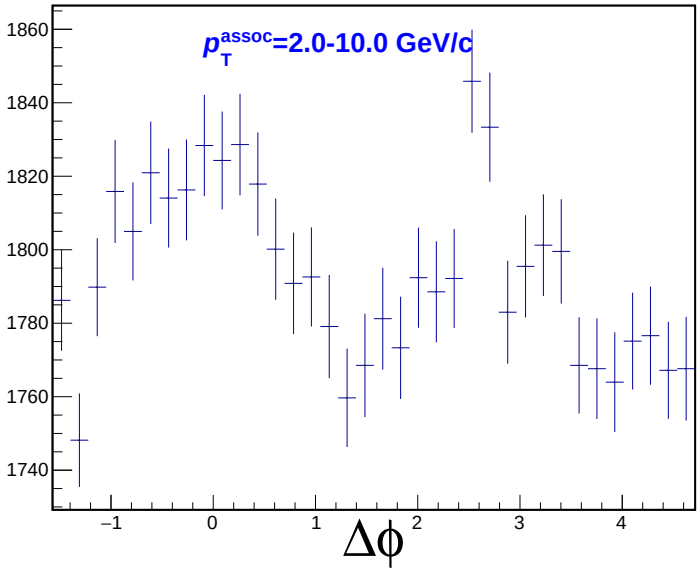

Figure C.10: $\Delta\phi$ projection of the mixed events for p_T^{assoc}=2.0-10.0 GeV/c tracks.

C.4 Event plane resolution systematic uncertainty

The errors on the event plane resolution calculation are very small, but as a conservative approach to calculate the systematics, the nominal values for $\Re$ were varied by ±1%. The uncertainties on R given are statistical, but since centrality bins 30-40% and 40-50% had to be combined, there is some ambiguity in exactly how the bins should be averaged. The difference between giving all events in the sample which contained a jet equal weight (and there are more jets in the 30-40% bin) and taking the arithematic average of the reaction planes was about 0.5%. To be conservative, we rounded this up to 1%. Even with the 1% variation, there was negligible effect on the final $\Delta\phi$ correlations and thus the final reported values for the yield and RMS. The statistical and background fit uncertainties dominate. Tab. C.1 shows the nominal yield and RMS values along with the % uncertainty from the statistical errors alone. Then the % difference is shown from the case of varying the $\Re$ by ±1%. And it is seen that the difference is completely negligible.

Table C.1: Event plane resolution systematic check. Calculated for p_T^{assoc} = 1.0-1.5 GeV/c, p_T^{jet} = 20-40 GeV/c, and 30-50% centrality collisions. Nominal Yield and RMS values along with only the % statistical errors are compared to case of varying $\Re_n$ by 1% where the % difference from the nominal value is shown.

orientation	nominal Yield	vary $\Re_n$ ±1%	nominal RMS	vary $\Re_n$ ±1%
In-plane: NS	0.59 ± 17%	0.24%	0.46 ± 34%	0.05%
In-plane: AS	0.37 ± 27%	0.38%	0.62 ± 19%	0.93%
Mid-plane: NS	0.89 ± 12%	0.06%	0.44 ± 41%	0.02%
Mid-plane: AS	0.45 ± 23%	0.11%	0.63 ± 17%	0.44%
Out-of-plane: NS	1.04 ± 10%	0.46%	0.39 ± 52%	0.10%
Out-of-plane: AS	0.47 ± 22%	1.03%	0.58 ± 25%	0.76%
ALL angles: NS	0.82 ± 8%	0.26%	0.41 ± 26%	0.06%
ALL angles: AS	0.43 ± 14%	0.50%	0.62 ± 12%	0.78%

C.5 Change to Loglikelihood for 2 highest transverse momenta bins

Tables of Yield/RMS values for different fit options are listed below. By default a χ^2 (least-square) fit is performed on the histogram. Bins with zero errors are excluded from the fit. The likelihood method has the advantage of treating correctly bins with low statistics.

Table C.2: Truncated RMS with uncertainties for Jets 20-40 GeV/c in 30-50% centrality events: in/mid/out-of-plane orientations for both the near-side and away-side. Included are the statistical, scale, and background uncertainties. The p_T ranges of 4-5, 5-6, and 6-10 GeV/c are compared for different fit options.

p_T GeV/c		Near-Side Yield	Away-Side Yield
Nominal option			
4.0-5.0	In-plane	0.312 ± 0.017 (st) ± 0.005 (sc) ± 0.014 (bg)	0.083 ± 0.011 (st) ± 0.005 (sc) ± 0.014 (bg)
	Mid-plane	0.286 ± 0.016 (st) ± 0.004 (sc) ± 0.007 (bg)	0.079 ± 0.011 (st) ± 0.004 (sc) ± 0.007 (bg)
	Out-of-plane	0.317 ± 0.018 (st) ± 0.004 (sc) ± 0.011 (bg)	0.104 ± 0.012 (st) ± 0.004 (sc) ± 0.011 (bg)
L option			
4.0-5.0	In-plane	0.289 ± 0.017 (st) ± 0.018 (sc) ± 0.017 (bg)	0.060 ± 0.011 (st) ± 0.018 (sc) ± 0.017 (bg)
	Mid-plane	0.252 ± 0.016 (st) ± 0.030 (sc) ± 0.007 (bg)	0.044 ± 0.011 (st) ± 0.030 (sc) ± 0.007 (bg)
	Out-of-plane	0.270 ± 0.018 (st) ± 0.043 (sc) ± 0.016 (bg)	0.058 ± 0.012 (st) ± 0.043 (sc) ± 0.016 (bg)
Nominal option			
5.0-6.0	In-plane	0.210 ± 0.013 (st) ± 0.001 (sc) ± 0.011 (bg)	0.043 ± 0.008 (st) ± 0.001 (sc) ± 0.011 (bg)
	Mid-plane	0.204 ± 0.014 (st) ± 0.001 (sc) ± 0.007 (bg)	0.042 ± 0.008 (st) ± 0.001 (sc) ± 0.007 (bg)
	Out-of-plane	0.220 ± 0.015 (st) ± 0.001 (sc) ± 0.013 (bg)	0.041 ± 0.008 (st) ± 0.001 (sc) ± 0.013 (bg)
L option			
5.0-6.0	In-plane	0.213 ± 0.013 (st) ± 0.003 (sc) ± 0.010 (bg)	0.045 ± 0.008 (st) ± 0.003 (sc) ± 0.010 (bg)
	Mid-plane	0.210 ± 0.014 (st) ± 0.006 (sc) ± 0.007 (bg)	0.047 ± 0.008 (st) ± 0.006 (sc) ± 0.007 (bg)
	Out-of-plane	0.229 ± 0.015 (st) ± 0.010 (sc) ± 0.010 (bg)	0.050 ± 0.008 (st) ± 0.010 (sc) ± 0.010 (bg)
Nominal option			
6.0-10.0	In-plane	0.137 ± 0.006 (st) ± 0.000 (sc) ± 0.003 (bg)	0.025 ± 0.003 (st) ± 0.000 (sc) ± 0.003 (bg)
	Mid-plane	0.146 ± 0.006 (st) ± 0.000 (sc) ± 0.002 (bg)	0.019 ± 0.003 (st) ± 0.000 (sc) ± 0.002 (bg)
	Out-of-plane	0.142 ± 0.007 (st) ± 0.000 (sc) ± 0.004 (bg)	0.018 ± 0.003 (st) ± 0.000 (sc) ± 0.004 (bg)
L option			
6.0-10.0	In-plane	0.138 ± 0.006 (st) ± 0.001 (sc) ± 0.003 (bg)	0.026 ± 0.003 (st) ± 0.001 (sc) ± 0.003 (bg)
	Mid-plane	0.149 ± 0.006 (st) ± 0.003 (sc) ± 0.002 (bg)	0.022 ± 0.003 (st) ± 0.003 (sc) ± 0.002 (bg)
	Out-of-plane	0.147 ± 0.007 (st) ± 0.005 (sc) ± 0.003 (bg)	0.023 ± 0.003 (st) ± 0.005 (sc) ± 0.003 (bg)

C.6 Background energy density, ρ, calculated for different thresholds

Figures C.11, C.12, and C.13 plots showing ρ vs centrality calculated for jets with different track constituent cuts. It can be seen that when track cuts are greater than 2.0 GeV/c, there are simply no statistics.

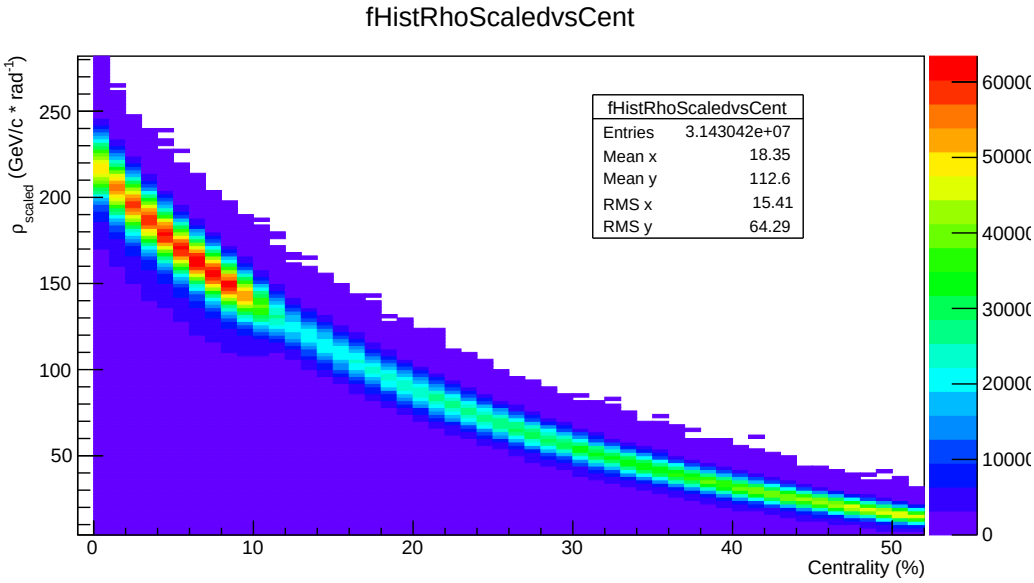

Figure C.11: ρ vs centrality for 0.15+ GeV/c tracks. Calculated for charged jets and scaled up.

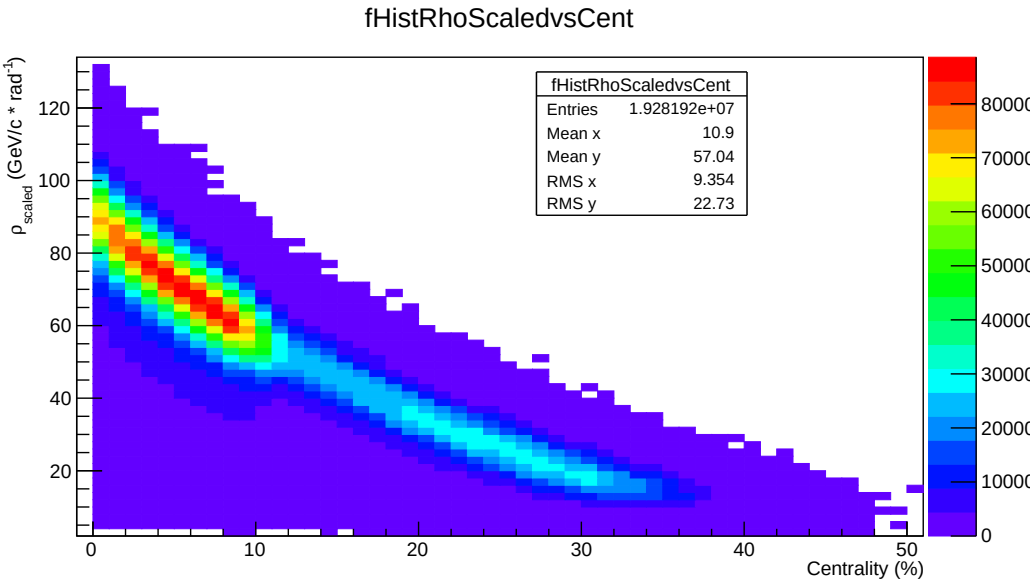

Figure C.12: ρ vs centrality for 1.0+ GeV/c tracks. Calculated for charged jets and scaled up.

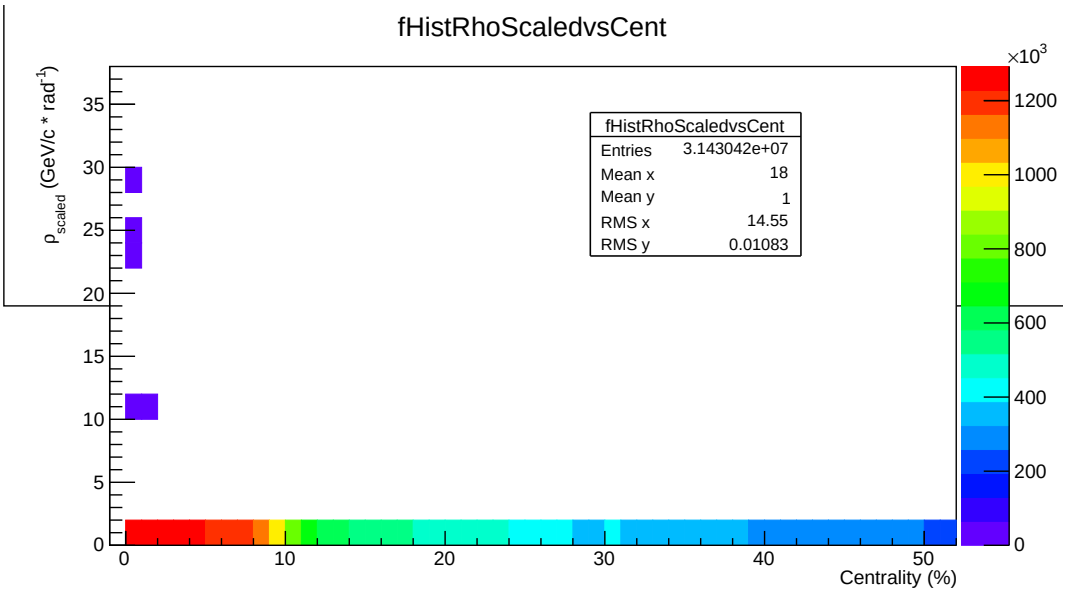

Figure C.13: ρ vs centrality for 2.0+ GeV/c tracks. Calculated for charged jets and scaled up.

Vita

Joel Mazer was born in Wilkes-Barre, PA. He attended Lake-Lehman High School in Lehman, PA. After graduation, he headed to Pennsylvania State University where he began pursuing Computer Engineering and Mathematics. After 2 years, his main focus changed from Computer Engineering to Physics. He graduated with his Bachelors degree in Physics and a Minor in Mathematics in May of 2009. After graduation, he continued work for Pennsylvania State University by teaching various undergraduate Physics labs, conducting research in the Astrophysics Department, and helping the instructional effort of the Physics Department.

In August 2010 he accepted a graduate teaching assistantship from The University of Tennessee - Knoxville in the Department of Physics and Astronomy. While at The University of Tennessee - Knoxville, Joel joined the Relativistic Heavy Ion Physics research group where he began studying jets as part of the ALICE Collaboration at CERN. He received his Masters of Science degree in Nuclear Physics in December of 2013. He continued his education at the University of Tennessee - Knoxville and defended his PhD in November of 2016. He will formally graduate with his Doctor of Philosophy degree in Nuclear Physics in May of 2017.